Blast and Impact Response of Elastomer-coated Concrete

Chanel Fallon

Peterhouse

University of Cambridge

This thesis is submitted for the degree of

Doctor of Philosophy

December 2018

Abstract

With global security concerns at the forefront of political and industrial agendas, growing attention is being focused on strategies to protect critical infrastructure from the detrimental effects of blast and impact. While new structures can be designed with this threat in mind, existing, ageing infrastructure remains vulnerable. Structural retrofit for blast and impact mitigation is one solution to this problem.

This work considers one practical, cost-effective retrofit solution: the application of a spray-on elastomer coating to concrete structural elements. While encouraging results have been reported in the literature for masonry and steel substrates, it remains to be understood if, and by what mechanism this retrofit can enhance the blast and impact resistance of concrete structures. The objective of this work is to understand the blast and impact response of elastomer-coated concrete and hence, to establish design guidelines, informing on effective implementation of this retrofit solution.

The response characteristics of concrete and elastomer materials are established and modelled across a range of stress states and loading rates, from quasi-static to dynamic. Numerical modelling and analytical techniques are used to interrogate the blast response of elastomer-coated concrete targets. It is found that commercially available coatings are most effective in regimes where there is severe blast-induced concrete damage, though they offer limited benefit during fluid-structure interaction and during dynamic flexure. Next, high speed experimentation is performed to assess the impact response of elastomer-coated concrete. The addition of a coating contributes a significant protective benefit in this regime. Numerical models are developed and used to establish the mechanisms of protection. Finally, simple analytical models are proposed, which reveal key parameter sensitivities, thus informing on effective coating design for concrete impact damage mitigation.

Declaration

I hereby declare that, except for commonly understood and accepted ideas, or where specific reference is made to the research of other authors, this dissertation is the result of my own work and includes nothing which is the outcome of work done in collaboration. The contents of this dissertation are original and have not been submitted in whole or in part for consideration for any other degree or qualification at the University of Cambridge, or any other University or similar institution. This dissertation contains approximately $54,000$ words including appendices, bibliography, footnotes, tables and equations and has 85 figures.

Chanel Fallon
December 2018

Acknowledgements

I would like to express my sincere gratitude to my Supervisor, Dr Graham McShane for being so generous with his time, advice and insights throughout my PhD. In addition, I am very grateful to the George and Lillian Schiff Foundation at the University of Cambridge for their financial support that allowed me to freely pursue my research of choice.

I would like to express thanks for the excellent technical support provided to me by Mr Simon Marshall, Mr Stefan Savage, Mr Graham Smith, Mr Len Howlett, Mr Phil McLaren and Mr Daniel Porter.

Furthermore, I would like to acknowledge the support provided to me by Peterhouse and Corpus Christi College at the University of Cambridge: my homes away from home.

Finally, to my family: my Mother, Helena, Father, Jim and Sister, Nicole:
thank you for simply everything.

Contents

CHAPTER 1

Introduction

With growing levels of concern surrounding the threat of malevolent attack, new strategies are needed to protect civilian infrastructure and its inhabitants from blast and impact events.

Upon detonation of an explosive device, rapid expansion of combustion gases generates a shock front which propagates radially outwards through the surrounding medium (typically, air). However, the blast pressure pulse itself is not the only hazardous consequence of an explosive event; the resulting fragmentation is often considered to pose the most significant risk to human life and to surrounding urban infrastructure [1]. Fragmentation is typically classified as either: (i) primary fragmentation (the high speed ejection of the material or casing comprising the explosive device) or (ii) secondary fragmentation (as a result of the blast pressure pulse and primary fragments interacting with nearby structures). Design for such extreme load events presents industry with a significant number of challenges, compounded by the lack of guidance provided by current building codes of practice [2].

In recent years, there has been increasing interest in the development of protective strategies that combine practicality and cost-effectiveness in the design of both new-build projects, and in the retrofit of older buildings, against the evolving threat of improvised explosive devices (including blast and fragment impact events). Although protective performance of the chosen solution is key, careful consideration must be given to reducing cost, ease of installation, low life-time maintenance requirements and preserving aesthetics.

Elastomeric materials have been widely investigated for their ability to enhance blast and impact resistance. The protective effect contributed by these materials has been reported in the literature in the context of a number of protective strategies: metallic bilayer and laminate structures [3–7], sandwich panel configurations [8–10], combat

helmet suspension pads [11–13] and composite panel retrofits [14, 15], to name but a few. A range of mechanisms have been postulated to explain the elastomer's blast and impact mitigating effects (for example, impedance mismatching [3], an impact-induced glass transition [3, 4] and projectile nose-shape changing effects [7]) but this still remains a topic of significant debate between researchers.

Of particular interest to this investigation is the use of spray-on elastomer coating retrofits, applied to existing urban infrastructure. Their spray application gives these coatings a distinct advantage over other candidate retrofits which are often more expensive and difficult to install. Early experimental blast trials examined such coatings applied to masonry wall structures which yielded encouraging results [16, 17]. Retrofitted walls were able to maintain structural integrity for significantly higher blast intensities and further, the coating was found to act as an effective fragment catcher, reducing the debris ejected from the damaged masonry.

Despite the potential demonstrated for spray-on elastomer coatings, a very limited number of studies have extended consideration to the retrofit of concrete and reinforced concrete (RC) structures. Concrete appears an ideal candidate to benefit from this type of retrofit, representing the most significant proportion of the ageing, vulnerable infrastructure in today's built environment. However, understanding the dynamic response of concrete itself can be particularly challenging. Its quasi-brittle, nonlinear characteristics require complex numerical and analytical modelling strategies. Further, experimental impact, and particularly blast testing, are often either too expensive or prohibited due to the sensitive nature of the topic. One of the few numerical studies in this area has reported positive results, indicating that the addition of a relatively thin elastomer coating to a RC slab results in significant deflection reductions in response to a simulated blast [18]. However, the mechanism by which the elastomer achieves this effect remains to be understood. Furthermore, to date, the ability of these coatings to contribute to the impact resistance of concrete targets remains to be established.

The objectives of this thesis are thus threefold. A combination of experimental, numerical and analytical techniques are used to:

- Establish and interrogate the influence of a typical, spray-on elastomer coating on the blast and impact response of concrete structural elements.
- Identify and understand the key mechanism(s) at play that contribute to any blast and/or impact mitigating effect contributed by the elastomer coating.
- Develop design guidelines, using the knowledge gained from these studies, to inform on effective implementation of this retrofit solution.

1.1 Thesis outline

To address these objectives, this thesis is structured as follows:

Chapter 2 presents a survey of the literature on the key topics of interest to this study: blast and impact load characterisation; capturing the response of concrete structures when subjected to such dynamic load events; and finally, the various strategies that have been studied to mitigate the effects of blast and impact in the built environment. The chapter concludes with a detailed assessment of the use of spray-on elastomer coatings applied to masonry and concrete structures.

Chapter 3 begins the investigation by establishing a fully-coupled, numerical modelling strategy to capture the response of an elastomer-coated concrete target subjected to simulated air blast loading. Concrete and elastomer constitutive models are developed and used to assess one candidate mechanism for the apparent blast mitigating capability of the elastomer coating: fluid-structure interaction effects.

Chapter 4 establishes the blast response regimes of a reinforced concrete beam using a numerical analysis to vary the intensity of the simulated blast loading. Throughout, emphasis is placed on ascertaining the regimes in which an elastomer coating contributes its greatest protective effect. Analytical modelling is used to further interrogate the regimes and to gain insights into the key parameters at play.

Chapter 5 focuses on establishing the impact mitigating effects of an elastomer coating, applied to a concrete substrate. Dynamic impact experiments are performed to examine the response to relatively heavy (0.1 kg), relatively slow ($45 - 150\,\mathrm{m\,s^{-1}}$) blunt, steel projectiles. A numerical model is developed to simulate these impact indentation experiments with a view to interrogating the mechanism by which the elastomer achieves its protective benefit.

Chapter 6 employs the numerical model developed in Chapter 5 to first, establish the impact-induced damage initiation mechanisms in the concrete and second, to establish the coating influence on these damage mechanisms. A study is then performed to identify and understand the protective effects of the coating.

Chapter 7 develops analytical models capable of predicting the onset of failure for an elastomer-coated concrete target subjected to blunt projectile impact. The key parameter sensitivities are examined to give insights into effective coating design for concrete impact damage mitigation.

Chapter 8 concludes the thesis and presents recommendations for future work.

CHAPTER 2

Literature review

A review of the literature is performed on the core topics of this study. It begins with an overview of the current practices for the characterisation of blast and impact load events. This is followed by a detailed survey of the existing work on the dynamic response of concrete structures, subjected to blast and impact. Examples of the various analytical, numerical and experimental approaches in the literature are presented. Finally, a review of a selection of blast and impact mitigation strategies is performed, with a specific emphasis on structural retrofit solutions. Throughout, the usage of elastomer coatings in these retrofit strategies is noted as they are of particular relevance to this study.

2.1 Blast and impact loading

Design for extreme load events, such as blast or impact, presents industry with a dilemma. Although these events may be very unlikely and costly to design against, they are catastrophic if they occur. Loss of life, human injury and destruction of infrastructure are but a few of the severe consequences. Elevated threat levels related to global security have placed these issues at the forefront of political, industrial and public agendas over recent years. This has posed a number of design challenges, with current building codes of practice providing little or no guidance on extreme load events [2]. The first challenge is to characterise the loading experienced by a structure when subjected to these dynamic loads. The following section presents a brief review of the literature on current practices for the characterisation of blast and impact loading.

2.1.1 Blast loading

In general, explosions can be classified as one of three types of event: physical, nuclear or chemical [19]. The most common example of a physical explosion is the rupture of a vessel containing liquid or gas under high pressure. It is usually an accidental occurrence and forms a shock wave as the contents expand freely in space. A nuclear explosion is caused by the fusion or fission of the nuclei of atoms. The resulting energy heats the surrounding air, causing it to expand, forming a blast wave. When used as a weapon, nuclear explosions are typically the largest and most destructive. A chemical explosion involves the exothermic decomposition (or combination) of fuel elements. In the case of materials such a trinitrotoluene (TNT), the molecule decomposes to generate combustion gases at high temperatures. The rapid expansion of these gases creates a shock wave that generates the explosive effect. In this work, the focus is on the particular case of chemical explosions: more specifically, the case of *air blast* — the detonation of conventional high explosive material, such as TNT, in air.

2.1.1.1 Blast load characteristics

Upon detonation, the rapid expansion of combustion gases generates a shock front which propagates radially outwards from the source of the explosion. The shock wave is characterised by a sharp discontinuity in pressure which reaches a peak value, p_s above atmospheric pressure, p_0. Figure 2.1 illustrates the typical pressure-time history of a blast wave observed at a stationary point, some distance away from the blast source. When the blast wave arrives at the stationary measurement point, there is a sharp discontinuity in pressure up to a value, p_s known as the *peak overpressure*. The pressure decays back to atmospheric level in a time, t^+ known as the *positive duration time*. This is usually followed by a negative (suction) phase where the pressure reduces below atmospheric conditions to a value, p^- before returning to atmospheric pressure, p_0 in a time t^-, known as the *negative duration time*.

A number of equations have been proposed to describe the typical blast wave profile illustrated in Fig. 2.1. One of the most frequently used relationships is a modified form of Friedlander's equation, Eq. 2.1, where b is a dimensionless waveform parameter [19].

$$p(t) = p_s \left(1 - \frac{t}{t^+}\right) e^{-(b\,t/t^+)} \tag{2.1}$$

Figure 2.1: A schematic representation of a typical blast wave overpressure profile, as presented by Kambouchev [20]. Reproduced from [20].

Indeed, more complex formulas have been proposed in the literature which provide even better agreement with experimental data [21]. However, it is often acceptable to make the simplification of neglecting the negative phase of the blast wave [22]. It contributes only a small negative impulse to the overall impulse and, since the underpressure would tend to reduce any transverse deflections, it is conservative to neglect it for structural analysis. This yields a much simpler expression for the typical blast wave profile. The most simple approximation is that of an exponential profile:

$$p(t) = p_s \, e^{-\frac{t}{t_i}} \qquad 0 \leq t \leq \infty \tag{2.2}$$

Thus, the incident impulse of the positive phase is given by:

$$I_i = \int_0^\infty p(t) \, dt = p_s \, t_i \tag{2.3}$$

where t_i is the decay time.

When a shock front is reflected, for example, from normal interaction with a fixed rigid wall in its path, the resulting *reflected* pressure, p_r is magnified compared with its incident value. Kambouchev [20] notes the nonlinear dependence of the reflected pressure on the magnitude of the incident shock pressure due to gas compressibility effects in air. Thus, a pressure reflection coefficient, C_R is defined [20]:

$$C_R = \frac{p_r}{p_s} = 2 \, \frac{7p_0 + 4p_s}{7p_0 + p_s} \tag{2.4}$$

From Eq. 2.4, it can be derived that the reflected pressure ranges from a minimum

of twice the incident pressure, to a limiting factor of eight times, for increasingly strong shocks in air.

Determining blast parameters

It is often useful to be able to determine the key blast parameters, namely, the peak overpressure, p_s and incident impulse, I_i based on physical quantities of the explosion of interest. To achieve this, there are a number of techniques described in the literature including graphical, empirical formulae and computer code.

In one of the most thorough bodies of work in this field, Baker *et al.* [21, 23] provide blast parameter data in a graphical format based on a large number of experimental blast trials. Often, however, empirical formulae are preferred, simply due to the ease of implementation. One popular set of empirical equations are those of Kingery and Bulmash [24], which define blast parameters as a function of scaled distance, Z:

$$Z = \frac{R}{W^{\frac{1}{3}}} \tag{2.5}$$

where R is the stand-off distance between the source of the explosion and the point of measurement in metres, and W is the mass of the explosive in units of kg of TNT.

In the literature, it is often the case that blast parameters are presented for a certain reference blast and a scaling law is used to obtain the blast parameters for the explosion of interest. The most common reference case considers the detonation of 1 kg of TNT in air under atmospheric conditions. For a chemical explosion produced from the detonation of high explosive, the Hopkinson scaling law is generally accepted as being the most appropriate [22]. This states that for two charges of the same explosive material, detonated in the same atmospheric conditions, a similar blast wave is generated at equivalent scaled distances, Z defined by Eq. 2.5.

The proposed Kingery and Bulmash empirical relations [24] are also based on a large number of experimental trials. These equations have been implemented in the US Department of Defense manual on the design of structures to resist accidental explosions (UFC-3-340-02, previously TM-5-1300) [25]. In turn, they have formed the basis for the automated CONWEP computer code [26] which has been incorporated into various finite element packages including ABAQUS/Explicit [27]. It is noted that because of the commercial significance of Kingery and Bulmash's work [24], it is not readily available in the public domain [22].

An alternative set of empirical relationships, proposed by Kinney and Graham [28]

are presented in Eqs 2.6 to 2.8. They derive values for the peak overpressure, p_s, positive duration, t^+ and incident positive impulse, I_i in terms of the scaled distance, Z:

$$\frac{p_s}{p_0} = \frac{808\left[1+\left(\frac{Z}{4.5}\right)^2\right]}{\sqrt{\left[1+\left(\frac{Z}{0.048}\right)^2\right]\left[1+\left(\frac{Z}{0.32}\right)^2\right]\left[1+\left(\frac{Z}{1.35}\right)^2\right]}} \tag{2.6}$$

$$\frac{t^+}{W^{\frac{1}{3}}} = \frac{980\left[1+\left(\frac{Z}{0.54}\right)^{10}\right]}{\left[1+\left(\frac{Z}{0.02}\right)^3\right]\left[1+\left(\frac{Z}{0.74}\right)^6\right]\left[1+\left(\frac{Z}{6.9}\right)^2\right]^{\frac{1}{2}}} \quad \text{ms kg}^{-\frac{1}{3}} \tag{2.7}$$

$$I_i = \frac{0.067\sqrt{1+\left(\frac{Z}{0.23}\right)^4}}{Z^2\sqrt[3]{1+\left(\frac{Z}{1.55}\right)^3}} \quad \text{bar ms} \tag{2.8}$$

In work by Florek [29], Kinney and Graham's [28] empirically derived blast parameters are compared with that of Baker [23] and the CONWEP code [26]. It is found that the peak overpressures match extremely well for $Z < 10$ and that although the predicted incident impulses are slightly greater than those predicted by Baker [23] and CONWEP [26], there is good agreement. In contrast, Kinney and Graham's prediction for the positive duration, t^+ is in poor agreement with Baker [23] and CONWEP [26]. It is noted that the positive duration time, t^+ given by Eq. 2.7, is not equivalent to the decay time, t_i defined in Eq. 2.2. Rather, the decay time can be calculated as, $t_i = I_i/p_s$ (Eq. 2.3) where p_s is given by Eq. 2.6 and I_i is given by Eq. 2.8.

2.1.2 Impact loading

When designing for an explosive load event, it is important not only to consider the effects of the blast pressure pulse, but also the resulting impacts from fragmentation. Generally, fragmentation can be classified as: (i) primary fragmentation or (ii) secondary fragmentation. Primary fragmentation occurs upon detonation and is a result of the high speed ejection of the material or casing surrounding the explosive device. Primary fragments are typically small, with irregular geometry and can have very high velocities. Secondary fragmentation results from both the blast pressure pulse and primary fragments interacting with nearby structures. Usually, secondary fragments are larger, with lower initial velocities than primary fragments [30].

2.1.2.1 Impact load characteristics

Impact load events can be characterised by several variables: (i) the projectile impact velocity and angle of incidence, (ii) the geometry and material properties of the projectile and (iii) the geometry and material properties of the target.

Specifically considering fragmentation impacts that arise from an explosive load event, Dusenberry [30] provides a comprehensive review of the current practices employed in the characterisation of primary and secondary fragmentation. Based on an assumed primary fragment shape and mass, the initial velocity may be calculated using the Gurney method [31]. Based on a series of experimental trials, Gurney states that the initial velocity of primary fragments produced from a cylindrical-cased explosive charge is a function of the explosive output energy and the ratio of the explosive charge weight to casing weight.

Secondary fragmentation, on the other hand, is much more difficult to characterise as it is represented by a wide array of fragment sizes, shapes and initial velocities. Dusenberry [30] presents graphical and empirical methods to predict the initial velocity of a secondary fragment, depending on whether it is initially unconstrained or constrained before the explosive event. Further, to establish the hazard that impact from a fragment poses to a certain target, the fragment trajectory and final velocity need to be determined, based on knowledge of the initial velocity, stand-off from the target and drag forces. The determination of fragment impact velocities, produced from an explosive event is beyond the scope of the present study. However, its importance is noted and forms the basis for a discussion of the *combined loading* phenomena, reviewed in Section 2.2.3.

The discussion here is simplified to consider probably the most fundamental basis for classification of impact events: the projectile impact velocity, as this has the greatest influence on the range of phenomena observed. A conventional laboratory drop tower apparatus can achieve impact speeds in the range, $0 - 25\,\mathrm{m\,s^{-1}}$, usually considered as low speed impact events. High velocity impact, at sub-ordnance velocities in the range $25 - 500\,\mathrm{m\,s^{-1}}$ can typically be achieved using laboratory gas gun apparatus. Higher impact speeds can be classified as ordnance ($500 - 1300\,\mathrm{m\,s^{-1}}$) and ultra-ordnance velocities ($1300 - 3000\,\mathrm{m\,s^{-1}}$), typically achieved by conventional guns and special-purpose guns, respectively [32]. This review will mostly focus on high velocity impact events, at sub-ordnance velocities which are more akin to impact from secondary fragmentation rather than primary.

2.2 Dynamic response of concrete structures

For many years, concrete has been of interest to both civil and military engineers in the design of infrastructure to resist the detrimental effects of both blast and impact. These load events may be accidental (*e.g.* pressure vessel explosion, forces of nature, vehicle and aircraft crashes) or malicious (*e.g.* terrorist bombing, the resulting fragmentation, ballistic weapons). A recent European Commission, Joint Research Centre technical report [33] has highlighted that the current Eurocode standards provide little or no guidelines for designing against these extreme load events. Although Eurocode EN 1991-1-7 [2] gives guidance for the cases of accidental load events, it is largely focused on the particular scenarios of impact from vehicle collision and internal gas explosion. As a result of this lack of uniform, early-design-stage guidance, designers have adopted other approaches for assessing how blast and impact loading affects key structural elements.

In this section a review of the large body of research that exists on the dynamic response of concrete structures is presented. Typically, researchers tend to employ three approaches in their analysis — analytical, numerical and/or experimental. Examples of each approach in the analysis of concrete's response to blast and impact will be considered.

2.2.1 Response to blast

2.2.1.1 Analytical approaches

One of the most common methods employed by civil engineering professionals in their preliminary design for blast loading is the use of single degree of freedom (SDOF) systems to model the response of structural elements. The technique is considered applicable to cases where the first mode of vibration dominates and therefore can be considered responsible for the overall structural response. A continuous structure can be transformed to an idealised SDOF system, as illustrated in Fig. 2.2 using the method described by Biggs [34].

The resulting undamped elastic dynamic equilibrium equation is given by Eq. 2.9, where, M is the equivalent lumped mass, K is the spring constant, $F(t)$ is the equivalent applied (idealised blast) loading and $y(t)$ is the vertical displacement. Equation 2.9 can then be solved to provide an approximation of the displacement or rotation at a particular point in the structure. The process is relatively simple for elastic deformations but typically, structural elements are expected to undergo large inelastic deformation when exposed to blast. In this case, designers often must

Figure 2.2: A simple elastic SDOF system for a structural mass, M under the effect of an external force, $F(t)$ where the structural resistance is expressed in terms of the spring constant, K and the vertical displacement, $y(t)$. Reproduced from Ngo *et al.* [35].

turn to explicit time-step numerical approaches to solve the SDOF system.

$$M\,\ddot{y}(t) + K\,y(t) = F(t) \tag{2.9}$$

In designing for blast, it can be useful to consider what loading combination gives rise to a particular level of damage. This damage criterion is often defined as a maximum allowable displacement or rotation for a particular structural element, which can be obtained using a SDOF analysis. Once a particular damage level is defined, a curve can be plotted in load-parameter space which represents constant damage. This is typically achieved by applying the law of conservation of mechanical energy to a SDOF model using the method proposed by Baker *et al.* [23]. The resulting graph is referred to as a p-I (pressure-impulse) diagram. These *iso-damage* curves are illustrated in Fig. 2.3. To the left and below the curves, represent combinations of pressure and impulse that will not cause the specified damage level whereas above and to the right of the curves represent blast loads which cause damage in excess of the specified level. In terms of loading, the p-I diagram can be split into three zones: impulsive loading (large magnitude loads but short in duration); quasi-static loading (very long duration, low magnitude loading); and dynamic loading (the zone lying between the impulsive and quasi-static loading zones). These zones are highlighted in Fig. 2.3.

The accuracy of a SDOF approach depends on the selection of an appropriate SDOF system to represent the governing failure mechanism of the structural element [30]. While most SDOF models are used to capture the flexural response of a structure, this may not be the most critical response characteristic, particularly for high intensity blast loading of concrete structures where brittle shear failure may prove critical. In the 2008 work of Shi *et al.* [37], a novel way of measuring reinforced con-

Figure 2.3: A typical pressure-impulse (p-I) diagram. Adapted from [36].

crete column damage is proposed that encompasses both shear and flexural damage — by assessing the RC column's axial load carrying degradation. By performing a series of numerical simulations, the axial load carrying capacity is assessed, degrees of damage are defined and an analytical formula is postulated to predict the shape of the p-I curve.

In general however, SDOF models are frequently criticised for being over-simplistic which has prompted some authors to implement a much more complex, multi degree of freedom (MDOF) approach which is capable of incorporating greater material detail. The work of El-Dakhakhni *et al.* [38] is one such example where a structural member is replaced with a series of discrete, connected nodes with material properties concentrated at each of these nodes. While this technique is capable of producing more accurate results, it is at the expense of time and ease of use and is therefore not favoured by industry. Further, SDOF and MDOF models of individual structural elements do not account for the interaction between connected elements, the phasing of their responses or actual boundary conditions. Therefore, these models provide little insight into the response of the overall structural system [30].

Other analytical approaches tend to use simplifying assumptions, such as rigid-perfectly plastic material behaviour or deformation shape functions that approximate global behaviour. Jones [39] defines a number of analytical solutions for the behaviour of rigidly-perfectly plastic plates, beams and shells, loaded dynamically. These solutions are widely used in the literature for metal plates subjected to blast loading [40, 41], but less so for reinforced concrete. In one notable exception, Luccionia and Luege [42] examine concrete pavement slabs under blast loading. Assuming the slab can be approximated as a circular plate, simply supported on its edges (and

that the soil foundation does not alter its collapse mechanism), an upper limit on the ultimate loading pressure is estimated using Lubliner's plasticity solutions [43].

Although these analytical approaches may be used by industry as an early-design-stage tool, it is acknowledged that they are over-simplistic, particularly when applied to concrete or indeed, reinforced concrete (RC) structures. Instead, researchers in the literature have often turned to experimental and numerical approaches to gain a greater understanding of the dynamic response of concrete.

2.2.1.2 Numerical approaches

While analytical approaches may be appropriate for early design stage estimations, finite element analysis (FEA) provides better confidence in a design. Complex and time-consuming, full-scale FEA allows the user to define the material model, geometry and loading parameters with a great deal of accuracy. Importantly, it can account for interactions between each of these design parameters for example, strain rate effects experienced by certain materials. In addition, FEA is an invaluable tool for modelling scenarios that are difficult to recreate experimentally. This is particularly relevant to blast experiments where the equipment, time and space requirements often preclude industry (and often academic researchers) from performing full-scale tests.

Explicit finite element analysis is typically employed for the modelling of highly dynamic events such as blast. Explicit formulations of the equations of motion express the displacement at a given time step in terms of displacements, velocities and/or accelerations at previous time-steps. These equations are solved at each node, using the current material properties and geometry at that point in time. An Implicit solution scheme, on the other hand, expresses the displacement of each node at a point in time in terms of all displacements, velocities or accelerations at that time; thus, the equations of motion of the entire system are solved simultaneously [30]. Explicit FEA is much more efficient for modelling the dynamic response of structures, particularly those which exhibit material and geometric non-linearities. However, it must be used with caution, as explicit formulations have a critical time-step above which the solution becomes unstable. Thus, FE models must be carefully validated by comparison with experimental test data and known analytical solutions in order to provide confidence in predictions.

Several commercial codes are employed in the literature for modelling the dynamic response of concrete, such as LS-DYNA [44], AUTODYN [45] and ABAQUS [27]. The success of these codes is heavily reliant upon being able to achieve a repre-

sentative concrete constitutive model. Typically, concrete must be idealised as a homogeneous continuum, with model definitions based on the macroscopic uniaxial or triaxial response. There is much debate in the literature regarding the optimum material model to capture the dynamic response of concrete, but most share a number of common features. For elastic-plastic deformation, non-linear plasticity theory is usually employed with a pressure-sensitive yield surface and a non-associated flow rule. A failure surface defines the onset of strain-softening in both tension and compression regimes. A damage model may be included, defined by the residual stress states. The following discussion reviews the numerical approaches in the literature for capturing the blast response of concrete structures. It is noted from the outset that there are very few examples of fully defined concrete constitutive models in the published literature.

The most popular explicit, nonlinear, finite element programme used in the literature for modelling the dynamic response of concrete is LS-DYNA [44]. This code provides a large number of built-in material models that require minimal user input, thereby greatly simplifying the problem of fully defining a concrete material model. Zhao and Chen [46] used LS-DYNA to model a square, reinforced concrete slab subjected to "close-in" blast loading and found that their results agreed well with experiment in terms of predicting damage characteristics such as spall and cracking. They used an Arbitrary-Lagrange-Euler approach in modelling the explosive, air and concrete. For the concrete, *material type 72* (*Mat_Concrete_Damage_Rel3*) was implemented, which is a form of the Karagozian and Case model [44]. This is a plasticity-based model using three shear failure surfaces and includes damage and strain rate effects [46]. The user supplies a value for the unconfined compressive strength and LS-DYNA generates the required parameters automatically. The same concrete model was employed by Lin *et al.* [47] and Yan *et al.* [48] in their studies on the response of RC panels and beams, respectively under close-in blast. In both cases, good agreement with experimental results was reported in terms of maximum deflections and cracking and spall distributions. Pantelides *et al.* [49] instead chose to use *material model 159* in LS-DYNA to model RC panels subject to blast detonations. This is a smooth, surface cap model *i.e.* there is a continuous intersection between the shear (failure) surface and the hardening compaction surface (cap). The damage formulation models both strain softening and modulus reduction. The user is only required to specify the concrete compressive strength and the maximum aggregate size. Predictions for the induced damage agreed qualitatively with that observed in experiments.

Another popular numerical technique for assessing the dynamic response of RC is the use of hydrocode software such as AUTODYN [45]. It is marketed as being

particularly suited to simulating the response of materials to severe loadings from impact, high pressure or explosions. Wang *et al.* [50] developed a sophisticated model in AUTODYN capable of predicting damage in square reinforced concrete slabs under close-in explosion. The Riedel, Hiermaier and Thoma (RHT) model [51] was implemented to model the concrete material. This is a macroscale material model incorporating strain rate effects and damage. The shear strength is described through the use of three surfaces; the inelastic yield surface, the failure surface and the residual surface, each dependent on pressure. Wang *et al.* [50] provide a detailed description of the theory behind the RHT model and include a list of the parameters implemented. The numerical results were compared with their experimental study and showed good agreement in terms of the cracking and spall patterns predicted.

Astarlioglu *et al.* [52] instead chose ABAQUS [27] to analyse the behaviour of RC columns subjected to combined axial and blast-induced transverse loading. Accurate predictions of midspan deflections were achieved. A modified Drucker-Prager-Cap model was used for the concrete but no details are presented on the parameters implemented. Luccionia and Luege [42] also employ a Drucker-Prager model in ABAQUS to examine concrete slabs on a soil foundation subjected to blast charges suspended above them. They performed a similar analysis using the hydrocode software, AUTODYN but due to the greater functionality available, they were also able to model the detonation process and the propagation of the pressure wave in the air. Both techniques were capable of approximately reproducing the deformation and failure shape of the plate observed experimentally.

In a further variation, Yi *et al.* [53] chose the Concrete Damaged Plasticity (CDP) model in ABAQUS to predict the response of shallowly buried, RC rectangular box structures subjected to blast loading on their top surface. Comparing results with experimental observations, it was concluded that the model was capable of predicting the dynamic responses and typical flexure, flexure-shear and direct shear failure modes.

It is apparent that there is a great deal of debate surrounding the optimal choice of modelling software and concrete constitutive model in the literature. To validate the chosen modelling approach, many authors choose to compare FE predictions with results from experimental blast trials.

2.2.1.3 Experimental approaches

Experiments are a key tool in assessing the response of concrete structures under blast loads. They serve as the benchmark in validating both analytical and numerical approaches and are invaluable in gaining a thorough understanding of how a complex material such as concrete behaves under dynamic loading. Unfortunately, testing is expensive due to difficulties in achieving appropriate set-up and safety requirements, so it is seldom performed by industry. Further, only a select group of researchers have capabilities in this field and since their results can be of military/defence importance, they may not be published. A selection of the available literature on blast experiments on concrete structures is now presented.

A series of experiments were performed by Silva and Lu [54, 55] in order to ascertain what blast intensity (in terms of charge weight and stand-off distance), gives rise to particular levels of damage in RC structures. This is a popular technique in the literature, whereby the damage inflicted to a RC member is assessed qualitatively and correlated with a "displacement ductility level" in the range $1 - 6$, where a level of 1, say, corresponds to the presence of minor cracking, and a level of 6 to major damage requiring repair. In practice, it is often not permissible to fit strain gauges or displacement measuring devices as they are likely to be damaged during testing. Therefore, descriptions of damage to RC structures under blast are typically limited to visual inspections and post-test measurements of crack widths and slab deformations [55].

Wang *et al.* [50] performed an experimental study on the damage mode of one-way square reinforced concrete slabs under close-in explosion. Full-scale testing was performed on the slabs with the blast intensity varying depending on the weight of explosive placed at a fixed stand-off distance. It was observed that the blast wave passed through the concrete and was reflected back as a tensile wave. There was a resulting high level of cracking and spallation on the bottom face of the slab. Further, it was concluded that as the explosive mass was increased, the failure mode changed from overall flexural failure to local punching failure. These insights were then used to establish empirical criteria for different levels of damage.

In an extension of this study, Wang *et al.* [56] addressed the scaling of the dynamic response of one-way square reinforced concrete slabs under close-in blast. As described, full-scale blast experiments can be prohibitively complex and costly so it would be desirable to achieve accurate results using a scaled-down experiment. Their results show good agreement for macrostructure damage and fracture patterns but found that larger specimens experienced more severe local damage than their scaled-down counterparts. A similar experimental scaling study was performed by

Zhang *et al.* [57] for RC beams under close-in blast loading and similar results were observed. An empirical equation was also proposed to correct the scaling model to account for the observed size effects.

In conclusion, it is clear that published results from experimental blast trials are limited and typically hindered by lack of appropriate instrumentation. Thus, assessment of the response of concrete structures subjected to blast is often restricted to qualitative statements. Further, many authors have recognised the necessity for more experimental studies to explore the interplay between loading intensity, geometrical and material effects [50, 56].

2.2.2 Response to impact

The wide range of projectiles that may be produced as a result of an explosive event in an urban environment means that developing a design strategy is not trivial. Further, the various local and global phenomena observed are highly dependent on the target structure and the rate of loading.

As illustrated in Fig. 2.4 and discussed by Li *et al.* [58], concrete may exhibit various phenomena in response to projectile impact:

- Perforation: the projectile completely penetrates the target.
- Penetration: the projectile penetrates part way through the thickness of the target, without complete perforation.
- Scabbing: concrete fragments are ejected from the distal face of the target.
- Spalling: concrete fragments are ejected from the proximal face of the target.
- Cone cracking and plugging [58]: the formation of a cone-shaped crack in the concrete at the impact site. In severe cases, this could lead to the formation of a punching shear plug.
- Radial cracking [58]: macroscopic, radial concrete cracks emanating from the impact site.
- Global target response: the overall structural response which may be dominated by bending flexure, shear and/or a membrane response.

Historically, studies on the response of concrete structures subjected to impact load events has been driven by military interest for the design of protective structures to withstand missile impacts. However, in recent years, the nuclear industry has driven forward this research, with the aim of designing effective containment vessels

Figure 2.4: Penetration and perforation mechanisms of concrete slabs by non-deforming projectiles. Reproduced from [59].

for nuclear reactors. Much of the research in this field tends to focus on the *local* impact response of concrete, with reviews presented by Kennedy [59], Corbett [60] and Li *et al.* [58], to name but a few. The key themes will be discussed here but consideration will also be given to studies on the *global* target response where informative. This review is restricted to considering hard, non-deforming projectiles, striking the target normally. Consideration will be given to concrete slab, beam and plate target geometries and although not the focus of the present investigation, variation in projectile nose-shape geometries are noted throughout.

2.2.2.1 Analytical approaches

The local response of concrete targets subjected to projectile impact is usually assessed in terms of four quantities in the literature:

- Perforation limit: the minimum target thickness to prevent perforation by the projectile.
- Penetration depth: the depth to which the projectile penetrates the target and is arrested without perforation.
- Ballistic limit: the minimum initial projectile velocity required to perforate the target.

- Scabbing limit: the minimum target thickness required to prevent scabbing.

Researchers must often rely on empirical or semi-empirical relationships for estimates of these local damage metrics, often based on curve-fitting to experimental data. Li *et al.* [58] provide a comprehensive review of the various formula available. One of the most widely recommended [58–60] formula is the Modified National Defense Research Committee (NDRC) formula. It has a semi-analytical basis and has been shown to hold well when extrapolated over a wide range of variables. The NDRC formula predicts the penetration depth, x_{pd} from a *G function* equation:

$$G = 3.8 \times 10^{-5} \frac{N^* M}{d_p \sqrt{\sigma_{cu}}} \left(\frac{V_0}{d_p}\right)^{1.8} \tag{2.10}$$

where

$$\frac{x_{pd}}{d_p} = 2\, G^{0.5} \quad for \quad G \geq 1 \tag{2.11}$$

or

$$\frac{x_{pd}}{d_p} = G + 1 \quad for \quad G < 1 \tag{2.12}$$

where N^* is the nose-shape factor for the projectile (1.0 for a blunt nose), d_p is the diameter of the projectile, M is the mass of the projectile and K is the target penetrability factor. Kennedy [59] proposed that the K factor was proportional to the square-root of the reciprocal of the ultimate compressive strength of the target concrete, σ_{cu} ($K = 180\sqrt{\sigma_{cu}}$). Further, he proposed relationships for the perforation and scabbing limit [59]. Like the majority of the empirical relationships proposed, the modified NDRC formula does not account for the effects of steel reinforcement. Penetration tests by Sliter [61] confirmed that penetration and scabbing metrics displayed only a weak dependence on reinforcing ratio while perforation resistance was improved only with very heavy reinforcement.

A number of military design codes, such as the US Army Manual, TM-5-855-1 [62] and the British Army manual [63] make other formula recommendations for the prediction of perforation, penetration and scabbing limits but the validity of these formula have only been verified over ordnance velocity ranges. Considering low to intermediate impact speeds, the UMIST formula [64] (based on work for the nuclear industry in the R3 Impact Assessment Procedure [65]) have been verified in the sub-ordnance range for the prediction of critical projectile energies to cause cone cracking, scabbing and perforation.

Clearly, significant research has been dedicated to predicting the *local* response of concrete subjected to projectile impact. However, analytical predictions for the *global* response are very challenging and thus limited, often requiring some compu-

tational input. One approach is to employ the SDOF method discussed in Section 2.2.1.1 in relation to blast. Krauthammer *et al.* [66] present an analytical method to understand the dynamic response of impulsively loaded RC beams and one-way slabs. The deformed configuration is computed at every load step and the parameters for a SDOF model are derived. The approach is validated by comparison with experimental measurements of peak and permanent displacements.

In another example, Fujikake *et al.* [67] developed a simple analytical model to predict the maximum midspan deflection of RC beams using a two degree-of-freedom mass-spring-damper model. The model was verified against drop-weight impact tests on RC beams and good agreement was achieved provided overall flexural failure dominated. This work highlights that simple analytical models fail to correctly predict global behaviour once local damage becomes significant; often because these models do not account for the energy dissipated in concrete penetration.

2.2.2.2 Numerical approaches

Often, designers must turn to finite element analysis (FEA) to capture the complexities of the concrete dynamic impact problem. The following section discusses how authors in the literature use numerical models to achieve good predictions of local responses, global responses and failure modes — something that analytical techniques can rarely achieve.

Numerical modelling strategies for analysing the impact response of concrete follow the same trends as those described for blast, in Section 2.2.1.2. Explicit solution schemes are favoured and the same commercial FEA codes tend to be employed, namely LS-DYNA, AUTODYN and ABAQUS as discussed. Once more, there is debate in the literature regarding the best material constitutive model to represent concrete, though most consider it as a solid continuum which exhibits pressure-dependent plasticity.

Adhikary *et al.* [68] used LS-DYNA [44] to perform numerical simulations of static and low velocity impact of RC beams. A parametric study was performed using *material model 159* for the concrete constitutive model, a continuous surface cap model with strain rate effects included. Most severe midspan deflections were reported for large impactor masses, lower reinforcement, lower concrete compressive strength and fixed-fixed end boundary conditions. Tai and Tang [69] also used LS-DYNA but instead chose the Johnson-Holmquist concrete material model. The impact of ogive-nosed projectiles on RC targets was modelled over the velocity range $300 - 1100\,\mathrm{m\,s^{-1}}$ and reasonable agreement was obtained with experimental obser-

vations [70].

Trivedi and Singh [71] used a different modelling approach to simulate a RC slab, impacted with a cylindrical drop hammer. Using ABAQUS [27], they employed the Concrete Damaged Plasticity (CDP) model and validated it against an experimental study from the literature [72]. Many of the material model parameters are presented. Their model was capable of predicting both local and global modes of failure through measurable parameters such as strain-based failure criteria, shear failure criteria, rebar strain and tensile damage patterns.

Mokhatar and Abdullah [73] presented a review of the concrete material models available in ABAQUS to capture impact loading of RC slabs. Three constitutive models are considered — the Drucker-Prager model, the Cap-Plasticity model and the Concrete Damaged Plasticity (CDP) model [27]. For each case, the authors have presented a comprehensive list of the modelling parameters (though no details are provided on how these parameters are derived). All models were capable of providing reasonable predictions of the RC slab response but some performed better than others, depending on the quantity of interest. For example, the Cap Plasticity model provided the closest agreement to the experimentally measured impact force-time response whereas the CDP model enabled interrogation of the damage wave propagation and final crack pattern, which agreed well with experimental observations.

The studies presented here highlight the necessity for careful consideration of the modelling software and concrete constitutive model. In all cases, the chosen model should be validated against known solutions or preferably, experimental tests to provide confidence in the predictions. Furthermore, it is noted that a more detailed interrogation of the popular continuum approaches for modelling the local impact of concrete is required, discussed further in Section 8.2.

2.2.2.3 Experimental approaches

Experimental studies on the impact response of concrete structures typically fall into two categories: (i) low velocity, drop-tower tests and (ii) high velocity gun tests (in the sub-ordnance range). Depending on the target geometry and/or rate of loading, local failure, global structural failure or a combination of both may dominate.

A common aim of experimental studies in this area is to study local damage effects to inform the development of empirical equations. In one notable example, Forrestal *et al.* [74] developed an empirical equation for the penetration depth of ogive-nose projectiles, impacting concrete targets normally. Impact experiments, using a powder

gun apparatus were performed at speeds in the range $250-800\,\mathrm{m\,s^{-1}}$ and good agreement was achieved between experimental measurements and equation predictions. Significantly, a projectile diameter scale effect was identified, limiting the validity of the derived equations over certain ranges of projectile mass and diameter [74, 75].

In a similar approach, Dancygier *et al.* [76] conducted an experimental programme on the impact of high strength concrete (HSC) plates with non-deforming, conical-nosed steel projectiles. While perforation resistance was increased compared with normal strength concrete, it was found that existing formulae (for example, the previously discussed NDRC formula [59]) over-estimated the perforation limit velocity for HSC targets due to the various effects of the concrete components and reinforcement design. This is an important conclusion, flagging up the influence of concrete microstructure on local impact response (which is later discussed in Section 8.2).

Experimental impact studies are particularly useful for examining the interplay between local and global responses and failure modes. Zineddin and Krauthammer [72] investigated the dynamic response of RC slabs under impact loading using drop-weight testing in an effort to understand how different reinforcement layouts influence the damage patterns and failure modes. The global failure modes are particularly sensitive to the rate of loading. For instance, quasi-static loading tends to produce a flexure-dominated response in which spalling and scabbing are most commonly observed. However, a soft impact is more likely to give rise to high stresses at the support region and thus direct shear failure at this location. For more impulsive (shorter duration) impacts, local damage such as punching failure dominates given the time is too short for stress wave propagation.

Kataoka *et al.* [77] illustrated that the failure modes observed are also influenced by the target geometry. RC slabs of different thickness were subjected to moderate velocity impacts ($65-90\,\mathrm{m\,s^{-1}}$) by heavy, 8 kg hemispherical steel projectiles. Perforation was observed for the thinnest slabs whereas thicker slabs experienced a transition from spalling dominated to scabbing with an increase in impact velocity.

This survey of the literature has highlighted the breadth of variables involved in the experimental analysis of the impact response of concrete structures. From microstructural effects to global failure modes, uncertainties are compounded by difficulties in performing high speed impact experiments and instrumenting them effectively. It is clear why there is a lack of uniform design guidance on this topic.

2.2.3 Response to combined loading

Another area of research that remains to be fully explored and understood is that of the *combined loading* scenario. Combined loading considers a blast pressure pulse in combination (either simultaneously or at a time offset) with (one or multiple) fragment impacts. This, of course, is more representative of a realistic explosive load event but is challenging to investigate, both experimentally and numerically.

Leppanen [78] analysed concrete blocks (of dimensions 0.75 m by 0.75 m by 0.5 m) struck by multi-fragment impacts and a blast wave. An explosive charge and multiple ball bearings were suspended above the concrete target. The ball bearings (acting as the fragments) reached velocities of c. 1650 $\mathrm{m\,s^{-1}}$. Post-impact specimens were assessed and subjected to uniaxial compressive and tensile splitting tests to study how the properties of the concrete were influenced. It was concluded that damage was localised in the impact zone and that concrete below twice the depth of the impact zone experienced little damage from blast or fragments. The post-impact compressive tests revealed that there was some increase in compressive strength below the spalling zone, probably due to compaction. The tensile splitting tests suggested that loading the specimen parallel to the cracking direction gave a lower measure of strength compared with loading perpendicular to the cracks. A numerical analysis was performed in AUTODYN using the RHT model for concrete. Predictions of damage were in good agreement with experiments. Leppanen studied the effects of fragment impact alone, and compared the results with the combined blast wave plus fragment impact scenario. The numerical model predicted greater concrete damage for the latter load case indicating that both the blast wave and fragment impact effects must be taken into account when designing for a realistic explosive event.

This synergistic effect was further verified by Nyström and Gylltoft [79], who also used AUTODYN and the RHT model for concrete to study the combined effects of blast and fragment impacts on a reinforced concrete wall. Full details of the material model parameters are presented. The damage caused by combined loading was more severe than the damage caused by adding the results of the blast and fragment impact separately. A SDOF model was employed to estimate wall deflections but in doing so, the limitations of the SDOF approach were exposed. For instance, the SDOF approach failed to capture the energy consumed in penetration and crushing of the concrete, the formation of flexural cracks, and inertia effects.

The combined loading scenario is a multi-physics problem, spanning a range of local and global phenomena to capture the overall structural response. Several com-

mercially available codes for dynamic structural simulations include a Lagrangian processor (typically used for solid continua, such as the structure) and an Eulerian processor (typically for modelling fluids and gases). These must often be combined to model blast and fragmentation loading of structures, and certainly to capture the synergistic effects of combined loading. One alternative is to employ a meshless technique to model the problem. To investigate the synergistic effects of blast and fragmentation impact loading on a concrete wall, Hu and Chen [80] employ one such meshless technique, the material point method (MPM) which is an extension from computational fluid dynamics to computational structural dynamics. Preliminary results on 1D and 2D blast and impact problems have yielded encouraging results but the authors call for more experimental and analytical evidence to verify and validate their proposed technique.

2.2.4 Strain-rate effects and lateral confinement

Blast and impact load events are likely to induce high strain rates in the range $10^0 - 10^3\,\mathrm{s}^{-1}$ [35, 81]. A well known, yet not well understood phenomenon exhibited by concrete is a strain rate sensitive strength enhancement over this particular range of strain rates. This strength enhancement can be quantified in terms of a dynamic increase factor (DIF), which is defined as the ratio of the unconfined dynamic uniaxial compressive strength to its quasi-static value. Many works in the literature have sought to quantify the relationship between the strain rate and the DIF, as illustrated in Fig. 2.5. Further, empirical relationships to estimate the DIF have been proposed by a number of authors [82, 83] as well as being implemented in the CEB design code [84]. It is generally agreed that the strain rate effect becomes significant beyond some critical value of strain rate, typically in the range $10^0 - 10^2\,\mathrm{s}^{-1}$ [81–83]. In recent times, the SHPB (Split-Hopkinson Pressure Bar) technique has been implemented as tool for assessing the dynamic strength of concrete structures and the results appear to confirm this apparent strength enhancement beyond a critical value of strain rate [82, 83].

However, the physical mechanisms that contribute to this strength enhancement are not well understood. A number of theories have been postulated in relation to free water content [85], cement viscoelasticity [58] and lateral confinement [86] for instance. A significant step towards understanding the key mechanisms at play came from Li and Meng's work [86] on assessing the validity of the SHPB technique for testing concrete-like materials. They show that the strain-rate dependence identified using the SHPB technique is caused mainly by the existence of lateral inertia confinement rather than a *genuine* strain rate effect. It is warned that misinterpreting

Figure 2.5: The strain rate effect on the unconfined uniaxial compressive strength of concrete [58, 81]. Reproduced from Bischoff and Perry [81].

this "pseudo-strain-rate effect" may lead to dangerous overestimates of the concrete compressive strength and thus, designers must use caution if they account for the DIF in their calculations.

2.3 Structural blast and impact mitigation strategies

Over the past number of years, industry's attention has become increasingly focused on the idea of designing for resilience, particularly in response to the threat posed by terrorist bomb blasts. Designers must balance a number of competing factors when deciding upon an optimum solution, especially when considering how to protect existing, vulnerable infrastructure. For example, the chosen protective strategy should be economically viable, have no significant maintenance requirements over its life-time and ideally should not detract from the aesthetics of the building.

Often, the simplest solution can be very effective — maintaining sufficient stand-off distance between the blast and target can significantly reduce structural damage. This can be achieved through the use of bollards or walls but often is not practical in cities where lack of space prevails. It is well-known that not only the primary blast effects cause serious human injury, but also the secondary effects, caused by blast debris and structural fragmentation. To protect inhabitants from fragmentation debris in the aftermath of an explosion, "catcher" systems can be fitted to the interior walls. With this technique, fabric must be anchored to the ceiling and floor of a building which may not be feasible for load-bearing walls or walls with

windows [87].

It is well documented that the blast and impact resistance of a structure can be improved by increasing its mass and strength by incorporating additional material or reinforcement. Retrofitting of reinforced concrete beams, walls and slabs using externally bonded steel plates has been attempted in the literature and has been found to successfully increase flexural strength [87]. However, long installation times, poor corrosion resistance, lifetime maintenance costs and material expense has prompted an investigation into alternative material solutions.

The following section will discuss novel material solutions that have been researched in recent years with a view to exploiting their blast and/or impact mitigating capabilities.

2.3.1 Cellular materials

Cellular structures are comprised of a network of repeating struts or plates that interconnect to form cells. The two most common topologies are honeycombs (two-dimensional cellular materials) and foams (three-dimensional cellular materials). The most influential structural property of a cellular structure is its relative density: the ratio of the density of the cellular material to that of the solid of which it is made. Typically, cellular structures possess relative densities of less than 30%, with many much lower than this [88]. This offers the advantage of high specific strength and stiffness properties and thus for many years, cellular structures have been studied with a view to exploiting their properties for protective means. They are particularly efficient in terms of energy absorption where they exhibit a long plateau in their stress-strain response arising from various energy absorption mechanisms such as cell wall yielding, crushing, fracturing or buckling. The level of this plateau, and thus energy absorption capacity can be tailored depending on the cellular material, density, cell size and topology [88].

When designing for structural blast and impact events, researchers have examined the efficacy of implementing cellular materials as protective strategies. Their use as a protective cladding, and more commonly, as the core material of sandwich structures, have been studied extensively. Sandwich structures are structural elements comprised of two stiff, strong face sheets, separated by a lightweight core, often made of a metallic cellular material [88]. Many investigations, both experimental and theoretical, have shown that sandwich structures' performance under dynamic loading is superior to that of monolithic structures of equivalent mass [89–91]. Their enhanced performance when subjected to shock front loading can be attributed to:

(i) increased flexural strength, (ii) fluid-structure interaction (FSI) effects and (iii) energy dissipation via core compression.

The increased flexural strength arises from the strong, stiff face sheets separated by a lightweight core which increases the moment of inertia of the panel without adding much to the weight. This increases the resistance to bending and buckling [88]. It has also been shown that sandwich structures are capable of exploiting FSI effects to reduce the momentum transferred to the structure by a blast (particularly, an underwater blast) [90, 92]. FSI effects were notably discovered by G.I. Taylor in his work on underwater explosions [93]. In brief, Taylor found that when exposed to blast, lighter plates accelerate faster than heavier plates, and as a result of this motion, the impulse transmitted to the structure is reduced.

The focus of many literature studies on the dynamic performance of sandwich structures is on investigating the influence of core topology on resistance to shock and impact loading. A number of core possibilities have been investigated: metallic foams [94, 95], prismatic cores such as hexagonal honeycombs, square honeycombs and corrugated cores [96–101] and lattice structures [102–104]. Examples of typical prismatic core topologies are illustrated in Fig. 2.6.

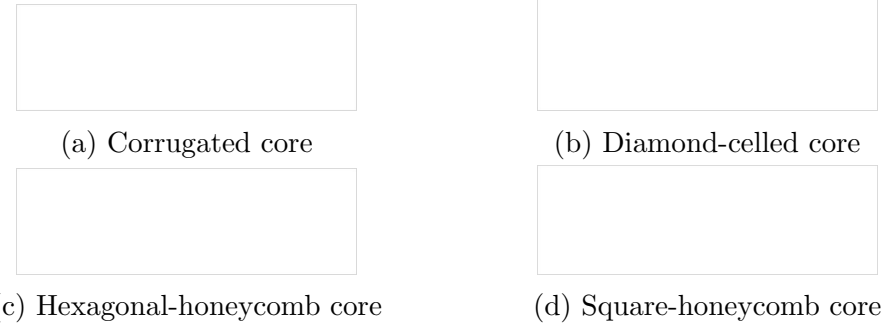

(a) Corrugated core (b) Diamond-celled core

(c) Hexagonal-honeycomb core (d) Square-honeycomb core

Figure 2.6: Sketches of sandwich panels with different core topologies. Reproduced from [90].

Work by Qi *et al.* [105] has considered the retrofit of a concrete panel using a conventional aluminium alloy honeycomb core sandwich panel. The response is compared with an auxetic (negative Poisson's ratio) cored panel by performing drop-weight impact and close-in blast tests. Tests were performed by placing the proposed sandwich panels on the load-receiving face of concrete slabs and adding a steel protective plate on top to prevent local failure (illustrated in Fig. 2.7). Numerical models were developed in LS-DYNA and results showed that both the conventional honeycomb and auxetic cored sandwich panels increased the energy absorption of the steel cover plate by a factor of 2.5. Furthermore, the auxetic core outperformed the conventional core, absorbing 19% more energy.

Figure 2.7: Blast test set-up, performed by Qi *et al.* [105]. Reproduced from [105].

A number of studies have set out to further improve the performance of sandwich panels under blast loading by including ductile interlayers in the sandwich plate design. For example, Bahei-El-Din *et al.* [8–10] studied the inclusion of a polyurea or polyurethane layer and/or elastomeric foam between the outer face sheet and core. These panels demonstrated an impressive ability to absorb incident energy and protect the core from excessive deformation.

There is clearly significant scope for the designer to tailor and tune the properties of the protective sandwich panel to the application of interest. Ongoing work in the literature seeks to develop novel geometries (for example, origami-inspired folded cores [106]) which offer even better mechanical properties and versatility in combination with reduction in manufacture time and cost.

2.3.2 Ceramic armour

Advanced ceramic materials have been extensively studied in relation to their impact mitigating capabilities. Most commonly, they are used in personnel or vehicular protective armour but also have applications in aircraft and structural protective systems. The high hardness of ceramic materials is exploited to defeat the projectile but low toughness results in extensive micro-cracking that significantly reduces resistance to further impacts. Consequently, researchers have proposed a number of ceramic-based armour designs which act to maximise both toughness and hardness in response to an impact event.

Ceramic armour systems are typically comprised of a front monolithic ceramic plate or a ceramic-metal composite, bonded to a high-tensile strength backing mate-

rial [107]. This backing material is often aramid-based or a polyethelene laminate such as Kevlar or Dyneema however, ductile metals such as aluminium plates may also be used [108–110]. In response to a projectile impact, this armour system contributes to the areal and temporal spreading of the impact load due to the dynamic failure processes of the ceramic. This spreading effect reduces the stress on the underlying backing material, thus improving impact performance. Furthermore, significant energy dissipation mechanisms are at play: the fracture and pulverising of the ceramic in response to a projectile impact and the erosion of the projectile tip as it penetrates through the hard ceramic [111]. The backing material serves to delay the onset of tensile failure in the ceramic, thereby enabling further projectile erosion and energy dissipation. Furthermore, the backing material absorbs the kinetic energy of the resulting fragmented ceramic and projectile debris [110]. In some cases, a spall cover may be attached to the impacted face of the armour.

A significant amount of research effort has been dedicated to understanding the dynamic fracture and failure of advanced ceramics and ceramic based armour systems with a view to design for optimum ballistic performance [107, 111, 112]. A number of different ceramics have been investigated including, most commonly alumina ceramics, but also non-oxide ceramics such as carbides, nitrides and borides [111, 112]. Alternative armour systems have also been examined, with the aim of exploiting the enhanced ceramic properties brought about by confinement strategies. Simple techniques such as wrapping the ceramic in a layer of prepreg fabric such as fibreglass is popular [107] but more elaborate systems have been analysed such as encasing in ductile metal [113] or even more advanced, sandwich panel designs [101]. While these techniques significantly improve performance, they come with a weight and cost penalty which has led researchers to consider alternative solutions. For example, metal-ceramic composites (in theory) combine the high hardness and stiffness of ceramics with the high toughness of metals for optimum performance. Materials containing more than 50 % volume metal are classified as MMCs (metal-matrix composites) and those containing more than 50 % volume ceramic as cermets [114]. The low ceramic content, and thus low hardness of MMCs has in general, meant that they are not favoured for impact-facing armour applications [114]. Cermets, on the other hand display high hardness, and much research has analysed how to improve the low toughness of the ceramic phase without excessively sacrificing this hardness [114–117].

In one of the few examples of ceramic armour used for structural protection, Sun *et al.* [118] investigated the use of a novel ceramic armour system designed to enhance the resistance of concrete structural elements to projectile impact. The concrete targets were covered in a layered and staggered system of ceramic mosaic tiles (CMTs)

(a) Front face (b) Back face

Figure 2.8: Typical CMT covering with epoxy adhesive interlayers subjected to drop-weight impact tests by Sun *et al.* [118]. Reproduced from [118].

with adhesive interlayers, illustrated in Fig. 2.8. Two types of interlayer were tested: epoxy and silicone sealant. CMTs are traditionally used for a decorative function but the authors postulate that they can serve an impact-mitigating role. Drop-weight tests and ballistic tests at velocities exceeding $500\,\mathrm{m\,s^{-1}}$ were performed and the resulting damage assessed. A significant beneficial effect was observed with the covered concrete experiencing no damage on the distal surface whereas uncovered concrete exhibited extensive through-thickness cracking. The projectile penetration depth was reduced by up to 77% with the CMT covering in place compared to the uncovered specimens. Although the protective covering with epoxy adhesive interlayers appeared more effective than the silicone sealant, it suffered greater damage due to its higher hardness.

Several researchers have commented on the breadth of design variables in this field and therefore, how it is not possible to recommend one, optimum solution [107, 111, 113]. Desired mechanical properties, including the ability to dissipate projectile impact energy are key but due consideration must also be given to preferred manufacturing routes, material expense and overall weight. Thus, appropriate armour design and material selection must be based upon the particular application of interest.

2.3.3 Composites

2.3.3.1 Fibre-reinforced polymer retrofit

One material solution that has been extensively researched since the early 1990s with regard to retrofitting for enhanced blast and impact resistance is fibre reinforced polymer (FRP) composites [87]. When compared with traditional methods

such as strengthening using bonded steel plates, FRPs have the advantage of high strength-to-weight ratios, high corrosion resistance and reduced installation times. In a state-of-the-art review paper by Buchan and Chen [87], they note that most work tends to focus on glass fibre reinforced polymers (GFRPs) and carbon fibre reinforced polymers (CFRPs) bonded to a structure's surface as continuous sheets, strips or rods. Typically, the structure is made from concrete, which will remain the focus of this discussion, but FRP retrofits may also be applied to masonry, metallic and timber structures. Most studies examine the blast response of FRP-retrofitted structures with results overwhelmingly positive, indicating an ability to enhance strength and ductility while reducing fragmentation [87]. Malvar *et al.* [119] also reported on the confinement effect of FRP wraps applied to concrete structures which serves to enhance strength.

Mosalam and Mosallam [120] performed a numerical study using the FE code, DIANA on RC slabs retrofitted with CFRP. They reported a 200% increase in the load-carrying capacity compared with un-retrofitted slabs and a $40-70\%$ reduction in slab deflections. Best results were obtained by applying the retrofit to both sides of the slab — the same conclusion was drawn by Silva and Lu [55] in their analysis of CFRP and SRP (steel fibre reinforced polymer) retrofits applied to blast-loaded RC slabs. Further promising results were obtained for RC slabs [121], RC beams [122], RC columns [123, 124] and RC walls [125].

In a novel approach to aid designers, Mutalib and Hao [126] performed numerical simulations in LS-DYNA which were used to construct pressure-impulse (p-I) diagrams (discussed in Section 2.2.1.1). The blast resistance capacities of RC columns with different FRP strengthening strategies were assessed. Residual axial load-carrying capacity was used as the damage metric and simulations were used to derive the empirical formula required to plot the p-I curves.

Muszynski and Purcell [125] exposed concrete cubicle structures to blast loading using 830 kg of TNT at a 15 m stand-off. The cubicle wall panels (of dimensions 2.7 m by 2.5 m by 0.2 m) were either left bare, bonded with CFRP laminate or Kevlar/Glass (K/G) knitted fabric. Masonry walls were also tested. Both the CFRP and K/G retrofits outperformed the bare walls in terms of residual displacement reduction but the K/G walls appeared to exhibit more ductile behaviour. Further, the CFRP walls experienced damage due to delamination and also failed in tension at mid-height. The K/G fabric tore at mid-height but experienced no delamination in the tests. It was noted that the K/G fabric reinforcement was cheaper and easier to apply than the rigid CFRP laminates with the authors tentatively suggesting that it was perhaps a more optimum solution. Mutalib and Hao [127] performed a

numerical study in LS-DYNA, which highlighted the influence of bond strength and prevention of delamination in maintaining the composite action of a FRP-retrofitted RC panel. They found that delamination could be prevented using an appropriate anchorage system but concluded that more research is required to develop an optimum system, given stress concentrations at the anchors increased the possibility of FRP rupture.

In a novel study by Ha *et al.* [14] they considered a hybrid retrofit solution comprised of CFRP and a polyurea layer applied to RC panels. Experimental blast tests were performed using 16 kg of ANFO[1] at a small stand-off of 1.5 m. The slabs were retrofitted with either CFRP (illustrated in Fig. 2.9), polyurea or the CFRP/polyurea hybrid. The aim was to combine the stiffness and strength of the CFRP with the highly ductile polyurea serving as a fragment catcher. Results showed that the hybrid composite outperformed the stand-alone FRP and polyurea retrofits in terms of energy absorption capacity and reduction in maximum slab displacements. This agrees with the findings of Tekalur *et al.* [15] who used shock tube experiments to study layered and sandwich composite configurations of polyurea and E-glass vinyl ester (EVE). Results indicated that the addition of the polyurea layer to the impacted face significantly increased blast resistance, with best results achieved for the sandwich configuration (EVE/polyurea/EVE).

(a) Brushing epoxy (b) Attaching CFRP

Figure 2.9: Preparing a CFRP-coated concrete specimen. Reproduced from [14].

Wu *et al.* [129] performed blast testing on normal reinforced concrete (NRC) slabs to compare the benefit of externally bonding CFRP to the compression face with unreinforced and reinforced ultra-high performance fibre concrete (UHPFC). UHPFC is achieved by adding small steel fibres to the concrete mix resulting in significantly elevated compressive (greater than 150 MPa) and tensile (greater than 30 MPa) strengths compared to NRC. Explosive charge sizes ranged from 1 to 20 kg with a stand-off of up to 3 m. Results showed that the CFRP retrofit improved

[1]The explosive energy of ANFO (ammonium nitrate and fuel oil) is 82% that of TNT [128].

blast resistance compared to a NRC slab, but the reinforced UHPFC outperformed all other slabs.

Ghani Razaqpur *et al.* [128] experimentally investigated the effect of externally bonded GFRP laminates to RC panels. Explosive charges of either 22 kg or 33 kg ANFO[1] were located at a relatively close stand-off of 3 m to the target. For the lower blast intensity, the GFRP-retrofitted panels performed significantly better than their bare counterparts, exhibiting a 75% higher post-blast static strength. However, the results of the higher intensity blast test was inconclusive with one of the retrofitted panels experiencing catastrophic damage unlike its bare companion panel. Results such as these illustrate the necessity for more blast testing to understand the complex interactions at play, that often cannot be captured with analytical or numerical models.

Despite the research effort focused on understanding the blast response of FRP retrofits, considerably less attention has examined the impact response. Recent work by Pham and Hao [130] provides an overview of the state-of-the-art understanding on FRP strengthened concrete and masonry structures subjected to impact. They point out that research on blast loading does not necessarily translate to impact given the relatively lower loading rates, local deformation and local failure phenomena at play. In particular, it is noted that RC beams and slabs tend to be dominated by shear, rather than flexure when subjected to impulsive loads. Despite these differences, researchers appear in general to agree that FRP retrofit of RC beams [131–134], RC columns [135–137] and RC slabs [138] serves to improve impact performance. However, it is noted that there is very limited research on high speed impact testing, with most studies performed using simple drop-weight apparatus.

Erik and Meier [133] performed impact tests on CFRP-strengthened RC beams by lifting one end of the beam and dropping it, achieving maximum strain rates in the range $10^{-1} - 10^{0}\,\mathrm{s}^{-1}$. They found that CFRP-retrofitted beams performed well under impact loading (though they were outperformed by RC beams retrofitted by steel plates). Debonding of the CFRP laminate was observed and thus, the authors recommend that additional anchoring of the laminate would improve impact resistance. Drop-weight tests were performed by Jerome and Ross [131], Cantwell and Smith [132], Tang and Saadatmanesh [134] and Bhatti *et al.* [138], all reporting significant improvements in the RC structures' capacity to resist impact loading.

It is well known that confining concrete improves its compressive strength under quasi-static conditions, but few studies have sought to examine the effect of confinement on the impact response. Of particular interest is when confinement is applied by externally wrapping with FRP. Yan and Yali [137] performed drop-tower tests

on CFRP-confined concrete filled tubes and showed that the additional confinement improved impact resistance in terms of reducing damage and deformation. In one of the few studies to examine high velocity impacts, Shan *et al.* [135] performed gas gun tests on concrete filled steel tubes, with and without a CFRP jacket. They found the dynamic strength was increased with the lateral confinement contributed by the CFRP.

In their review papers on FRP retrofits for blast and impact mitigation, Buchan and Chen [87], and Pham and Hao [130], highlight that much research has been qualitative in nature and is coupled with a lack of understanding of the fundamental behaviour of blast and impact-loaded FRP structures. Both types of load event give rise to complex phenomena which are difficult to accurately simulate numerically, and challenging to measure experimentally. This is coupled with a lack of published design guidance. There is significant evidence that FRP retrofits are capable of enhancing both the blast and impact resistance of individual structural elements but there is a lack of confidence in applying them to large scale applications because such little research exists on understanding the global dynamic structural response.

2.3.3.2 Combat armour

Although not currently used in a structural retrofit context, there appears some scope for applying recent research on combat armour, specifically for head injury protection, to other protective strategies [11–13]. In this field of research, there is specific focus on the detailed modelling of blast and/or impact, target and armour interactions, something which is often lacking in a structures context. For example, Grujicic *et al.* [11, 12] perform a coupled Eulerian-Lagrangian numerical study on the fluid-solid interactions for the blast response of a helmet/head assembly to understand the mechanisms responsible for blast-induced traumatic brain-injury. The helmet under investigation was comprised of a Kevlar/phenolic resin, forming a hard, outer shell and an underlying suspension pad system, illustrated in Fig. 2.10. Grujicic *et al.* [11] studied the benefits of replacing the conventional foam suspension pads with polyurea. Their numerical study showed a significant reduction in the peak loading experienced by the brain at relatively high blast pressures, when polyurea suspension pads were used instead of foam. The authors argue that the high compressibility of foam, while often beneficial in quasi-static loading conditions, can be detrimental in shock-loading scenarios.

In a study by Rahimzadeh *et al.* [13], the authors seek to optimise armour design using a novel strategy based on exploiting the viscoelastic properties of polymer-based protective armour. Typically, blast and impact events induce stress waves comprised

(a) External side view

(b) Internal polyurea suspension system

Figure 2.10: Advanced combat helmet analysed by Grujicic *et al.* [11, 12]. Reproduced from [11].

of a broad range of frequencies. A multi-layer armour design is proposed where the outer layer *tunes* these stress waves to match the critical damping frequency of an inner viscoelastic layer. Upon entering the viscoelastic layer, the now tuned stress wave undergoes multiple loading-unloading cycles which result in significant energy dissipation. Proof-of-concept numerical testing yielded encouraging results with the authors' attention turning to selecting the optimum material properties for the outer layer (for example, high acoustic impedance, relatively high modulus) and viscoelastic layer (for example, very low ratio of relaxed to unrelaxed modulus, high critical damping frequency).

There is an obvious overlap between the results of these studies and the potential for designing more optimum structural retrofit solutions; however, as yet, this potential has remained relatively unexplored in the literature.

2.3.4 Polymer-metal laminates

A developing area of research has concerned itself with the retrofit of metallic plates using a polymer (typically, elastomer) layer. While much remains to be understood about the mechanisms at play, many studies have claimed that metallic/polymer bilayers or laminates achieve enhanced blast and impact mitigation properties when compared to monolithic plates of equivalent mass. Intuitively, perhaps, it appears surprising that such a relatively soft, ductile layer could achieve the effects reported in the literature; but authors have argued that a number of physical mechanisms contribute to the enhanced energy absorption observed. The following discussion highlights some of the key studies in this field, the points of contention and the proposed mechanisms by which the polymer achieves its effect.

The idea of layering plates of dissimilar materials and properties for enhanced impact resistance has been receiving attention for many years [139]. Early studies considered metallic laminates and results suggested that placing a ductile metal,

say aluminium on the impacted face, backed by a stronger, stiffer metal, say steel resulted in a better energy absorption capacity compared with monolithic metallic layers of equivalent mass [140–142]. The potential demonstrated in these studies has encouraged a research effort towards developing alternative layering strategies which offer similar impact mitigation properties but that are more cost-effective and easier to manufacture. One solution that has gained increasing attention is the use of polymer-metal bilayer plates and laminates for blast and impact mitigation.

Roland *et al.* [4] performed an experimental study on the impact response of polyurea and butyl rubber coatings on a metallic substrates. Ballistic testing was performed using a rifled Mann barrel firing 13 mm blunt, steel projectiles. A significant protective benefit contributed by the coating was identified and the effect of a number of variables were considered: (i) the substrate material and thickness, (ii) the coating location and (iii) the coating thickness. Firstly, a number of substrates were tested; four grades of steel (including high hard steel (HHS) and ultra high hard steel (UHHS)), three aluminium alloys and titanium. It was found that the coating contribution increased with the hardness of the substrate (reaching its optimum effectiveness for the UHHS substrate). A sharp increase in performance was observed for substrates greater than 3 mm in thickness with a slow decline in ballistic limit once the thickness exceeded 5 mm. Next, it was shown that the coating is significantly more effective when placed on the impacted face of the bi-layer, with a 50% increase in ballistic limit velocity measured for a front surface coating and only 9% for the back face. Further, it was noted that there was no difference in performance between the butyl rubber and polyurea coatings. Interestingly, although results exhibited a sharp increase in performance for even very thin coating thicknesses (c. 2 mm relative to a 5 mm HHS substrate), only a very small beneficial effect was observed by increasing coating thickness thereafter (about $7\,\mathrm{m\,s^{-1}}$ in ballistic limit velocity per mm of coating). The authors postulate that the energy absorption transpires in the initial $2-3$ mm of the coating which may be exploited by using a multi-layer design [3]. Thus, in summary the authors conclude that an optimum design to resist the impact from a blunt projectile would place a thin polymer layer, c. $2-3$ mm on the impacted face of a hard substrate.

Roland *et al.* [3, 4] have postulated that an important mechanism at play is an impact-induced transition from the rubbery to glassy state in the elastomer. This transition is accompanied by large viscoelastic dissipation and brittle fracture. They argue that when the polymer glass-transition temperature is close to, but less than the operating temperature, sufficiently high strain rates can induce this transition and thus enhanced energy absorption. This phenomena was observed by Bogoslovov *et al.* [143] and Sarva *et al.* [144].

Further, Roland *et al.* [3] performed ballistic testing on elastomer-steel multi-layer laminates to investigate the effect of multiple layers on impact resistance. The ballistic limit for a double bilayer configuration was 23% higher than for a single bilayer of equivalent weight. However, with four bilayers, performance reduced. The authors claim that the structure must retain a certain level of bending stiffness to prevent flexure and allow sufficient compression of the elastomer to induce the transition to the glassy state. Substantial gains in ballistic limit (up to 60%) were also achieved when HHS was coated with successive layers of thin aluminium and polyurea. Roland *et al.* [3] claim that the impedance mismatching between layers gives rise to break up and dissipation of the compression wave, resulting in a series of lower amplitude impacts.

Amini *et al.* [5] reported on the response of steel-polyurea bilayer plates subjected to impulsive blast loads produced in direct pressure-pulse experiments. The simulated shock loading achieved a peak pressure of c. 80 MPa and duration c. 50 μs. The steel plates had a nominal thickness of 1 mm and the polyurea layers had a typical thickness of 3.75 mm. In contrast to the work discussed thus far, the authors suggest that the presence of polyurea on the front face has a detrimental effect, serving to magnify the initial shock effect and promote failure. They postulate that under pressure, the polyurea experiences a substantial increase in stiffness, bringing it into closer agreement with the impedance of the steel substrate thereby increasing the energy transferred to the plate. Conversely, when applied to the back face, the coating contributes to energy absorption via viscoelastic dissipation and thus serves to mitigate plate failure. A further experimental and numerical study, by the same authors, on the response of steel-polyurea bilayers to impulsive loads agreed with these findings and thus it was concluded that placing polyurea on the back surface was most beneficial (illustrated in Fig. 2.11) [145, 146].

The influence of bond strength was highlighted by Ackland *et al.* [147] when they tested the response of mild steel plates with polyurea backings, subjected to localised blast loading. The plates varied in thickness from $4-6$ mm with coating thicknesses of 7.7 mm and 15.7 mm chosen to give all specimens the same areal density over the test area. Experimental blast trials and a numerical model in AUTODYN appeared to confirm that the residual deformations of the plates increased with coating thickness. High speed video footage showed the debonding of the polyurea coatings, resulting in hyperelastic extension and a maximum transient deformation of approximately twice that of bare steel plates. It is interesting to note that the authors conclude that bare steel plates dissipate the blast energy more effectively than their coated counterparts, which is in direct contrast to many other studies in the literature.

(a) Bilayer with polyurea on the back face

(b) Monolithic steel plate

Figure 2.11: Post-impulse specimens tested by Amini *et al.* [145]. Reproduced from [145].

Mohotti *et al.* [6] performed high velocity impact testing on different multilayer combinations of 5 mm and 8 mm aluminium alloy plates and relatively thick polyurea layers, either 6 mm or 12 mm. Steel-tipped, sharp-nosed ballistic projectiles were fired at the configurations at a velocity of $945\,\mathrm{m\,s^{-1}}$. The authors reported that a thick polyurea coating on the back face of the composite system was more effective in terms of energy absorption compared to when it was used as an interlayer. Another study on the impact of polyurea/steel laminates performed by Xue *et al.* [148] led to similar conclusions *i.e.* polyurea-backed steel plates were superior in terms of ballistic limit compared to when polyurea was used as an interlayer in a sandwich configuration. They postulate that a significant amount of energy is absorbed in polyurea stretching and when sandwiched between two steel plates, the polyurea cannot stretch freely, thus causing a fall in energy absorption capacity. Interestingly, this study analysed the effect of projectile nose-shape by comparing the ballistic limit for flat-nosed and pointed impactors. For the polyurea-backed plate, the pointed-nose projectile saw a ballistic limit rise of 42% compared to the blank plate whereas this fell to a 13% rise for the flat-nose projectile. It is reported that for the flat-nose projectile, the polyurea backing actually reduces the energy absorbed by the steel plate (though ultimately this is still outweighed by the energy absorbed in polyurea stretching).

A further possible energy absorption mechanism was investigated by Xue and Hutchinson [149, 150]: the retardation of necking in metallic plates when bonded to an

elastomer layer. The necking in steel/elastomer bilayer plates was studied both quasi-statically and dynamically. The idea behind this theory is based on the fact that if necking in the bilayer can be delayed to larger strains, it will be able to absorb more energy than a monolithic metal plate of equivalent mass. Necking instabilities are tied to a decrease in the incremental modulus, and under stretching, the effective incremental modulus of the bilayer decreases at a lower rate than the metal itself. Hence, the bilayer can outperform the monolithic metal in terms of energy absorption. In a later paper by the same authors [150], it was shown that inertia in dynamic stretching plays a dominant role in neck retardation in the metal layer. The authors conclude that the picture is fairly complex but is controlled by two ratios: the ratio of the elastomer to metal thickness and the ratio of the elastomer Young's modulus to the metal flow stress in uniaxial tension at a strain of unity. Interestingly, the authors note that in bilayers having equal thicknesses of metal and elastomer, necking behaviour is governed by the latter ratio. Thus, the higher the strength of the metal, the more difficult it is to find an elastomer capable of retarding necking. Note, perfect bonding between the metal and elastomer layers was assumed in these studies.

Other researchers have investigated alternative mechanisms to explain the impact mitigating capabilities of an elastomer layer placed in frictional contact (*i.e* not bonded) to metallic substrates [7]. Mohagheghian *et al.* [7] investigated the impact perforation of polyethylene/aluminium alloy plates by projectiles of various nose-shape geometries (blunt, hemi-spherical and conical). The effectiveness of the polymer layer was sensitive to both thickness and projectile-nose shape geometry. In all cases, the greatest perforation resistance was identified with the polymer placed on the impacted face of the bilayer. For thin coatings, the effect was largest for the blunt projectile (followed by hemi-spherical and then conical). Increasing the polymer thickness (to approach that of the projectile radius) results in the performance converging for all nose-shape geometries. The authors have suggested that the blunt indenter is particularly effective in terms of altering its effective nose shape, thus delaying the onset of failure and changing the failure mode of the metallic plate. For thicker coatings, the loss in nose-shape sensitivity can be attributed to the convergence in nose-shape change offered by the deforming elastomer and thus convergence in failure mode of the metal layer.

Finally, some authors [151, 152] have argued that the addition of a polymer layer to a metallic specimen serves to add extra mass to the structure thereby resulting in a non-negligible inertial effect which reduces overall straining and deformation in the metallic layer. For example, Morales *et al.* [151] used an expanding ring technique to test aluminium tubes, coated with polyurea and polycarbonate layers

under dynamic conditions. The additional mass contributed by the coating was deemed to reduce overall metal straining and secondly, the polymer's resistance to expansion dissipated additional energy. Polycarbonate's higher flow resistance meant that it contributed more to energy dissipation than the polyurea.

It is clear that significant debate exists in the literature regarding the efficacy and mechanisms behind elastomer-metal armour. This is no doubt due to the significant number of variables involved: load characteristics (blast, projectile velocity, projectile geometry), type of substrate (material properties, thickness), laminate configuration, (bilayer, multilayer, polymer on impacted or distal face, bond strength), polymer properties and thickness. In general, it is accepted that under certain conditions, the addition of an elastomer layer to a metallic plate can serve to enhance energy absorption and mitigate failure, outperforming monolithic metal plates of equivalent mass. With the performance benefits and reduction in cost, elastomer coating retrofits appear a very promising solution.

2.3.5 Spray-on elastomer coating

The previous sections have described the recurrent interest in using elastomeric coatings to provide structural blast and impact resistance. The discussion has included their use as interlayers in sandwich panels [8–10], fibre-reinforced polymer retrofits [14, 15], combat helmets [11–13] and extensively reviewed their use in metallic bilayer and laminate structures [3–7]. Throughout the literature, significant evidence exists that these coatings can serve a blast and/or impact mitigating role, as well perform a fragment catcher function for structures prone to spallation. Their high ductility, low cost and ease of application has prompted further studies on their application to other substrates. This section discusses the literature on the use of elastomer coatings applied to masonry and concrete structures, subjected to blast and impact load events.

2.3.5.1 Masonry

One of the first large scale experimental programmes in this field was the 1999 work by the Air Force Research Laboratory (AFRL) at Tyndall Air Force Base, USA [16]. Using a commercially available spray-on truck bed liner as the elastomer coating, blast testing was performed on unreinforced masonry block infill walls. The coatings were applied using a spray technique where the liquid polymer can be applied to almost any surface using a spray gun (see Fig. 2.12a). The sprayed polymer rapidly cures, making application to vertical and overhead structures feasible. Although

the masonry blocks were severely damaged in the tests, the wall remained in place and the polymer coating effectively contained the resulting fragment debris, as illustrated in Fig. 2.12b. Further proof-of-concept explosive testing was performed on lightweight modular structures which also yielded encouraging results.

(a) Pre-test (b) Post-test

Figure 2.12: Masonry block wall before and after blast testing at pressures exceeding 550 kPa [16]. Reproduced from [16].

The research team behind the initial tests at the Tyndall Air Force Base, Davidson *et al.* later published the results from a comprehensive experimental programme on the use of spray-on polymers applied to concrete masonry walls [17]. Their goal was to identify a polymer capable of increasing blast resistance but that was also practical and low-cost. Initially, a total of 21 polymers were considered: 13 extruded thermoplastics, 1 brush-on polymer and 13 spray-on polymers. The extruded thermoplastics were very strong and stiff but the extruded panel configuration was difficult to implement and did not form the continuous protective layer that the experimenters desired, and thus, they were eliminated from the investigation. The brush-on polymer proved weak and brittle and its long cure times made it impractical so it too was eliminated. The remaining 13 spray-on polymers comprised of seven polyurethanes, one polyurea and five polyurea/polyurethane hybrids. A pure polyurea was eventually selected based on its strength, lack of flammability and cost. The masonry walls were 2.2 m by 3.7m and were constructed and tested in reusable reaction structures. Details on the explosive charges and stand-offs were not provided due to the sensitive nature of the research. However, measured peak reflected pressures across the tests were in the range $300-1600$ kPa with reflected impulses of $1100-2900$ Pa s. By applying a thin coating (c. 3 mm) of the polymer on the interior (non-blast-receiving) face of the walls, the wall could resist peak pressures greater than 400 kPa compared to 35 kPa for unreinforced masonry walls. Furthermore, the coating was effective in containing fragmentation debris. Although coating both the interior and exterior faces of the wall resulted in some additional blast resistance, it was concluded that the added benefit did not outweigh the extra cost.

In a subsequent paper, the same authors performed further explosive testing on polymer-reinforced masonry walls to develop understanding of the damage and failure mechanisms [1]. Further insight was gained through the use of a numerical model in LS-DYNA. Once more, a significant blast mitigating ability was observed, in combination with the ability to minimise fragmentation. Significant arching effects were evident and front face fracture of the masonry and mortar bond fracture at the joints were common damage mechanisms observed. Strong bond between the polymer and masonry was deemed critical to the effectiveness of the retrofit. With no bond, the polymer acted as a *catcher-membrane* which resulted in tearing at the connection between the polymer and host structure and collapse of the wall. Strong bond, on the other hand precludes the full strain energy absorption potential of the polymer membrane with tests indicating that the polymer is only minimally strained. Tests also showed that a simple spray overlap of 15 cm between the polymer and host reaction structure was enough to prevent collapse of the wall. The authors suggest that a more effective reinforcement system could be designed with an optimised balance between bond strength, strain energy absorption and overlap strength.

Hoo Fatt *et al.* [153] extended this work into an analytical framework by developing an equivalent single degree-of-freedom (SDOF) model to predict the dynamic response of polyurea-retrofitted masonry units subject to blast loading. This model was based on coupling the structure's bending and membrane resistance and the equivalent mass and loads were found by assuming parabolic shape functions for the transverse deflection and velocity of the wall. An average, reduced concrete masonry modulus was assumed in the model which the authors recommend to be about 5% of its initial, undamaged value. The equivalent SDOF results compared well with numerical simulations performed using ABAQUS, provided the maximum wall deflections were between one to two times the wall thickness.

In an experimental study by Baylot *et al.* [154], 1/4-scale concrete masonry unit (CMU) walls were exposed to a number of explosive tests generating maximum impulses in the range $180 - 1100\,\mathrm{Pa\,s}$. Three types of retrofit were tested: E-glass FRP attached to the back face, a spray-on polyurea coating on the back face and a 1 mm galvanised steel sheet placed on the back of the wall. Although all walls failed during the test, the FRP and polyurea were able to contain the fragments and debris. For partially grouted, lightly reinforced walls, the main failure mechanisms observed were disconnection between the wall and the reaction structure (in the case of the polyurea) or pull out of the retrofit from the plates clamping it to the reaction structure (in the case of the FRP and steel plate). This study highlights the relevance of Davidson *et al.*'s [1] conclusions which call for a more optimised design based on

bond strength, overlap strength and strain energy absorption capacity.

2.3.5.2 Concrete

Concrete represents a significant proportion of today's ageing infrastructure, and would be an ideal candidate to benefit from an effective, low-cost retrofit solution. Particularly one which encompasses ease of application and low maintenance requirements. Despite the positive literature studies directed towards spray application elastomers applied to masonry units, limited research exists on this retrofit applied to reinforced concrete structures.

Raman *et al.* [18] have performed one of the few studies on RC panels, retrofitted with a polyurea coating. A numerical model was developed in LS-DYNA to model the response of retrofitted slabs to 2 kg of TNT at a stand-off of 1.6 m, giving a peak reflected pressure and impulse of 2480 kPa and 518 Pas, respectively. The panel depth was 60 mm and coating thicknesses of 4 mm and 8 mm were investigated, applied to the blast-receiving (top) face, non-blast-receiving (bottom) face and both. By applying a 4 mm coating to the bottom face of the panel, maximum displacements were reduced by 41% and permanent displacements by 50%, compared to a bare panel. Applying the coating to the top face reduced the benefit considerably with maximum and permanent deflection reductions of only 18% and 28%, respectively. While increasing the thickness of the coatings proved beneficial, the effect was relatively small. Further, coating both faces of the panel resulted in minimum recorded deflections. However, the authors point out that it may not be feasible in practical situations to coat both panel sides and thus, the increased performance may not outweigh the extra time and cost. This is similar to the conclusions drawn by Davidson *et al.* [17] in their work on polymer-coated masonry walls. Although limited details are available in the public domain, a number of experimental blast trials, performed by the same authors, appear to confirm that polyurea-retrofitted RC slabs display enhanced blast resistance, particularly when the coating is applied to both the top and bottom surface of the slab [155, 156].

In recent work, Iqbal *et al.* [157] used a shock tube facility to subject polyurea-coated concrete tiles to high pressure dynamic loading. Coating thickness was varied between $1 - 6$ mm relative to a tile thickness of 200 mm and applied to the non-blast-receiving face. Un-retrofitted concrete tiles failed at peak reflected pressures of c. 350 kPa whereas when coated with 6 mm of polyurea, they could withstand pressures up to c. 620 kPa. Although thinner coatings (c. $1 - 4$ mm) did not prevent concrete cracking, they were capable of holding the cracked tile together and were particularly effective at preventing fragment ejection. Interestingly, a dynamic

mechanical analysis indicated that significantly higher frequencies were required to induce a glass transition in the polymer, compared to those associated with the blast loading. It appears that an impact-induced glass transition [3, 4] (discussed in Section 2.3.4) is not one of the key energy dissipative mechanisms at play here. Instead the authors postulate that shock wave induced micro-structural changes are responsible, brought about by strain-induced crystallisation of polyurea's soft matrix, strain-induced crystallisation of the hard domains and realignment of the hard domains with the direction of deformation [158].

Carey *et al.* [159] have also examined the blast response of RC panels coated with four polyurea-based coated systems: two plain polyureas and two discrete fibre-reinforced polyureas (DFRP). Chopped E-glass fibres were integrated in a polyurea to make the DFRP system in an effort to exploit the high stiffness and strength of the fibres and the high ductility of the polymer. Blast testing was performed on reduced scale panels and a numerical model was developed in LS-DYNA. Experimental measurements of panel deflections were hindered due to lack of appropriate instrumentation but the numerical analysis predicted deflection reductions of up to 60% with a polyurea coating on the non-blast-receiving face. Interestingly, the DFRP systems provided relatively little benefit in terms of deflection reduction in comparison to their plain polyurea counterparts.

These studies appear to agree that coating a reinforced concrete panel, particularly on its non-blast-receiving face is beneficial for two reasons: (i) the elastomer serves to reduce slab deflections and (ii) it acts to hold together failed concrete specimens, reducing fragmentation debris. Once more, the recurring debate surrounding the mechanism by which the coating achieves these effects is raised.

2.4 Conclusions

As one of the most widely used construction materials in the world, concrete represents a significant proportion of today's ageing, vulnerable infrastructure. Understanding the response of concrete structures to extreme load events such as blast and impact represents a number of challenges. Experimental impact, and particularly blast trials are often prohibitively expensive to perform and sometimes precluded due to the sensitive nature of the topic. Thus, researchers must turn to analytical and more commonly, numerical models to analyse this multi-phase, brittle, highly nonlinear material. One of the main challenges is choosing a representative constitutive model and unfortunately, many of the commercial finite element codes implement "black box" approaches, requiring little user input beyond knowledge of the concrete compressive strength. This contributes to uncertainty, especially

when modelling dynamic load events such as blast, which itself is a highly complex, transient phenomenon.

Elastomeric coatings for enhanced blast and impact resistance are a recurring theme in the literature when exploring novel structural retrofit strategies. Their spray application technique makes them an attractive option for industry seeking a practical, low-cost, easy to apply solution. This chapter has discussed their use within sandwich panel configurations [8–10], composite panel retrofits [14, 15], combat helmet suspension pads [11–13] and in metallic bilayer and laminate structures [3–7]. It has been demonstrated that they serve an energy dissipating role, but the mechanisms by which they achieve this are the subject of significant debate. For example, impedance mismatching [3], contributing additional mass [151, 152], impact-induced glass transition [3, 4], delaying necking in the metallic substrate [149, 150] and nose-shape changing effects [7] have all been postulated throughout the literature.

Encouraging results from blast trials on masonry structures have suggested that an elastomer coating retrofit can serve to maintain structural integrity for significantly higher blast intensities compared to un-retrofitted structures. Furthermore, an added benefit of the coating was highlighted: it acts as a fragment catcher, substantially reducing debris ejected from the damaged structure (which is the primary source of risk to life in a real-life explosive event). Despite the obvious potential demonstrated, further studies have been limited, particularly with regard to retrofitted concrete (and reinforced concrete) substrates and their response to impact. Experimental challenges and numerical modelling uncertainties still persist.

It is apparent that there are limited studies on the use of elastomer coatings for the retrofit of concrete structures subjected to extreme load events. There is a lack of clear design guidance, compounded by significant debate surrounding the mechanisms by which these coatings achieve their blast and/or impact mitigating effect. These themes will be explored in the following chapters within the framework presented in Section 1.1.

CHAPTER 3

Fluid-structure interactions for air blast loading of elastomer-coated concrete

3.1 Introduction

As discussed in Section 2.3.5, spray application elastomer coatings have been recently investigated for their reported ability to protect infrastructure from blast load events. A number of experimental studies on masonry structures have yielded encouraging results [16, 17, 154]. However, to date, comparatively little work has focused on elastomer-coated concrete, despite concrete representing a significant proportion of the ageing, vulnerable infrastructure in today's built environment. In one of the few studies on this topic, Raman *et al.* [18] performed a numerical analysis to investigate the performance of a polyurea-coated, reinforced concrete slab. Results indicated that polyurea coatings can significantly contribute to controlling panel displacement, and deflection reductions of more than 40% were reported. However, the question remains as to what mechanism is responsible for this apparent enhancement in blast resistance. In this chapter, one possible candidate mechanism is investigated — a fluid structure interaction (FSI) effect. There are various examples in the literature whereby the introduction of a compliant layer gives rise to beneficial FSI effects. For example, this phenomenon was discussed in Section 2.3.1 where it has been exploited for blast mitigation in the case of sandwich panels subject to underwater blast loading [90, 92].

G.I. Taylor [93] performed one of the first investigations to explore FSI effects for the case of underwater explosions. In short, Taylor found that when exposed to a blast pressure, lighter plates accelerated faster than heavier plates, and this motion resulted in the impulse transmitted to the structure being reduced. He analysed the interaction between a 1D blast wave and a rigid plate and proposed that the

FSI effect was governed by a single, non-dimensional parameter. Further, he was able to quantify the relative impulse transmitted to the plate, as a function of this non-dimensional parameter. The 2006 work of Kambouchev *et al.* [160] expands upon the work of Taylor [93] to account for non-linear compressibility effects during FSI for air blast loading. They consider the case of a free-standing rigid plate, of arbitrary mass, impacted by a planar blast wave, propagating in a compressible medium. If the blast pressure pulse is approximated as an exponential profile, given by Eq. 2.2, the incident impulse can be expressed using Eq. 2.3. Kambouchev *et al.* [160] thus postulate an expression (Eq. 3.1) for the relative transmitted impulse to the plate, I_p/I_i:

$$\frac{I_p}{I_i} = \gamma_R \left(\frac{C_R \, f_R}{\gamma_R} \right)^{\beta_s/(1+\beta_s)} \beta_s^{\beta_s/(1-\beta_s)} \tag{3.1}$$

where I_p is the transmitted impulse to the plate, I_i is the incident blast impulse, C_R is the reflection coefficient (Eq. 2.4) and γ_R and f_R are parameters derived in [160].

The compressibility is encapsulated in the revised FSI parameter, β_s that is now dependent on blast intensity parameters:

$$\beta_s = \frac{t_i \, \rho_s \, U_s}{\rho_p \, h_p} \tag{3.2}$$

where h_p is the plate thickness and ρ_p is the density of the plate; ρ_s is the density of the compressed blast medium and U_s is the shock propagation speed, each defined by Rankine-Hugoniot relations in [160]. Similarly to Taylor [93], this parameter represents the relative time scales of the blast wave duration, t_i and of the fluid-structure interaction, t_s^*.

This chapter employs Kambouchev *et al.*'s [160] theoretical framework to study the air blast response of an elastomer coating applied to a concrete structural element. The objective of this chapter is to answer the following question: is the elastomer effect a purely mechanical one, or does it introduce an FSI effect?

The chapter is structured as follows. First, a fully coupled Eulerian-Lagrangian (CEL) finite element model is developed. Appropriate constitutive models for concrete and an elastomer coating are attained. Next, a high resolution 1D investigation is performed to study the stress wave interactions between the air/polymer/concrete interfaces over very short timescales. This enables consideration of the various non-linear effects in the air (compressibility), polymer (hyperelasticity, viscoelasticity)

and the quasi-brittle substrate, concrete. This is followed by longer duration 1D calculations to interrogate the effect of these non-linearities on the total impulse transmission. For a practical range of concrete and coating thicknesses, the influence of coating on the imparted momentum to each layer is assessed. The investigation is then extended to the 2D response to examine any interplay between FSI effects (acting over short timescales) and any longer timescale mechanical benefit that might arise from the elastomer coating, for both a low and high intensity blast. It emerges that the function of the elastomer depends on the response regime of the slab and thus motivates a need for further interrogation of performance sensitivity to the coating, substrate and blast parameters. In order to facilitate this, the suitability of simplified numerical modelling strategies, that would enable such a study at reduced computational cost, are quantitatively assessed.

3.2 Numerical model development

3.2.1 Concrete constitutive model

Throughout this chapter, finite element analysis is employed using the commercial code, ABAQUS/Explicit [27]. The Concrete Damaged Plasticity (CDP) model in ABAQUS/Explicit is chosen for the concrete material model. The model considers concrete as a continuum which exhibits isotropic, damaged elasticity and isotropic, pressure-dependent plasticity. Pressure dependent damage is prescribed via compressive crushing and tensile cracking responses. A continuum damage mechanics approach has been shown by many authors [161–165] as appropriate in the constitutive modelling of concrete (and other quasi-brittle materials).

The model parameters are summarised here, with further details provided in Appendix A.1. To implement this model, the compressive behaviour is defined in terms of the uniaxial compressive stress, σ_c *vs* inelastic strain, $\tilde{\epsilon}_c^{in}$ according to the empirical relationships set out in the CEB-FIP Model Code [84]. The tensile response is based on the relationship proposed by Hordijk [166] for the uniaxial tensile stress, σ_t in terms of cracking displacement, u_t^{ck}. Damage is incorporated through the use of compressive and tensile damage parameters, d_c and d_t which quantify the degradation of elastic stiffness and can take values between zero (undamaged material) and one (fully damaged material). The compressive and tensile damage parameters are defined as a function of inelastic strain, $\tilde{\epsilon}_c^{in}$ and cracking displacement, u_t^{ck}, respectively, according to the relationship proposed by Birtel and Mark [167]. To complete the definition, the CDP model employs the yield function proposed by Lubliner *et al.* [168] and includes the modifications suggested by Lee and Fenves [169]. Further, a non-associated plastic flow rule is assumed whereby the flow potential takes the form

of the Drucker-Prager hyperbolic function [27]. A concrete compressive strength of 39.5 MPa and tensile strength, 4.2 MPa is assumed. The undamaged elastic modulus is 28.3 GPa, the Poisson's ratio is 0.2 and the density is 2550 $\mathrm{kg\,m^{-3}}$.

In this investigation, strain rate dependence is omitted in the constitutive response of the concrete. There is currently a lack of published data on the strain rate dependence of the full suite of constitutive parameters in the CDP model. This constitutive assumption might affect the model fidelity, in terms of reproducing specific experimental results (for which a more detailed representation of the blast loading conditions would also be required). However, within the scope of this investigation, it provides an adequate model for studying the fundamentals of FSI effects for a quasi-brittle substrate, representative of concrete. Additional calculations were performed to check, nonetheless, that the predictive quality of the model is reasonable, for dynamic structural response in the regimes of interest. Details of this model validation are provided in Appendix A.2.

3.2.2 Elastomer constitutive model

To help develop a representative material model for the elastomer, a sample of commercially available, spray application polyurea/polyurethane hybrid was obtained[1]. The sample coatings were sprayed to a thickness of around $3-5$ mm (precise control of thickness was not possible) onto an untreated steel plate and then peeled off. Characterisation tests on the coating were performed in tension, compression and shear, as follows.

Uniaxial tension tests were performed on dogbone specimens, machined from this sheet, shown in Fig. 3.1. The geometry was based on the ASTM D182 standard [171], but modified to ease manufacture and enable testing on a servo-hydraulic materials testing rig.

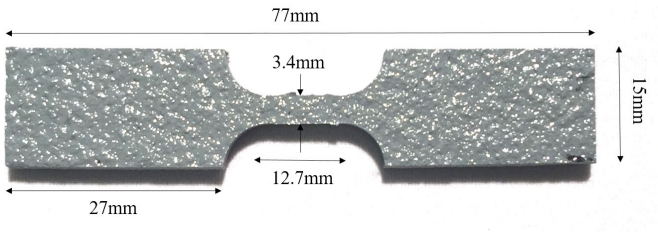

Figure 3.1: Tensile specimen used to characterise the polyurea/polyurethane hybrid spray-on elastomer. The thickness of the specimen is 3.5 mm, though this varied between specimens.

An Instron screw-driven materials testing machine was used to perform tensile test-

[1]Polymer specimens courtesy of I. Mohagheghian, University of Cambridge [170].

ing at low to moderate nominal strain rates, in the range $10^{-3} - 10^{0}\,\mathrm{s}^{-1}$. Strains were measured using a laser extensometer. Higher nominal strain rates, in the range $10^{0} - 10^{2}\,\mathrm{s}^{-1}$ were achieved using a servo-hydraulic materials testing machine. The resulting nominal stress-nominal strain results up to failure are presented in Fig. 3.2. It is observed that the response is non-linear and strain rate dependent. A substantial increase in failure stress with increasing strain rate is noted, though failure strains do not show considerable strain rate dependency.

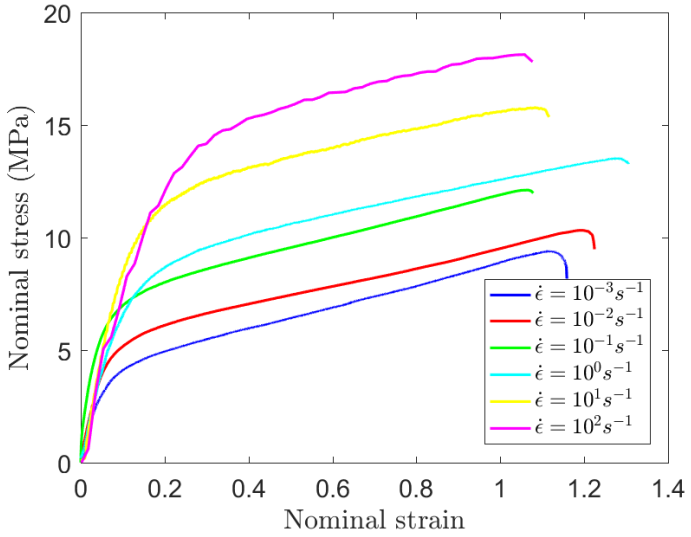

Figure 3.2: Uniaxial tensile results at various strain rates, $\dot{\epsilon}$ for the elastomer sample.

Next, a constitutive model is developed for the polymer on the basis of the tensile data. This will subsequently be validated against characterisation tests performed in compression and shear. Rather than trying to match precisely the response of a particular coating, the aim is to achieve a material model representative of a realistic elastomer coating to allow subsequent interrogation of the key phenomena at play. First, a hyperelastic constitutive relationship is fitted to the uniaxial tensile response up to a nominal strain $\epsilon = 1$, using the data obtained at a nominal strain rate, $\dot{\epsilon} = 10^{-3}\,\mathrm{s}^{-1}$ (assumed to be the long term *i.e.* relaxed response). A Yeoh strain energy potential is found to give the best fit. Further details on the form of the Yeoh model are described in [27]. A nearly incompressible variant of the model was selected, corresponding to a Poisson's ratio of $\nu = 0.475$ (a small degree of compressibility was required for numerical reasons). The density was chosen as $\rho_e = 1.1\,\mathrm{Mg/m^3}$. A Prony series is used in conjunction with this hyperelastic model to provide a viscoelastic model suitable for a finite strain analysis (see [27]). The Prony series parameters (non-dimensional shear relaxation modulus $\overline{g_n}$ and corresponding time constants, τ_n) were obtained from a literature source for a similar material [172] and are tabulated in Table 3.1.

Table 3.1: Prony series parameters, obtained from [172] and defined in [27].

n	$\overline{g_n}$	$\tau_n(s)$
1	0.94159	1.49E-6
2	1.31E-2	2.93E-5
3	1.01E-2	2.79E-4
4	7.62E-3	3.02E-3
5	5.69E-3	3.77E-2
6	4.17E-3	0.55586
7	3.01E-3	10.035
8	2.13E-3	236.29
9	1.43E-3	7521

In order to validate the material model, first the ability of the viscoelastic model to predict the experimentally measured strain rate dependence in uniaxial tension was tested. ABAQUS/Explicit was used to simulate a uniaxial tension test at strain rates of up to $10^2\,\mathrm{s}^{-1}$, which is indicative of the blast regime [35]. The resulting nominal stress-nominal strain plot is compared with that obtained experimentally in Fig. 3.3a. No failure criterion was included in the numerical model so the failure stresses and strains are not comparable. In order to isolate the effect of the Prony series on the shape of the stress-strain curve at higher strain rates, an additional result is shown (labelled inviscid) for which the Prony series is removed, but the hyperelastic strain energy potential is re-fitted to the higher strain rate data measured at $10^2\,\mathrm{s}^{-1}$.

Reasonable agreement is observed between the numerical model and the experiment in terms of the strain rate dependence and the stresses at larger strains. However, the model underpredicts the initial modulus, not capturing precisely the shape of the measured tensile response curve.

To test the material model under alternative stress states, shear punch experiments were performed using the rig illustrated in Fig. 3.4a. The polymer specimen (thickness $h_e \approx 3.5\,\mathrm{mm}$) was clamped between a pair of steel plates, and loaded through a hole in the centre of the plates by a circular cylindrical punch (diameter $d_p = 8\,\mathrm{mm}$), driven by a servo-hydraulic test machine. The test machine cross-head velocities spanned several orders of magnitude to simulate the strain rates expected during a blast loading event.

ABAQUS/Explicit was then used to simulate the shear punch experimental test at the highest cross-head velocity achievable by the servo-hydraulic machine, $\dot{x} = 900\,\mathrm{mm/s}$, indicative of a nominal strain rate, $\dot{\epsilon} = 10^2\,\mathrm{s}^{-1}$. A plot of the nominal shear stress at the perimeter of the punch (given by $P/\pi d_p h_e$, where P is the punch force) *vs* nominal shear strain (given by δ_p/h_e, where δ_p is the punch dis-

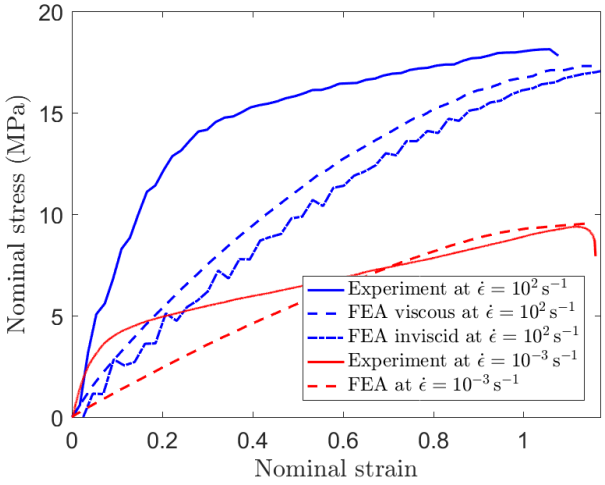

(a) Uniaxial tension

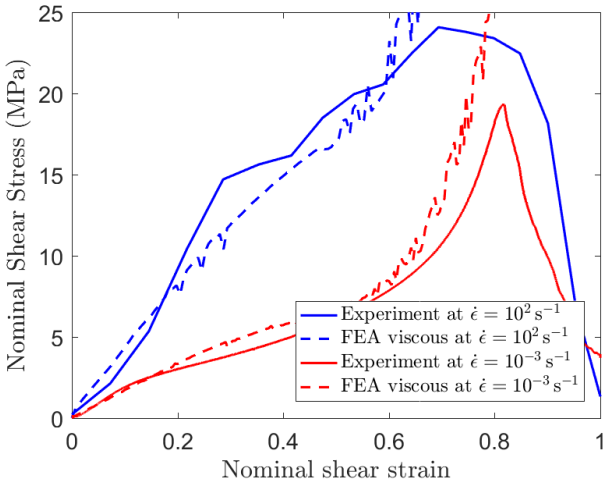

(b) Shear punch

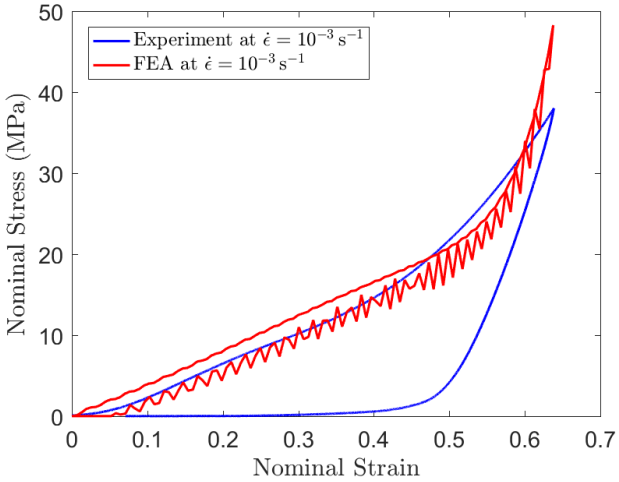

(c) Compression

Figure 3.3: Comparison between experimental results and those obtained via the numerical model. Uniaxial tension and shear punch results are compared for strain rates, $\dot{\epsilon} = 10^{-3}\,s^{-1}$ and $\dot{\epsilon} = 10^2\,s^{-1}$. Compression data is presented for $\dot{\epsilon} = 10^{-3}\,s^{-1}$. Two numerical models are considered—an inviscid model based on data measured at $\dot{\epsilon} = 10^2\,s^{-1}$ and a viscous model based on data measured at $\dot{\epsilon} = 10^{-3}\,s^{-1}$.

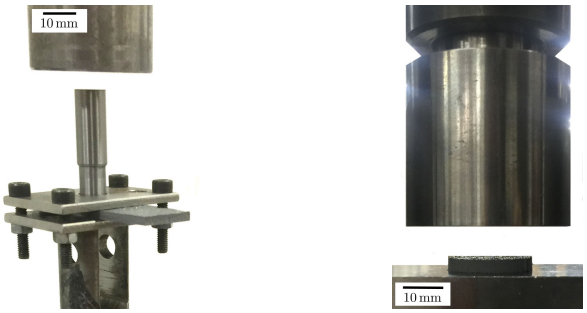

(a) Shear punch (b) Compression

Figure 3.4: Rigs used for the shear punch and compression disc experiments. For shear punch, the specimen is sandwiched between steel plates of thickness 3 mm and impacted by a rigid punch of diameter 8 mm. For compression, 25.9 mm diameter samples, 3.68 mm in thickness are compressed by a platen 40 mm in diameter.

placement) is compared with the experimental results in Fig. 3.3b. Once again, no failure criterion was included in the numerical model. Again, the viscoelastic model captures the strain rate dependence well. The model also predicts the initial stiffness better for shear loading, compared to uniaxial tension. To further validate the model, compression of thin discs was performed at $\dot{\epsilon} = 10^{-3}\,\mathrm{s}^{-1}$ on an Instron screw-driven materials testing machine as illustrated in Fig. 3.4b. In all FE cases, frictionless contact is assumed at elastomer/steel interfaces based on best agreement with experimental tests. Results are compared with numerical predictions in Fig. 3.3c. Loading and unloading is shown. Although the model fails to capture the observed hysteresis, very good agreement is achieved for the loading portion of the curve. This study will proceed with this viscoelastic material model in the numerical analysis of the spray-on elastomer. Although the strain energy potential fails to capture accurately the shape of the tensile response, the model does capture well the strain rate dependence, and the responses in compression and shear. For future studies, in which the intention may be to accurately capture the unloading behaviour, alternative techniques may be pursued in order to capture the material hysteresis. For example, fractional derivative models appear promising, based on the idea of introducing fractional derivatives into the elastomer's constitutive equation, to provide a dependence on the material's loading history. Studies have shown that these approaches have proved successful in accurately modelling the viscoelastic behaviour of elastomers [173–175].

3.2.3 Coupled Eulerian-Lagrangian (CEL) model

In order to capture the fully coupled air blast response, a Coupled Eulerian-Lagrangian (CEL) model was developed in ABAQUS/Explicit. A Lagrangian domain is used for the target structure, with the Eulerian domain capturing the air. In order to

validate the model, a one-dimensional test case was developed. It simulates the behaviour of a rigid plate (Lagrangian domain), placed in an air column (Eulerian domain), impacted by a blast wave. The model is illustrated in Fig. 3.5 where point A corresponds to the point at which the blast pulse enters the air column and point B corresponds to the point of first impingement by the blast wave on the rigid target. The CEL model and its validation are summarised here, with further details provided in Appendix A.3.

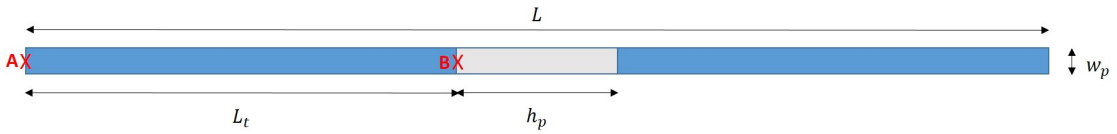

Figure 3.5: A schematic illustration of the 1D CEL model in ABAQUS/Explicit.

It is assumed that the air can be modelled as an ideal gas [176] with the model parameters presented in Table A.3. The blast pulse is generated by specifying a velocity-time boundary condition to the end of the column at A. The velocity is specified in the direction AB, to generate a compressive pressure pulse. After having determined a finite element mesh density that can adequately resolve the propagating shock front, an iterative process can be employed to determine what velocity-time history is necessary at point A, to achieve the desired pressure-time history at point B. Iteration is necessary as the wave shape changes during propagation. This iterative process is similar to that presented by Chen *et al.* [177] using the Rankine-Hugoniot equations to relate particle velocity to peak overpressure.

To validate the CEL technique, in terms of its ability to resolve FSI effects, calculated results for the relative transmitted impulse are compared with Kambouchev *et al.*'s [160] analytical expression for a free-standing, rigid plate of arbitrary mass, given by Eq. 3.1. Very good agreement is achieved (see Fig. A.6). This gives a strong indication that the CEL approach in ABAQUS/Explicit is capable of accurately analysing fluid-structure interaction problems across the range of blast intensities of interest. The results indicate that for the case of low β_s values, the relative transmitted impulse becomes insensitive to β_s. This suggests that there is negligible fluid-structure interaction in this regime, as there is little plate movement during its interaction with the blast. Conversely, for lighter plates, as β_s increases, there is a significant reduction in relative transmitted impulse to the plate relative to this heavy plate limit. This can be attributed to motion of the plate during the period of blast loading.

3.3 1D wave interaction study

We begin the study by first examining in 1D the details of pressure wave propagation through the air/polymer/concrete interfaces. The very short timescale response is examined, using a high resolution numerical calculation, with the objective of determining whether the presence of a thin elastomer coating can serve to distort the blast wave. A number of non-linear effects are at play, such as air compressibility, concrete damaged elasticity and plasticity, and hyperelasticity and viscoelasticity in the polymer. Thus, the effect of the polymer can not necessarily be determined *a priori*, by analytical means.

We implement the 1D CEL model described above, replacing the rigid plate with a deformable, Concrete Damaged Plasticity part of density, $\rho_p = 2550\,\mathrm{kg\,m^{-3}}$ and compressive strength, $\sigma_{cu} = 39.5\,\mathrm{MPa}$. A concrete plate depth, $h_p = 100\,\mathrm{mm}$ is considered. On the basis of a mesh sensitivity study, it is determined that the shock front width (which is of the order of 20 mm in the concrete, and 4 mm in the air column) is adequately resolved with a mesh size of 1 mm in all material layers. 3D stress (C3D8) elements are used for the concrete and polymer while 3D Eulerian (EC3D8R) elements are chosen for the air column. All elements are constrained to permit only 1D deformations. A 5 mm thick elastomer coating is considered, positioned on the blast-receiving face, and a perfect bond is assumed between the concrete and polymer, simulated by tying all degrees of freedom at the interface. The intermediate blast intensity case considered by Kambouchev *et al.* [160] corresponding to a peak overpressure of $p_s/p_0 = 3.29$ is examined. As described in Appendix A.3, $p_s/p_0 = 3.34$, $I_i = 698\,\mathrm{Pa\,s}$ and $t_i = 2.0\,\mathrm{ms}$ is achieved in the CEL model.

Figure 3.6 illustrates the spatial variation in the compressive stress at various times after impingement on the blast-receiving face, for three configurations: concrete alone, concrete coated with a hyperelastic polymer on its blast-receiving face and concrete coated with a visco-hyperelastic polymer on its blast-receiving face. It is noted that in the latter case, when unloading occurs, the FE model predictions may lose fidelity, as the elastomer constitutive model does not capture the hysteresis of the polymer accurately. (However, as discussed subsequently, the key longer timescale effects appear to be relatively insensitive to this.)

It is observed that the addition of a polymer layer causes significant distortion to the wave front due to both the non-linear elasticity and viscoelasticity in the polymer. Higher peak stresses are observed in the concrete as a consequence of the coating. It is therefore necessary to examine the longer timescale response, including the total impulse transmission and the development of any plasticity or damage in the

substrate, which is discussed next.

3.4 1D air blast response of a concrete part

Before proceeding to study the influence of an elastomer coating, the longer timescale air blast response of uncoated concrete is first considered. The aims, for a realistic range of areal mass and blast parameters, are; (i) to determine the regime of FSI response relative to the heavy and light plate limits identified by Kambouchev *et al.* [160] and (ii) to identify any FSI effects attributable to concrete elasticity, plasticity or damage. In this section, the scope is restricted to the 1D FSI response. The 2D response of a slab will be described subsequently.

For a fixed concrete density of $\rho_p = 2550\,\mathrm{kg\,m^{-3}}$, four different plate thicknesses were considered: $h_p = 25\,\mathrm{mm}$, $50\,\mathrm{mm}$, $75\,\mathrm{mm}$ and $100\,\mathrm{mm}$. This corresponds to areal densities of 63.75 , 127.5, 191.25 and $255\,\mathrm{kg\,m^{-2}}$, respectively. Two different blast intensity cases were examined; the first is the intermediate intensity case considered by Kambouchev *et al.* [160] corresponding to a peak overpressure of $p_s/p_0 = 3.29$. As described in Appendix A.3, $p_s/p_0 = 3.34$, $I_i = 698\,\mathrm{Pa\,s}$ and $t_i = 2.0\,\mathrm{ms}$ is achieved in the CEL model.

Using the empirical relationships proposed by Kinney and Graham [28], the blast parameters corresponding to examples of realistic threats in the built environment are presented in Table 3.2. The second blast case considered in this study corresponds to 20 kg of TNT at a stand-off distance of 15 m, indicative of a "suitcase bomb". β_s values were calculated for each case and are summarised in Table 3.3.

Table 3.2: Examples of realistic blast threats where the peak overpressure, p_s and incident impulse, I_i are calculated using Kinney and Graham's empirical relationships [28].

Threat [178]	kg of TNT	Stand-off (m)	p_s (kPa)	I_i (Pa s)
Pipe bomb	3	15	9.4	19
Suitcase bomb	20	15	24	34
Car bomb	300	15	158	80
Truck bomb	5000	15	1320	120

The model set-up is as described in Appendix A.3 except that the rigid plate is replaced with a deformable part assigned the Concrete Damaged Plasticity material model with a compressive strength, $\sigma_{cu} = 39.5\,\mathrm{M\,Pa}$. The mesh consists of 8-node linear elements (C3D8) of side length 5 mm, chosen on the basis of a mesh sensitivity study. The relative transmitted impulse, I_p/I_i to the concrete plates is compared with Kambouchev *et al.*'s theoretical expression for a rigid plate, Eq. 3.1 [160] as

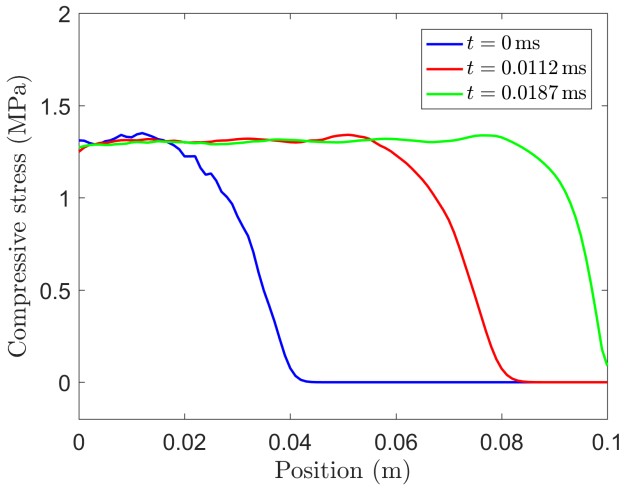

(a) Concrete only

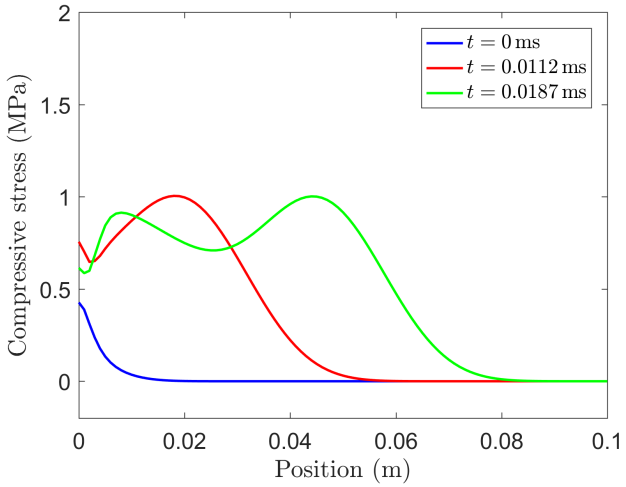

(b) Concrete coated with hyperelastic polymer

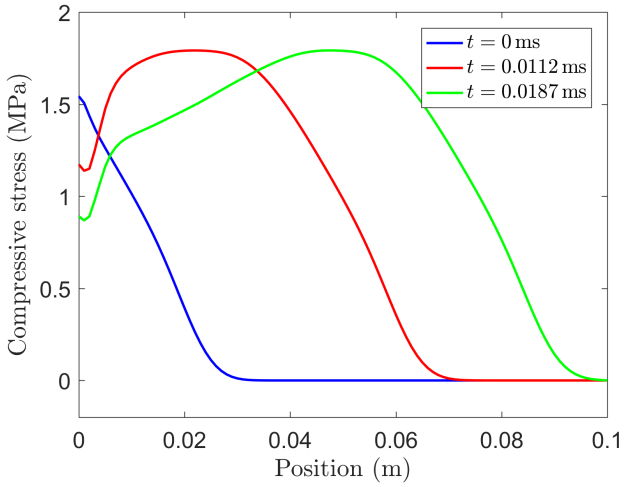

(c) Concrete coated with visco-hyperelastic polymer

Figure 3.6: Stress profile in the concrete plate at three different time steps: $t = 0\,\text{ms}$, $t = 0.0112\,\text{ms}$ and $t = 0.0187\,\text{ms}$ where t is the time after first impingement of the blast wave on the target structure. Plotted for three configurations: a) concrete only, b) concrete coated with a hyperelastic polymer on its blast-receiving face and c) concrete coated with a visco-hyperelastic polymer on its blast-receiving face.

Table 3.3: Summary of the β_s values obtained using Eq. 3.2 for each concrete depth, h_p considered, for both blast intensity cases.

	β_s	
h_p (mm)	Case 1, $p_s/p_0 = 3.34$	Case 2, $p_s/p_0 = 0.24$
25	0.068	0.012
50	0.034	0.006
75	0.023	0.004
100	0.017	0.003

well as the numerical predictions for a rigid plate of equivalent β_s. The results are presented in Fig. 3.7.

Firstly, the concrete plates appear to lie on the "heavy plate" plateau of Kambouchev *et al.*'s theoretical expression. It would appear that for realistic concrete density and slab depths, the calculated β_s values are relatively low. In this region, I_p is relatively insensitive to β_s *i.e.* to the blast intensity and to the plate mass per unit area. On closer inspection (Fig. 3.7b), it is observed that the FSI response of the concrete is close to that of a rigid plate of the same mass. This can be explained as follows. First, the model predicted no plasticity or damage occurring in the concrete during either load case. So, the plate remained elastic throughout FSI. Secondly, it can be shown that the transit time of an elastic wave through the plate is short compared to the duration of loading, and so the influence of stress wave propagation on FSI would be negligible. The elastic wave speed in concrete is, $c_d = \sqrt{E_0/\rho_p}$. For the largest concrete plate depth considered, $h_p = 100\,\text{mm}$, the transit time for the elastic wave is given by;

$$t_T = \frac{h_p}{c_d} = \frac{h_p}{\sqrt{E/\rho_p}} = 30\,\mu\text{s} \tag{3.3}$$

Considering a blast intensity corresponding to $p_s/p_o = 3.34$, the propagation time, t_T is much smaller than the decay time of the incident blast wave, $t_i = 2\,\text{ms}$.

Incidentally, it is noted that Kambouchev *et al.*'s [160] theory gives a slightly lower prediction of the transmitted impulse in this regime compared to the numerical calculations.

3.5 1D air blast response of an elastomer-coated concrete part

In the final phase of the 1D investigation, an elastomer layer is applied to the concrete plate to assess whether it enables an FSI effect that might offer a contribution to

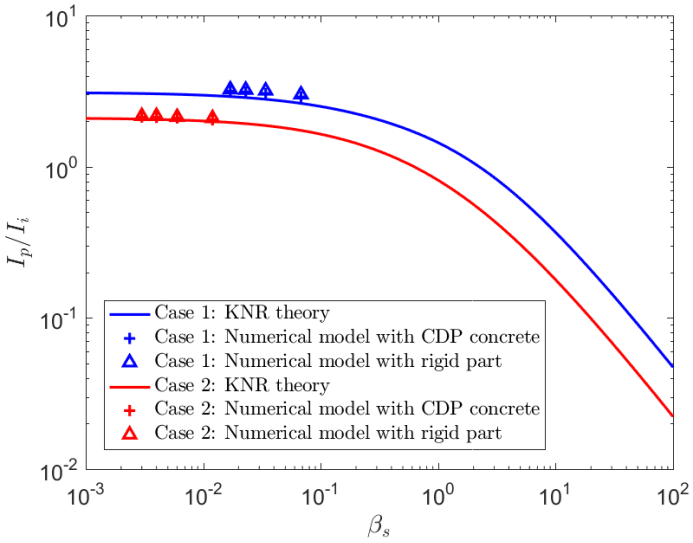

(a) Log-log plot

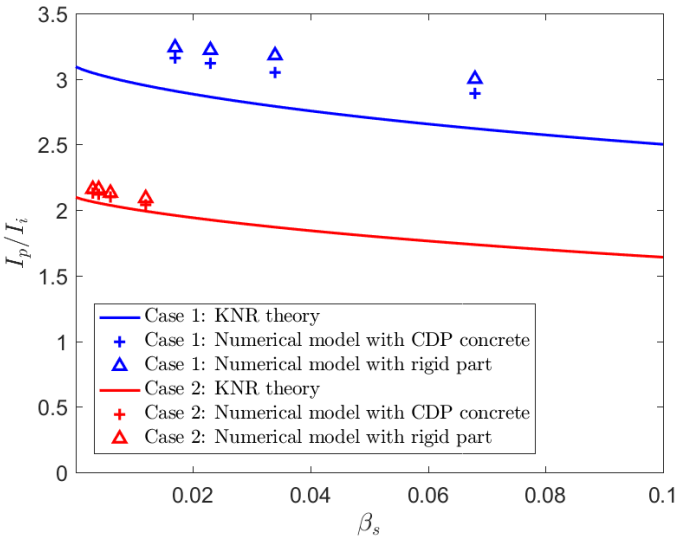

(b) Non-log plot of region of interest

Figure 3.7: Comparing numerical predictions with Kambouchev *et al.*'s (KNR) theory [160] for a rigid plate and concrete plates of depth: 25 mm, 50 mm, 75 mm and 100 mm. Case 1 refers to the intermediate intensity blast referred to in Kambouchev *et al.*'s work where $p_s/p_o = 3.34$ and $I_i = 698\,\text{Pa}\,\text{s}$. Case 2 refers to the "suitcase bomb" reference blast indicative of 20 kg of TNT at a stand-off distance of 15 m; $p_s/p_o = 0.24$ and $I_i = 34\,\text{Pa}\,\text{s}$.

protection.

A 5 mm thick elastomer layer is modelled as a deformable part, and meshed with 5 mm 3D stress (C3D8) elements. A mesh refinement investigation is performed on the 1D model (and for the 2D model, discussed subsequently). It is found that the overall response is relatively mesh insensitive, provided the Eulerian, air mesh density is matched to that of the Lagrangian concrete and elastomer coating. Boundary conditions are prescribed to ensure plane strain conditions throughout. In this study, perfect bond is assumed between the concrete and polymer, simulated by tying all degrees of freedom at the interface. Three plate configurations are analysed, illustrated in Fig. 3.8. The reference case is an uncoated concrete plate at a stand-off, $s = 3\,\text{m}$. Next, a 5 mm elastomer layer is applied to either the blast-receiving or non-blast-receiving face of a CDP plate. In both cases, the stand-off, $s = 3\,\text{m}$ measured to the blast-receiving face of the target is held constant. Thus, the shape of the incident pressure pulse by the time it has reached the blast-receiving face is the same in all cases. Figure 3.9 presents the calculated total transmitted impulse for plates of different mass per unit area for two blast intensities. Four plate thicknesses are considered — 25 mm, 50 mm, 75 mm and 100 mm. This corresponds to a mass per unit area of, 63.75, 127.5, 191.25 and 255 kgm^{-2} for the uncoated concrete, and 69.32, 133.07, 196.82 and 260.57 kgm^{-2} for the coated cases. The coatings therefore increase the mass of the target by 8.7%, 4.4%, 2.9% and 2.2%, respectively. In each configuration, the impulse imparted to the complete target plate (concrete plus elastomer, if present) is plotted, as well as the impulse transmitted to the concrete layer alone, when in its coated configuration. Also, comparison is made in each case with the response of a rigid plate of the same mass.

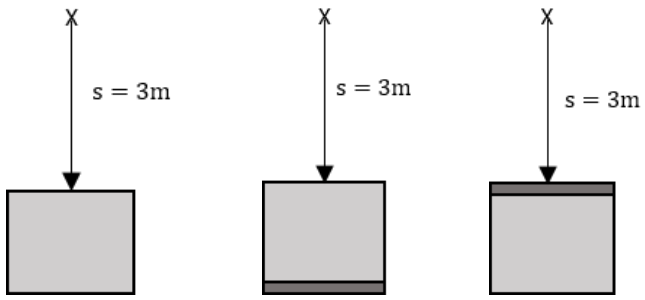

(a) Case *i* (b) Case *ii* (c) Case *iii*

Figure 3.8: Schematic illustrating the stand-off distance, s for analysis of both coated and uncoated cases.

3.5.1 Discussion

Considering the results in Fig. 3.9, four key observations are made:

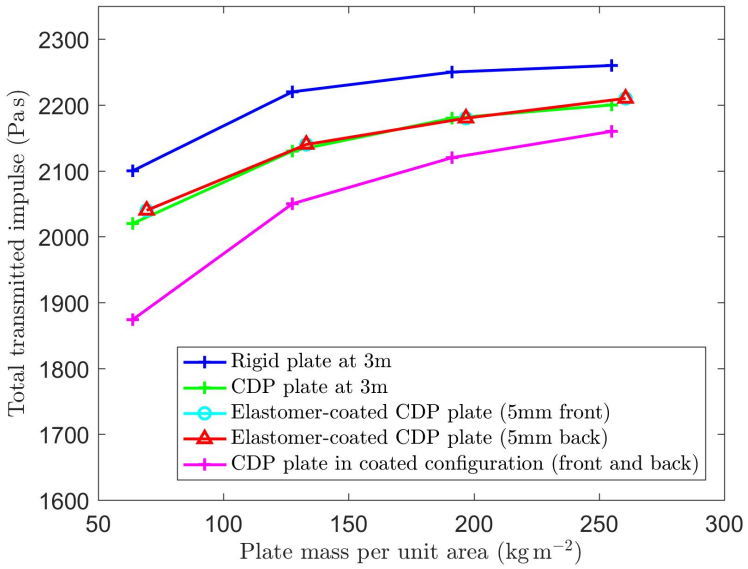

(a) Blast Case 1: $p_s/p_o = 3.34$ and $I_i = 698\,\mathrm{Pa\,s}$

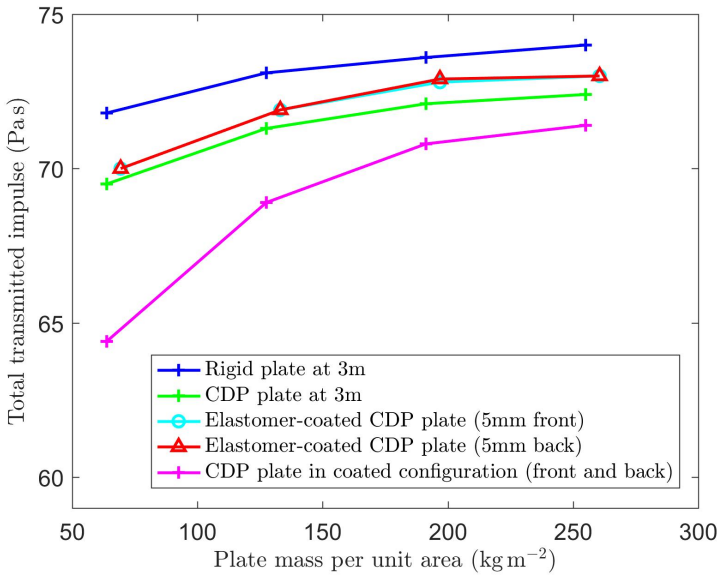

(b) Blast Case 2: $p_s/p_o = 0.24$ and $I_i = 34\,\mathrm{Pa\,s}$

Figure 3.9: A plot showing how total transmitted impulse varies with plate mass per unit area for four plate configurations: uncoated rigid and CDP plates of depth: 25 mm, 50 mm, 75 mm and 100 mm, and for CDP plates of these depths, coated with 5 mm elastomer on either the blast-receiving or the non-blast-receiving face.

- Firstly, it is found that the concrete elasticity (compliance and thus, impedance) has the effect of reducing the imparted momentum, compared to a rigid plate of the same mass.
- It appears that the imparted impulse to the composite configuration (coated concrete) is insensitive to the coating location, thus suggesting that coated concrete behaves as a monolithic plate, of mass equal to the mass of the concrete plus the mass of the polymer, from the perspective of FSI.
- The coated concrete composite acquires slightly more momentum than a monolithic concrete plate *of the same mass*. However, this effect is negligible and is likely due to a change in effective compliance of the plate. Figure 3.6 illustrated that during the short timescale response, the effect of adding a viscoelastic polymer layer led to substantial wave distortion and an increase in peak compressive stress in the concrete. Here, it is shown that while this has a small effect on the transmitted impulse to the coated configuration (pushing it towards that of a rigid plate), it is apparent that the longer timescale response is relatively insensitive to the short timescale pulse distortion effects.
- Although the composite plate acquires slightly more momentum than an uncoated concrete plate, the *concrete* layer in the composite configuration acquires less. This is because each layer acquires a fraction of the total imparted momentum in proportion to the mass fraction of that layer (assuming perfect bonding *i.e.* both concrete and elastomer acquire the same velocity). The effect is most significant for the lightest plate tested ($63.75\,\mathrm{kgm^{-2}}$) where there is an 8 % reduction in transmitted impulse to the concrete. This diminishes as the plate mass increases. For the $255\,\mathrm{kgm^{-2}}$ plate, the reduction is 2 %. Any mechanical benefit of this *momentum sharing* between the concrete and elastomer layers on critical slab deflections and failure mechanisms remains to be determined.

3.6 2D coupled Eulerian-Lagrangian model

In this section, the analysis is extended to consider the 2D response of coated and uncoated concrete slabs to explore any interplay between the short timescale FSI effects and any mechanical benefit offered by the coating during slab flexure. The 2D model geometry is illustrated in Fig. 3.10. A concrete slab of dimensions typical of structural elements is considered: 50 mm deep, with a span of 1 m. The boundary conditions at the end of slab are illustrated in Fig. 3.10. The end faces of the slab are fully constrained, with all degrees of freedom set to zero. To avoid unrealistic stress concentrations at the boundary, a degree of boundary compliance is introduced: a

50 mm length at the end of the slab is placed between rigid, frictionless surfaces, which terminate with a radius of curvature of 90 mm. The slab is placed in a 6 m long air column, at a target distance, $L_t = 3$ m. In all cases, a planar blast wave is modelled. A half-model only is simulated, using symmetry boundary conditions at midspan. The slab is modelled in 2D plane strain.

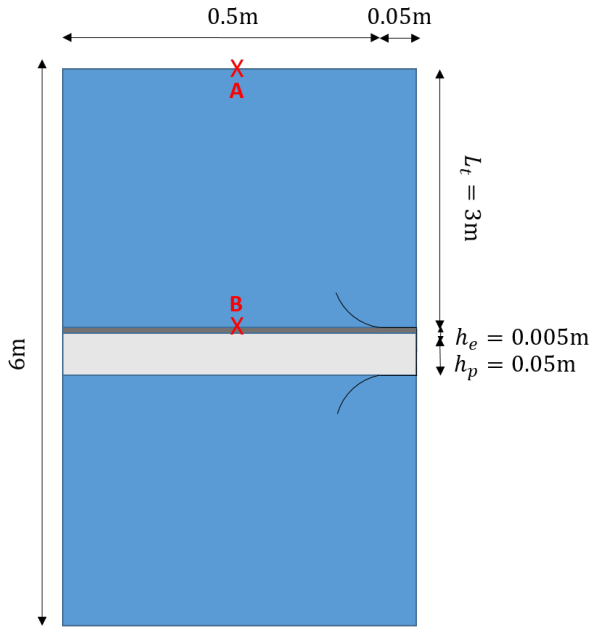

Figure 3.10: A schematic illustration of the 2D CEL 1/2-model in ABAQUS/Explicit. A CDP part of depth, $h_p = 0.05$ m and width 0.55 m is placed in a 6 m long air column, at a target distance, $L_t = 3$ m. The CDP part is coated with elastomer of depth, $h_e = 5$ mm. Point A corresponds to the inflow of the air column and point B corresponds to the point of first impingement by the blast wave on the elastomer-coated concrete. The diagram is not to scale.

As before, two blast intensities are considered and for each case, the central deflection-time response is compared for an uncoated concrete slab, a concrete slab coated with a 5 mm elastomer on the blast-receiving face and a concrete slab coated with a 5 mm elastomer on the non-blast-receiving face. The results are presented in Fig. 3.11. Two distinct response regimes are observed by comparing the two loading cases.

For the higher blast impulse, Case 1, total failure of the slab occurs early in its motion. This occurs at a time of around 0.0063 s, as indicated by the dashed line in Fig. 3.11a. Failure occurs by extensive tensile cracking and significant damage near the support region. The effect of the polymer coating in this regime is to reduce the midspan deflection at a given time, before failure. This reduction is $\sim 5\%$ for coating on either the blast-receiving or non-blast-receiving face. However, the coating does not have a significant effect on altering the mechanism or onset of failure for this loading intensity.

For the lower blast impulse, Case 2, the slab responds by elastic-plastic bending.

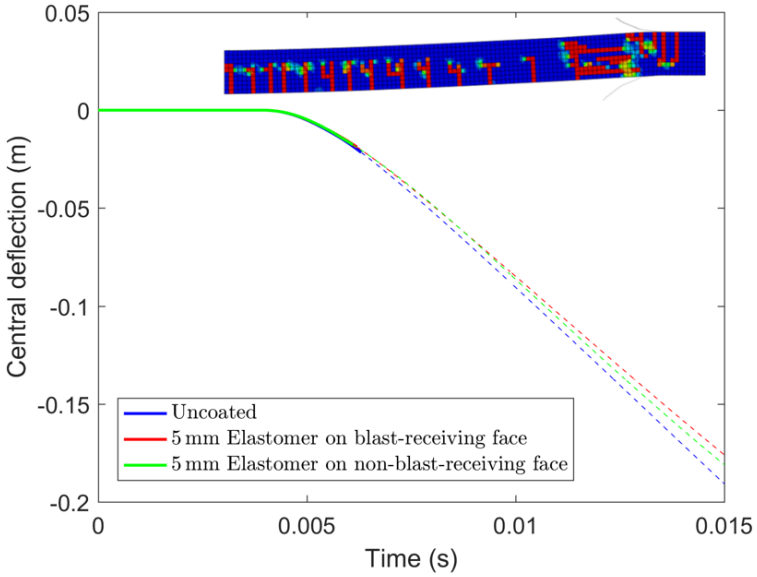

(a) Blast Case 1: $p_s/p_o = 3.34$ and $I_i = 698\,\mathrm{Pa\,s}$

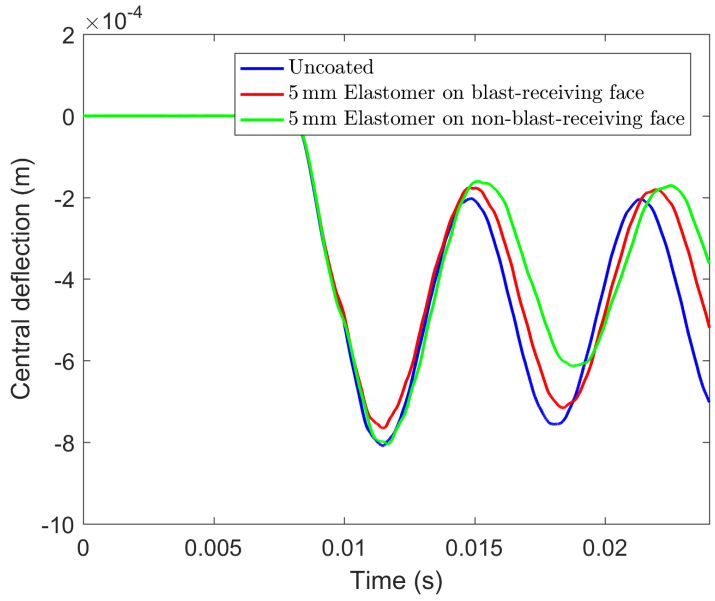

(b) Blast Case 2: $p_s/p_o = 0.24$ and $I_i = 34\,\mathrm{Pa\,s}$

Figure 3.11: Central deflection (m) *vs* time (s) for the slab geometry illustrated in Fig. 3.10 for two blast intensity cases. Results are compared for an uncoated concrete slab, a concrete slab with a 5 mm elastomer coating applied to the blast-receiving face and a concrete slab with a 5 mm elastomer coating applied to the non-blast-receiving face. Inset to a) is a snapshot at a step time of 0.0063 s of the damaged uncoated slab for Blast Case 1.

The deflections are small, with a peak predicted deflection of 0.81 mm (1.6% of the slab thickness), before elastic oscillations about a permanent deflection of around 0.48 mm for the uncoated case. The polymer coatings serve to reduce permanent slab deflections by 5% and 18% when located on the blast-receiving and non-blast-receiving faces, respectively. Although the coating appears to have no significant effect on the total transmitted impulse to the target, it appears to contribute an additional mechanical resistance to bending.

In summary, the regime of response was not affected by the coating for these load cases, though a protective benefit is observed in terms of reduced deflections. The load cases here represent lower and upper bounds on realistic blast impulses in a structural protection context. However, there are a wide range of other possible regimes of response at intermediate impulse levels, for other pressure-impulse combinations, and for other slab geometries. The role of the polymer coating across this full regime map requires further analysis.

3.6.1 Coupled *vs* decoupled response

In order to tackle the problem of identifying the full range of response regimes for coated structural elements, it is useful to consider the necessity of a fully coupled Eulerian-Lagrangian analysis. This adds significantly to the computational cost, but may not be justified if the coatings do not induce a strong FSI effect. In this section, the scope for simplifying the load case is assessed.

Three simplified load cases are considered, progressively decoupling the loading from the slab response, for comparison with the fully coupled CEL simulations.

(i) A pressure-time history, $p_1(t)$ is applied directly to the blast-receiving face of the slab, in a purely Lagrangian analysis (*i.e.* with no air domain). However, the applied loading is obtained by outputting the pressure-time history calculated at the slab-air interface (at point B in Fig. 3.10) in the coupled simulation. This is the pressure *felt* by the slab in a fully coupled FSI analysis.

(ii) A pressure-time history, $p_2(t)$ is again applied directly to the blast-receiving face of the slab in a Lagrangian analysis. However, this time, the applied pressure-time history is obtained by applying a pressure reflection coefficient factor, C_R (Eq. 2.4, defined in [160]) to the *free-field* incident overpressure, p_s measured at point B in Fig. 3.10. It is assumed that the decay time of the applied pressure-time history remains the same as the incident value, t_i.

The value of C_R is taken to be the heavy plate limit (*i.e.* $\beta_s = 0$ [160]). This

gives $C_R = 3.9$ for the higher intensity blast case considered ($p_s/p_o = 3.34$) and $C_R = 2.2$ for the lower intensity blast case considered ($p_s/p_o = 0.24$). (Note that in the acoustic limit, C_R would be equal to 2). Thus, FSI effects are removed (because the heavy plate limit for C_R is used), but a loading timescale is retained.

(iii) Lastly, impulsive loading is considered, in which an initial velocity is imparted uniformly to the slab, again in a fully Lagrangian simulation. Here, the initial velocity is equal to the imparted impulse, I_p (obtained by integrating the $p_2(t)$ profile) divided by the mass per unit area of the slab, $m = \rho_p h_p + \rho_e h_e$ [89]. Thus, both the FSI effect and the timescale of loading are removed.

Results for the slab geometry illustrated in Fig. 3.10, are presented in Fig. 3.12 for the high intensity blast ($p_s/p_o = 3.34$) and Fig. 3.13 for the low intensity blast ($p_s/p_o = 0.24$). The results suggest that the slab's deflection-time history can be accurately represented using a simpler load case, though the accuracy depends on the blast intensity. For both blast intensities, direct application of $p_1(t)$ or $p_2(t)$ matches well the response of the fully coupled analysis. Impulsive loading is reasonably accurate for the higher blast impulse case, apart from at short timescales (of the order of t_i). However, it significantly over-predicts the slab deflections for the lower blast impulse case.

3.7 Conclusions

Elastomer coatings have been previously reported as an effective solution for protecting structural components against blast loading. However, to date, the mechanisms responsible have not been clearly identified. This investigation presents the first detailed study of one candidate mechanism for concrete structural elements: fluid-structure interaction (FSI) effects during blast loading.

- Representative constitutive models for concrete and a spray-on elastomer are developed using a combination of published data and characterisation experiments.
- A Coupled Eulerian-Lagrangian finite element model is verified as an effective tool for studying the fully coupled FSI response for air blast loading. Comparison with Kambouchev *et al.*'s theory [160] over a wide range of the non-dimensional FSI parameter, β_s verifies the model fidelity.
- A high resolution, short timescale, 1D stress wave interaction study shows that the presence of an elastomer coating influences the transient stress state in the concrete during initial wave propagation through the layered structure. The

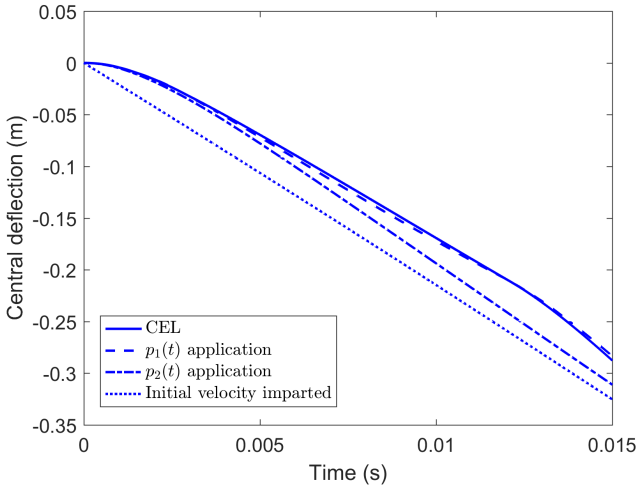

(a) Uncoated

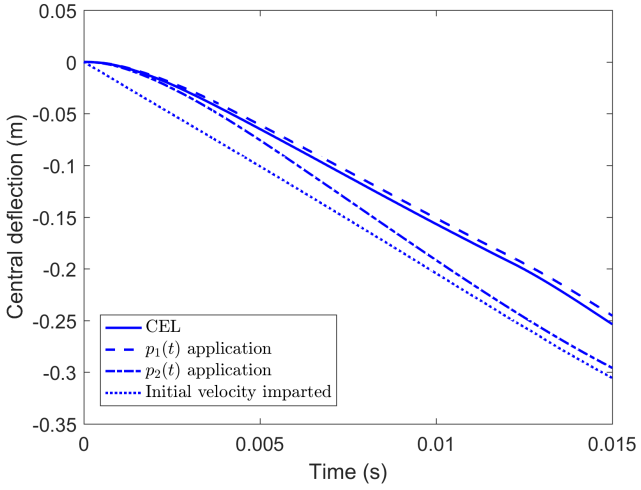

(b) Coated on blast-receiving face

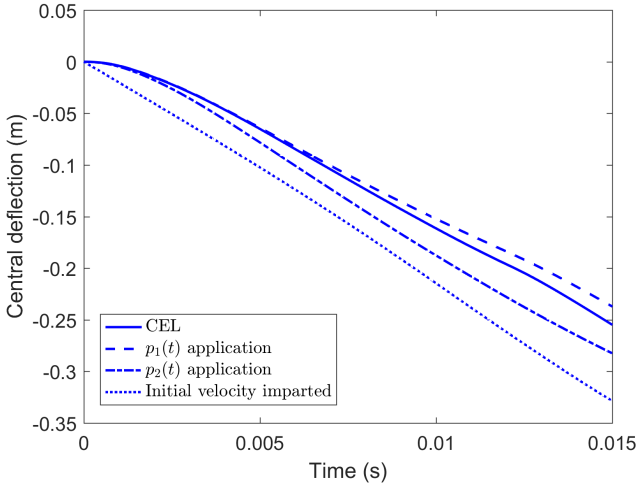

(c) Coated on non-blast-receiving face

Figure 3.12: Central deflection (m) *vs* time (s) for the slab geometry illustrated in Fig. 3.10 for Blast Case 1: $p_s/p_o = 3.34$ and $I_i = 698\,\mathrm{Pa\,s}$ ($t_i = 0.00205\,\mathrm{s}$). Results are compared for a Coupled Eulerian-Lagrangian (CEL) model, a purely Lagrangian model with loading applied by direct application of a pressure-time history, $p_1(t)$, $p_2(t)$ and for a purely Lagrangian model with impulsive loading applied by imparting an initial velocity. Note, total failure of the slab occurs early in its motion, *c.* 0.0018 s after first impingement.

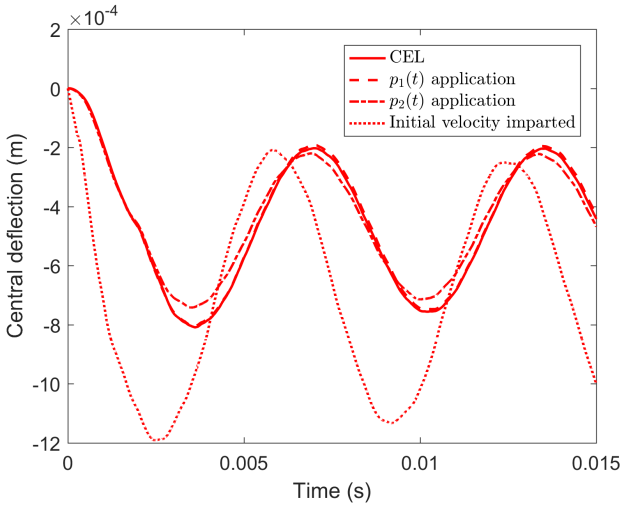

(a) Uncoated

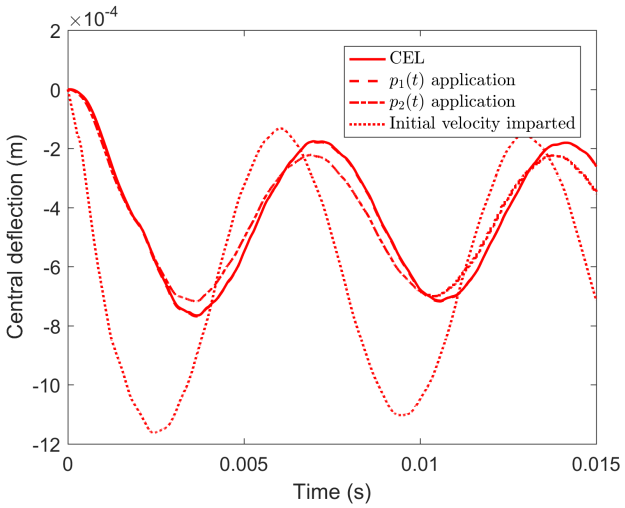

(b) Coated on blast-receiving face

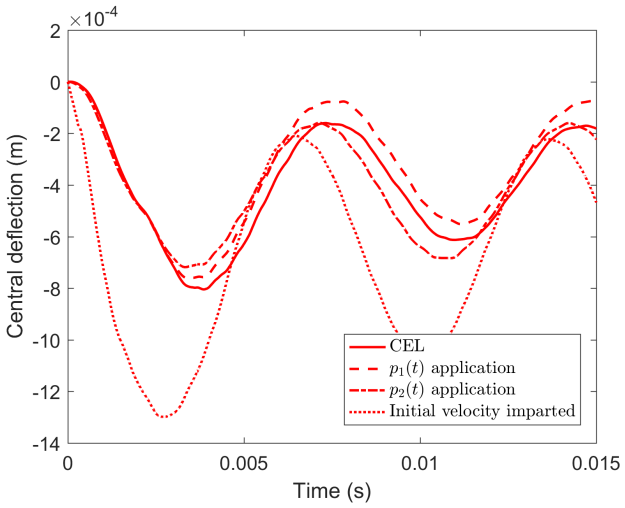

(c) Coated on non-blast-receiving face

Figure 3.13: Central deflection (m) *vs* time (s) for the slab geometry illustrated in Fig. 3.10 for Blast Case 2: $p_s/p_o = 0.24$ and $I_i = 34\,\text{Pa}\,\text{s}$ ($t_i = 0.0014\,\text{s}$). Results are compared for a Coupled Eulerian-Lagrangian (CEL) model, a purely Lagrangian model with loading applied by direct application of a pressure-time history, $p_1(t)$, $p_2(t)$ and for a purely Lagrangian model with impulsive loading applied by imparting an initial velocity.

non-linear elasticity of the polymer reduces the peak compressive stress, but introducing viscoelasticity results in a net increase.

- The longer timescale, 1D FSI response of coated and uncoated concrete is then assessed, to identify the effect of coating on the total imparted momentum. It is found that, for practical concrete thicknesses and blast impulses, the transmitted impulse for both coated and uncoated plates approaches the heavy plate limit as defined by Kambouchev *et al.*'s theory [160]. In this regime of β_s, the imparted impulse is insensitive to the target mass.
- It is found that the imparted momentum is sensitive to the elasticity of the concrete. Replacing a rigid target with a concrete target reduces the imparted momentum, for a given target mass. But the effect is small ($\sim 3\%$).
- It is also found that coating (on either face) has a negligible influence on the total imparted momentum. However, due to momentum sharing, the impulse imparted to the concrete plate is reduced in the coated configuration (by up to $\sim 8\%$ for the lightest plates).
- For blast impulses representative of a small improvised explosive device, a small additional mechanical resistance to bending is identified with the addition of the coating. The net effect is that peak deflections are largely unchanged, though permanent deflections are reduced by between $5 - 18\%$, depending on the polymer location.
- For a much higher blast impulse, the slab undergoes extensive cracking, and failure at the support. The coating provides a small reduction in slab deflection, but does not prevent slab failure.
- Finally, it is concluded that a partially decoupled Lagrangian analysis, maintaining the timescales of loading but assuming the heavy plate limit of imparted impulse, provides a reasonable substitute for the fully coupled FSI calculation. This result facilitates further investigation of the dynamic mechanical benefit offered by the coatings across a wider range of blast pressure-impulse regimes.

CHAPTER 4

Blast response regimes of elastomer-coated concrete

4.1 Introduction

Chapter 3 developed a fully coupled Eulerian-Lagrangian approach to capture the full details of the air-blast-structure interactions during the blast response of elastomer-coated concrete. It was found that the addition of an elastomer layer did not contribute a significant fluid-structure interaction effect during air blast loading. It was noted that the permanent deflections of a concrete slab structure tended to be reduced with the addition of the coating (particularly when located on the non-blast-receiving face) but the magnitude of this effect was dependent on the blast intensity. To understand this behavior, this chapter aims to map the response regimes of a reinforced concrete beam, subjected to a range of simulated blast loading using finite element analysis and analytical techniques. Based on the conclusions in Chapter 3, a simplified, purely Lagrangian numerical modelling strategy is deemed appropriate to capture the structural deflections. Throughout the study, particular emphasis will be placed on ascertaining the regimes in which the concrete is likely to experience a protective coating effect.

The chapter is structured as follows. First, a numerical model is developed in ABAQUS/Explicit [27] for an unreinforced and a reinforced concrete beam. The concrete and elastomer constitutive models are kept consistent with those developed in Sections 3.2.1 and 3.2.2. A range of simulated blast loads are applied to the structures and the response regimes of uncoated concrete sections are first identified. Next, the response regimes of two coated configurations are examined: (i) a reinforced concrete beam coated on the blast-receiving face and (ii) a reinforced concrete beam coated on the non-blast-receiving face. Analytical modelling is then used to

further describe these regimes of response, and to understand the key parameters at play. Finally, the findings are summarised on a response map, highlighting the regime boundaries and the regimes in which the coating is likely to offer effective protection.

4.2 Numerical model development

Finite element analysis (FEA) is performed using the commercial code ABAQUS/ Explicit [27]. It is used to interrogate the behaviour of unreinforced and reinforced concrete structural elements subjected to a range of simulated blast intensities.

A beam is modelled, subjected to plane strain boundary conditions on two faces — analogous to a representative element of a slab of infinite width. For the unreinforced case; a beam of dimensions 500 mm × 50 mm × 10 mm is modelled in ABAQUS/Explicit as a 3D deformable part illustrated in Fig. 4.1a. A symmetry boundary condition is applied at the midspan. The concrete is meshed with 3 mm 3D, 8-node linear elements (C3D8), chosen on the basis of a mesh sensitivity study on the deflection response. The support conditions at the ends of the beam are illustrated in Fig. 4.1. A degree of boundary compliance is introduced to avoid unrealistic stress concentrations — a 50 mm length at the end of the beam is placed between rigid, frictionless surfaces which terminate with a radius of curvature of 90 mm. The support condition is the same as that used in Section 3.6.

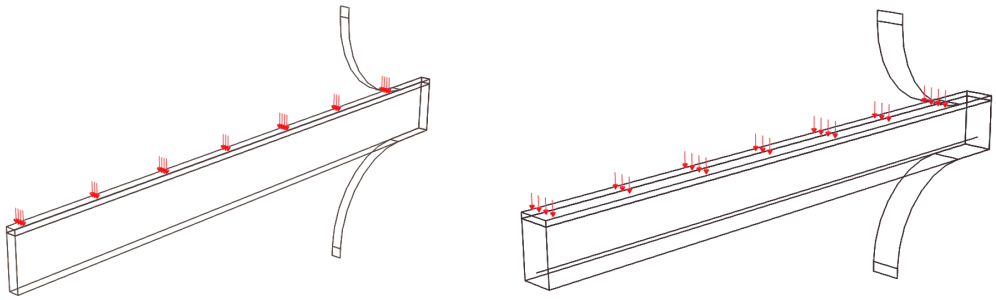

(a) Unreinforced section (b) Reinforced section

Figure 4.1: The beam geometries used in the numerical modelling of: (a) an unreinforced concrete section and (b) a reinforced concrete section. The examples show a 5 mm elastomer layer on the blast-receiving face of each section.

Blast loading is modelled using a pressure-time history and is applied uniformly to the top surface of the beam. It is noted that this omits some of the detailed interactions experienced during an explosive detonation near to a structure. However, as shown in Section 3.6.1, this approach provides a good match to a fully coupled Eulerian-Lagrangian simulation for a planar blast wave interaction. The blast wave is approximated by the exponential time-dependence in Eq. 4.1, where

p_a is the peak *applied* blast pressure and t_i is the decay time. The impulse, I_a is thus given by Eq. 4.2. Note, although they have the same form, the quantities in these equations differ from those in Eqns. 2.2 and 2.3 which describe the *incident* blast parameters.

$$p_a(t) = p_a\, e^{-\frac{t}{t_i}} \tag{4.1}$$

$$I_a = \int_0^\infty p_a(t)\, dt = p_a\, t_i \tag{4.2}$$

4.2.1 Concrete and elastomer constitutive models

The concrete and elastomer constitutive models are the same as those described in Chapter 3.

The Concrete Damaged Plasticity model, available in ABAQUS/Explicit [27] is employed for the concrete and is described in detail in Section 3.2.1.

The elastomer constitutive model is based on a hyperelastic response (using a Yeoh strain energy potential) and a Prony series captures the strain rate dependence. Section 3.2.2 provides further details. For the coated beam cases, an elastomer coating thickness of 5 mm is considered and a perfect bond is assumed between the concrete and elastomer. This is simulated by tying all degrees of freedom at the interface. The elastomer mesh and plane strain boundary conditions match those prescribed for the concrete, defined previously.

4.2.2 Reinforcing steel constitutive model

For the reinforced concrete beams (Fig. 4.1b), the reinforcing steel is modelled as a 5 mm diameter bar, positioned to give 10 mm of concrete cover. The steel material model is chosen as the Johnson Cook plasticity model with values based on typical steel 4340 with a yield strength, $\sigma_{ys} = 600$ MPa [50]. The same model is described in Appendix A.2.

To aid the analytical analysis discussed subsequently, a balanced design was chosen *i.e.* one in which failure occurs by concrete crushing and steel yielding simultaneously. Considering longitudinal equilibrium at the ultimate limit state (discussed subsequently in Fig. 4.10a), Eq. 4.3 is derived for the balanced reinforcing ratio, ρ_b [179, 180]:

$$\rho_b = \frac{A_s}{b\,d} = \frac{\gamma_s\,0.6\,\sigma_{cu}}{\gamma_c\,\sigma_{ys}}\frac{\epsilon_{cu}}{\epsilon_y + \epsilon_{cu}} \tag{4.3}$$

where A_s is the cross-sectional area of the steel reinforcing bar, b is the beam width and d is the *effective depth i.e.* the depth to the steel rebar. $\gamma_s = 1.15$ and $\gamma_c = 1.5$ are material partial safety factors for steel and concrete, respectively [180]. The ultimate compressive concrete strain is assumed to be, $\epsilon_{cu} = 0.0035$ and the steel yield strain, $\epsilon_y = 0.003$ [179, 180].

For the geometry described, it is calculated that a section width of $b = 30\,\text{mm}$ provides an approximate balanced section for the chosen rebar diameter. The reinforcing bars are defined as a wire truss and incorporated using the embedded element constraint available in ABAQUS.

4.3 Response regimes of uncoated concrete

4.3.1 Regime identification

First, the response of uncoated concrete is considered. A series of numerical simulations are performed on the beams described in Section 4.2, at various combinations of peak pressure, p_a and impulse, I_a (I_a is varied for a given p_a by varying the decay time, t_i). Figure 4.2 presents the deflection-time history plots for an uncoated, reinforced concrete beam, subject to three different load intensities. Also plotted is the energy dissipated by damage in each case (obtained by interrogating the ALLDMD output in ABAQUS/Explicit [27]). Examination of these plots identifies three distinct regimes of response, defined as follows:

- Regime 1: For low impulses, the beam undergoes completely elastic oscillations about a zero level permanent displacement. In addition, the energy dissipated by damage is zero. This is readily observed in Fig. 4.3a.
- Regime 2: For intermediate impulses, elastic-plastic behaviour is observed, characterised by oscillations about a permanent displacement. Further, the beam achieves a well-defined, stable plateau in energy dissipated by damage, which occurs well after the maximum displacement attained by the beam. (Construction lines on Fig. 4.2b illustrate how this is verified for cases when the plateau transition is not sharp.) Figure 4.3b illustrates that the beam exhibits minor damage at the midspan and at the supports.
- Regime 3: At higher impulses and pressures, reinforced concrete beams achieve a plateau in ALLDMD which occurs before the beam has attained its max-

imum midspan displacement. The level of damage in this regime is severe, as illustrated in Fig. 4.3c. A mesh sensitivity study has identified numerical stability problems in this regime so it is necessary to define a time at which the beam has *failed*, beyond which the calculation is deemed inaccurate. This avoids any misleading comparison between stable and unstable numerical solutions.

To enable comparison, a *critical displacement* is defined in each regime as follows:

- Regime 1: The critical displacement is taken as the maximum midspan transverse displacement.
- Regime 2: The critical displacement is again taken as the maximum midspan transverse displacement.
- Regime 3: The *knee* point in the ALLDMD *vs* time graph is chosen as an arbitrary failure time, and the corresponding displacement is noted and recorded as the critical displacement. No physical significance is attached to this indicative value. However, it represents the time at which there is a drop in the rate of further damage propagation, on account of the loss of concrete integrity. In Fig. 4.2c, the response beyond this point is shown as a dotted line.

Figure. 4.4 presents contours of critical displacement in $p_a - I_a$ space for an uncoated, reinforced concrete beam. It is observed that at lower impulses, in the range $10^1 - 10^2\,\mathrm{Pa\,s}$, the level of critical displacement is relatively insensitive to the level of the peak pressure, for a given impulse. At higher impulses ($c.\,10^3\,\mathrm{Pa\,s}$), the critical displacement is sensitive to the corresponding peak pressure, with the most severe blast intensities giving rise to the highest critical displacements experienced by the beam. This response map provides a reference against which to compare the effect of the coating, described subsequently.

4.3.2 Reinforced *vs* unreinforced, uncoated concrete beams

For completeness, the sensitivity of this reference response map to the presence of steel reinforcement is briefly assessed. Figure 4.5 considers slices through a $p_a - I_a$ diagram at three values of applied peak pressure, p_a for an uncoated concrete beam. The critical displacements for unreinforced and reinforced configurations are compared.

Generally it is observed that the critical displacement increases with increasing impulse. However, for high intensity blasts (higher peak pressure, p_a and impulse,

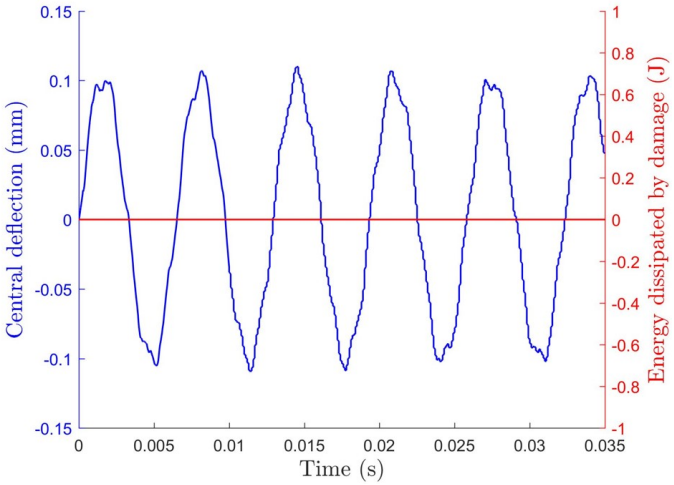

(a) Regime 1

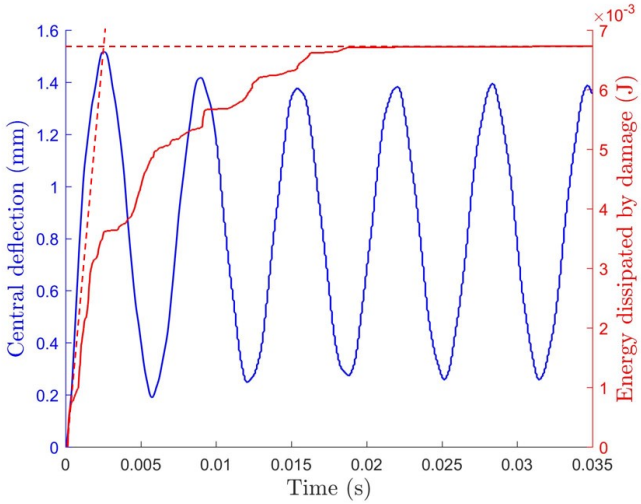

(b) Regime 2

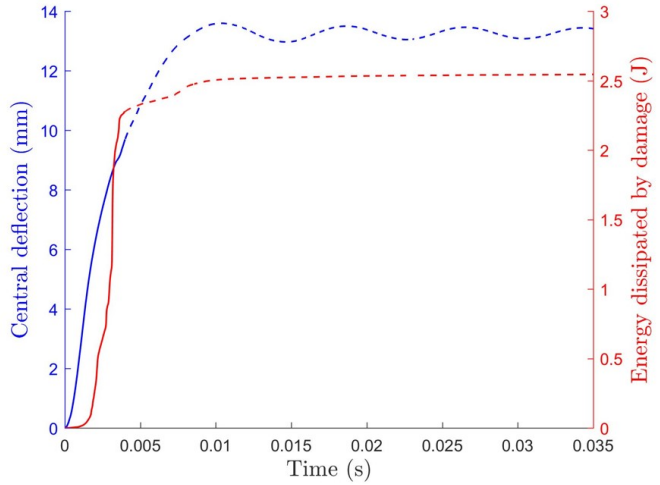

(c) Regime 3

Figure 4.2: Central deflection - time and energy dissipated by damage - time histories plotted for an uncoated, reinforced concrete beam subjected to three different blast intensities: a) $p_a = 1000\,\text{kPa}$, $I_a = 10\,\text{Pa s}$ b) $p_a = 1000\,\text{kPa}$, $I_a = 100\,\text{Pa s}$ and c) $p_a = 1000\,\text{kPa}$, $I_a = 500\,\text{Pa s}$.

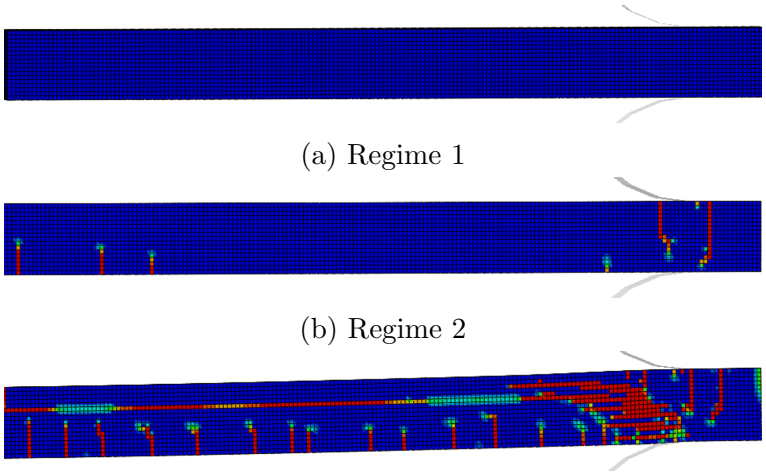

(a) Regime 1

(b) Regime 2

(c) Regime 3

Figure 4.3: Damaged beam configurations in each response regime. Plotting contours of tensile damage parameter, d_t where red contours indicate $d_t > 0.9$ which is assumed to be analogous to cracking. Image is taken at the time corresponding to the critical displacement.

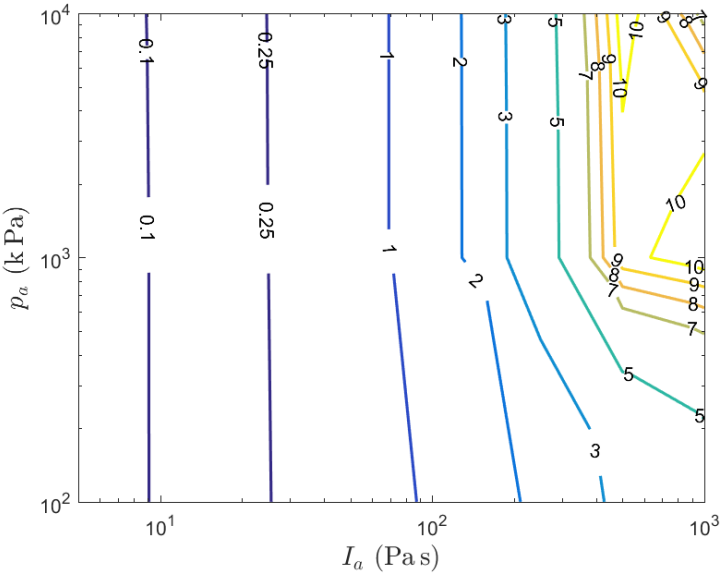

Figure 4.4: Contour plot mapping the $p_a - I_a$ (applied pressure - applied impulse) space for an uncoated, reinforced concrete beam of the geometry described in Section 4.2. Contours are isolines of critical displacement in millimeters.

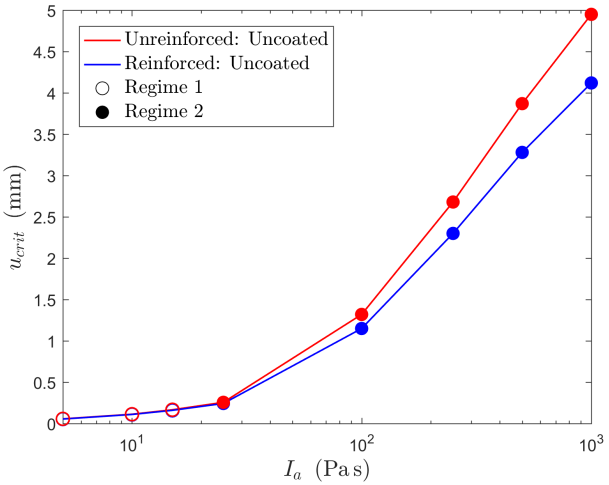

(a) $p_a = 100\,\text{kPa}$

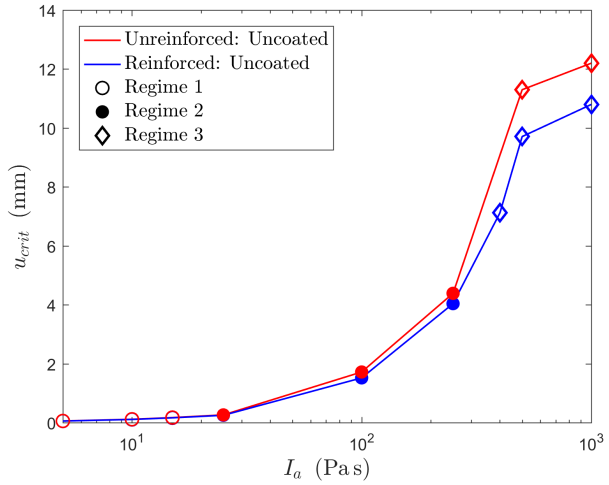

(b) $p_a = 1000\,\text{kPa}$

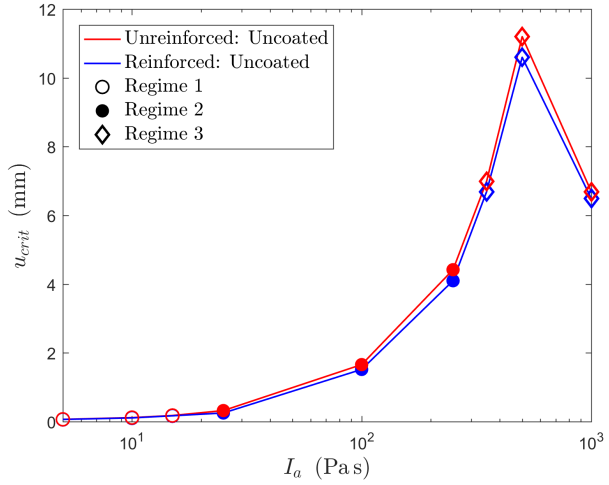

(c) $p_a = 10,000\,\text{kPa}$

Figure 4.5: Critical displacement, u_{crit} variation with applied impulse, I_a at three different peak pressures, p_a. Results are plotted for uncoated, reinforced and unreinforced concrete beams.

I_a), the critical displacement starts to fall with increasing I_a. This is because beam failure is occurring earlier in the beam's motion, with increasing impulse. The presence of reinforcing bar has only a small effect in Regimes 1 and 2 which will be explained by analytical reasoning in Section 4.5.1. In Regime 3, comparison is made difficult given that the simulation must be halted at an early time step, before severe concrete damage leads to mesh sensitivity. Instead, in Fig. 4.6, central deflection-time histories are compared for uncoated, unreinforced and reinforced concrete beams exhibiting a Regime 3 response. The unreinforced beam fails to reach a permanent deflection, in contrast to the reinforced case where the presence of the reinforcing bar serves to stabilise the deflections of a severely damaged beam. However, the overall picture remains unaffected, since the critical displacement is defined well before this effect becomes significant. Thus, the following investigation will focus only on reinforced concrete.

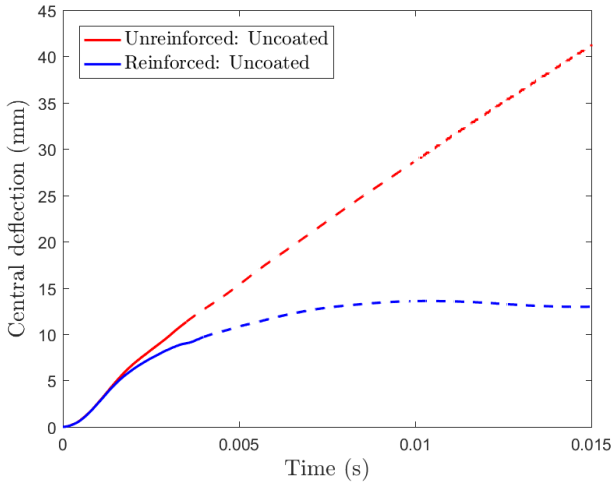

Figure 4.6: Central deflection - time history for an uncoated, reinforced and unreinforced concrete beam subjected to $p_a = 1000\,\text{kPa}$ and $I_a = 500\,\text{Pa s}$, behaving in response Regime 3. A critical displacement is defined, beyond which, the deflection is shown as a dotted line.

4.4 Response regimes of coated, reinforced concrete

With the response regimes of uncoated, reinforced concrete beams established, the influence of the addition of an elastomer coating is now interrogated. Three configurations are considered: (i) uncoated, (ii) coated on the blast-receiving (front) face and (iii) coated on the non-blast-receiving (back) face. The numerical modelling strategy is as described in Section 4.2. Figure 4.7 plots the variation in critical displacement, u_{crit} with applied impulse, I_a for three values of peak applied pressure, p_a.

First, it is observed that for beams behaving in Regimes 1 and 2, at the lower load intensities, the addition of a 5 mm elastomer coating to either the blast-receiving or

non-blast-receiving face contributes a negligible effect to the critical displacements experienced. There is some evidence that coating on the front face, in Regime 2, is most beneficial in terms of reducing u_{crit}. Future studies will seek to assess the interplay between the additional mass contribution and any pulse-shaping or mechanical coating benefits in these low intensity regimes. However, the effect here is a minor one and furthermore, the addition of the coating does not affect the boundary between Regimes 1 and 2, in terms of applied impulse.

At higher load intensities, in Regime 3, interpretation of FE results is hindered by severe concrete damage which leads to inherent mesh sensitivity. However, significant effects can be observed when considering the critical displacements and impulses close to the boundary between Regimes 2 and 3. Figure 4.8 plots the displacement-time history for the beam when subjected to a blast intensity, $p_a = 10,000\,\text{kPa}$ and $I_a = 350\,\text{Pa s}$. This corresponds to a load case that gives rise to a beam response in the vicinity of the Regime 2 - 3 boundary. For the uncoated RC beam and that coated on its blast-receiving face, the beam exhibits a Regime 3 response whereas, when coated on its non-blast-receiving face, it behaves with a Regime 2 response. This shift from Regime 3 to Regime 2 behaviour results in a significant reduction of 48% in the permanent displacement experienced by the beam. It is observed that in Regime 3, one mechanism of failure is tensile cracking, propagating perpendicular to the rear, tensile face of the beam. The other mechanism is extensive damage locally at the supports. The polymer appears most effective at suppressing this particular failure mechanism.

4.5 Analytical modelling

In this section, analytical models are used to support the interpretation of the FE predictions and to help explain the predicted sensitivity to the elastomer coating in each of the identified regimes.

4.5.1 Regime 1

Regime 1 is characterised by purely elastic bending of the beam. To capture this, Timoshenko *et al.*'s [181] theory on the transverse vibrations of an elastic beam is employed. An impulsive load is assumed, with an instantaneous transverse velocity, V_{inst} applied along the length of the beam. This assumption is valid for cases when the blast pulse duration, t_i is much shorter than the structural response time *i.e.* when the peak pressure, p_a is large for a given impulse, I_a. The instantaneous velocity, V_{inst} is related to the imparted impulse, I_a by Eq. 4.4 [89].

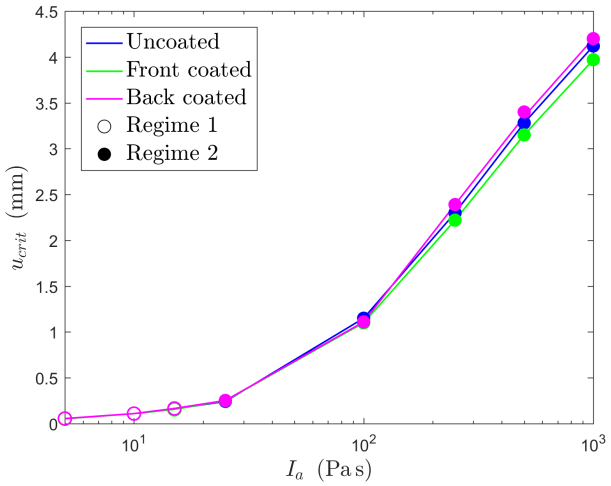

(a) $p_a = 100\,\text{kPa}$

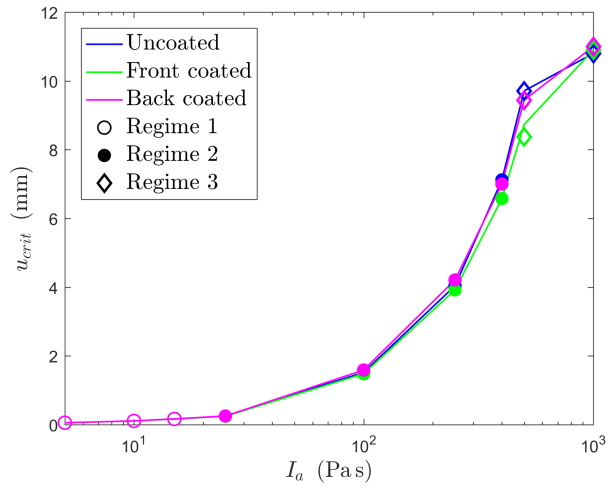

(b) $p_a = 1000\,\text{kPa}$

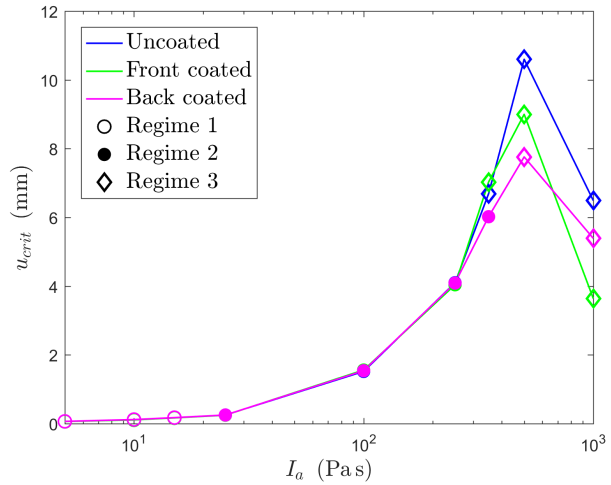

(c) $p_a = 10,000\,\text{kPa}$

Figure 4.7: Critical displacement, u_{crit} variation with applied impulse, I_a at three different peak applied pressures, p_a. Results are plotted for a reinforced concrete beam in three configurations: (i) uncoated, (ii) front coated (on the blast-receiving face) and (iii) back coated (on the non-blast-receiving face).

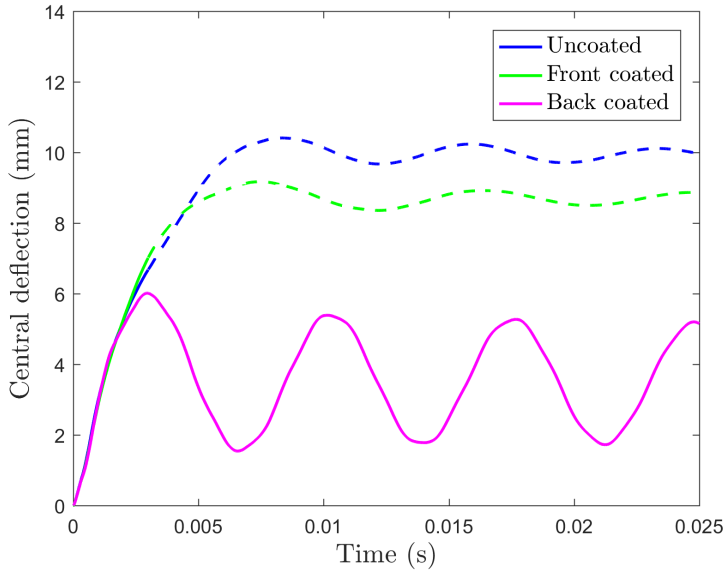

Figure 4.8: Central deflection - time history for a reinforced concrete beam subjected to $p_a = 10,000\,\text{kPa}$ and $I_a = 350\,\text{Pa s}$. Three configurations are considered: (i) uncoated, (ii) front coated (blast-receiving face) and (iii) back coated (non-blast-receiving face). A failure time is defined in Section 4.3.1, beyond which, the deflection is shown as a dotted line.

$$I_a = \int_0^\infty p_a\, e^{-\frac{t}{t_i}}\, dt = p_a\, t_i = m_a\, V_{inst} \tag{4.4}$$

where m_a is the mass per unit area of the beam.

First, a simply supported beam (of length, $2L$, axial co-ordinate, x and transverse deflection, y) is considered. The transverse vibrations may be described by Eq. 4.5, derived from the theory in [181].

$$y(x,t) = \frac{4\,V_{inst}}{\pi} \sum_n \frac{1}{n\,\omega_n} \sin\frac{n\pi x}{2L} \sin\omega_n t \quad \text{for} \quad n = 1,3,5...\infty \tag{4.5}$$

where

$$\omega_n = \frac{n^2\,\pi^2}{4L^2} \sqrt{\frac{E^*\,I_{xx}}{\rho\,A}} \tag{4.6}$$

where I_{xx} is the second moment of area of the cross-section about its major axis; ρ is the material density and A is the cross-sectional area of the beam. Here, the modulus $E^* = E$ in plane stress, and $E^* = E/(1-\nu^2)$ in plane strain. The latter is used for comparison with the plane strain FE calculations.

Alternatively, a different support condition may be considered. The transverse vibrations of a beam with both ends clamped (or fixed) may also be derived using

Timoshenko theory [181]:

$$y(x,t) = V_{inst} \sum_n \frac{X_n}{p_n\, k_n} \sin p_n\, t(\sinh 2k_n\, L - \sin 2k_n\, L - \alpha_n\, \cosh 2k_n\, L \\ -\alpha_n\, \cos 2k_n\, L - 2\,\alpha_n) \quad \text{for} \quad n = 1, 3, 5...\infty \tag{4.7}$$

where

$$X_n = \cosh k_n\, x - \cos k_n\, x - \alpha_n(\sinh k_n\, x - \sin k_n\, x) \tag{4.8}$$

and

$$\alpha_n = \frac{\cosh 2k_n\, L - \cos 2k_n\, L}{\sinh 2k_n\, L - \sin 2k_n\, L} \tag{4.9}$$

And, $k_n = (2\,n + 1)\pi/4L$ and $p_n = a\, k_n^2$ where $a = \sqrt{E^*\, I_{xx}/\rho\, A}$ [181].

In the elastic regime, the effect of a 5 mm thick elastomer coating can be accounted for using the *transformed section* approach, whereby the elastomer coating is *transformed* to an equivalent area of concrete in the ratio of the elastic moduli, $\phi_e = E_e/E_0$. For a reinforced concrete section of elastic modulus, $E_0 = 28.3\,\text{GPa}$ coated with an elastomer of elastic modulus, $E_e = 80\,\text{MPa}$, the modular ratio, $\phi_e = 2.8 \times 10^{-3}$. Thus, the addition of an elastomer coating has a negligible effect on the position of the neutral axis and the value of the second moment of area, I_{xx} of the section. Indeed, for any realistic coating and beam depths, the effect remains negligible. The method of *transformed section* can also be used to explain why there is such a small difference in the Regime 1 deflections exhibited by the reinforced and unreinforced sections in Fig. 4.5. The area of steel rebar, A_s is converted to an equivalent area of concrete using the modular ratio, $\phi_s = E_s/E_0 = 7.1$ where the elastic modulus of steel, $E_s = 200\,\text{GPa}$. The addition of steel rebar has a small (less than 10%) effect on the neutral axis position and second moment of area.

Thus, Equations 4.5 to 4.9 can be used to provide analytical estimates for the maximum transverse displacement of both coated and uncoated beams. Considering a 50 mm thick, reinforced concrete beam of the geometry described in Section 4.2, a comparison between the FEA results and analytical predictions is presented in Fig. 4.9.

The clamped-clamped beam analysis predicts deflections which are in very close agreement with the FEA results. In this low blast intensity regime, the simply-

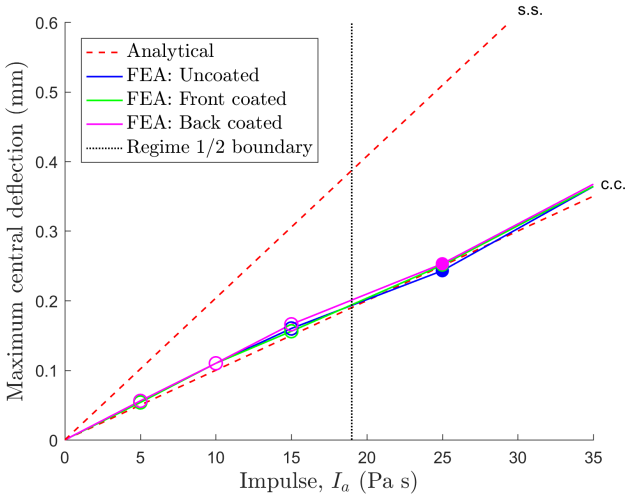

(a) $p_a = 100\,\text{kPa}$

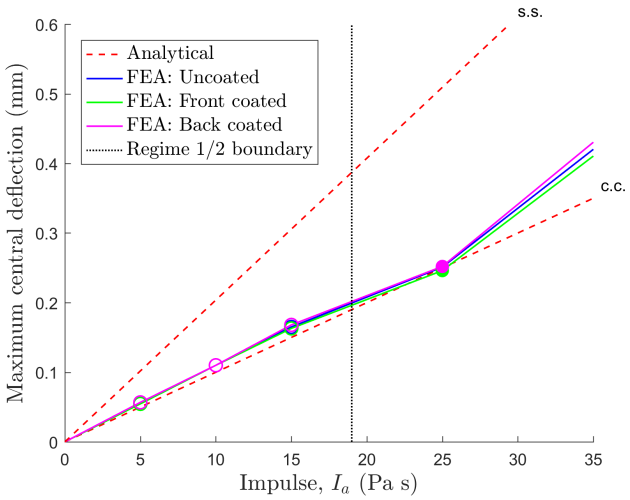

(b) $p_a = 1000\,\text{kPa}$

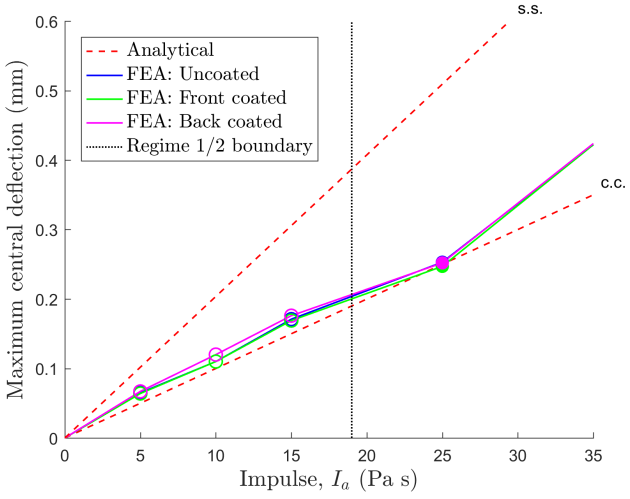

(c) $p_a = 10,000\,\text{kPa}$

Figure 4.9: Comparison between maximum central deflection predicted by the FE model and analytical theory for reinforced concrete beams at low blast intensities. Three configurations are considered: (i) uncoated, (ii) front coated (blast-receiving face) and (iii) back coated (non-blast-receiving face). Analytical predictions are presented for two support conditions: simply supported (s.s.) and clamped-clamped (c.c.). The dotted line at $I_a = 19\,\text{Pa s}$ indicates the analytically predicted boundary between Regimes 1 and 2. ○ represents Regime 1 behaviour and • is Regime 2.

supported model consistently overpredicts beam deflections. Nevertheless, both models are sufficient to explain the insensitivity of the beam to the coating in Regime 1, as observed in the FE analysis.

4.5.2 Regime 1 - 2 transition

Extending the relatively simpler analysis for the simply-supported beam, the relationship presented in Eq. 4.10 is obtained for the dynamic stress on the cross-section, $\sigma(x,t)$ at a distance, z from the neutral axis, at an axial position, x and time, t.

$$\sigma(x,t) = -E^* z \frac{\partial^2 y}{\partial x^2} = 4\pi E^* z V_{inst} \sum_n \frac{n}{4\,\omega_n\,L^2} \sin\frac{n\pi x}{2L} \sin\omega_n t \quad \text{for} \quad n = 1,3,5...\infty \tag{4.10}$$

Using Eq. 4.10, the maximum stress on the cross-section can be calculated at the extreme fibre, $z = 25\,\text{mm}$. Assuming that purely elastic behaviour ceases when the maximum stress on the cross-section reaches the value of the concrete tensile strength, $\sigma_{t0} = 4.2\,\text{MPa}$; a script can be implemented to find the instantaneous velocity, V_{inst} and hence the impulse, I_a when this criterion is first reached. This provides an analytical estimate for the boundary between Regimes 1 and 2. For the reasons described previously, the addition of an elastomer coating has a negligible effect on the maximum stress experienced by the reinforced section in the elastic regime. Thus, the critical velocity in Regime 1 for both coated and uncoated cases is $V_{inst} = 0.15\,\text{m}\,\text{s}^{-1}$ and the critical impulse is $I_a = 19\,\text{Pa}\,\text{s}$. This predicted boundary is marked on the plots in Fig. 4.9. It is found to be a good match to the FEA which predicts a Regime 1 - 2 transition between $I_a = 15 - 25\,\text{Pa}\,\text{s}$. Assuming the critical location to be at the midspan, the critical impulse is calculated to be the same for both simply-supported and clamped beams (it is noted however that in the clamped case, the critical location may well be at the supports; in this case a lower critical impulse, $I_a = 14\,\text{Pa}\,\text{s}$ is predicted).

4.5.3 Regime 2

Regime 2 behaviour is characterised by oscillations about a permanent level of deflection. The transition from the purely elastic Regime 1 is accompanied by the onset of damage. To interrogate this regime, Jones' [39] solutions for the deformation of a rigid-perfectly plastic beam, loaded impulsively are employed. Jones justifies the rigid-perfectly plastic analysis by assuming that elastic effects can be neglected

when the external dynamic energy *i.e.* the kinetic energy, K_e is much larger than the maximum strain energy, S_e that the beam can absorb elastically. As before, if it is assumed that the beam acquires an instantaneous velocity, V_{inst} when loaded impulsively, the following non-dimensional group, E_r provides an indication of when elastic effects can be neglected:

$$E_r = \frac{K_e}{S_e} = \frac{\rho E_0 V_{inst}^2}{\sigma_o^2} >> 1 \tag{4.11}$$

where ρ is the density of the beam and σ_o is the yield stress of a rigid-perfectly plastic material, which for concrete, is estimated as the tensile strength, $\sigma_{to} = 4.2$ MPa. $E_r = 1$ is achieved for a velocity, $V_{inst} = 0.5\,\mathrm{m\,s^{-1}}$ which corresponds to an impulse, $I_a = 63\,\mathrm{Pas}$.

Jones [39] provides the following prediction for the permanent transverse displacement, u_{perm} of a simply-supported beam, of length, $2L$ loaded impulsively:

$$u_{perm} = \frac{m_L\, V_{inst}^2 L^2}{3\, M_0} \tag{4.12}$$

Further, Jones' [39] solution for a clamped-clamped beam loaded impulsively is also considered:

$$u_{perm} = \frac{m_L\, V_{inst}^2 L^2}{6\, M_0} \tag{4.13}$$

where m_L is the mass per unit length of the beam and M_0 is the collapse moment for the cross-section.

One of the inherent assumptions in Jones' theory [39] is that the beam is ductile — this is not the case for an unreinforced concrete section which undergoes brittle failure. Therefore, Jones' solutions are not valid in this case.

To obtain a value for the collapse moment, M_0 for a reinforced concrete beam, the ultimate limit state is considered where two simplifying assumptions are made: the tensile strength of the concrete is assumed to be zero and the concrete compressive behaviour can be approximated using an equivalent rectangular stress block, illustrated in Fig. 4.10. For simplicity, a mean stress of $0.6\,\sigma_{cu}$ is assumed based on the BS8110 recommendation [179] (where σ_{cu} is the compressive strength of the concrete, 39.5 MPa). Assuming that the steel yields at the same time as the concrete

fails (*i.e.* a balanced cross-section), longitudinal equilibrium for the uncoated beam in Fig. 4.10a gives the neutral axis depth, z;

$$z = \frac{\overline{A_s}\,\sigma_{ys}}{0.6\,\sigma_{cu}} \tag{4.14}$$

Moment equilibrium gives the ultimate moment per unit width of the beam:

$$\overline{M_0} = \sigma_{ys}\,\overline{A_s}\,(d - 0.5\,z) \tag{4.15}$$

where for the geometry discussed in Section 4.2:

d is the effective depth of the cross-section (to the reinforcing bar), 40 mm;
$\overline{A_s}$ is the area of the reinforcing steel per unit width of the beam, $A_s/b = 19.6\,\text{mm}^2/30\,\text{mm}$;
σ_{ys} is the yield strength of the reinforcing steel, 600 MPa.

The addition of a coating to either the blast-receiving (Fig. 4.10b) or non-blast-receiving (Fig. 4.10c) face introduces an additional longitudinal stress equal to, $\epsilon_e\,E_e\,b\,h_e$. E_e is the Young's Modulus of the elastomer which is assumed to be 80 MPa (measured from Fig. 3.2 at small strain) and h_e is the depth of the elastomer coating, 5 mm. The strain in the elastomer, ϵ_e can be estimated given the ultimate compressive concrete strain, $\epsilon_{cu} = 0.0035$ and the steel yield strain, $\epsilon_y = 0.003$. This extra term has only a small influence on the neutral axis position and $\overline{M_0}$. The calculated values of neutral axis depth, z and ultimate moment per unit width, $\overline{M_0}$ are summarised in Table 4.1. Note that this estimate of $\overline{M_0}$ is a conservative value given that the tensile strength of concrete is assumed to be zero.

Table 4.1: Neutral axis depth, z and ultimate moment per unit width, $\overline{M_0}$ predictions for a reinforced concrete beam in three configurations: (i) uncoated, (ii) coated on the front (blast-receiving) face and (iii) coated on the back (non-blast-receiving) face.

	Uncoated	Front Coated	Back coated
Neutral axis depth, z (mm)	16.5	16.5	16.7
Ultimate moment per unit width, $\overline{M_0}$ (kN)	12.4	12.5	12.8

The predictions for the permanent displacement, u_{perm} of simply supported and clamped-clamped beams in their uncoated, front coated and back coated configurations are compared with FEA results in Fig. 4.11.

For an intermediate value of p_a (Fig. 4.11b) there is very good agreement between the FEA results and analytical predictions. The FE results fall between the simply

(a) Uncoated

(b) Coated on blast-receiving face

(c) Coated on non-blast-receiving face

Figure 4.10: Schematic of a reinforced concrete section at its ultimate limit state in three configurations: (i) uncoated, (ii) coated on its blast-receiving face and (iii) coated on its non-blast-receiving face. The stress, σ profiles are presented to illustrate how the ultimate moment, M_0 can be derived by equilibrium.

supported and clamped-clamped analytical predictions which matches the boundary condition employed in the FE model (discussed in Section 4.2). For this load case, the results sit consistently within Regime 2, and hence Jones' theory is effective at predicting permanent deflections. Furthermore, the analytical model confirms the insensitivity to the coating in Regime 2.

For the highest peak pressure (Fig. 4.11c) there is also good agreement between the analytical model and the FE for results within Regime 2. As the impulse is increased, moving into Regime 3, the discrepancies increase. The FE results predict that the boundary between Regimes 2 and 3 lies between $I_a = 350 - 500\,\mathrm{Pa\,s}$ (for $p_a = 10,000\,\mathrm{kPa}$).

For the lowest value of p_a (Fig. 4.11a), although the beam is responding in Regime 2, the analytical model provides a good prediction of deflections only at the lowest values of impulse. High impulse, low peak pressure load cases correspond to a large blast duration, t_i. In these cases, the value of t_i is no longer small with respect to the structural response time. As a consequence, the impulsive loading assumption in the analytical model ceases to be realistic.

4.5.4 Regime 3

The Regime 3 response is dominated by concrete damage. The beam undergoes continued plastic deformation and damage throughout the FE calculation. Note that damaged elements are not deleted from the FE model, which may affect the reliability of the predictions when the volume of damaged concrete is significant. As described in Section 4.3.1, the simulations must therefore be halted at a time step corresponding to a defined critical level of damage. Analytical methods are also limited in their ability to predict the extensive cracking and damage.

However, some insight is gained by qualitatively examining the damaged beam configurations at the time at which the critical displacement (defined in Section 4.3.1) is reached. Figure 4.12 illustrates that by increasing the blast intensity, within Regime 3, a switch in the pattern of damage is observed to one which is dominated by failed elements near the support region (Fig. 4.12b). This indicates that at the highest blast intensities considered, the beam undergoes a transverse shear failure mechanism at the supports. This has been widely reported in the literature for RC structures subjected to high intensity impulsive loading [71, 72]. In the following section, an analytical technique is described which can be used to investigate the effect of a polymer coating on this particular failure mechanism.

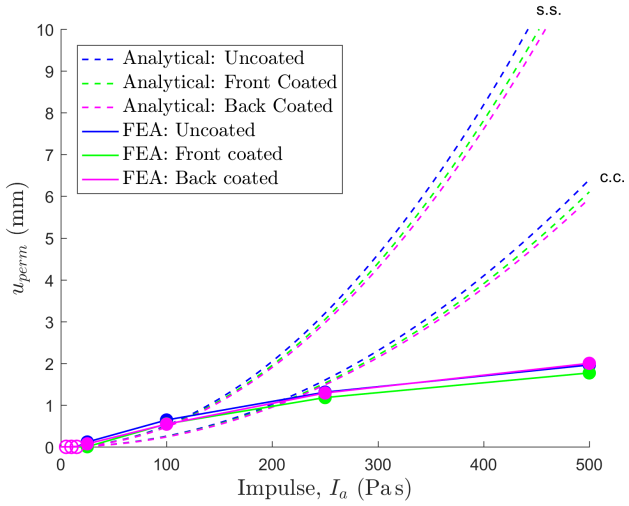

(a) $p_a = 100\,\text{kPa}$

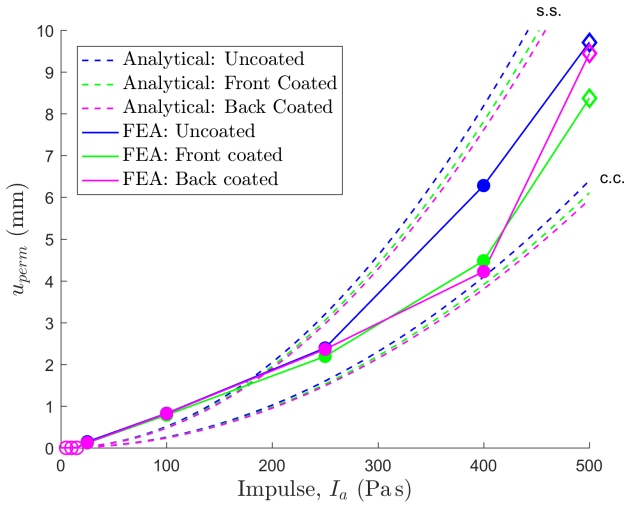

(b) $p_a = 1000\,\text{kPa}$

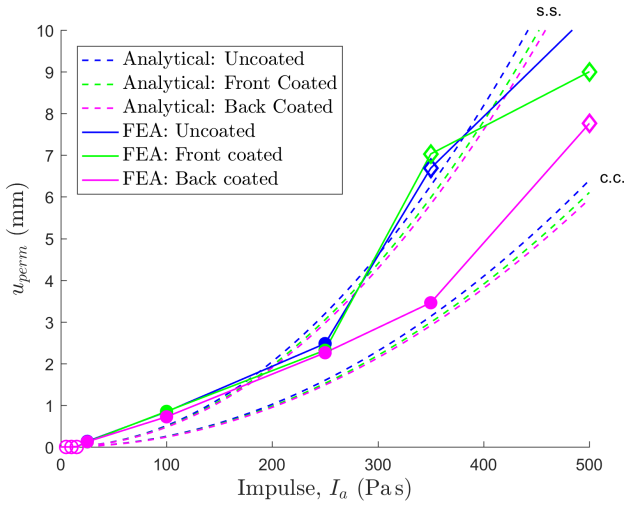

(c) $p_a = 10,000\,\text{kPa}$

Figure 4.11: Comparison between midspan permanent displacement, u_{perm} predicted by the FE model and analytical theory. Analytical predictions are presented for two support conditions: simply supported (s.s.) and clamped-clamped (c.c.). Three configurations are considered: (i) uncoated, (ii) front coated (blast-receiving face) and (iii) back coated (non-blast-receiving face). ∘ represents Regime 1 behaviour, • is Regime 2 and ⋄ is Regime 3.

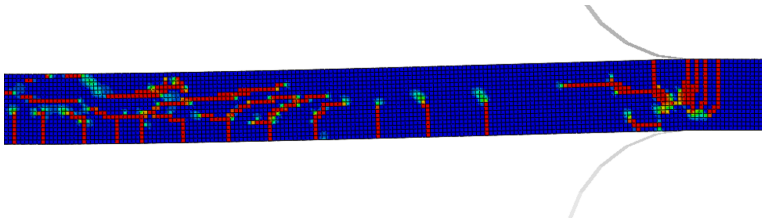

(a) Flexural cracking response

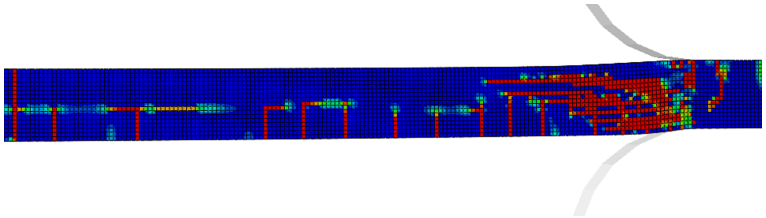

(b) Transverse shear failure response

Figure 4.12: Damaged beam configurations for an uncoated, reinforced concrete beam subjected to: (a) $p_a = 1000\,\text{kPa}$ and $I_a = 1000\,\text{Pa s}$, (b) $p_a = 10,000\,\text{kPa}$ and $I_a = 1000\,\text{Pa s}$. Plotting contours of tensile damage parameter, d_t where red contours indicate $d_t > 0.9$ which is assumed to be analogous to cracking. Images taken at the time corresponding to the critical displacement (defined in Section 4.3.1): (a) $t = 2.2\text{E-}3\,\text{s}$, (b) $t = 9.0\text{E-}4\,\text{s}$.

4.5.4.1 Transverse shear failure

To interrogate the transverse shear failure response, the shear capacity of reinforced concrete is first estimated. The shear resistance of reinforced concrete (without internal shear reinforcement) arises due to a complex interaction between aggregate interlock, concrete compressive strength and dowel action of the longitudinal steel reinforcing bars. Various empirical relationships based on experimental data have been proposed to approximate the shear capacity of a reinforced concrete beam. Eurocode 2 [180] provides the following relationship for the design shear resistance per unit width, $\overline{Q_c}$ (in N m^{-1}) of a reinforced concrete beam, without shear reinforcement, in the absence of axial force:

$$\overline{Q_c} = \left[\frac{0.18}{\gamma_c}\,\kappa\,(100\,\frac{\overline{A_s}}{d}\,\sigma_{ck})^{1/3}\right] d\,\times 10^3 \geq (0.035\,\kappa^{3/2}\,\sigma_{ck}^{1/2})\,d\,\times 10^3 \tag{4.16}$$

where
$\sigma_{ck} \approx 0.8\sigma_{cu}$; the characteristic concrete cylinder compressive strength in MPa;
$\kappa = 1 + \sqrt{200/d} \leq 2.0$; with d (the effective depth, defined in Section 4.2.2) in mm.
Thus, $\overline{Q_c} = 35.6\,\text{kNm}^{-1}$ for a RC beam of the geometry described in Section 4.2.

When the coating is applied to either the blast-receiving or non-blast-receiving face of a reinforced concrete beam; there is an additional contribution to the shear strength. This contribution is estimated from the experimental shear punch test

performed on a commercially available sample of polyurea/polyurethane elastomer at nominal strain rates, $\dot{\epsilon} = 10^0 - 10^2\,\mathrm{s}^{-1}$, as described in Section 3.2.2. According to the notation defined in Section 3.2.2, an estimate of the work done in shearing the polymer per square metre, $\overline{Q_e}$ is obtained by;

$$\overline{Q_e} = \frac{\int_0^{\delta_{max}} P\, d\delta_p}{\pi\, d_p\, \delta_{max}} \quad \approx \quad \frac{0.5\, P_{max}\, \delta_{max}}{\pi\, d_p\, \delta_{max}} \quad \approx \quad \frac{0.5\, \tau_{max}\, \pi\, d_p\, h_e}{\pi\, d_p} \tag{4.17}$$

where P_{max} is the maximum punch force and δ_{max} is the maximum punch displacement. A rate-dependent, maximum shear strength of approximately, $\tau_{max} = 20\,\mathrm{MPa}$ is measured from Fig. 3.3b. And thus; $\overline{Q_e} \approx 50\,\mathrm{kNm}^{-1}$.

A first order estimate of the total shear capacity per unit width of a coated, reinforced concrete beam is therefore; $\overline{Q_{total}} = \overline{Q_c} + \overline{Q_e}$.

Jones [39] considers the transverse shear response of an impulsively loaded, simply supported beam of length, $2L$. A summary of this method is provided in Appendix B.1 where the velocity for severance is estimated for uncoated and coated RC beams. These analytical predictions are presented in Table 4.2 assuming failure occurs at $k = 1$.

Table 4.2: Analytical predictions [39] for the transverse shear failure of a simply supported, reinforced concrete beam of the geometry described in Section 4.2 (assuming failure occurs at $k = 1$).

For $k = 1$	Uncoated	Front Coated	Back Coated
Velocity for severance ($\mathrm{m\,s}^{-1}$)	7.4	16.9	16.7
Impulse for severance ($\mathrm{Pa\,s}$)	970	2310	2280

Table 4.2 shows that, as a result of the relatively low resistance of the concrete to this shear failure mode, a polymer coating may provide significant additional resistance in this mode of deformation. The key elastomer properties required to achieve this protective benefit appear to be high ductility and a large shear strength, τ_e.

This result is difficult to verify using the current FE modelling strategy, as it does not capture the response post significant concrete damage. However, it is noted that the differences in critical displacement between coated and uncoated beams are most significant in Regime 3 where the coated structures begin to show a performance benefit.

The predicted benefit is also supported by early blast trials on masonry wall structures (which might be considered analogous to a concrete beam that has undergone

extensive cracking) which also showed benefits of polymer coating [17, 154]. In these cases, the masonry block wall relies on the membrane action of the elastomer under blast loading to prevent collapse.

Alternative numerical techniques are required to interrogate Regime 3 behaviour in order to confirm the protective function of the polymer here.

4.6 Discussion: response map

Figure 4.13 presents a summary of the response regimes of a reinforced concrete beam of the geometry described in Section 4.2 when uncoated and coated with a 5 mm elastomer on its non-blast-receiving face. Also plotted are the analytical predictions of the Regime 1 - 2 boundary and the impulse for transverse shear failure.

The analytical models are effective at predicting the regime transition for Regimes 1 - 2 and give a good indication for an upper bound on Regimes 2 - 3. The analytical models and FE predictions also agree with regard to the coating influence in each regime. For a beam exhibiting a Regime 1 or 2 response, the coating influence is negligible. Instead, it appears that the coating serves its greatest protective benefit in Regime 3, when the concrete is severely damaged. For load cases with an impulse close to the Regime 2 - 3 boundary and above, an elastomer coating appears to provide a protective effect in terms of reducing deflections and delaying global failure.

4.7 Conclusions

Numerical and analytical modelling is used to ascertain how the response of unreinforced and reinforced concrete beams varies with simulated blast load intensity and the presence of an elastomer coating. The following conclusions are established:

- Three beam response regimes are identified, each characterised by beam deflections and energy dissipated by damage.
- In Regime 1, the beam behaves purely elastically and thus an analytical technique based on Timoshenko *et al.*'s [181] theory on the transverse vibrations of an elastic beam is proposed. Beam deflections are predicted well assuming clamped-clamped boundary conditions, and the model proves capable of predicting the boundary between Regimes 1 and 2 with accuracy. The beam is found to be insensitive to polymer coating in this regime.

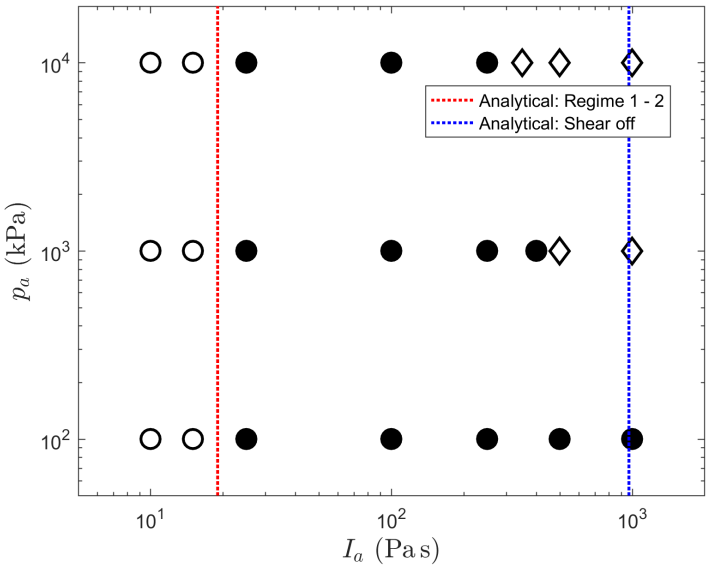

(a) Uncoated

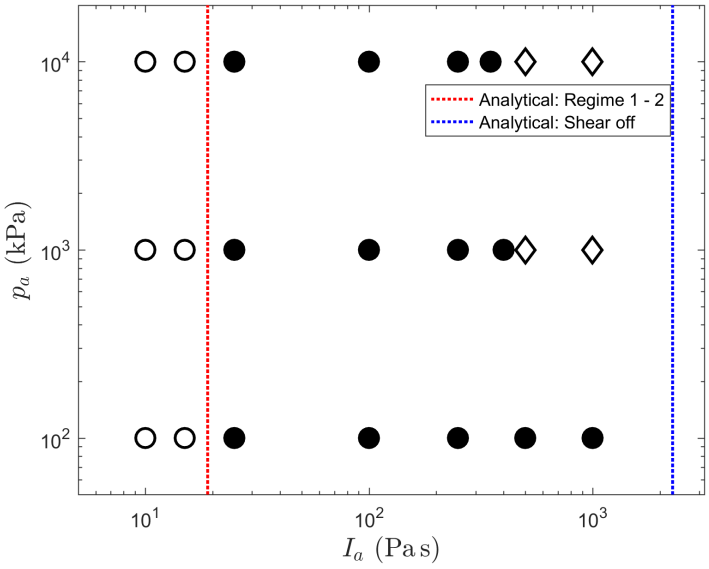

(b) Coated on the non-blast-receiving face

Figure 4.13: The regime responses predicted by FEA of a reinforced concrete beam (a) uncoated and (b) 5 mm coated on its non-blast-receiving face. ○ represents Regime 1 behaviour, ● is Regime 2 and ◇ is Regime 3. The regime boundaries predicted by the proposed analytical models for a simply-supported boundary condition are also plotted.

- Regime 2 is characterised by oscillations about a permanent displacement and the attainment of a plateau in damage energy dissipated (that occurs well after the maximum beam deflection). Jones' [39] rigid-plastic solutions agree well with the FE predictions of permanent displacement in this regime. Once again, the beam remains relatively insensitive to the presence of an elastomer coating.
- At higher blast intensities, in Regime 3, the beam undergoes continued plastic deformation and damage. A critical displacement is therefore defined, to identify the time at which the beam fails. In this regime, a greater sensitivity to the presence of a polymer coating is identified.
- By probing the regime boundary between Regimes 2 and 3, the FE results indicate a substantial reduction in beam deflections, by up to 48% for coating on the back (non-blast-receiving) face. With the coating on the back face, the beam exhibits a Regime 2 response, whereas when uncoated, or coated on its front face, it behaves in Regime 3.
- At the highest load intensities, the damage patterns observed in the FEA indicate a shift in failure mechanism to one dominated by transverse shear failure at the supports. An analytical model for shear failure indicates that the coating can offer a significant protective benefit against this particular failure mechanism due to its high shear strength and ductility.

CHAPTER 5

Impact response of elastomer-coated concrete

5.1 Introduction

Thus far, this investigation has sought to understand the blast mitigating capabilities of an elastomer coating applied to concrete structural elements. Indeed, to date, the majority of studies in the literature on the protection of quasi-brittle structures have tended to focus on the mitigating capabilities of such coatings in response to blast pressure pulses only. Promising results have been reported for coatings applied to masonry [1, 17, 154] and reinforced concrete [18] substrates where experiments have shown that the coating serves to maintain structural integrity, catch fragmentation debris and reduce reinforced concrete slab deflections. Despite some encouraging results, an understanding of how the elastomer achieves its mitigating effect remains lacking. Chapter 4 sought to interrogate the blast response regimes of an elastomer-coated, reinforced concrete beam in more detail. It was concluded that in the low blast intensity Regimes 1 and 2, when the beam deforms elastically and elastic-plastically, the coating serves a negligible effect in terms of reducing maximum deflections. However, at higher blast intensities, when the concrete has experienced severe damage, the coating serves its greatest protective benefit. This chapter will examine elastomer-coated concrete in response to a different type of dynamic load event: impact indentation.

When designing to protect infrastructure from an explosive load event, it is important not only to consider the blast pressure pulse, but also impact from fragmentation. As discussed in Section 2.1.2, the fragmentation resulting from a bomb blast can be classified as either; (i) primary (referring to the ejection of the casing surrounding the explosive device) or (ii) secondary (referring to the debris produced

from the interaction of the blast pressure pulse and primary fragments with nearby structures). This fragmentation poses the most significant threat to life during an explosive event [1] and thus, it is important to assess a candidate retrofit's *impact* mitigating abilities.

Many studies have been performed on the impact response of elastomer-metallic bilayer and laminate plates [3, 4, 6, 7, 145, 146, 148–150, 182–184], which have, in the most part, demonstrated a beneficial coating effect; though there still exists some debate regarding the influence of the coating location (impacted or distal face), construction (bilayer, sandwich or laminate) and mechanism by which the elastomer achieves its mitigating effect. Researchers have postulated that an elastomer layer on the impacted face gives rise to energy dissipation via an impact-induced glass transition [3, 4] while some report it serves to stabilise the onset of necking in the metal [149, 150]. Others have argued that when positioned on the impacted face, the elastomer serves to alter the effective nose shape of the indenter, changing the deformation mode in the metal layer [7, 184].

Despite the encouraging results achieved with metal substrates, to the author's knowledge there has been no exploration into how the elastomer performs when applied to concrete structures, subjected to projectile impact. One concrete retrofit strategy that has been investigated for physical protection is the use of fibre reinforced polymers (FRP). Pham and Hao [130] present a review of the studies performed to assess the impact resistance of reinforced concrete (RC) beams, slabs and columns, strengthened with FRP and conclude that, while further research is required, FRP retrofits can indeed enhance the impact resistance of RC. However, if competitive, a spray-application elastomer would offer significant benefits in terms of practicality and cost.

In this chapter, experimental and numerical techniques are used to examine the influence of a typical spray-on elastomer coating, applied to the impacted face of a concrete cube, subjected to 0.1 kg, blunt projectile impacts between $45 - 150\,\mathrm{m\,s^{-1}}$. Thus, attention is restricted to relatively heavy, relatively slow projectiles. The chapter is structured as follows. First, high speed, gas gun experiments are performed to establish if, and over what range of impact velocities, the elastomer coating serves a damage mitigating effect. A numerical model is developed in ABAQUS/Explicit [27] and predictions are compared with experimental measurements for quasi-static indentation and then dynamic impact of uncoated and coated concrete specimens. Careful validation of the FE model is performed to establish under what circumstances it may be deemed an appropriate analysis tool. The validated numerical model is then used to interrogate the coating's influence on damage initiation in

the concrete substrate, thus revealing details of the underlying protective mechanisms.

5.2 Projectile impact experiments

Projectile impact tests are performed using a gas gun apparatus, illustrated in Fig. 5.1. A blunt (*i.e.* circular cylindrical) steel projectile of diameter 28.5 mm, length 20 mm and mass 0.1 kg is fired at a concrete cube, of side length 100 mm, supported on its back face and resting upon a wooden block support. The projectile geometry chosen for this study is idealised, simpler than a typical fragment simulating projectile (FSP). However, it enables study of the target's response to a sharp edged projectile in a well controlled manner. The axisymmetric geometry also simplifies the numerical analysis of the experiments, as discussed subsequently.

Two configurations are tested: (i) the concrete in its uncoated state and (ii) the concrete with an elastomer layer, approximately 5 mm thick, placed on its impacted face. The elastomer layer is not bonded to the concrete and is in frictional contact only. Small pieces of double-sided adhesive tape, located at each corner, are used to ensure the correct initial positioning of the layer.

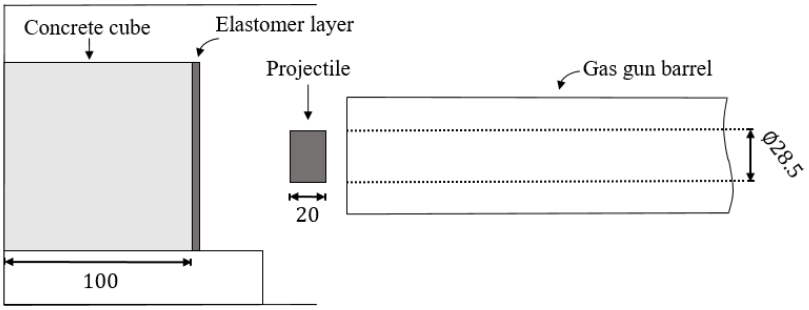

Figure 5.1: Schematic of the gas gun apparatus used for the impact tests (not to scale). All dimensions are in mm.

The elastomer layer was chosen to be the same commercially available spray application, polyurea/polyurethane hybrid discussed in Chapters 3 and 4. The coatings were obtained by spraying the polymer onto an untreated steel plate and then peeling it off[1]. Note, this technique resulted in the thickness of the elastomer layer varying by approximately 15% between tests since precise control of the thickness was not possible. The average thickness of the elastomer layer in each test is measured and is recorded in the caption of Figs. 5.4 to 5.8.

Concrete cubes, of side length 100 mm were designed and cast. The Department of Environment mix design method [185] is employed to achieve a characteristic

[1]Polymer specimens courtesy of I. Mohagheghian, University of Cambridge [170].

strength at 28 days of 40 MPa. The characteristic strength is defined as the cube strength below which not more than 5% of test results fall. Assuming normal distribution and good mix control, the mix must be designed to have a target mean strength equal to the desired characteristic strength plus 1.64 times the expected standard deviation (in this case, 4.5 MPa is chosen according to the guidance in [185]). Thus, a target mean strength of 47 MPa is designed for. Rapid-hardening Portland Cement is used with uncrushed coarse gravel aggregate of maximum size 10 mm. The mix is designed to have high workability with $60 - 180$ mm slump. In terms of volume %, the final design mix ratio is chosen as follows — cement: water: fine aggregate (sand): coarse aggregate = 15% : 23% : 28% : 34%. After 28 days, a compressive test was performed on a concrete cube using an Instron screw-driven materials testing machine at a nominal strain rate, $\dot{\epsilon} = 10^{-3}\,\mathrm{s}^{-1}$. The nominal stress-strain response, corrected for cross-head compliance is presented in Fig. 5.2, illustrating that a compressive strength of 47 MPa is attained.

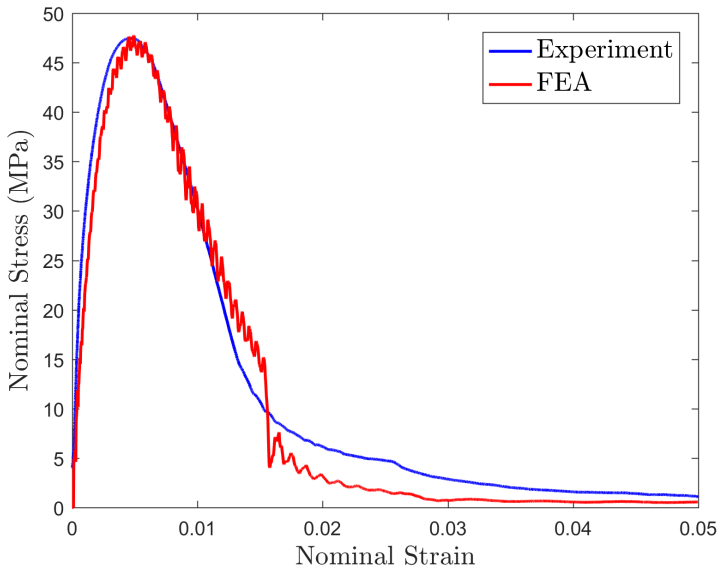

Figure 5.2: Nominal compressive stress-strain response of a 100 mm concrete cube, tested at a nominal strain rate, $\dot{\epsilon} = 10^{-3}\,\mathrm{s}^{-1}$. Also plotted is the FE model prediction discussed subsequently.

5.2.1 Results

Impact tests are performed for projectile velocities spanning the range *c.* $45 - 145\,\mathrm{m\,s}^{-1}$. Coated and uncoated cubes are tested at each impact velocity, and the level of damage is assessed. The projectile was machined to match closely the internal diameter of the gun barrel, thus helping to ensure a repeatable, normal impact. This was verified using high speed photography (at 49000 frames per second) which showed that for all tests, a normal impact was achieved, within $\pm 3°$. An example

of the high speed photography is shown in Fig. 5.3. Images of the post-impact specimens are presented in Figs. 5.4 - 5.8.

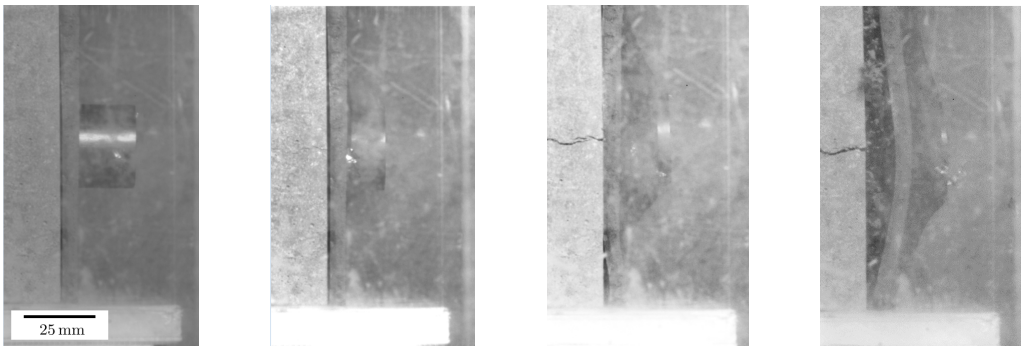

(a) $t = 0\,\mu$s (b) $t = 82\,\mu$s (c) $t = 286\,\mu$s (d) $t = 960\,\mu$s

Figure 5.3: High speed photographs of the impact test performed for a coated specimen at a projectile impact speed of $124\,\mathrm{m\,s^{-1}}$. The time $t = 0\,\mu$s corresponds to first contact with the elastomer coating. The scale bar is the same for all images.

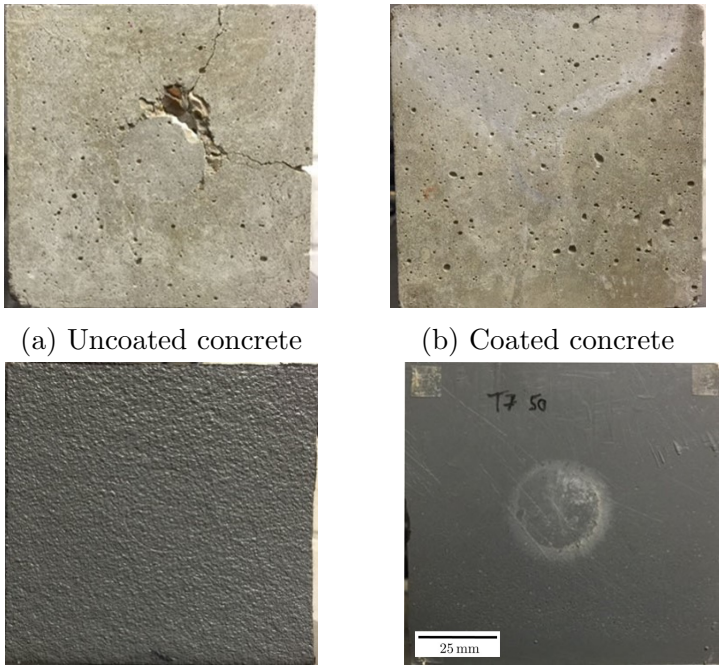

(a) Uncoated concrete (b) Coated concrete

(c) Coating - impacted face (d) Coating - distal face

Figure 5.4: Photographs of the test specimens for a projectile impact velocity of $45\,\mathrm{m\,s^{-1}}$ for both uncoated and coated specimens. The elastomer thickness for the coated specimen was 5.53 mm. The scale bar is the same for all images.

5.2.2 Discussion

A substantial, beneficial effect of the elastomer coating is observed across the full range of velocities tested. For the uncoated concrete, increasing the projectile speed increases the extent of damage and radial cracking, as shown in Figs. 5.4 - 5.6. At

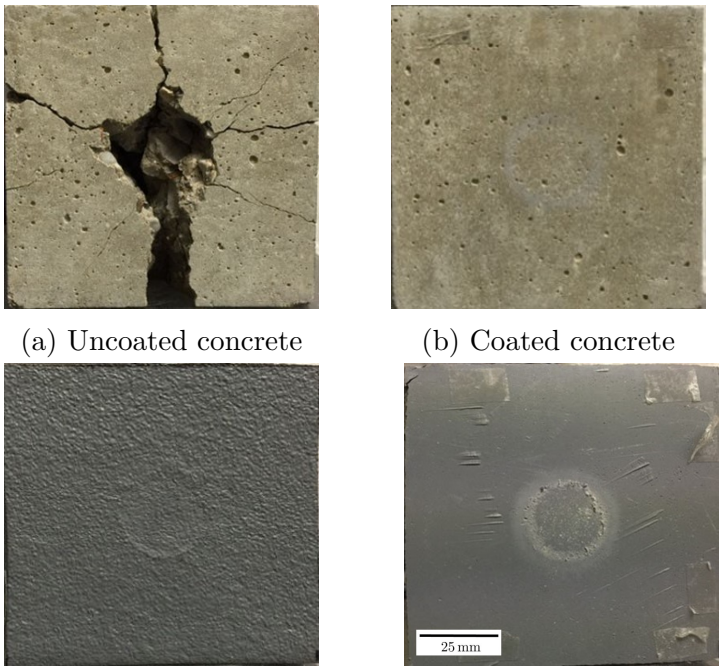

(a) Uncoated concrete (b) Coated concrete

(c) Coating - impacted face (d) Coating - distal face

Figure 5.5: Photographs of the test specimens for a projectile impact velocity of $68\,\mathrm{m\,s^{-1}}$ for the uncoated specimen and $64\,\mathrm{m\,s^{-1}}$ for the coated specimen. The elastomer thickness for the coated specimen was 5.35 mm. The scale bar is the same for all images.

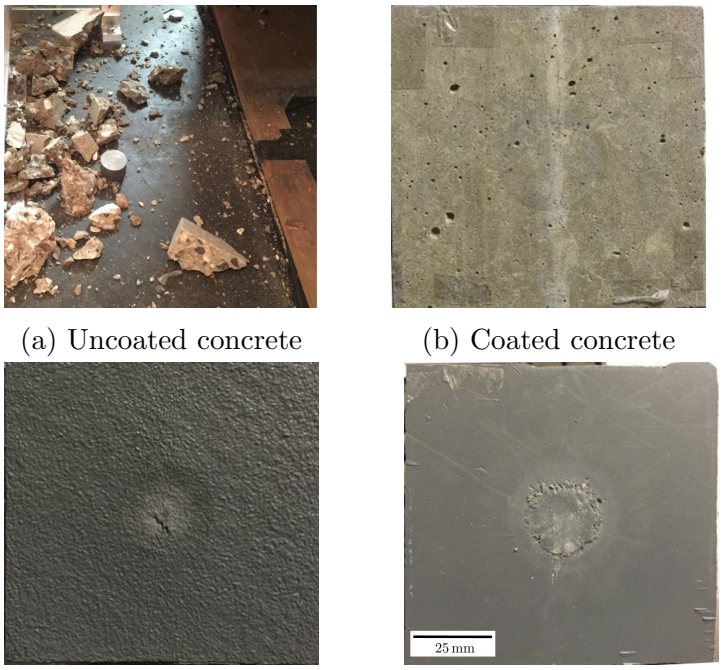

(a) Uncoated concrete (b) Coated concrete

(c) Coating - impacted face (d) Coating - distal face

Figure 5.6: Photographs of the test specimens for a projectile impact velocity of $100\,\mathrm{m\,s^{-1}}$ for the uncoated specimen and $101\,\mathrm{m\,s^{-1}}$ for the coated specimen. The elastomer thickness for the coated specimen was 6.02 mm. The scale bar is the same for images b), c) and d).

(a) Coated concrete

(b) Coating - impacted face

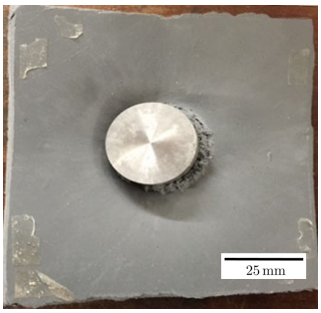

(c) Coating - distal face

Figure 5.7: Photographs of the coated test specimen for a projectile impact velocity of $124\,\mathrm{m\,s^{-1}}$. The elastomer thickness was 5.21 mm. The scale bar is the same for all images.

(a) Coated concrete

(b) Coating - impacted face

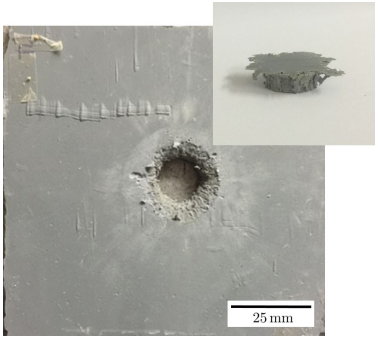

(c) Coating - distal face with polymer plug (inset)

Figure 5.8: Photographs of the coated test specimen for a projectile impact velocity of $142\,\mathrm{m\,s^{-1}}$. The elastomer thickness was 5.36 mm. The scale bar is the same for images b) and c).

speeds of $100\,\mathrm{m\,s^{-1}}$ and beyond, the cube is entirely fragmented. For the coated concrete cubes, there is no evidence of concrete damage (based on visual inspection) for impact speeds up to and including $100\,\mathrm{m\,s^{-1}}$. Further, below impact speeds of $100\,\mathrm{m\,s^{-1}}$, there is no visible tearing of the elastomer. However, the presence of elastomer damage is apparent in optical micrographs, increasing in severity with the impact velocity, as shown in Fig. 5.9.

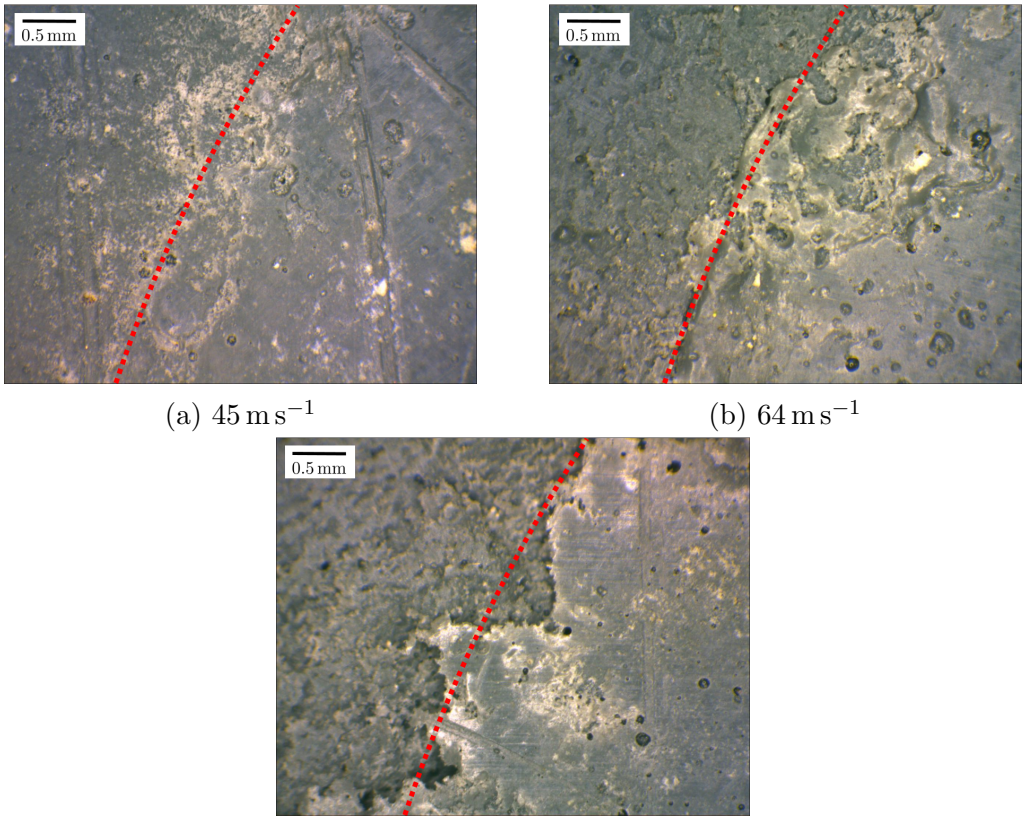

(a) $45\,\mathrm{m\,s^{-1}}$ (b) $64\,\mathrm{m\,s^{-1}}$

(c) $101\,\mathrm{m\,s^{-1}}$

Figure 5.9: Micrographs showing the distal face of the elastomer coating, at the edge of the impact site, for projectile velocities of 45, 64 and $101\,\mathrm{m\,s^{-1}}$. The dotted line indicates the perimeter of the projectile contact patch.

A band of damaged material is evident around the perimeter of the projectile impact site. Voids form, which grow and coalesce — these are readily observed in the micrograph at $64\,\mathrm{m\,s^{-1}}$ (Fig. 5.9b). At higher impact velocities (above around $100\,\mathrm{m\,s^{-1}}$), there is evidence of ductile tearing around the perimeter of the impact site (Fig. 5.9c).

The coated concrete cube is completely fragmented at an impact velocity of $142\,\mathrm{m\,s^{-1}}$. The elastomer fails around the perimeter of the projectile, forming a plug. The polymer plugs are recovered after the experiment, and are found to have a diameter of around 14 mm, which is about half that of the projectile. This indicates that the coating undergoes significant elastic straining prior to failure. The residual hole in the coating is, similarly, much less than the projectile diameter (Fig. 5.8b - c). Ex-

amination of the polymer coating in the vicinity of the hole shows a rough surface indicative of ductile tearing, accompanied by significant elastic contraction. This observation suggests that an impact-induced glass transition [3, 4] is not a dominant energy dissipation mechanism for these impact conditions and coating, at even the highest strain rates seen in the impact tests ($c.\, 10^4\,\mathrm{s}^{-1}$). To explain this observation, the glass transition temperature of the polymer is measured using dynamic mechanical analysis (see Appendix C.1). Although the glass transition will shift to higher temperatures with increasing strain rate, it is found to be too low in this polymer to likely play a major role for the strain rates encountered in these experiments.

Probing the range of impact velocities between 100 and $142\,\mathrm{m\,s}^{-1}$, the projectile first fully penetrates, and is completely arrested by, the polymer coating at a speed of $124\,\mathrm{m\,s}^{-1}$. This can be interpreted as a perforation velocity for the coating. This case is shown in Fig. 5.7. The concrete exhibits damage immediately under the projectile and radial cracking on the impacted face of the cube, but remains otherwise intact. In this case the elastomer plug remains *welded* to the face of the concrete cube after impact.

In summary, the concrete cube appears to be completely undamaged for impact velocities up to $100\,\mathrm{m\,s}^{-1}$ in its coated configuration. Severe concrete damage is observed in the uncoated cubes for impact velocities of $64\,\mathrm{m\,s}^{-1}$ and above. When coated, impact velocities in excess of $124\,\mathrm{m\,s}^{-1}$ are required to achieve a similar level of damage.

5.3 FE model development

To gain a greater insight into the underlying protective mechanisms at play, a finite element (FE) model is developed using the code ABAQUS/Explicit [27].

5.3.1 Concrete

As a first step, it is necessary to obtain a concrete constitutive model that matches the behavior of the cast concrete used in the experimental study.

The same Concrete Damaged Plasticity (CDP) model is chosen as developed in Section 3.2.1, which is available in ABAQUS/Explicit. The concrete is modelled as a homogeneous continuum that exhibits isotropic, damaged elasticity and isotropic, pressure-dependent plasticity. A continuum damage mechanics approach has been shown by many authors in the literature [161–165] to be appropriate for the constitutive modelling of concrete (and other quasi-brittle materials). It is noted that

microstructure sensitivity of the localised impact damage of concrete is an important consideration, and one that requires further research. However, confidence is gained from the experimental comparisons discussed subsequently, that the continuum model fidelity is sufficient for the effects studied here.

The compressive, tensile and damage parameters (derived in Section 3.2.1) are scaled to achieve a good match with the quasi-static, compressive stress-strain response presented in Fig. 5.2. The resulting numerical prediction is compared with the experimental curve in Fig. 5.2, illustrating that a good match is obtained.

5.3.2 Elastomer

The methodology used to obtain a constitutive model for the elastomer coating was described in Section 3.2.2. The same model is employed in this chapter.

5.4 Quasi-static indentation

Before proceeding to simulations of the impact tests, the predictive capabilities of the model are first assessed for the quasi-static indentation response of uncoated and coated concrete cubes. This allows a clearer comparison with experimental measurements, to help interrogate modelling decisions.

5.4.1 Uncoated concrete

A quasi-static indentation test is performed on a 100 mm concrete cube. A circular cylindrical steel indenter of diameter 28.5 mm (identical to the projectiles used in the impact tests) is pressed into the surface of the concrete cube using an Instron screw-driven test machine, at a speed of $1 \times 10^{-4}\,\mathrm{m\,s^{-1}}$. Indenter force was measured using the test machine load cell. Indentation depth was measured using cross head displacement, adjusted for compliance using a laser extensometer.

The same test is simulated in ABAQUS/Explicit. The concrete block is modelled axisymmetrically, with a radius of 50 mm and a height of 100 mm. A mesh size of 0.5 mm is used for a domain of size 40 mm around the contact patch. This is then graded to a mesh size of 5 mm at the edge of the block. ALE (Arbitrary Lagrangian-Eulerian) adaptive meshing is used in the concrete region directly under the indenter in an effort to maintain a high quality mesh throughout the analysis. The indenter is modelled as an axisymmetric rigid part with a small corner radius of 1.5 mm added to prevent a stress singularity at the indenter perimeter. Frictionless contact conditions are prescribed between the indenter and the concrete.

The chosen mesh and corner radius combination is a result of a detailed sensitivity study. It was found that while a coarse mesh was insufficient to accurately capture indentation behaviour, an extremely fine mesh resulted in extensive, unrealistic crack branching (indicated by the distribution of damaged elements). Further, the indentation response was relatively sensitive to the chosen indenter corner radius. Therefore, it was necessary to identify the smallest value (*i.e.* closest to a perfectly sharp edge) that could be adequately resolved by the FE mesh, while avoiding excessively small elements (for the reasons outlined above). To help confirm the final choice of corner radius and mesh, the predicted distribution of stress under the indenter is compared with the existing theoretical solution for a flat-ended circular cylinder with a sharp corner, indenting an elastic half space. The results are presented in Appendix C.2 and show good agreement between the FE model and the theoretical result.

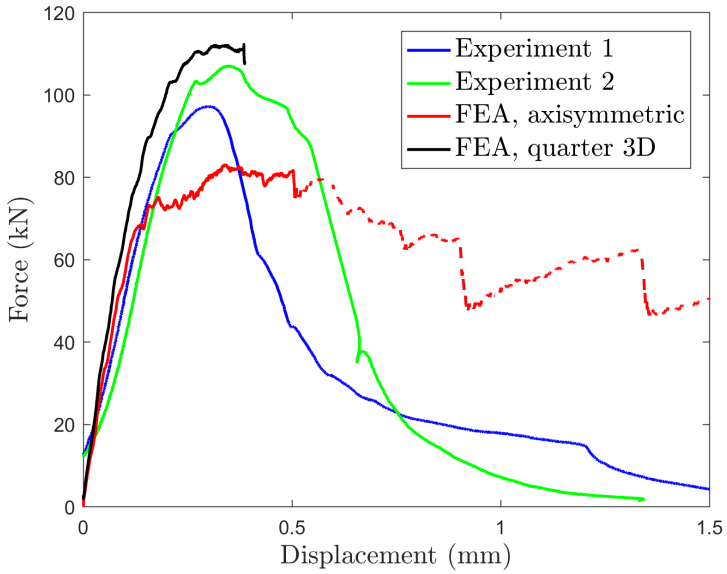

Figure 5.10: Quasi-static indenter force-displacement response for uncoated concrete. For the FE results, the dotted line indicates the prediction after the first significant drop in load, at which point extensive damage has occurred.

Comparison between the FE predictions and experiment are presented in Fig. 5.10. The FE model provides an accurate prediction of the indentation stiffness which appears to be experimentally repeatable. However, there is some scatter in the yield point obtained experimentally and it appears that the FE model underpredicts this. Inherent material variability may be a factor in this discrepancy, including sensitivity to local effects such as coarse aggregate distribution near the surface and local indenter geometry. The indentation yield point might also be sensitive to the details of the indenter corner radius, in both the experiment and model, and the effect this has on the local stress and stress triaxiality. Furthermore, the stress

triaxiality dependence of the concrete constitutive model may lose fidelity under the complex stress state under the indenter.

There is also some discrepancy between model and experiment in terms of post-peak response. The experiments show strong softening after the onset of damage, with complete failure of the block occurring at indenter displacements of approximately $1 - 1.5\,\text{mm}$. The FE prediction, however, gives a more progressive propagation of damage, that continues after the first significant load drop. Note that damaged elements are not deleted in the FE model. Also, the axisymmetric model will not permit radial cracks to develop. These factors may alter the predicted mode of global failure of the block. Hence, the FE predictions should be interpreted with caution once damage development is extensive (as indicated by the dotted line in Fig. 5.10). Also plotted on Fig. 5.10 is the prediction obtained using a 3D quarter model. Once more, the indentation stiffness is accurately predicted and in this case, a good match is achieved to the measured peak strength. The post-peak behaviour is not captured as the model suffers from excessive element distortions due to the nature of the loading. For this reason, coupled with the large computational cost, it is decided to proceed with the axisymmetric approach. The axisymmetric model will not capture 3D failure mechanisms such as radial cracking. However, it is believed that the key damage phenomena occur at earlier timescales compared to radial cracking, and thus a full 3D model is not critical to the subsequent analysis of damage initiation.

5.4.2 Coated concrete

Next, the quasi-static indentation of a 100 mm concrete cube, coated on its indented face with a 4 mm thick elastomer layer is considered. The experimental technique is as described in Section 5.4.1, above. Similarly, an axisymmetric FE model is used for the concrete and polymer coating, with the constitutive behaviour of each material as defined in Section 5.3. The finite element mesh for the concrete part is identical to that defined in Section 5.4.1. The polymer is discretised using an identical mesh size to the concrete: 0.5 mm elements are used over a 40 mm radius in the vicinity of the contact patch, transitioning to 5 mm at the edges.

Frictionless contact is prescribed between the indenter and the elastomer. Two contact conditions are examined between the elastomer and concrete: frictionless and Coulomb friction with a friction coefficient of $\mu = 0.8$ (a reasonable value for concrete/rubber interactions [186]). A plot of the indenter force-displacement response for each case is compared with the experimental measurement in Fig. 5.11.

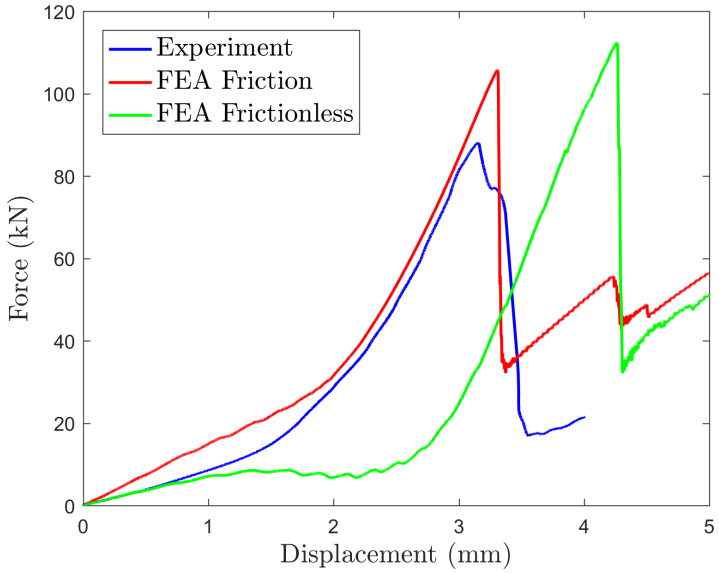

Figure 5.11: Comparison between experiment and two FE models of the quasi-static indenter force-displacement response for coated concrete. One FE model includes frictionless contact between the elastomer layer and concrete, while the other assumes Coulomb friction with a friction coefficient of $\mu = 0.8$.

As noted for the uncoated concrete, the FE does not exactly predict the peak force, and there is some discrepancy after the first load drop. But, overall, the FE predicts the indentation response well, as long as frictional effects between the elastomer and concrete are accounted for. This interface condition will therefore be assumed in all subsequent calculations.

5.5 Impact indentation

Satisfied with the agreement obtained between the FE models and the quasi-static indentation experiments, the modelling of the impact experiments described in Section 5.2 is pursued next. An axisymmetric representation of the concrete, polymer coating and projectile is again used in the FE analysis. The modelling parameters are identical to those described in Section 5.4. The projectile mass is 0.1 kg, and it is assigned an initial velocity in the simulations to match the experimental values, obtained from high speed photography. Rigid body motion of the concrete target is prevented by constraining the vertical displacement of the distal face.

5.5.1 Uncoated concrete

First, the uncoated concrete cases are considered. The projectile velocity-time histories predicted by the model are compared in Fig. 5.12 with experimental measurements, obtained from high speed photography.

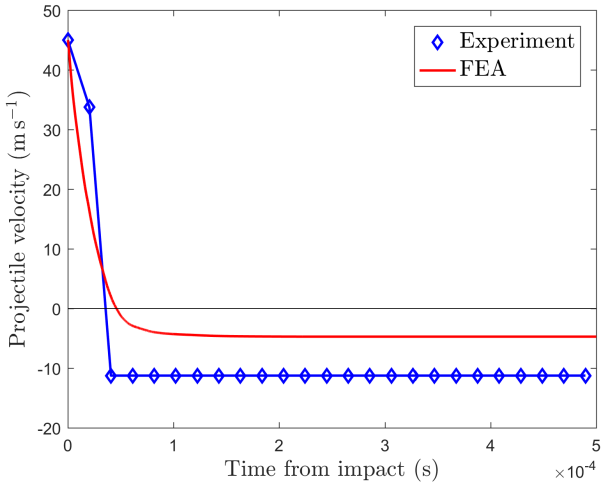

(a) 45 m s^{-1}

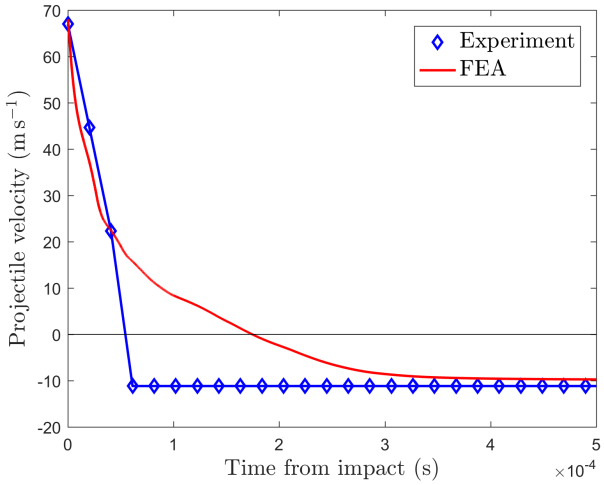

(b) 68 m s^{-1}

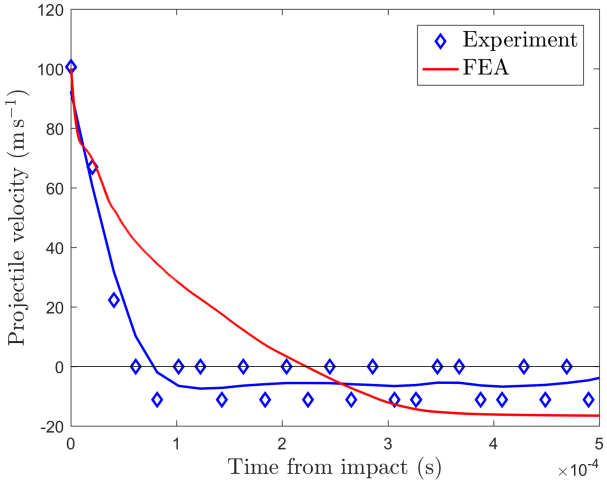

(c) 100 m s^{-1}

Figure 5.12: Projectile velocity-time history obtained from the impact experiments and the FE analysis, for the uncoated concrete specimens.

The FE model provides reasonably accurate predictions of the projectile velocity-time histories across the range of impact speeds considered, both for the loading portion of the response (up to zero projectile velocity) and also for the projectile rebound velocity. It is noted, however, that the ability of the model to accurately capture the shape of the velocity-time curve diminishes with higher projectile impact speeds. In these cases, damage development is extensive, and for the reasons highlighted in Section 5.4.1, the FE predictions should be interpreted with caution.

Figure 5.13 presents the FE model predictions for the compressive damage experienced by the uncoated concrete targets for the three projectile impact speeds considered.

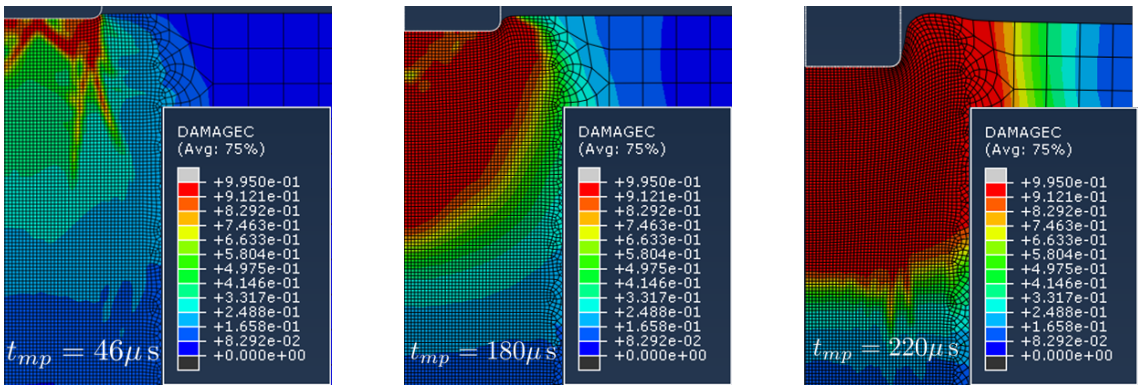

(a) $45\,\mathrm{m\,s^{-1}}$ (b) $68\,\mathrm{m\,s^{-1}}$ (c) $100\,\mathrm{m\,s^{-1}}$

Figure 5.13: Contours of the compressive damage parameter, d_c for the impact simulations of uncoated concrete cubes at projectile impact velocities of $45\,\mathrm{m\,s^{-1}}$, $68\,\mathrm{m\,s^{-1}}$ and $100\,\mathrm{m\,s^{-1}}$. $d_c = 0$ represents completely undamaged material and $d_c = 1$ is completely damaged. Images taken at the time of maximum indenter penetration, t_{mp}.

As was observed in the experiments (Figs. 5.4 - 5.6), the level of damage experienced by the concrete target increases with increasing projectile impact speed. For impact speeds of $68\,\mathrm{m\,s^{-1}}$ and $100\,\mathrm{m\,s^{-1}}$, a significant amount of damage is predicted (*i.e.* $d_c = 1$) which agrees well with experimental observations. Figure 5.14 shows the progress of damage for the $45\,\mathrm{m\,s^{-1}}$ impact case, illustrating that the damage continues to propagate after the point of maximum projectile penetration, though not significantly.

Complete fragmentation of the block, observed in the experiments for a projectile impact speed of $100\,\mathrm{m\,s^{-1}}$ (Fig. 5.6), cannot be predicted by the FE model given the lack of element deletion. However, this is likely to occur in the later stages of projectile penetration. The FE is therefore best used to predict the earlier stages of damage initiation and development in these cases.

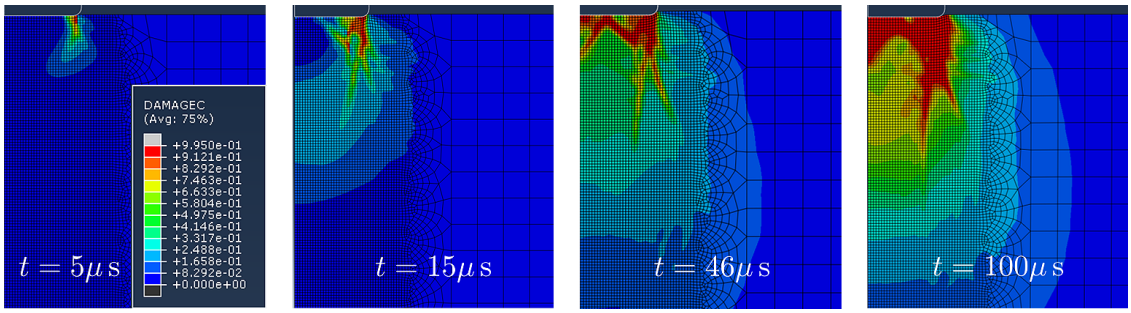

Figure 5.14: Progress of damage for the impact indentation of an uncoated cube with an initial projectile speed of $45\,\mathrm{m\,s^{-1}}$. Plotting contours of the compressive damage parameter, d_c where $d_c = 0$ represents completely undamaged material and $d_c = 1$ is completely damaged. The image at $t = 46\,\mu$s corresponds to the time of maximum indenter penetration.

5.5.2 Coated concrete

Next, the coated concrete targets are considered. Figure 5.15 compares the FE predictions for the projectile velocity-time histories with those measured using high speed photography during the impact experiments. The FE modelling parameters are again identical to those described in Section 5.4, with a coefficient of friction, $\mu = 0.8$ between the polymer and concrete layers and frictionless contact is assumed between polymer/steel interfaces.

The FE model provides excellent agreement with the experimental measurements for the loading portion of the response, up to the point of maximum projectile penetration (*i.e.* zero projectile velocity). Beyond this point, the FE model overestimates the projectile rebound velocities. As was noted in Section 3.2.2, the elastomer constitutive model fails to capture well the measured hysteresis upon unloading, which may account for this discrepancy. This is supported by a supplementary investigation of the sensitivity to the viscoelastic model, described in Appendix C.3.

Figure 5.16 illustrates the compressive damage patterns predicted by the FE model for the coated concrete cubes, at the three projectile impact speeds considered.

No severe ($d_c = 1$) concrete damage is predicted for projectile impact speeds of $45\,\mathrm{m\,s^{-1}}$ and $64\,\mathrm{m\,s^{-1}}$, though significant straining of the elastomer under the corner of the projectile is observed. These predictions agree well with the experimental observations in Figs. 5.4, 5.5 and 5.9, which show that the concrete exhibits no visible damage, while the elastomer coating undergoes minor damage at the perimeter of the contact patch.

The FE model predicts that severe compressive damage occurs to a depth of around 10 mm, for the coated cube impacted at $101\,\mathrm{m\,s^{-1}}$. This is in contrast to the apparently undamaged concrete specimen recovered from the experiment (Fig. 5.6). This

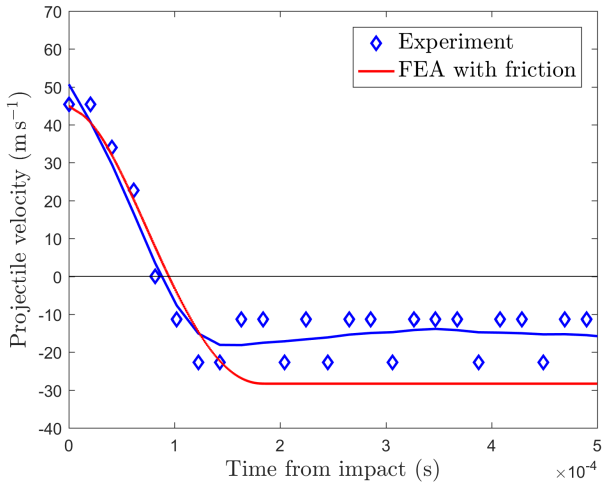

(a) 45 m s^{-1}

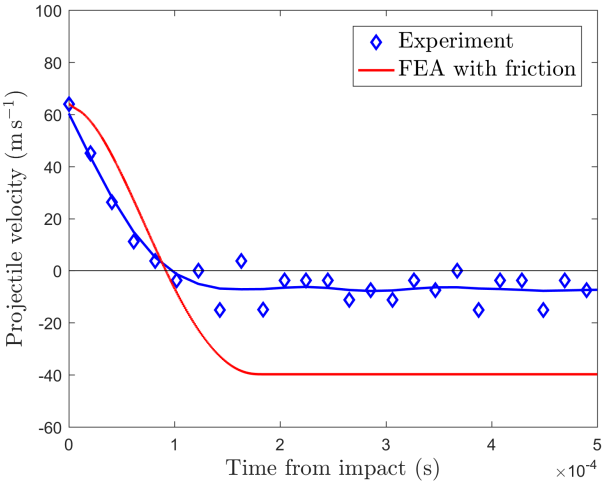

(b) 64 m s^{-1}

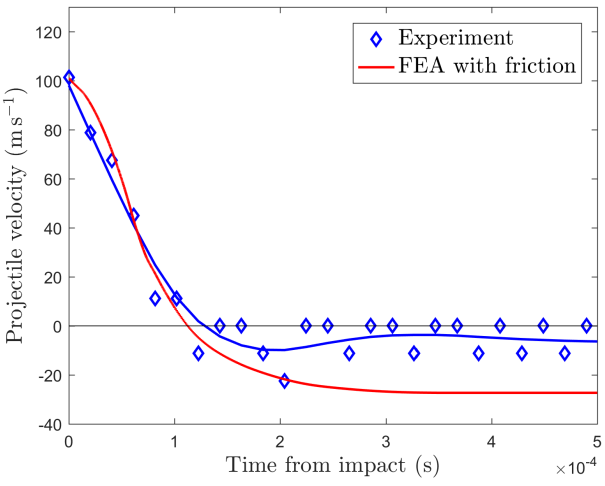

(c) 101 m s^{-1}

Figure 5.15: Projectile velocity-time history obtained from the impact experiments and the FE analysis for coated concrete specimens. The FE model considers a friction coefficient, $\mu = 0.8$ between the elastomer and concrete.

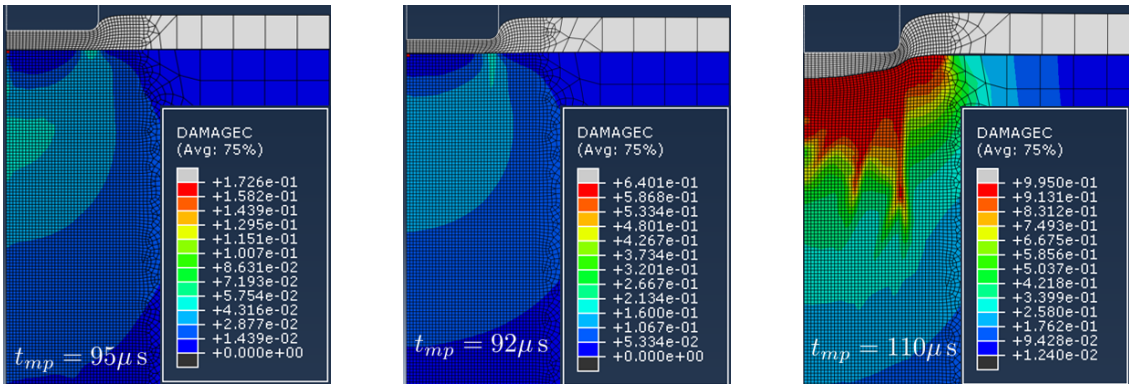

(a) $45\,\mathrm{m\,s^{-1}}$ (b) $64\,\mathrm{m\,s^{-1}}$ (c) $101\,\mathrm{m\,s^{-1}}$

Figure 5.16: Contours of the compressive damage parameter, d_c for the impact simulations of coated concrete cubes at projectile impact velocities of $45\,\mathrm{m\,s^{-1}}$, $64\,\mathrm{m\,s^{-1}}$ and $101\,\mathrm{m\,s^{-1}}$. $d_c = 0$ represents completely undamaged material and $d_c = 1$ is completely damaged. Images taken at the time of maximum indenter penetration, t_{mp}.

discrepancy could be due to a number of factors. First, no strain rate dependence is accounted for in the concrete constitutive model which could influence the concrete strength at these higher projectile impact speeds. Furthermore, the elastomer constitutive model does not include a failure criterion. Thus the elastomer tearing observed in the experiment (Fig. 5.9c) is not predicted explicitly. This would provide an additional dissipative mechanism, absent from the current analysis. Nonetheless, the significant protective effect of the coating is captured by the model. The following section proceeds to interrogate the protective mechanisms in more detail.

5.6 Discussion: influence of coating on impact damage initiation

In the following section, the FE model is used to gain an insight into how the elastomer is achieving its damage mitigating effect. Focusing attention on the early time steps of indenter penetration, the coating influence on damage initiation in the concrete target is interrogated.

Figures 5.17 and 5.18 show the distribution of the concrete damage parameter, d_c taken at a time, t_{di} corresponding to the point of damage initiation for uncoated and coated concrete cubes, respectively for three impact speeds. Note that $d_c = 0$ represents undamaged material, and $d_c = 1$ is completely damaged. The *initiation* of damage is defined to occur when the damage parameter, $d_c > 0.9$ is calculated to a depth of at least 1 mm in the concrete. Values of the time after impact at which damage initiates, t_{di}, and the depth of projectile penetration at this time, δ_{di}, are also quoted in the Figures.

Using this definition of damage initiation, the minimum impact velocity at which this

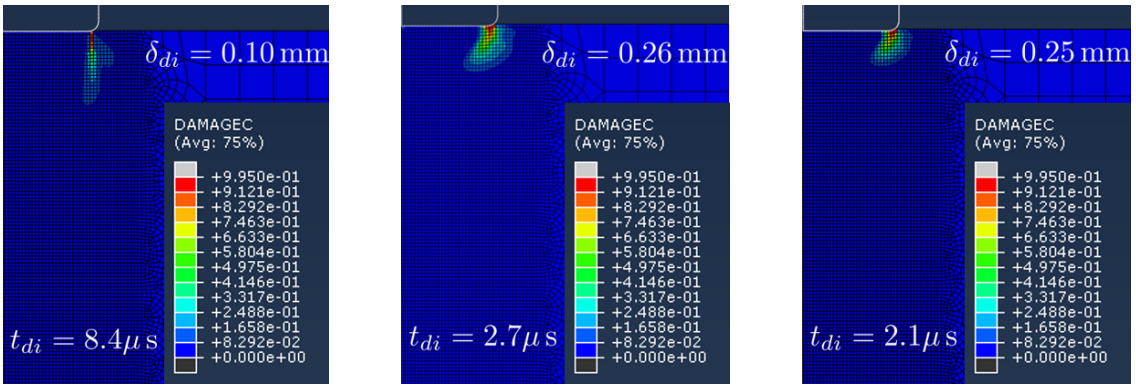

(a) $15\,\mathrm{m\,s^{-1}}$ (b) $101\,\mathrm{m\,s^{-1}}$ (c) $124\,\mathrm{m\,s^{-1}}$

Figure 5.17: Contours of the compressive damage parameter, d_c for the impact indentation simulations of uncoated concrete targets at impact velocities of $15\,\mathrm{m\,s^{-1}}$, $101\,\mathrm{m\,s^{-1}}$ and $124\,\mathrm{m\,s^{-1}}$. Images are shown at the point of damage initiation, as defined in the main text.

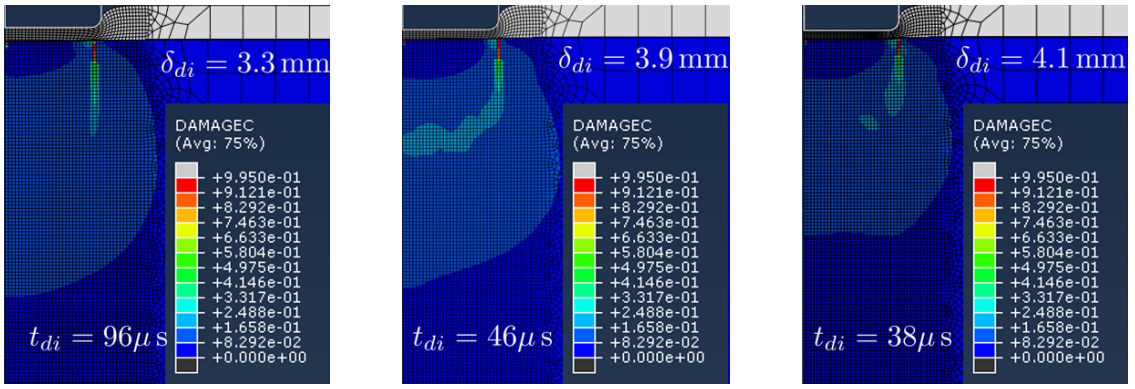

(a) $63\,\mathrm{m\,s^{-1}}$ (b) $101\,\mathrm{m\,s^{-1}}$ (c) $124\,\mathrm{m\,s^{-1}}$

Figure 5.18: Contours of the compressive damage parameter, d_c for the impact indentation simulations of coated concrete targets, coated with a 5 mm elastomer layer, at impact velocities of $63\,\mathrm{m\,s^{-1}}$, $101\,\mathrm{m\,s^{-1}}$ and $124\,\mathrm{m\,s^{-1}}$. Images are shown at the point of damage initiation, as defined in the main text.

criterion is met can be found. This occurs at an impact speed of $15\,\mathrm{m\,s^{-1}}$ for the uncoated concrete (Fig. 5.17a) and $63\,\mathrm{m\,s^{-1}}$ for the coated concrete (Fig. 5.18a).

Comparing these two cases, three key effects of the coating are apparent. (i) The time taken to initiate concrete damage is at least an order of magnitude larger in the coated case. (ii) The projectile has indented the coating by a large fraction of its thickness at the onset of concrete damage. (iii) The critical location for concrete damage remains at the projectile perimeter, but with the coating in place, there is a more diffuse distribution of concrete damage when the initiation criterion is met. (i) and (ii) indicate that a polymer coating reduces projectile decelerations and therefore contact stresses, for a given impact scenario. Table 5.1 presents the average projectile decelerations, calculated from the projectile velocity-time histories obtained from the high speed photography (plotted in Figs. 5.12 and 5.15). Taking the average projectile deceleration to be indicative of the average contact pressure, it can be inferred that the coating does indeed serve to reduce the contact stresses. The FE models also support the conclusion that the average projectile decelerations are reduced by between $40 - 60\%$ with the addition of the polymer coating.

Impact speed	$45\ \mathrm{m\,s^{-1}}$		$\approx 65\ \mathrm{m\,s^{-1}}$		$\approx 100\ \mathrm{m\,s^{-1}}$	
	FE	Experiment	FE	Experiment	FE	Experiment
Uncoated	980	1250	1140*	1260	2180*	1280
Coated	470	500	700	650	920	780

Table 5.1: Average projectile decelerations (up to maximum projectile penetration) in $10^3\,\mathrm{m\,s^{-2}}$ measured from Figs. 5.12 and 5.15. For cases marked with an asterisk, average deceleration is measured up to the time that FE predictions depart from experimental measurements as a result of severe concrete damage. Refer to Figs. 5.4 - 5.8 for exact impact velocities for each case.

Furthermore, observation (iii) indicates delocalisation of concrete damage. In combination, these effects appear to explain the protective benefit of the coating. Similar trends are observed at higher velocities (Figs. 5.17b, c and 5.18b, c) where the elastomer also acts to significantly delay the onset of damage initiation, and leads to a more diffusive pattern of damage. Note that at these higher impact speeds, the projectile is still in motion at the instant of damage initiation shown in Figs. 5.17 and 5.18.

This investigation identifies the protective effect of a polymer coating, for a particular combination of polymer type, coating thickness, concrete strength and projectile geometry. Further work is required to identify how sensitive the coating performance and protective mechanisms are to variations in these parameters, and hence how to optimise the coating design.

5.7 Conclusions

An experimental and numerical investigation has been conducted to assess the impact mitigating capabilities of a typical spray-on elastomer coating, applied to the impacted face of a concrete target. An FE model is developed and validated with a view to interrogating how the elastomer influences damage initiation in the concrete substrate. The following conclusions are established:

- An elastomer coating significantly reduces impact damage in the concrete over the full range of projectile velocities tested, $c.\,45-150\,\mathrm{m\,s^{-1}}$. For the particular geometry considered, an uncoated concrete cube experiences severe damage at a projectile velocity of $c.\,60\,\mathrm{m\,s^{-1}}$ whereas in its coated configuration, velocities of $c.\,120\,\mathrm{m\,s^{-1}}$ are required to achieve a similar level of damage.
- The elastomer coating remains intact until impacted at a speed of $c.\,120\,\mathrm{m\,s^{-1}}$. Damage remains local to the perimeter of the projectile, where there is evidence of ductile tearing. At higher impact velocities, a polymer plug is detached. The plug and corresponding hole in the coating undergo significant elastic contraction after projectile penetration.
- A finite element model in ABAQUS/Explicit is validated as an effective analysis tool for impact indentation of uncoated and coated concrete cubes under certain conditions. The FE model is deemed valid at early time steps, before the concrete becomes severely damaged. Further, for the coated cases, experimental comparisons are limited up to the point of maximum indenter penetration to avoid modelling inaccuracies associated with the unloading phase.
- The finite element analysis indicates that for this projectile geometry and coating thickness, the elastomer acts to alter damage initiation in the concrete. The time taken for damage to initiate is increased by an order of magnitude, and occurs after significant polymer indentation. The spatial distribution of concrete damage is also affected, with damage delocalised by the coating.

CHAPTER 6

Impact damage protection mechanisms for elastomer-coated concrete

6.1 Introduction

Chapter 5 established that an elastomer coating can contribute a significant impact mitigating effect when applied to a concrete substrate. Experimental impact testing examined the influence of a *c.* 5 mm elastomer layer, placed on a concrete cube of side length 100 mm subjected to impact from a 0.1 kg, blunt steel projectile. Over the range of impact velocities tested ($c.\, 45 - 150\,\mathrm{m\,s^{-1}}$), the elastomer markedly reduced the damage experienced by the concrete substrate. A numerical model was developed in ABAQUS/Explicit [27] to interrogate the mechanism behind the protective benefit offered by the coating. The model was validated at early time steps, before severe concrete damage and during the loading phase of elastomer penetration. Results indicated that the elastomer served to reduce projectile decelerations, thereby influencing the stress state and time evolution of damage initiation in the concrete substrate. In this chapter, the aim is to establish the elastomer influence on concrete damage across a range of impact velocities and boundary conditions. Further, a more detailed understanding of the protective mechanism(s) at play is developed.

This chapter is structured as follows. The numerical model, developed in Chapter 5, is used to span a range of impact velocities ($5 - 150\,\mathrm{m\,s^{-1}}$) in order to interrogate the concrete damage mechanisms and the influence of an elastomer coating on these mechanisms. The sensitivity to the concrete and polymer boundary conditions and coating thickness is then examined. Next, the mechanism by which the elastomer achieves its protective benefit is interrogated, building upon the findings from Chapter 5. Simplified 1D and 2D numerical models are employed with the aim

of understanding the protective effects contributed by the elastomer coating.

6.2 Impact indentation damage mechanisms

6.2.1 Numerical model development

Impact indentation of a concrete circular cylinder of diameter 100 mm and height 100 mm is simulated using an axisymmetric model in ABAQUS/Explicit, illustrated in Fig. 6.1. The same FE models (including the material constitutive definitions) employed for simulating the impact indentation of uncoated concrete (in Section 5.5.1) and coated concrete (in Section 5.5.2) are used in this chapter.

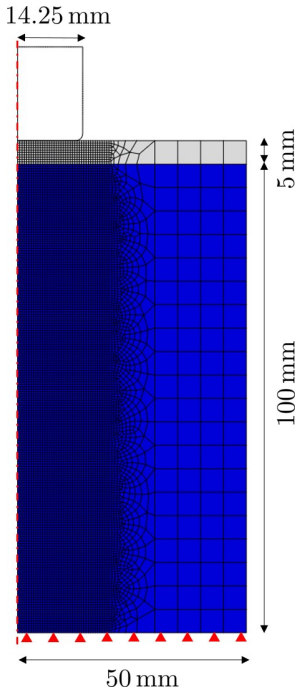

Figure 6.1: Reference geometry case: axisymmetric model in ABAQUS/Explicit of the impact indentation of a coated concrete cylinder. The concrete is supported on its non-impacted face (displacement is constrained in the direction of impact) and the outer edges of the concrete and polymer are free.

6.2.2 Damage mechanisms: reference geometry

Considering the range of impact velocities, $V_0 = 5 - 150\,\mathrm{m\,s^{-1}}$, the damage development is assessed by examining the contours of the compressive damage parameter, d_c. Figures 6.2 and 6.3 present the results for the uncoated and coated cases, respectively.

On each of the images presented in Figures 6.2 and 6.3, the value of normalised displacement, $\bar{u}$ is labelled. This corresponds to the time at which the image is

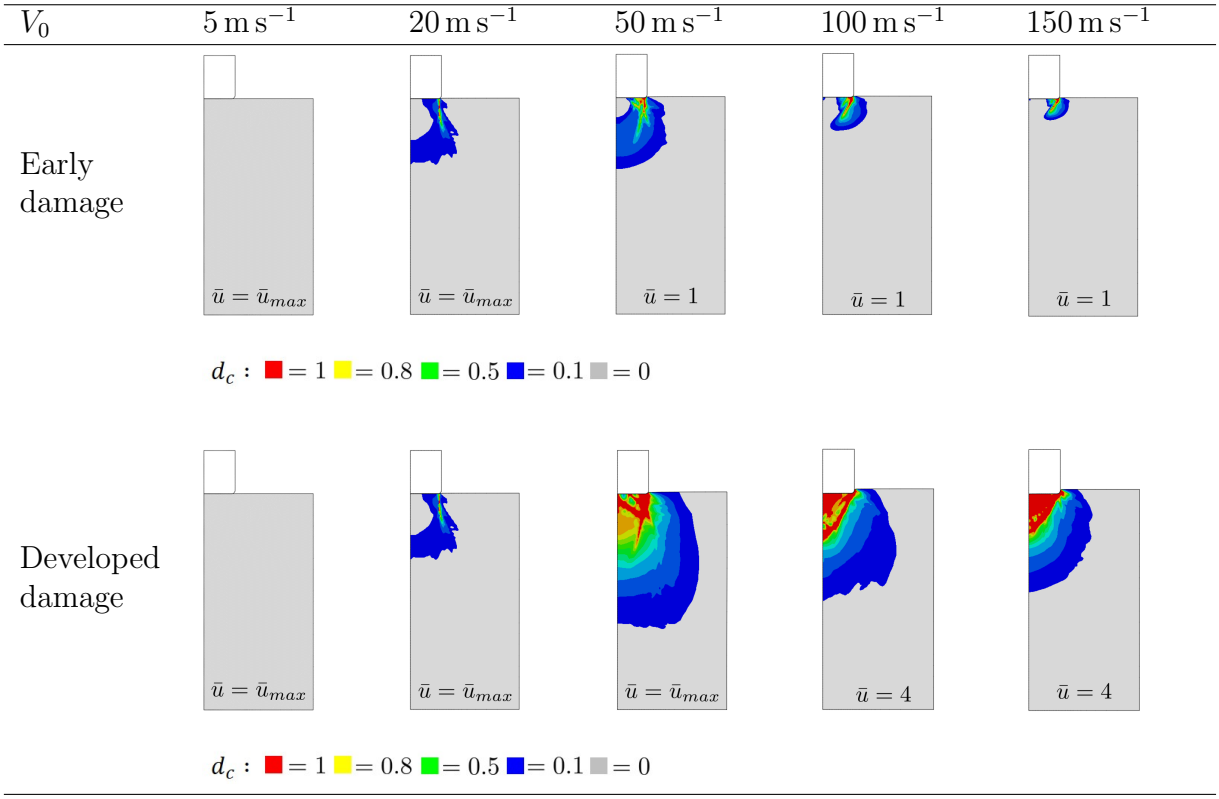

Figure 6.2: Comparing contours of the compressive damage parameter, d_c for uncoated concrete, subjected to projectile impacts at various velocities, V_0.

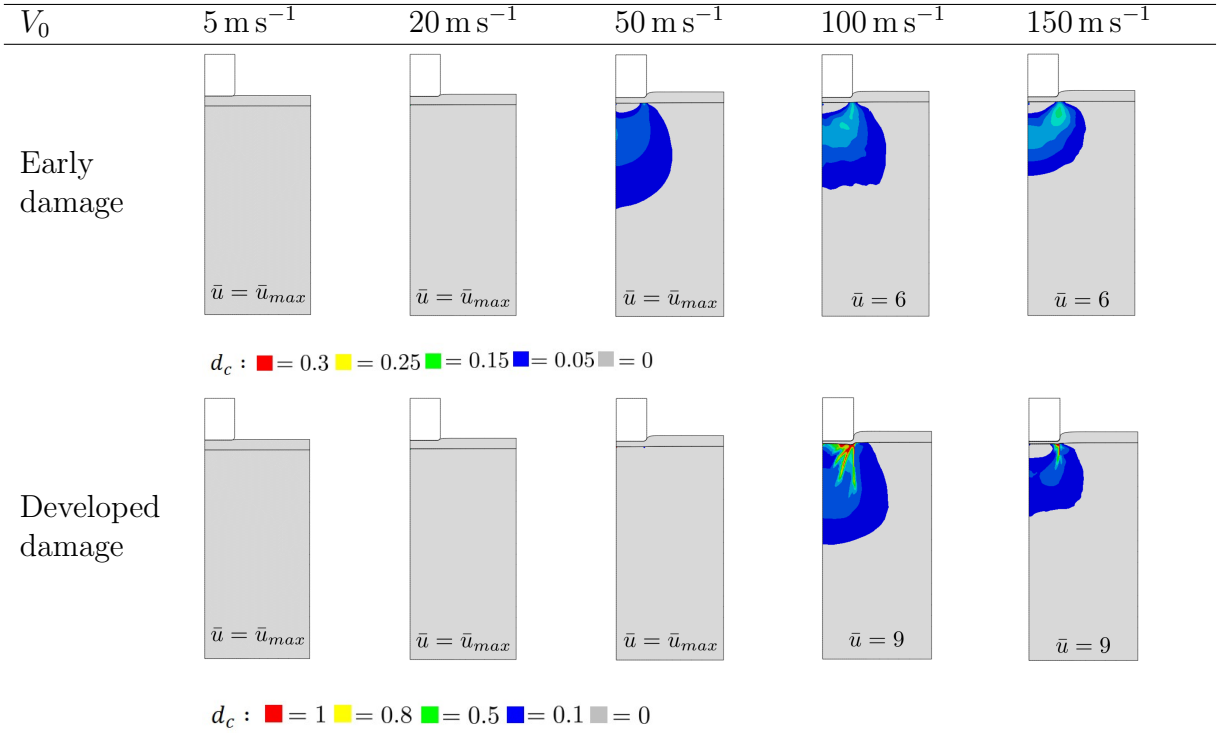

Figure 6.3: Comparing contours of the compressive damage parameter, d_c for concrete coated with a 5 mm elastomer layer, subjected to projectile impacts at various velocities, V_0.

taken. Normalised displacement, $\bar{u}$ is defined according to Eq. 6.1, where u is the displacement of the indenter, H is the height of the concrete block ($H = 100\,\text{mm}$) and ϵ_{cu} is the strain at the maximum compressive strength of the concrete ($\epsilon_{cu} = 0.005$ according to the uniaxial, quasi-static compression test performed in Chapter 5 and presented in Fig. 5.2).

$$\bar{u} = \frac{u}{\epsilon_{cu} H} \tag{6.1}$$

Damage patterns are compared at two phases of the impact response, denoted early damage and developed damage, each defined by a specific $\bar{u}$. The early damage images are taken at a time corresponding to $\bar{u} = 1$ for the uncoated cases and $\bar{u} = 6$ for the coated cases. The time for developed damage is defined to correspond to $\bar{u} = 4$ and $\bar{u} = 9$ for uncoated and coated cases, respectively. For all cases in which the projectile fails to reach this prescribed $\bar{u}$, the image presented corresponds instead to $\bar{u}_{max} = u_{max}/\epsilon_{cu} H$ where u_{max} is the maximum penetration depth of the projectile.

Comparison between Figures 6.2 and 6.3 reveals a difference in the early damage behaviour between uncoated and coated targets. This prompts the definition of two distinct damage mechanisms:

- Mechanism 1: Severe damage initiates early in the impact, under the corner of the indenter.
- Mechanism 2: Diffuse sub-surface damage develops in the region below the indenter, which eventually concentrates under the corner of the indenter.

For the uncoated targets, Mechanism 1 is observed for all but the very lowest impact velocities ($V_o = 5\,\text{m}\,\text{s}^{-1}$), where no damage is observed. The application of a 5 mm elastomer layer serves two effects: (i) the impact speed at which damage first occurs is increased, and (ii) the damage patterns shift to Mechanism 2. At high impact velocities ($V_o \geq 100\,\text{m}\,\text{s}^{-1}$), for the uncoated cases, the damage pattern develops to a cone of damaged material directly below the indenter. For the coated cases, there is a more diffuse distribution of concrete damage, although the location of greatest damage is again under the corner of the indenter. The damage again develops to form a cone under the indenter as the impact speed is increased. However, the coating serves to increase both the time and the impact velocity required for this to develop. These findings are consistent with the experimental observations in Chapter 5 (Section 5.6). The underlying causes of this protective effect provided by the polymer coating are interrogated in more detail in this chapter subsequently.

6.2.3 Sensitivity to boundary conditions

In this section, the influence of the concrete and polymer boundary conditions, and the polymer thickness, on the damage mechanisms are examined.

6.2.3.1 Edge constraint

First the effect of constraining the outer edges of the concrete cylinder is considered. The axisymmetric model illustrated in Fig. 6.1 (the reference case) is subjected to an additional boundary condition on the outer edges to constrain the lateral displacement of the elastomer and concrete. The early and developed damage patterns are compared with the reference case in Appendix D.1.1, for one projectile velocity, $V_o = 100\,\mathrm{m\,s^{-1}}$. This comparison illustrates that the additional edge constraint has no effect on the damage mechanisms or the mitigating effect of the elastomer.

6.2.3.2 Target geometry

Next, the effect of a change in target geometry is assessed. A more practical structural concrete slab configuration is considered: 50 mm deep, with a span of 1 m. Once more, an axisymmetric model is employed for computational efficiency, illustrated in Fig. 6.4. The edge of the slab (at its outer perimeter) is fully constrained, with all degrees of freedom set to zero. To avoid unrealistic stress concentrations at the perimeter, a degree of boundary compliance is introduced: a 50 mm wide region at the edge of the slab is placed between rigid, frictionless surfaces, which terminate with a radius of curvature of 90 mm. For the coated cases, a 5 mm elastomer layer is modelled on the impacted face and Coulomb friction, with a friction coefficient of $\mu = 0.8$ is assumed at the concrete/elastomer interface. Frictionless conditions are assumed at elastomer/steel and concrete/steel interfaces based on the findings in Section 5.4. The indenter geometry and mesh details remain unchanged, with a fine 0.5 mm mesh in the central 40 mm portion of the slab, transitioning to a much coarser mesh away from the impact site.

Figure 6.5 compares the early and developed damage patterns for the reference geometry (Fig. 6.1) and the slab (Fig. 6.4) for a projectile impact at $V_0 = 100\,\mathrm{m\,s^{-1}}$. There is no significant difference between the damage patterns for the cylinder and the slab, for these timescales. This indicates that damage initiation in a cylindrical target is fully representative of that in a slab of practical dimensions, that is free to bend.

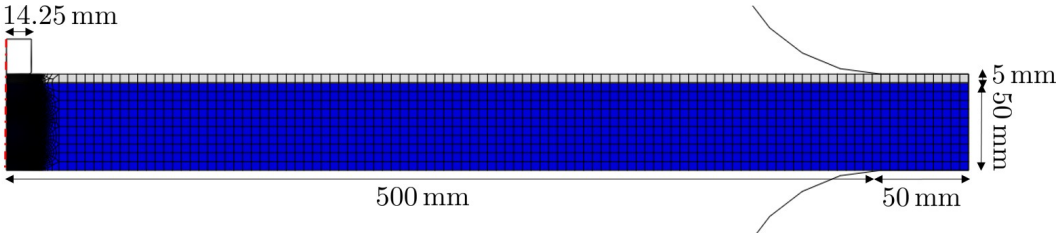

Figure 6.4: Axisymmetric model in ABAQUS/Explicit of the impact indentation of a coated concrete slab.

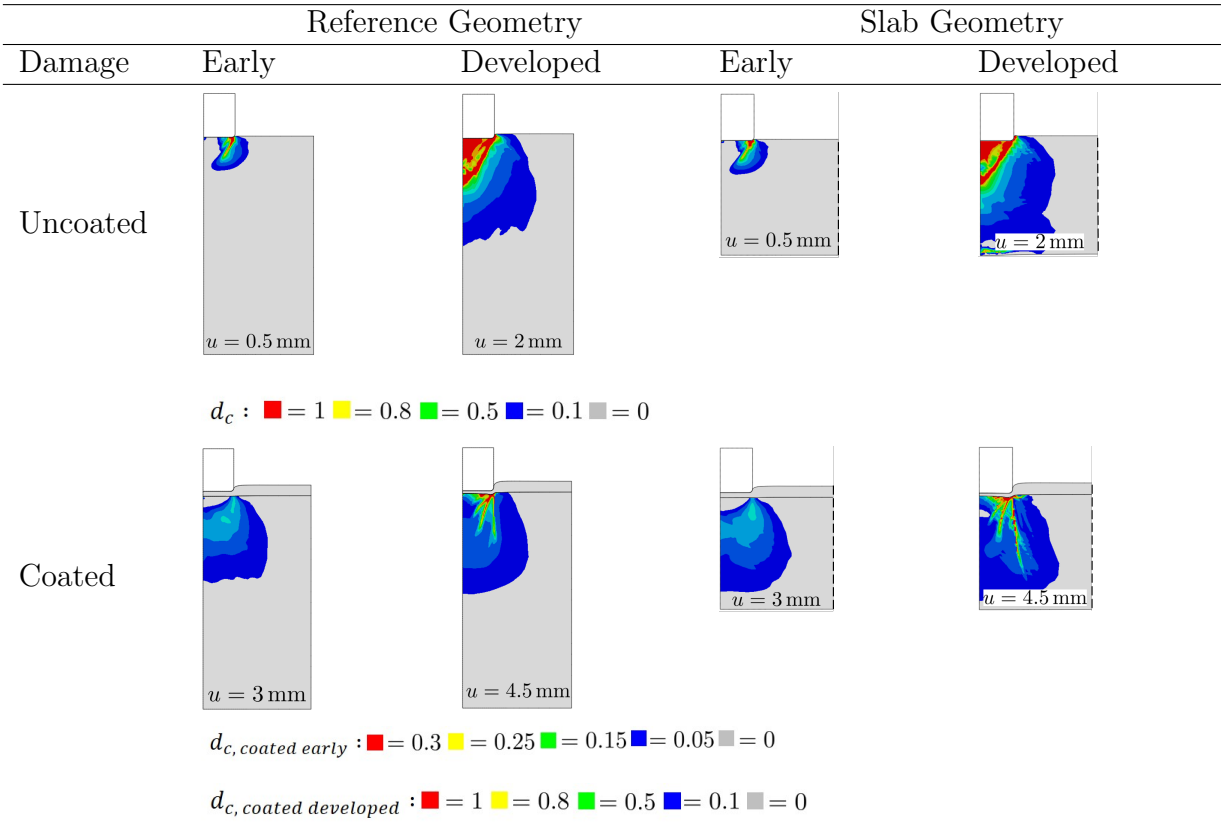

Figure 6.5: Comparing contours of the compressive damage parameter, d_c for the reference geometry (Fig. 6.1) and the slab geometry (Fig. 6.4). A projectile impact at $V_0 = 100\,\mathrm{m\,s^{-1}}$ is considered.

6.2.3.3 Elastomer-concrete bond strength

To explore the influence of contact conditions at the elastomer/concrete interface, two limiting cases are compared — frictionless and perfectly bonded (tying all degrees of freedom at the interface). This is compared with the reference case, assuming Coloumb friction with a friction coefficient of $\mu = 0.8$ (determined in Chapter 5 to give the best fit to quasi-static experimental data). The effect on the early and developed damage patterns is presented in Figure 6.6 for the reference geometry (Fig. 6.1) subjected to a projectile impact at $V_0 = 100\,\mathrm{m\,s^{-1}}$.

First, it is noted that the elastomer/concrete interface strength does not affect the damage initiation mechanism in the concrete: this remains Mechanism 2 for all coated cases. However, the interface does appear to have an influence on the level of developed damage in the concrete. While the perfectly bonded interface and $\mu = 0.8$ cases result in similar developed damage patterns, the frictionless case shows less damage. This would imply that reducing shear tractions at the interface is beneficial to reducing impact damage. However, a frictionless interface would be challenging to realise in practice.

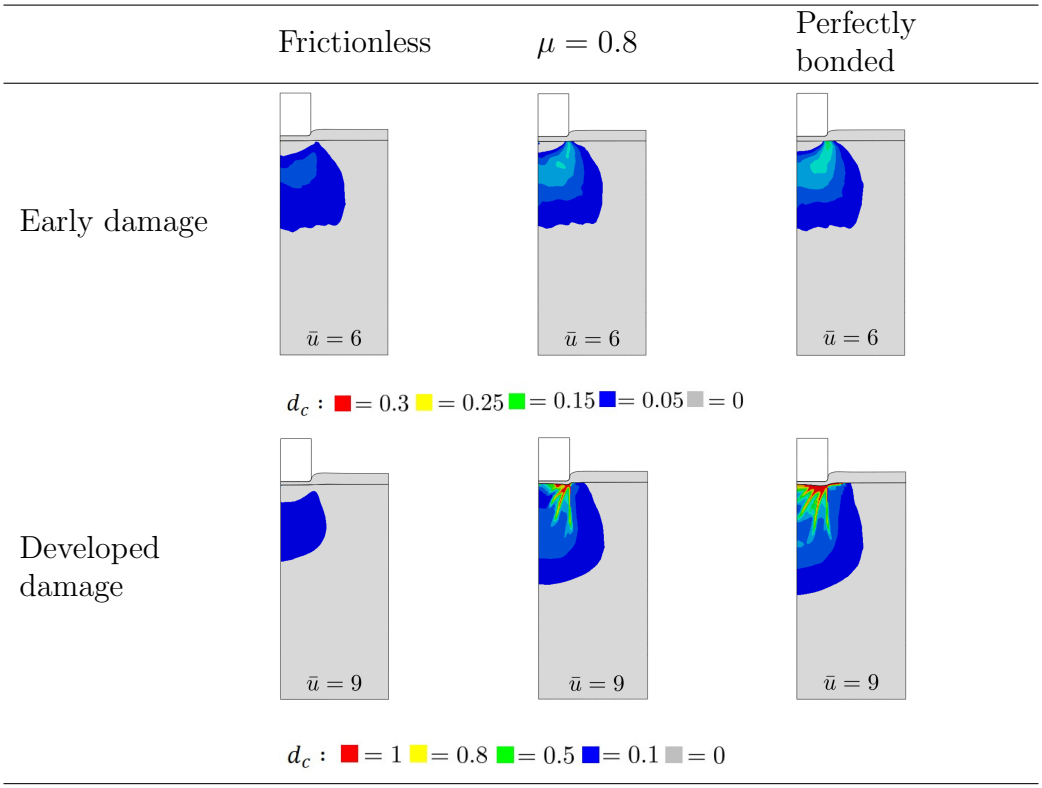

Figure 6.6: Comparing contours of the compressive damage parameter, d_c for the reference geometry (Fig. 6.1) when subjected to a projectile impact at $V_0 = 100\,\mathrm{m\,s^{-1}}$. Three cases are considered for the contact condition at the elastomer/concrete interface: frictionless, friction coefficient of $\mu = 0.8$ and perfectly bonded.

6.2.3.4 Coating thickness

Finally, the effect of varying the coating thickness on the damage mechanisms is considered. Figure 6.7 compares a 5 mm coating with a 10 mm coating, assuming a coefficient of friction, $\mu = 0.8$ at the elastomer/concrete interface. It is clear that the thicker coating serves to delay the onset of damage in the concrete substrate. Minimal damage is observed for an impact velocity of $100\,\mathrm{m\,s^{-1}}$ for a 10 mm thick coating. Therefore, as expected, a thicker coating appears to increase the protective benefit. However, from a design perspective, this added benefit must be weighed against the increase in weight and cost.

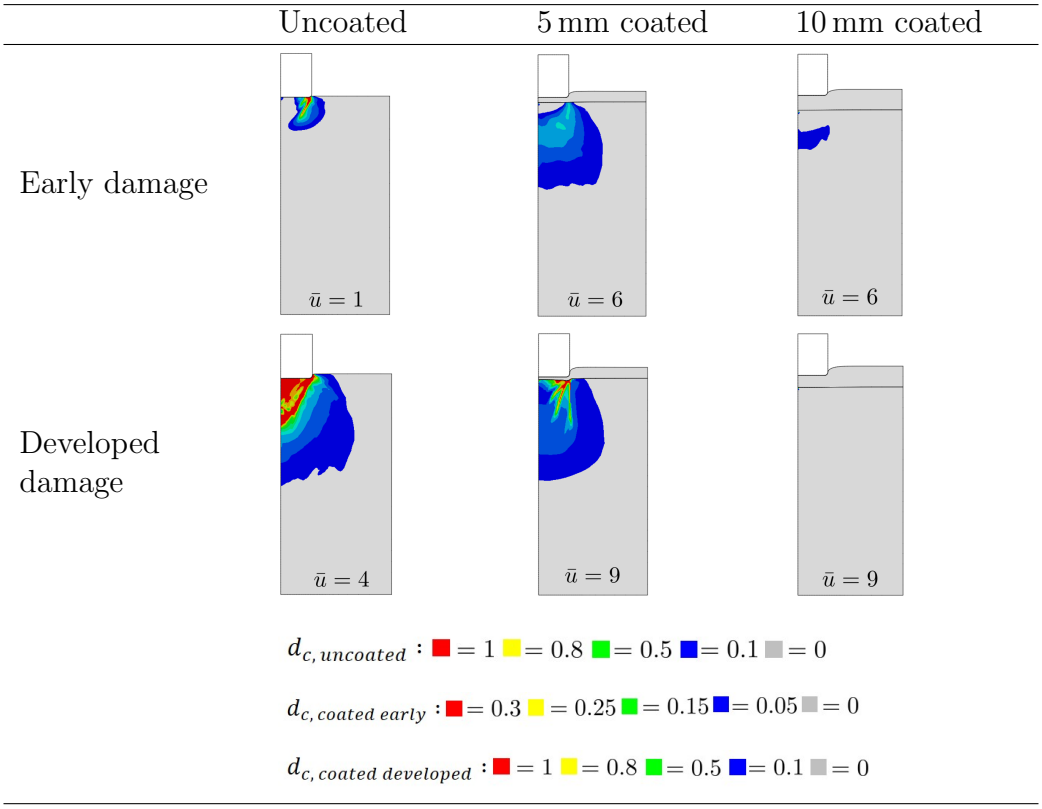

Figure 6.7: Comparing contours of the compressive damage parameter, d_c for the reference geometry (Fig. 6.1) when subjected to a projectile impact at $V_0 = 100\,\mathrm{m\,s^{-1}}$. Three cases are considered: Uncoated, coated with a 5 mm elastomer layer and coated with a 10 mm elastomer layer. A coefficient of friction, $\mu = 0.8$ is assumed between the elastomer/concrete interface.

6.3 Investigating the protective effect of the coating

The previous section has highlighted that the application of a relatively thin elastomer layer to a concrete substrate affects the damage mechanisms in the underlying concrete, providing a significant protective benefit across a range of impact indentation velocities. In this section, the objective is to understand precisely how the elastomer achieves this effect.

6.3.1 Projectile acceleration and contact pressure

Considering first the reference geometry and boundary conditions, illustrated in Fig. 6.1. The numerical model, defined in Section 6.2.1, is used to interrogate the projectile acceleration-time histories for two different impact velocities and the results are presented in Fig. 6.8.

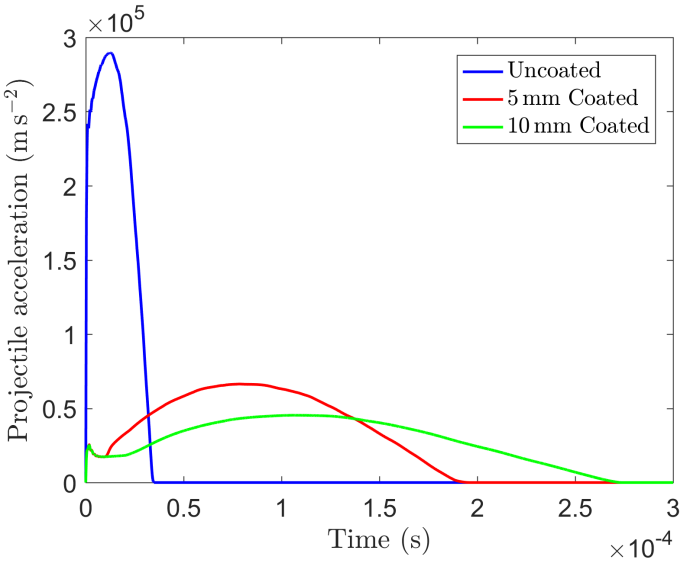

(a) $5\,\mathrm{m\,s^{-1}}$

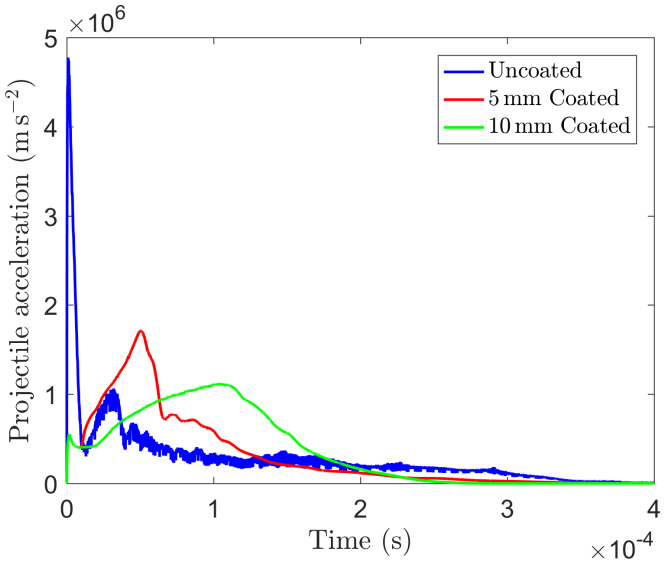

(b) $100\,\mathrm{m\,s^{-1}}$

Figure 6.8: Projectile acceleration - time histories for the reference geometry (Fig. 6.1) subjected to projectile impacts at $V_0 = 5$ and $100\,\mathrm{m\,s^{-1}}$. Three configurations are considered at each velocity: Uncoated, coated with a 5 mm elastomer layer and coated with a 10 mm elastomer layer.

For the low velocity impact case (Fig. 6.8a), the concrete exhibits an elastic response and the shape of the acceleration-time profiles of both uncoated and coated cases are approximately sinusoidal. The peak acceleration recorded for the 5 mm coated

case is significantly lower in magnitude than that for the uncoated case. Increasing the coating thickness to 10 mm reduces the peak acceleration further. Additionally, the duration of contact is much longer with the coating present, with the duration increasing with coating thickness. There is therefore a fall in the *average* projectile accelerations with the addition of a coating. For the lower velocity case, average accelerations are measured up to the time when acceleration falls to zero ($t = 35\,\mu$s and $t = 195\,\mu$s for the uncoated and 5 mm coated cases, respectively). Table 6.1 compares peak and average accelerations for the uncoated and 5 mm coated cases.

V_0 ($\mathrm{m\,s^{-1}}$)	Peak Acceleration ($\times 10^6\,\mathrm{m\,s^{-2}}$)		Average Acceleration ($\times 10^6\,\mathrm{m\,s^{-2}}$)		Average Acceleration† ($\times 10^6\,\mathrm{m\,s^{-2}}$)	
	Uncoated	5 mm Coated	Uncoated	5 mm Coated	Uncoated	5 mm Coated
5	0.3	0.07	0.2	0.04	0.2	0.04
100	4.8	1.7	0.3	0.4	4	0.97

Table 6.1: Peak and average accelerations measured from the plots in Fig. 6.8. † denotes average accelerations measured up to the point of severe concrete damage only (defined in the main text).

Next, the higher velocity impact case in Fig. 6.8b is examined. For the uncoated case, there is an initial transient on impact, giving a high peak acceleration. This is followed by a slower rise in acceleration as the projectile indents the concrete. The acceleration then tails off, as plastic deformation and damage develops in the concrete. For the 5 mm coated case, damage initiation in the concrete is also predicted, and is evident in a drop in acceleration at around $50\,\mu$s. The coating serves to reduce the magnitude of the initial transient peak in acceleration, delaying the time at which damage develops (indicated by the drop in acceleration), and to increase the duration of interaction between projectile and target. These effects are denoted collectively as the *temporal effect* contributed by the elastomer.

Table 6.1 shows that while peak accelerations for the higher impact velocity case are significantly reduced with the addition of the coating, *average* accelerations are not. This is in contrast to what was observed for the lower impact velocity case and is likely due to the severe concrete damage experienced after the initial transient peak in acceleration. Average accelerations are measured up to the time when acceleration falls to zero ($t = 400\,\mu$s and $t = 300\,\mu$s for the uncoated and 5 mm coated cases, respectively). However, as discussed in Chapter 5, the FE model is only deemed valid at time steps before the concrete becomes severely damaged. An extra column is added to Table 6.1, tabulating average accelerations, measured up to the time step when severe concrete damage initiates (examining the FE simulations, this time corresponds to the first sharp drop in acceleration-time, at $t = 1\,\mu$s for the uncoated

case and $t = 50\,\mu$s for the 5 mm coated case). These average accelerations are significantly reduced with the addition of the coating in the higher impact velocity case. Since no damage is observed for the lower velocity impact case, the average accelerations are unchanged.

Next, the spatial contact pressure variation is interrogated in Fig. 6.9. For both low and high impact velocity cases, the magnitude of the contact stresses experienced by the concrete are significantly reduced with the coating present. This is due to the significant reduction in peak accelerations discussed previously. However, another coating benefit is also identified. Examining the lower velocity impact case in Fig. 6.9a, the addition of the coating results in a much more uniform distribution of contact pressure under the indenter. When uncoated, there is a concentration in contact pressure under the indenter corner. With the coating in place however, the magnitude of the contact pressure remains spatially more uniform. Similar effects are observed for the higher impact velocity case in Fig. 6.9b.

Furthermore, Fig. 6.10 provides evidence that the coating also serves to change the sub-surface stress state. The stress triaxiality is more uniformly distributed in the coated case. However, the magnitude of the compressive stress triaxialities (plotted negative in Fig. 6.10) also tends to reduce for the coated case. This may be of concern, as the strength of the concrete is sensitive to the stress state, and increases with the magnitude of the compressive stress triaxiality. However, the triaxiality is similar in the coated and uncoated cases at the critical locations of maximum contact pressure. And so, reducing the magnitude of the contact pressures with the coating offers a net benefit for delaying damage initiation. Also, the more uniform distribution of stress triaxiality observed for coated concrete (Fig. 6.10b) may account for the more uniform distribution of sub-surface damage that characterises the early damage response of coated concrete (illustrated in Figure 6.3 and defined as Mechanism 2.)

These effects are denoted collectively as the *spatial effect* contributed by the elastomer.

6.3.2 Interrogation of the protective mechanisms

In this section, simplified 1D and 2D models are used to understand to what extent the protective mechanisms described above rely on indentation, *i.e.* to what extent they are 2D, rather than 1D, phenomena. This provides insights that may help the future development of simplified models to capture these effects and support coating design.

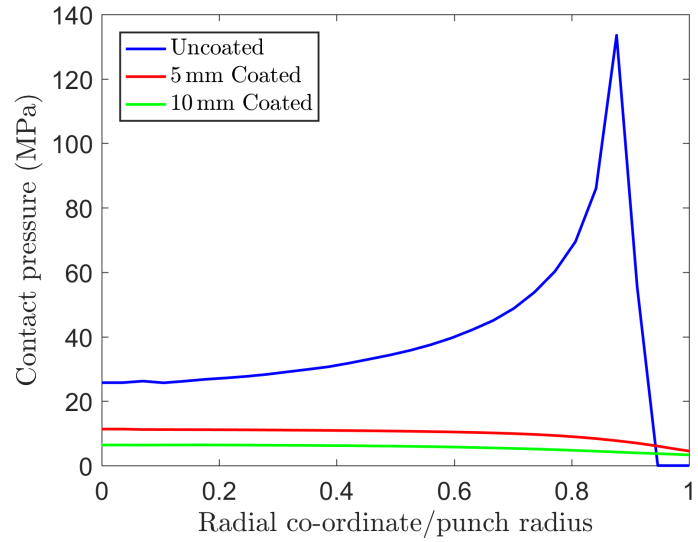

(a) $5\,\mathrm{m\,s^{-1}}$

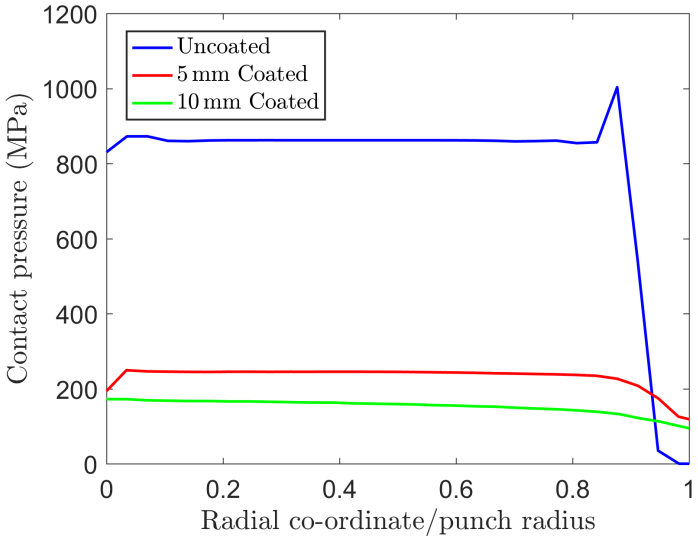

(b) $100\,\mathrm{m\,s^{-1}}$

Figure 6.9: Concrete contact pressure variation with normalised radial co-ordinate for the reference geometry (Fig. 6.1) subjected to projectile impacts at $V_0 = 5$ and $100\,\mathrm{m\,s^{-1}}$. Three configurations are considered at each velocity: Uncoated, coated with a 5 mm elastomer layer and coated with a 10 mm elastomer layer. Contact pressure outputs are taken at a step time corresponding to the peak projectile acceleration in each case (for $V_0 = 5\,\mathrm{m\,s^{-1}}$: $t = 12.5\,\mu$s for uncoated, $t = 78\,\mu$s for 5 mm coated and $t = 108\,\mu$s for 10 mm coated. For $V_0 = 100\,\mathrm{m\,s^{-1}}$: $t = 1\,\mu$s for uncoated, $t = 50\,\mu$s for 5 mm coated and $t = 103\,\mu$s for 10 mm coated.).

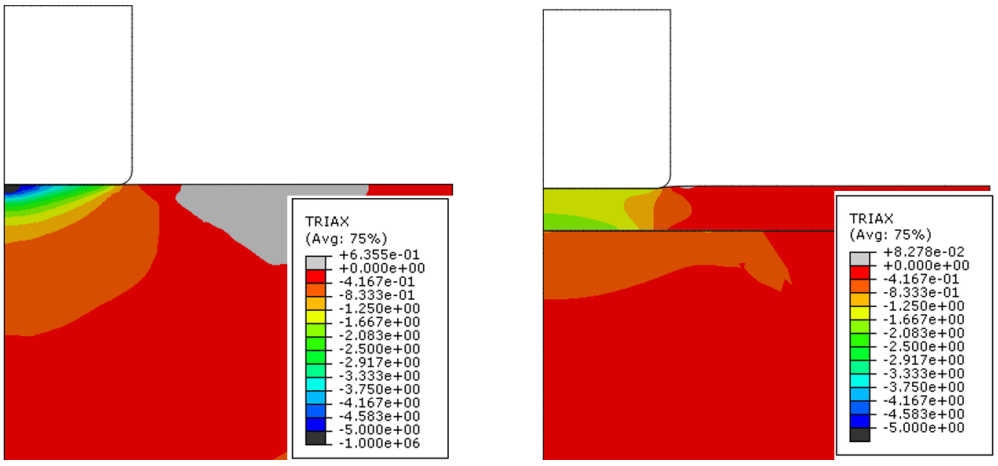

(a) Uncoated (b) 5 mm Coated

Figure 6.10: Contours of stress triaxiality (TRIAX in ABAQUS notation) for (a) uncoated and (b) 5 mm coated concrete subjected to projectile impact at $5\,\mathrm{m\,s^{-1}}$. Images taken at a time corresponding to peak projectile acceleration in each case ($t = 12.5\,\mu$s for uncoated, $t = 78\,\mu$s for 5 mm coated).

6.3.2.1 1D model

Figures 6.11a and 6.11b illustrate simplified models giving a 1D representation of the projectile impact on uncoated and coated targets. Thus, any 2D indentation phenomena are eliminated from the analysis.

A linear elastic model is chosen for the concrete target in this simplified analysis, with a Young's Modulus, $E_0 = 28.3\,\mathrm{GPa}$ and a Poisson's ratio, $\nu = 0.2$. The concrete column is also made long enough to avoid internal reflections, so that the target can be assumed effectively semi-infinite. The elastomer model remains unchanged from that described in Section 6.2.1. The boundary conditions on the column are as illustrated in Figs. 6.11a and 6.11b. The flat-faced projectile is again modelled as a rigid body. The projectile acceleration-time histories obtained using these 1D models are presented in Fig. 6.12.

It is observed that the addition of the elastomer coating in a purely 1D analysis replicates the *temporal effect* observed for the impact on the concrete targets in Fig. 6.8. The presence of the coating reduces the magnitude of the peak accelerations (and hence contact pressures). Furthermore, the coating serves to increase the duration of the response. Thus, it is established that 2D indentation effects are not required to reproduce the *temporal effect* of the coating — a 1D analysis is sufficient.

In a 1D analysis, no *spatial effect* can be predicted — the contact pressure must be spatially uniform. However, the contact pressures (and thus sub-surface stresses) for the coated case are significantly reduced in the 1D calculations, confirming the protective benefit of the *temporal effect*. For projectile impact at $5\,\mathrm{m\,s^{-1}}$, the peak

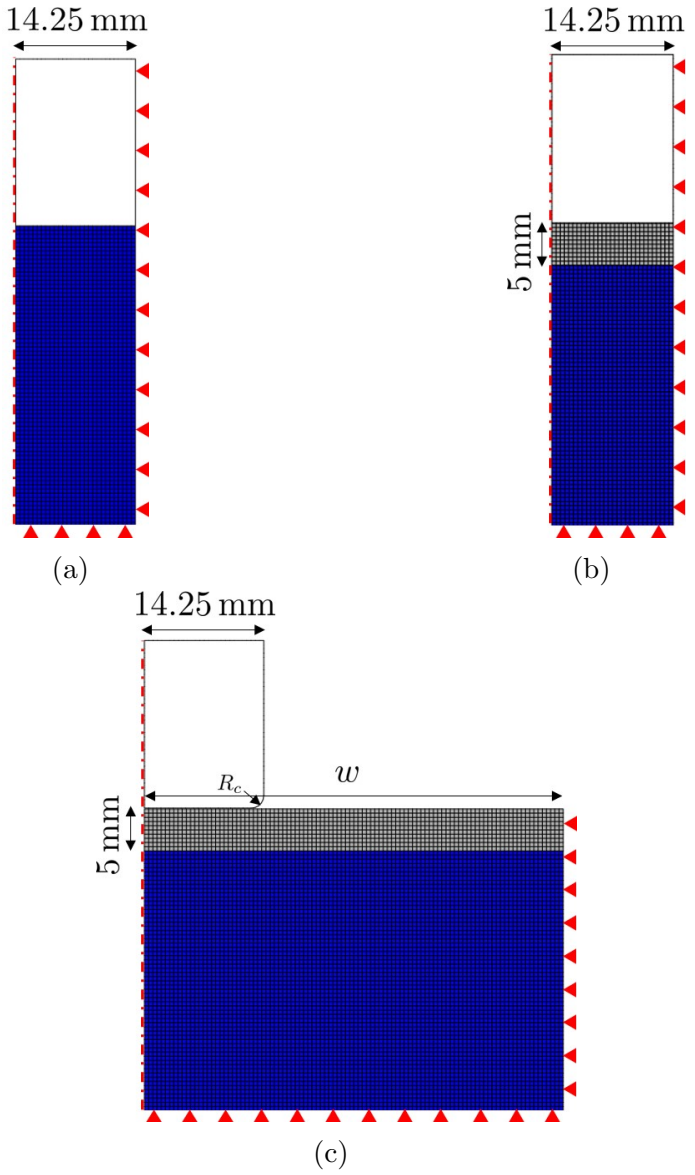

Figure 6.11: Axisymmetric models used to interrogate the protective mechanisms; a) 1D model, uncoated; b) 1D model, coated; c) 2D model, coated, indenter radius, R_c. In all cases, the concrete column is made long enough to prevent interference from wave reflections. Not to scale.

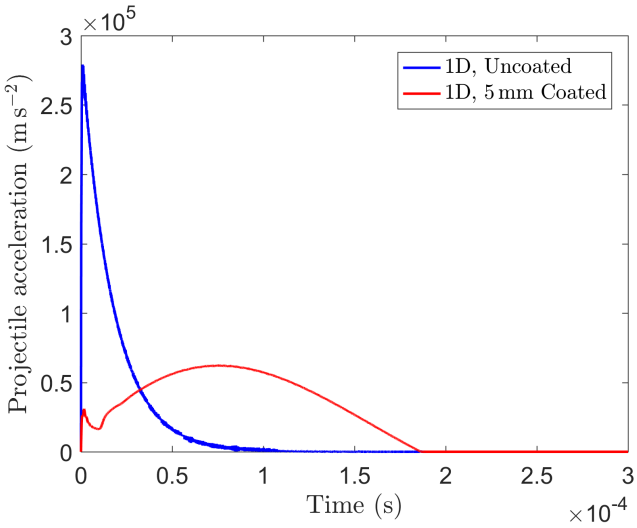

(a) $5\,\mathrm{m\,s^{-1}}$

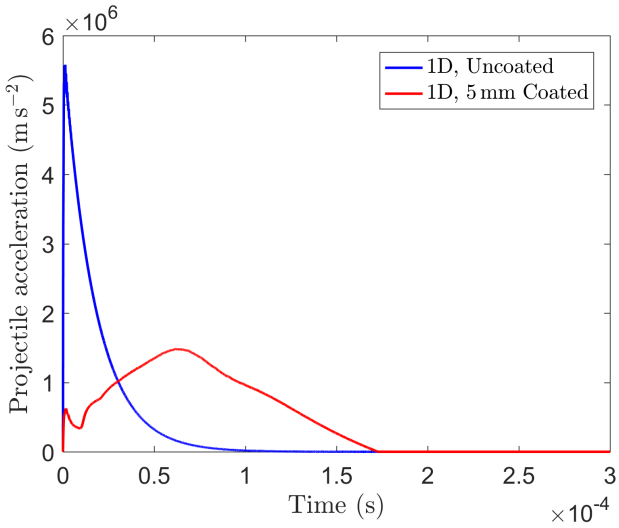

(b) $100\,\mathrm{m\,s^{-1}}$

Figure 6.12: Projectile acceleration - time histories for the axisymmetric, 1D models in Figs. 6.11a and 6.11b, subjected to projectile impacts at $V_0 = 5$ and $100\,\mathrm{m\,s^{-1}}$. Two configurations are considered at each velocity: Uncoated and coated with a 5 mm elastomer layer.

contact pressure recorded is 44 MPa for the uncoated case compared with 10 MPa for the 5 mm coated case, each recorded at the time corresponding to peak projectile acceleration, $t = 0.9\,\mu$s for uncoated and $t = 76\,\mu$s for coated.

6.3.2.2 2D model

The *spatial effect* observed for the concrete targets, involving radial variations in contact pressure, is necessarily a 2D phenomenon, and hence likely to be linked to target indentation effects. A simplified 2D model is now used to interrogate the transition from the 1D case to the indentation of an effectively semi-infinite half space, to see at what point the *spatial effect* becomes apparent. The same target properties described in Section 6.3.2.1 are used, but now a 2D axisymmetric calculation is performed with a variable target radius, w (Fig. 6.11c). Simulations for increasing values of w show that the *spatial effect* may be reproduced once the concrete domain width, w becomes even slightly larger than the indenter radius, R_i (*i.e.* for $w/R_i \approx 1.1$).

Indentation of the polymer is therefore key to delivering the *spatial effect*. Next, we consider whether this effect is equivalent to changing the projectile tip geometry. It was shown by Mohagheghian *et al.* [7] that for thin metallic targets, the *spatial effect* induced by a polymer coating was key to the protective benefit, and could therefore be reproduced to a large extent by altering the projectile tip geometry. To investigate this for the current problem, a number of variations on the model presented in Fig. 6.11c are considered. A large concrete domain width is selected ($w/R_i = 3$), a 5 mm coating is included and the indenter corner radius is reset to its initial value, $R_c = 1.5$ mm (all as defined in Section 6.2.1). The acceleration-time history and contact pressure spatial variation are compared with uncoated cases, impacted by projectiles of increasing corner radius: $R_c = 1.5$ mm, $R_c = 3$ mm and $R_c = 14.25$ mm (*i.e.* hemispherical). The results are presented in Fig. 6.13.

First, the spatial variation in contact pressure is examined in Fig. 6.13b. Doubling the corner radius to $R_c = 3$ mm has a negligible influence on the magnitude of the contact pressures recorded. The spatial variation in contact pressure is also unchanged and it is clear that considering impact from an indenter with a larger corner radius does not produce a similar *spatial effect* to that observed for the coated case. Impact from a hemispherical projectile produces a very different response compared with the other cases. There is a sharp stress concentration at the punch tip, reaching much higher pressures than those recorded for the other cases. This rapidly reduces to zero a short distance away from the impact site. Once more, this response is very different to the *spatial effect* identified for the coated case. These

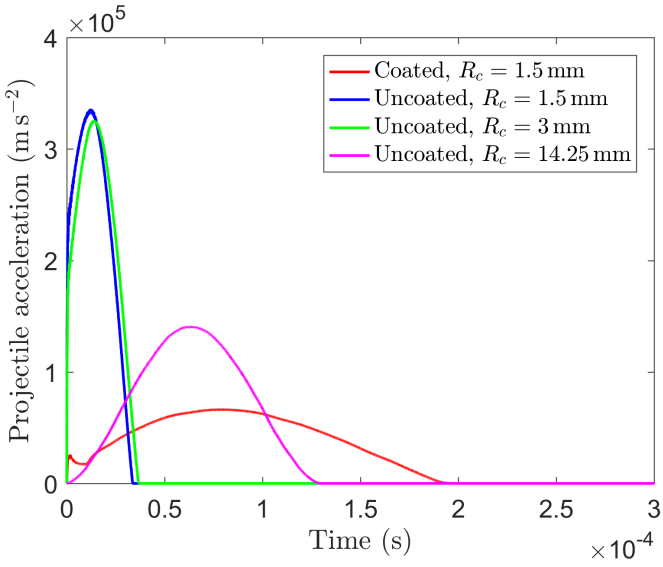

(a) Acceleration - time history

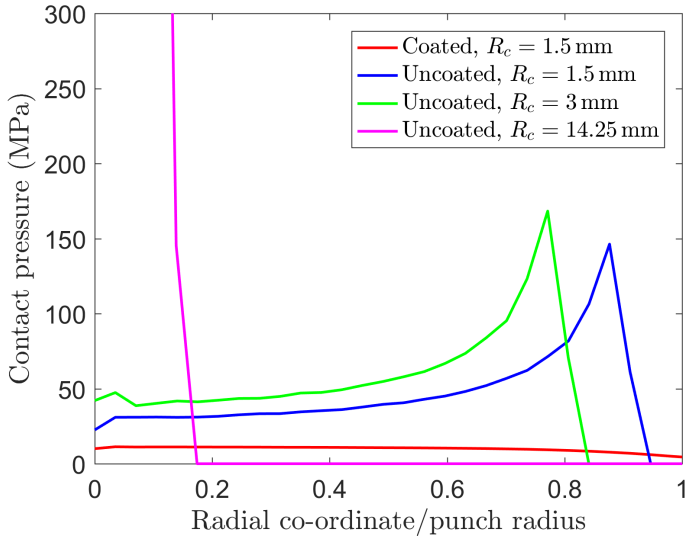

(b) Contact pressure variation

Figure 6.13: (a) Projectile acceleration - time history and (b) spatial contact pressure variation for a projectile impact at $V_0 = 5\,\mathrm{m\,s^{-1}}$. Four variations on the model illustrated in Fig. 6.11c are considered: coated with 5 mm elastomer and $R_c = 1.5$ mm, uncoated and $R_c = 1.5$ mm, uncoated and $R_c = 3$ mm and uncoated and $R_c = 14.25$ mm. Contact pressure outputs are taken at a step time corresponding to the peak projectile acceleration in each case (for coated and $R_c = 1.5$ mm: $t = 78\,\mu$s; uncoated and $R_c = 1.5$ mm: $t = 12.5\,\mu$s; uncoated and $R_c = 3$ mm: $t = 14\,\mu$s, uncoated and $R_c = 14.25$ mm: $t = 63\,\mu$s).

results suggest that the redistribution of contact stresses provided by the coating are not equivalent to a projectile nose-shape change, for this target configuration.

Next, considering the acceleration-time histories in Fig. 6.13a, doubling the corner radius to $R_c = 3\,\text{mm}$ for an uncoated target has an almost negligible effect on the peak acceleration and pulse duration. Considering impact from a hemispherical projectile ($R_c = 14.25\,\text{mm}$) on uncoated concrete, the peak accelerations are reduced and the pulse duration is lengthened. Thus, the projectile nose-shape change can provide a *temporal effect*, but this is much less pronounced than that provided by the polymer coating.

In summary, it has been shown that indentation of an elastomer coating is required to achieve both the protective *temporal* and *spatial* effects. The *temporal effect* is essentially a 1D phenomenon where the key consequence is to reduce peak accelerations and thus contact pressures. The *spatial effect* is observed when there is indentation of the target (even when the concrete domain size is relatively small with respect to the indenter *i.e.* $w/R_i > 1.1$). Furthermore, the *spatial effect* contributed by the elastomer is not equivalent to impact from a projectile with a more rounded tip geometry. Instead, the elastomer coating is required to reduce the stress concentrations under the indenter.

6.4 Conclusions

A numerical study is performed in ABAQUS/Explicit to interrogate the impact indentation of a concrete cylinder of diameter, 100 mm and height, 100 mm in two configurations: uncoated and coated with a 5 mm elastomer layer on the impacted face. The concrete damage mechanisms are identified and the elastomer's influence is assessed. The following conclusions are established:

- Two distinct damage initiation mechanisms are observed. Mechanism 1 is characterised by severe concrete damage, initiating over shorter timescales under the indenter corner. Mechanism 2 is characterised by more diffuse, sub-surface concrete damage which develops over longer timescales, before eventually concentrating under the indenter corner.
- For all but the very lowest impact velocities, where no damage is observed, uncoated targets exhibit Mechanism 1 and coated targets exhibit Mechanism 2. By shifting the damage mechanism, the coating achieves a significant increase in the projectile velocity required to cause severe damage. Increasing the coating thickness provides an increased protective benefit.
- A frictionless interface between the concrete and elastomer appears to provide

a protective benefit. However, this would be difficult to achieve in practice.

- The elastomer achieves its protective benefit via two mechanisms — a *temporal effect* (a reduction in the magnitude of the peak acceleration and an increase in the duration of contact between projectile and target) and a *spatial effect* (a more uniform contact pressure distribution is achieved, removing the stress concentration under the indenter corner and providing a more uniform state of stress triaxiality under the indenter).
- To achieve both *temporal* and *spatial* effects, the indentation of an elastomer coating is required. The *temporal effect* is essentially a 1D phenomenon but the *spatial effect* is only observed when there is indentation *i.e.* once the concrete domain width is larger than the projectile radius ($w/R_i > 1.1$). Furthermore, the *spatial effect* cannot be reproduced by a projectile with a more rounded tip geometry.

CHAPTER 7

Design of elastomer coatings for concrete impact damage mitigation

7.1 Introduction

An experimental investigation on the impact response of elastomer-coated concrete was presented in Chapter 5, which established that an elastomer coating can significantly reduce the damage experienced by an underlying concrete substrate. A significant protective benefit was observed across the range of impact velocities tested, $c.\,45 - 150\,\mathrm{m\,s^{-1}}$ for impact from a 0.1 kg blunt steel projectile. This prompted the development of a numerical model to simulate the dynamic impact tests with the objective of interrogating the mechanism by which the elastomer achieves its impact mitigating effect.

Focusing on damage initiation in the concrete, two damage mechanisms were identified in Chapter 6. Mechanism 1, characterised by severe concrete damage, initiating early under the indenter corner, and Mechanism 2, characterised by more diffuse, sub-surface concrete damage developing over longer timescales. It was established that the addition of an elastomer coating serves two effects: (i) the impact speed at which damage first occurs is increased and (ii) the damage initiation mechanism shifts from Mechanism 1 to Mechanism 2. Upon detailed interrogation of simplified FE models, it was concluded that the elastomer achieves its protective effect via two mechanisms — a *temporal effect* (a reduction in the magnitude of the peak acceleration and an increase in the contact duration between the projectile and target), and a *spatial effect* (a more uniform contact pressure distribution is achieved, removing stress concentrations under the indenter corner).

The objective of this chapter is to build upon the aforementioned work in Chapters 5 and 6, to develop guidelines for effective coating design for concrete impact damage

mitigation. The chapter is structured as follows. The experimental results and numerical model predictions from Chapters 5 and 6 are first compared and used to identify the regimes of concrete failure/no failure for a range of realistic coating thicknesses and projectile impact velocities. From a design perspective, delaying the failure of the concrete substrate is of critical importance. Section 7.3 develops an analytical model capable of predicting the onset of failure for an elastomer-coated concrete target subjected to blunt projectile impact. Practical design maps are derived using the proposed analytical models, taking the key variables as the coating thickness, elastomer modulus and projectile impact velocity. Finally, the analytical model is validated by comparison with experimental results and FEA predictions obtained in Chapters 5 and 6.

7.2 Identification of impact response regime boundaries

The same FE models and material constitutive definitions, discussed previously, used for modelling the impact indentation of uncoated concrete targets (in Section 5.5.1) and coated concrete targets (in Section 5.5.2) are used in this chapter.

These FE models are used to vary the projectile velocity, V_0 and the polymer thickness, h_e, in order to populate a map, plotting the combination of these variables that give rise to concrete damage. This map is illustrated in Fig 7.1a. The compressive damage parameter, d_c is used as the concrete damage metric. When a specified number of concrete elements (extending to a depth of approximately 5 mm) have reached $d_c > 0.9$ during the loading portion of the indentation response, the concrete is deemed to be damaged. Also plotted on Fig. 7.1a are the results from the experimental gas gun tests from Chapter 5. In the experimental tests, concrete damage is determined on the basis of post-impact visual inspection, where a block exhibiting visible cracking or complete fragmentation is deemed damaged.

Comparing the FE predictions and experimental observations in Fig. 7.1a, the results agree well, particularly for $V_0 < 75\,\mathrm{m\,s^{-1}}$ and $V_0 > 120\,\mathrm{m\,s^{-1}}$. However the FE model appears to underpredict the impact damage resistance, predicting damage for a 6 mm elastomer-coated block impacted at $V_0 = 100\,\mathrm{m\,s^{-1}}$, when there was no visible damage observed in the corresponding experiment.

As described in Chapter 5 (Section 5.4.2), frictional contact is chosen, with a friction coefficient of $\mu = 0.8$ at the concrete/elastomer interface, based on best fit with quasi-static experimental results. However, it is indicated in Appendix C.3 that frictionless contact at this interface agreed better with dynamic tests, providing a closer estimate of the projectile rebound velocities measured using high speed photography. For that study, the influence of these frictional effects were difficult

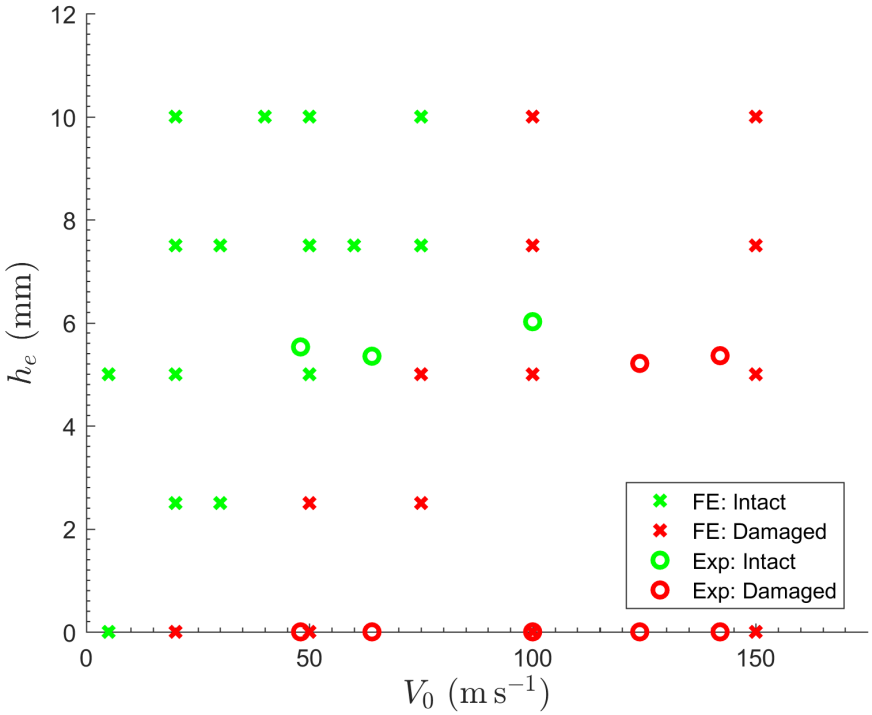

(a) Friction with coefficient, $\mu = 0.8$

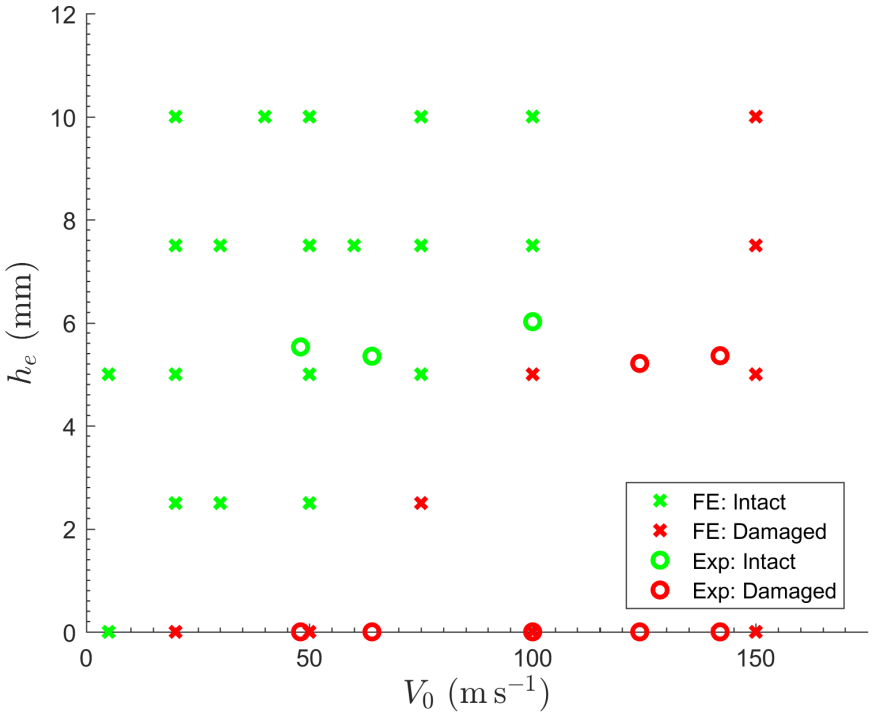

(b) Frictionless

Figure 7.1: Comparison between FE predictions and experimental observations. Two variations of the FE model are considered: (a) Frictional contact at the concrete/elastomer interface with a coefficient, $\mu = 0.8$ and (b) Frictionless contact at the concrete/elastomer interface. Legend: $\times$ represents FE predictions and $\circ$ represents experimental observations; green indicates intact concrete and red indicates damaged concrete.

to determine given other obscuring factors such as severe concrete damage and lack of elastomer hysteresis in the numerical model. Here, this question is revisited. Figure 7.1b plots the comparison between the experimental results and the FE predictions, assuming frictionless contact at the elastomer/concrete interface. This serves to reduce predicted concrete damage for a given impact velocity, bringing the FE predictions more into line with the experimental observations.

This suggests that the frictional contact conditions may, indeed, depend on the strain rate. Considering that the elastomer is not bonded to the concrete substrate, it is reasonable to assume that the frictional conditions experienced at this interface may be influenced by the elastomeric response, which is itself time-dependent. Alternatively, premature concrete failure during the dynamic FE simulations assuming frictional contact may be due to the sensitivity of the concrete failure model to the induced surface tractions at the concrete/elastomer interface. The model may lose fidelity under the complex stress state at this interface, resulting in a more severe damage prediction.

In the following sections, FE predictions are presented for both contact conditions: (i) frictional contact at the elastomer/concrete interface (with a coefficient of friction, $\mu = 0.8$) and (ii) frictionless contact at that interface.

7.3 Analytical modelling

The aim now is to derive an analytical model capable of predicting the onset of failure for elastomer-coated concrete targets. The motivation is derived from the findings in Chapter 6, which identify the key mechanisms responsible for the elastomer's protective effect.

Normal impact from a rigid projectile of radius, R and mass, M_i is considered. The projectile displaces a vertical distance, x_i into an elastomer layer atop a rigid concrete half space. The design variables are taken to be the projectile impact velocity, V_0 and the properties of the elastomer layer, namely, the thickness, h_e and modulus, E_e.

For an incompressible (*i.e.* Poisson's ratio, $\nu = 0.5$) Neo-Hookean material, the principal stretches are related by $\lambda_1 \lambda_2 \lambda_3 = 1$. And, the strain energy per unit (undeformed) volume is given by:

$$U = \frac{E_e}{6} (\lambda_1^2 + \lambda_2^2 + \lambda_3^2 - 3) \tag{7.1}$$

Note that a simpler strain energy potential is employed in the analytical model

compared to the FE model of the spray-on elastomer coating. This is a reasonable approximation, given the simplified kinematics in the analytical model.

If the elastomer is assumed incompressible, then the principal Cauchy stresses, σ_i are related to U by [187]:

$$\sigma_i = -\alpha + \lambda_i \frac{\partial U}{\partial \lambda_i} \tag{7.2}$$

where α is an unknown scalar (interpreted as any applied hydrostatic pressure).

Since the deformation of the polymer layer under the indenter is complex, particularly in the vicinity of the corner (see Fig. 7.2), simplifying assumptions are required to progress with the analytical model. In the following, it is assumed that in all cases, the deformed material instantaneously under the indenter is in a state of uniaxial compression. This implies that there is no effect of friction at the sliding interfaces, and no constraining effect of the polymer sheet in the vicinity of the indenter. Taking $\lambda_1 = \lambda = 1 - x_i/h_e$; $\lambda_2 = \lambda_3 = 1/\sqrt{\lambda}$; $\alpha = 0$, then the contact pressure under the projectile:

$$p = -\sigma_1 = -\lambda_i \frac{\partial U}{\partial \lambda_i} = -\frac{E_e}{6}\Big(2\,\lambda - \frac{2}{\lambda^2}\Big)\,\lambda \tag{7.3}$$

It therefore remains to relate the magnitude of λ to the projectile impact velocity.

This is achieved by equating the kinetic energy of the projectile to the maximum strain energy in the polymer (*i.e.* neglecting other sources of dissipation). To achieve this, the total strain energy in the polymer, $W(\lambda)$, is decomposed into two terms:

$$W(\lambda) = W_0(\lambda) + W_p(\lambda) \tag{7.4}$$

where $W_0(\lambda)$ is the strain energy in the material instantaneously under the projectile and $W_p(\lambda)$ is the strain energy in a perimeter zone in the vicinity of the projectile.

Considering a projectile of mass, M_i, impacting the elastomer with an initial velocity, V_0, applying conservation of energy for a maximum polymer stretch of, λ_{max}, gives:

$$\frac{M_i\,V_0^2}{2} = W(\lambda_{max}) \tag{7.5}$$

Throughout, to simplify the analysis, we assume that the presence of a perimeter strain energy does not alter the stress state under the indenter. (An alternative strategy, not pursued here, would be to account for the perimeter deformation through a constraining pressure, and hence the unknown constant, α in Eq. 7.2).

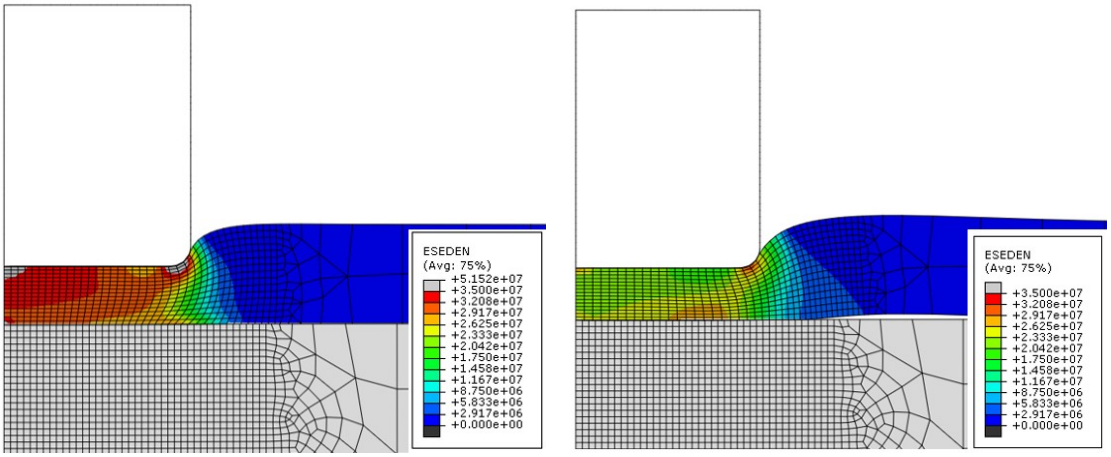

(a) Friction with coefficient, $\mu = 0.8$ (b) Frictionless

Figure 7.2: The elastic strain energy density (ESEDEN in ABAQUS notation) predicted by the FE model, at the instance of maximum projectile penetration depth, for a projectile impact velocity of $50\,\mathrm{m\,s^{-1}}$. Two variations on the FE model are considered: (a) frictional contact at the concrete/elastomer interface with a coefficient, $\mu = 0.8$ and (b) frictionless contact at the concrete/elastomer interface.

Examination of the FE results in Fig. 7.2 shows that the deformation in this perimeter zone is complex. Two models for the perimeter energy, $W_p(\lambda)$, are thus considered.

7.3.1 *Model (i)*

The simplest model is to assume that the perimeter energy is zero *i.e.* $W_p(\lambda) = 0$ in Eq. 7.4. The work done in deforming the polymer instantaneously under the projectile, as a function of stretch, $W_0(\lambda)$, is therefore given by:

$$W(\lambda) = W_0(\lambda) = -\pi\, R^2\, h_e \int_1^{\lambda} p(\lambda)\, d\lambda = \frac{\pi\, R^2\, h_e\, E_e}{3}\left(\frac{\lambda^3}{3} - \ln(\lambda) - \frac{1}{3}\right) \qquad (7.6)$$

Substituting into Eq. 7.5 will represent a lower bound on the energy absorbed by the coating.

7.3.2 *Model (ii)*

Alternatively, it can be assumed that the deformation in the perimeter zone matches that under the projectile (*i.e.* $\lambda_1 = \lambda$; $\lambda_2 = \lambda_3 = 1/\sqrt{\lambda}$). And so;

$$W(\lambda) = W_0(\lambda) + W_p(\lambda) = \pi\, R^2 h_e\, U(\lambda) = \frac{\pi\, R^2\, h_e\, E_e}{6}\left(\lambda^2 + \frac{2}{\lambda} - 3\right) \tag{7.7}$$

Substituting from Eq. 7.6 for $W_0(\lambda)$, the energy in the perimeter zone may be calculated:

$$W_p(\lambda) = \frac{\pi\, R^2\, h_e\, E_e}{3}\left(\frac{\lambda^2}{2} + \frac{1}{\lambda} - \frac{\lambda^3}{3} + \ln(\lambda) - \frac{7}{6}\right) \tag{7.8}$$

This would represent an upper bound on the perimeter energy. However, considering the FE results in Fig. 7.2, it is apparent that *Model (ii)* would significantly overpredict the deformation in the perimeter zone. This is particularly the case as x_i tends to h_e, as *Model (ii)* would give a perimeter energy (and perimeter radius) that tends to infinity.

7.3.3 Refined *Model (ii)*

Model (ii) can be refined by using a more general power law form of the strain energy in the perimeter zone:

$$W_p(\lambda) = \frac{\pi\, R^2\, h_e\, E_e}{3}\left(a\,(1-\lambda)^b\right) \tag{7.9}$$

For the choice of parameters, $a = 13/2$ and $b = 5$, Eq. 7.9 matches Eq. 7.8 reasonably well up to $\lambda \approx 0.2$, but tends to a finite perimeter energy for large projectile displacements (Fig. 7.3).

This can be interpreted as a capped upper bound on the perimeter energy. Substituting Eqs 7.6 and 7.9 into Eq. 7.4, and then Eq. 7.5, yields the energy balance for impact from a projectile.

In the subsequent analysis, this refined version of *Model (ii)* is used.

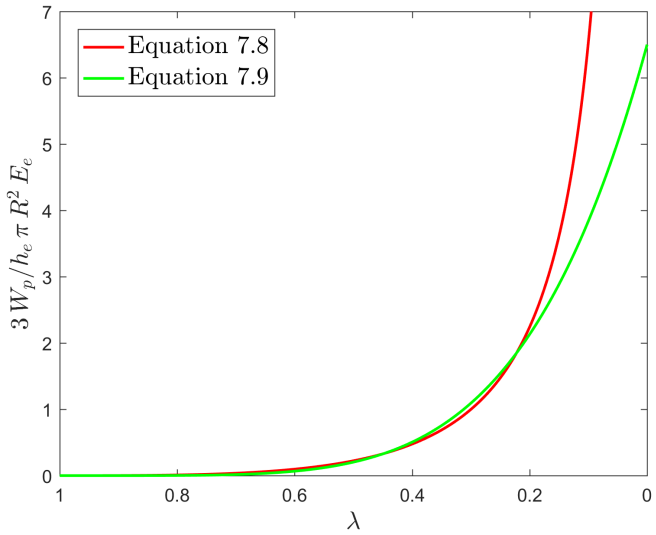

Figure 7.3: Analytical estimations of the strain energy in the perimeter zone according to Eqs 7.8 and 7.9, with $a = 13/2$ and $b = 5$.

7.3.4 Discussion: model applicability

It is noted that the proposed analytical model, and the underlying assumptions, make it applicable under the following conditions:

- The concrete target is large with respect to the indenter, and has a large modulus with respect to the polymer coating, so that it can be considered effectively a rigid half space.
- The impact velocities are sufficiently low with respect to the elastic wave speed in the polymer such that wave propagation effects can be neglected.
- The stiffness and strength of the projectile are high with respect to the polymer stiffness, so that it can be considered effectively rigid.
- The polymer layer thickness, h_e is sufficiently small with respect to the indenter radius so that the stress state under the indenter can be considered uniform through the polymer thickness.
- Viscous dissipation effects in the polymer are negligible. However, for realistic polymer coatings, and for the range of strain rates considered here, viscous effects have been shown to be present (for example, in Chapters 3 and 5). Thus, it must be noted that in neglecting viscous effects in order to keep the analytical model practical, the model will underestimate energy dissipation in the coating.

7.4 Critical impact velocities

Having derived relationships between the impact velocity, polymer deformation and contact pressure under the projectile, the next step is to determine critical values for failure of the target.

7.4.1 Concrete failure, $p = p_{crit}$

Hawkins [188] developed analytical expressions for the bearing strength of concrete members loaded through rigid plates. The study considered the case of concentric loadings *i.e.* cubes loaded through a central square plate or cylinders loaded through a central circular plate which is assumed to be analogous to the present case of interest. A failure model, based upon observations from a large number of experimental tests is proposed. It assumes that for collapse, a limiting shearing stress develops on the surface of a failure cone directly under the indenter. The limiting stress on the failure plane can be described using the familiar Mohr-Coulomb (MC) failure criterion:

$$\tau = \tau_0 + \sigma \, \tan\psi \tag{7.10}$$

where τ is the shearing resistance on the failure plane, σ is the pressure normal to the failure plane, τ_0 is the shear strength at zero σ on the failure plane and ψ is the angle of internal friction. If the concrete compressive strength, σ_{cu} and tensile strength, σ_{to} are known; then ψ and τ_0 can be calculated from the geometry of the MC criterion. This leads to:

$$\frac{\sigma_{cu}}{\sigma_{to}} = \frac{1 + \sin\psi}{1 - \sin\psi} \tag{7.11}$$

$$\tau_0 = \frac{\sigma_{to}}{2}\left(\frac{1}{\cos\psi} + \tan\psi\right) \tag{7.12}$$

Hawkins' expression for the bearing strength, q is given by:

$$\frac{q}{\sigma_{ck}} = 1 + \frac{K}{\sqrt{\sigma_{ck}}}(\sqrt{A} - 1) \qquad for\, A < 40 \tag{7.13}$$

where σ_{ck} is the concrete cylinder strength which is $\approx 0.8\,\sigma_{cu}$. A is the ratio of the *effective* unloaded area to the loaded area. K is a constant which depends upon the characteristics of the concrete:

$$K = \frac{\sigma_{to}}{\sqrt{\sigma_{ck}}} \cot^2 \alpha \tag{7.14}$$

where $\alpha = 45° - \psi/2$.

Based on extensive comparisons with experimental tests, Hawkins recommends that the factor K can be taken as $50\,(\mathrm{lb/in^2})^{1/2}$ which equates to approximately $4.15\,(\mathrm{MPa})^{1/2}$. For the geometry involved in this study, this gives a bearing strength estimate of 101 MPa.

However, calculating K for the concrete designed in Chapter 5, assuming $\sigma_{cu} = 47\,\mathrm{MPa}$ and $\sigma_{to} = 5\,\mathrm{MPa}$, then $K = 7.67\,(\mathrm{MPa})^{1/2}$. Assuming an axisymmetric concrete domain of radius 50 mm, concentrically loaded by an indenter of radius 14.25 mm, this leads to a bearing strength estimate of 160 MPa which is in very close agreement with that measured in the quasi-static indentation experiments on uncoated concrete cubes, described in Section 5.4.1 and illustrated in Fig. 7.4.

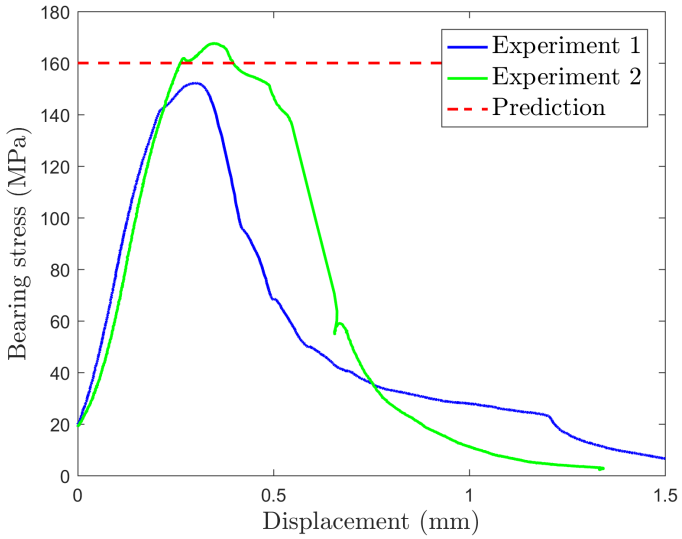

Figure 7.4: Bearing stress measured in the quasi-static indentation tests performed on two apparently identical concrete cubes in Section 5.4.1. Also plotted is Hawkins' prediction of the bearing strength of the concrete specimen [188].

The analysis proceeds by assuming that the critical contact pressure to cause concrete failure, p_{crit}, is equivalent to Hawkins' estimate of the bearing strength, $q = 160\,\mathrm{MPa}$.

From Eq. 7.3, the stretch in the polymer is related to the contact pressure, p by:

$$\lambda^3 + \frac{3\,p\,\lambda}{E_e} - 1 = 0 \tag{7.15}$$

Solving Eq. 7.15 for λ and setting $p = p_{crit}$ yields an expression for λ as a function

of p_{crit} and E_e. Substituting this for λ_{max} in Eq. 7.5 yields the energy balance at concrete failure. The *Model (i)* and *Model (ii)* predictions are derived by altering the assumptions about the elastic strain energy distribution in the polymer, discussed previously in Sections 7.3.1 and 7.3.3, respectively.

7.4.2 Elastomer failure

Of primary concern for coating design is to delay the point at which the concrete substrate fails. However, it is necessary to also estimate the conditions under which polymer failure might occur before concrete failure, as the response of the coated target is likely to change under those conditions. Setting $\lambda_{max} = \lambda_{crit}$ (*i.e.* the critical stretch to cause elastomer failure) in Eq. 7.5 yields the energy balance at elastomer failure. Once more, the *Model (i)* and *Model (ii)* assumptions are discussed in Sections 7.3.1 and 7.3.3, respectively.

The boundary between the *concrete failure* regime and the *elastomer failure* regime occurs when simultaneously, $p = p_{crit}$ and $\lambda_{max} = \lambda_{crit}$. Thus, from Eq. 7.3, the following relationship applies:

$$p_{crit} = \frac{E_e}{3}\left(\frac{1}{\lambda_{crit}} - \lambda_{crit}^2\right) \tag{7.16}$$

Setting $\lambda_{crit} = 0.1$ (*i.e.* $x_i = 0.9\,h_e$, indicative of the deformations at failure observed in experimental shear punch tests in Section 3.2.2), the model predicts that for $E_e < 0.3\,p_{crit}$, elastomer failure occurs before concrete failure (*i.e.* at a lower projectile impact speed, V_0). For $E_e > 0.3\,p_{crit}$, the model predicts a *concrete fails first* regime.

7.5 Design maps

For a projectile of radius, $R = 14.25\,\text{mm}$ and mass, $M_i = 0.1\,\text{kg}$, and assuming $p_{crit} = 160\,\text{MPa}$ and $\lambda_{crit} = 0.1$, the design maps illustrated in Fig. 7.5 are plotted. These maps plot contours of the critical projectile impact velocity for failure, V_{crit}. The solid lines indicate the model predictions for the critical impact velocity for concrete failure, which is of most interest to the designer. The predictions for elastomer failure are overlayed as dotted lines.

The boundary between the *elastomer fails first* and *concrete fails first* regimes occurs at a small strain elastomer modulus, $E_e = 0.3\,p_{crit} = 48\,\text{MPa}$. Note that this regime change occurs at a value of E_e within a realistic range of elastomer moduli, representative of typical spray application elastomers. Plotting a marker, ◇, at the

location which corresponds to the elastomer coating tested in Chapter 5, it is noted that the coated concrete target is predicted to fall within the *concrete fails first* regime.

First, the *Model (i)* map in Fig. 7.5a is examined. Both the elastomer and concrete failure contours exhibit a similar shape. For very low polymer stiffnesses ($E_e < 5\,\text{MPa}$), the critical impact velocity becomes very sensitive to the polymer modulus. Consequently, very thick coatings ($h_e > 10\,\text{mm}$) are required to achieve a critical impact velocity in excess of $20\,\text{m}\,\text{s}^{-1}$.

The sensitivity of V_{crit} at concrete failure to the polymer stiffness diminishes rapidly above the regime boundary at $E_e = 48\,\text{MPa}$. This suggests that when designing within the *concrete fails first* regime, the critical design parameter is the polymer thickness, h_e. For the *Model (i)* case, in this regime, V_{crit} can reach values of about $60 - 70\,\text{m}\,\text{s}^{-1}$ before the required coating thicknesses exceed 10 mm.

For the high speed gas gun tests performed in Chapter 5, $E_e = 80\,\text{MPa}$ (measured from Fig. 3.2) and h_e varied between $5-6\,\text{mm}$. Those tests predicted concrete failure for projectile impact velocities in the range $V_0 = 100 - 124\,\text{m}\,\text{s}^{-1}$. The marker, ⋄, corresponding to these tests on Fig. 7.5a shows that concrete failure is predicted for $V_0 \approx 50\,\text{m}\,\text{s}^{-1}$ which is considerably lower than that observed experimentally. Thus, the design map based on *Model (i)* appears rather conservative in terms of concrete failure predictions.

Next, the map based on *Model (ii)* is plotted in Fig. 7.5b. The regime boundary, at $E_e = 48\,\text{MPa}$ remains unchanged and both the concrete and elastomer failure contours are of a similar shape to those derived for *Model (i)*. Once more, in the *elastomer fails first* regime, very soft polymers require very large coating thicknesses ($h_e > 10\,\text{mm}$) to sustain even very low impact velocities. Higher polymer stiffnesses are likely to be in the *concrete fails first* regime where the critical design parameter once more is the coating thickness. Upon closer examination of the concrete failure contours at higher impact speeds, for example, $V_{crit} = 75\,\text{m}\,\text{s}^{-1}$ and $100\,\text{m}\,\text{s}^{-1}$, there appears to be a particular value of the polymer modulus, E_e that minimises the coating thickness required. Taking $V_{crit} = 100\,\text{m}\,\text{s}^{-1}$ for example, it appears that a polymer stiffness of around $E_e = 90\,\text{MPa}$ is an optimum choice in terms of minimising the coating thickness required to prevent failure. It is noted however that there is only a weak sensitivity to polymer modulus in this regime.

The critical velocities predicted using *Model (ii)* differ significantly from those predicted by *Model (i)*. For a given E_e, h_e combination, the predicted V_{crit} is increased by almost a factor of two. The experimental gas gun tests (from Chapter 5), represented by the marker, ⋄, on Fig. 7.5b measured concrete failure for projectile impact

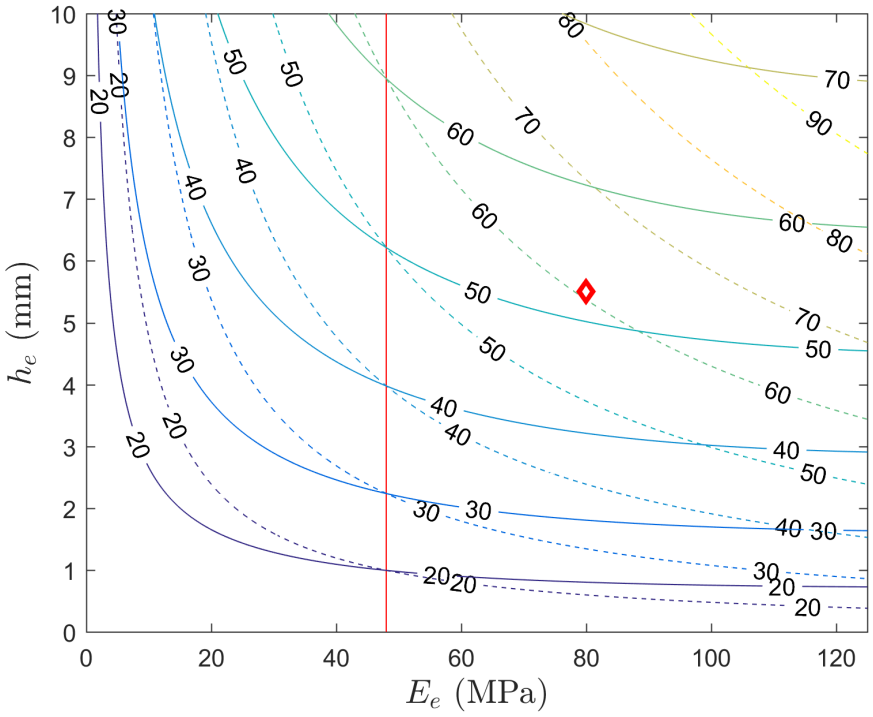

(a) *Model (i)*

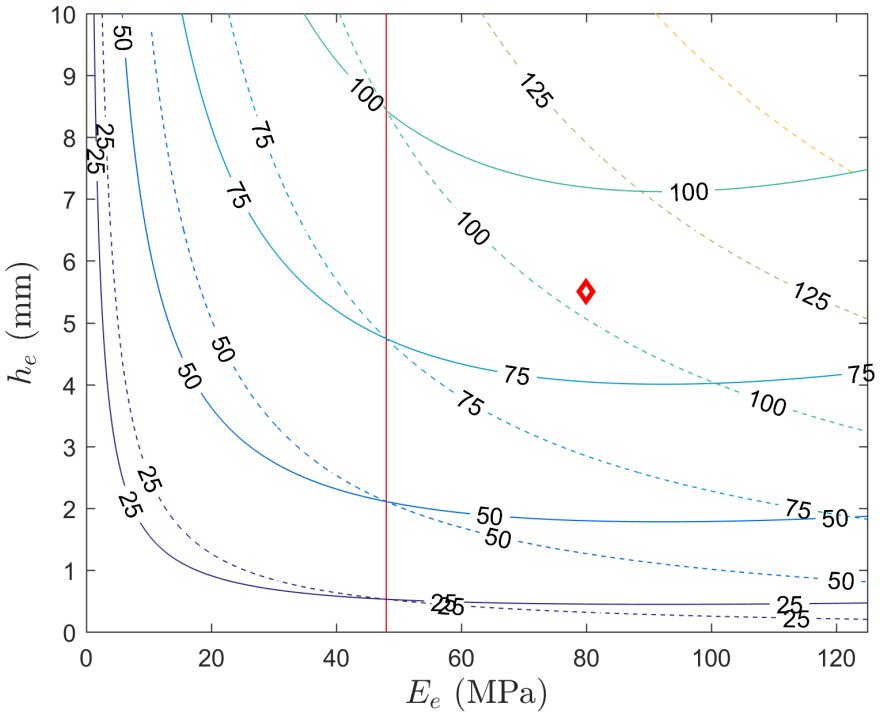

(b) *Model (ii)*

Figure 7.5: (a) *Model (i)* and (b) *Model (ii)* contours of V_{crit}. Solid lines indicate concrete failure and dotted lines indicate elastomer failure. To the left of the vertical red boundary, the model predicts elastomer failure before concrete failure; to the right, the model predicts concrete failure before elastomer failure. ◇ indicates the experimental test performed in Chapter 5 and referred to in the text.

velocities in the range $V_0 = 100 - 124\,\mathrm{m\,s^{-1}}$. The *Model (ii)* analytical approach predicts failure for an impact velocity, *c.* $90\,\mathrm{m\,s^{-1}}$ which agrees well with the experiments. The discrepancy is likely due to the omission of viscous dissipation in the analytical model, as discussed in Section 7.3.4 which would serve to push the critical velocities for failure even higher. Nevertheless, the *Model (ii)* analysis appears to provide a good match to the experiments and in the following section, the validity of the models are assessed in more detail.

7.6 Validation cases

This section compares the analytical predictions of concrete failure with the results of the FE models and experiments (from Fig. 7.1). Figure 7.6 plots the *Model (i)* and *Model (ii)* analytical predictions for an elastomer coating with modulus, $E_e = 80\,\mathrm{MPa}$, subjected to impact from a projectile of mass, $M_i = 0.1\,\mathrm{kg}$ and radius, $R = 14.25\,\mathrm{mm}$. The model is compared with the experimental results, and the finite element analysis (the latter considering alternative friction conditions at the interfaces, as described subsequently).

Comparison with the experimental results is considered in Fig. 7.6a. The *Model (ii)* estimate provides the closest match with experimental results, though it provides a conservative prediction of the critical velocity to cause concrete failure. As discussed previously, viscous dissipation in the elastomer layer is omitted which, if included would serve to increase the predicted critical velocities. Furthermore, concrete strain rate dependence has been neglected which again, would serve to boost the concrete strength, elevating p_{crit} and thus the critical impact velocities for failure. Nevertheless, the analytical estimates, in particular the *Model (ii)* approach, give a good match to the experimental results.

Next, the analytical and FE predictions of concrete failure are compared. As described in Section 7.2, two variations of the FE model are considered: one with frictional contact at the elastomer/concrete interface and one with frictionless conditions at this interface. Quasi-static tests in Section 5.4.2 suggested best agreement was achieved with frictional contact whereas Fig. 7.1 shows that frictionless conditions bring the FE predictions more into line with the impact experiments. It can therefore be deduced that the rate of loading has an effect on the interface frictional conditions. For the FEA case with interface friction, in Fig. 7.6b, the true boundary between concrete failure/no failure occurs between the analytically derived *Model (i)* and *Model (ii)* predictions. Considering the FEA case without interface friction, in Fig. 7.6c (which matched the experiments well), the *Model (i)* prediction is overly conservative. Instead, the *Model (ii)* estimate provides a very close match to the

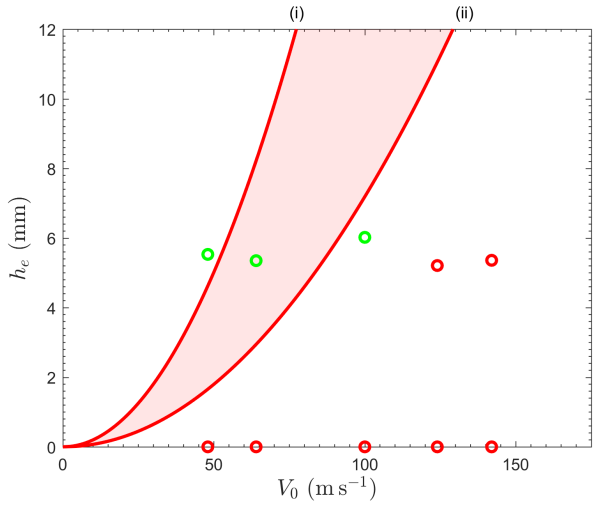

(a) Analytical predictions *vs* experiments

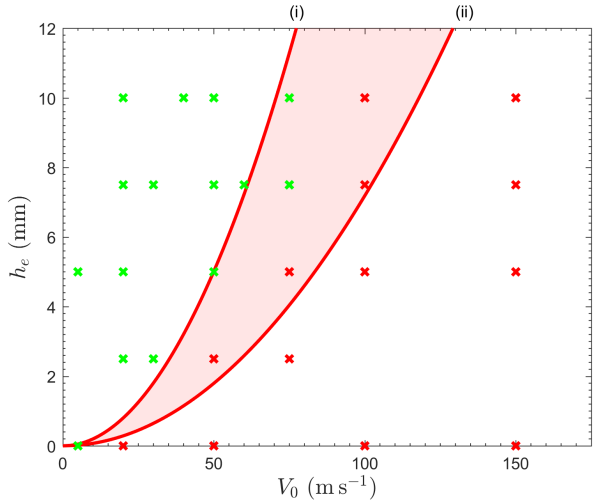

(b) Analytical predictions *vs* FE results (with friction)

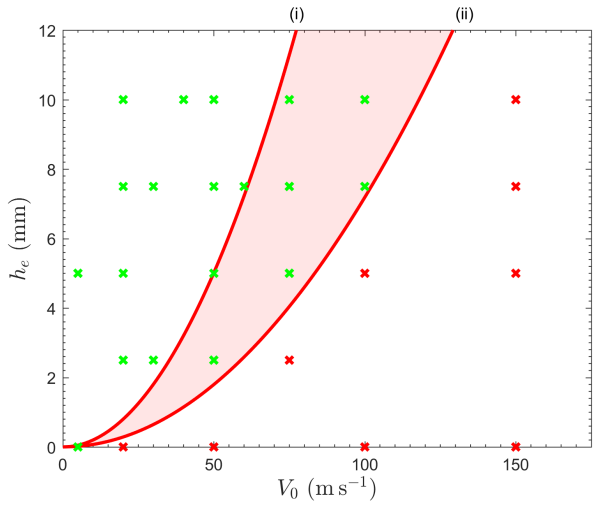

(c) Analytical predictions *vs* FE results (frictionless)

Figure 7.6: Comparing *Model (i)* and *Model (ii)* analytical predictions with (a) experimental observations, (b) FE results with frictional contact (coefficient, $\mu = 0.8$) at the elastomer/concrete interface and (c) FE results with frictionless contact at the elastomer/concrete interface. Legend: $\times$ represents FE predictions and $\circ$ represents experimental observations; green indicates intact concrete and red indicates damaged concrete.

failure boundary.

In summary, the analytical models perform very well in terms of predicting the boundary between concrete failure and no failure, when compared to experiments and FEA predictions. The *Model (i)* approach provides a conservative estimate of the critical projectile velocities for failure whereas the *Model (ii)* approach predicts the failure boundary with good accuracy. Further refinement of the analytical model to account for viscous dissipation effects in the polymer would likely bring the predictions even closer to the experimental and FE results.

7.7 Conclusions

Analytical models are developed in order to predict the onset of failure for an elastomer-coated concrete target subjected to blunt projectile impact. The model is validated against experimental observations and FEA predictions (based on work in Chapters 5 and 6). Design maps are produced, predicting the critical projectile impact velocity for failure, V_{crit} based on two design variables — the coating thickness, h_e and the elastomer modulus, E_e. The following conclusions are established:

- The analytical models are able to accurately predict the trends in critical projectile impact velocities as a function of polymer modulus and thickness, as shown by experiment and finite element analysis.
- The analytical predictions for critical projectile impact velocity are bounded by altering assumptions related to the distribution of elastic strain energy in the polymer.
- The *Model (i)* analytical estimates appear overly conservative, underestimating the critical failure velocities by approximately a factor of two when compared with experiments and FEA predictions.
- The *Model (ii)* analytical estimates are in closer agreement with experimental results and in particular, FEA predictions obtained by assuming frictionless contact at the elastomer/concrete interface.
- Over a realistic range of elastomer moduli, representative of typical spray application polymers, a regime change is predicted in the impact response of elastomer-coated concrete. It is predicted that the regime boundary depends only on E_e, and not h_e. For $E_e < 50\,\text{MPa}$, it is predicted that the elastomer will fail first. For $E_e > 50\,\text{MPa}$, the concrete is predicted to fail first.
- The analytical models also reveal key parameter sensitivities underlying protective coatings for concrete. In the polymer fails first regime, there is a much

higher sensitivity to polymer modulus, E_e, compared to polymer thickness, h_e. In the concrete fails first regime, the critical velocity is most sensitive to the polymer thickness, and relatively insensitive to the modulus.

CHAPTER 8

Conclusions and future work

The objectives of this thesis were threefold, as set out in Chapter 1: (i) to establish the influence of a typical spray-on elastomer coating on the blast and impact response of concrete structural elements; (ii) to understand the key mechanisms at play that give rise to any protective benefit identified; (iii) to develop design guidelines to inform on effective implementation of this retrofit solution. These objectives were addressed in Chapters 3 to 7 and the conclusions drawn during this investigation are summarised as follows.

8.1 Conclusions

8.1.1 Blast response

Chapter 3 numerically studied the fluid-structure interaction (FSI) effect experienced by elastomer-coated concrete subjected to blast loading in air.

- A 1D FSI analysis suggested that an elastomer coating (applied to either face of a concrete structure) had a negligible influence on the *total* imparted momentum. However, due to momentum sharing, the impulse imparted to the *concrete* was reduced in the coated configuration.
- In 2D, permanent displacements of a concrete slab were marginally reduced with the addition of a coating. Thus, it was postulated that the elastomer contributes a small, beneficial mechanical effect.
- The need for a fully coupled (CEL) approach to model the blast-structure interaction was interrogated. For a wide range of cases, the results suggested that using a purely Lagrangian approach, in which a pressure-time history is directly applied to the structure thereby neglecting full representation of FSI effects, was suffi-

cient to capture the deflection behaviour of elastomer-coated concrete structures. It was shown that the significance of the error associated with this simplification depends on the blast intensity under consideration.

Chapter 4 employed the simplified Lagrangian numerical approach, validated in Chapter 3 to model elastomer-coated, reinforced concrete beams subjected to varying intensities of simulated blast loading. Analytical techniques were used to understand the predicted sensitivity to the elastomer coating in each regime.

- By varying the loading intensity, three response regimes were identified.
- Regimes 1 and 2 were characterised by elastic and elastic-plastic behaviour, respectively. Good agreement was achieved between numerical predictions and simple analytical models for beam deflections. The beam was relatively insensitive to the elastomer coating in these regimes.
- Regime 3 behaviour was observed at higher load intensities, where the concrete exhibited severe damage. The beam experienced continued plastic deformation and damage and thus, a critical displacement was defined to identify the time at which the beam failed. A greater sensitivity to the presence of a polymer coating was identified in this regime.
- Insight was gained by interrogating the Regime 2 - 3 boundary where FE results indicated a significant beneficial coating effect, with a reduction in permanent beam deflections, of up to 48% for coating on the back (non-blast-receiving) face.
- At the highest loading intensities, a shift in failure mechanism was observed to one dominated by transverse shear at the supports. An analytical model predicted a substantial coating benefit in protecting against this failure mechanism due to the additional shear capacity and ductility contributed by the coating.

8.1.2 Impact response

Chapter 5 considered the impact response of elastomer-coated concrete. A series of quasi-static indentation and dynamic impact experiments were performed using a 0.1 kg blunt, steel projectile over the velocity range, $c.\,45 - 150\,\mathrm{m\,s^{-1}}$.

- The coating displayed a significant protective capability over the full range of velocities considered.
- The coating remained intact until impacted at a velocity of $c.\,120\,\mathrm{m\,s^{-1}}$ when it failed by a ductile, tearing mechanism, forming a plug which underwent large elastic contraction after projectile penetration.

- A numerical model of the impact indentation of uncoated and coated concrete targets was developed and validated against both quasi-static and dynamic experiments. The model was deemed an appropriate analysis tool at early time steps, before the concrete underwent severe damage and before maximum projectile penetration in the coated cases.
- Both numerical model predictions and high speed photography measurements indicated that the elastomer significantly reduced projectile decelerations.

Building upon these findings and using the numerical model developed in Chapter 5, **Chapter 6** sought to determine the elastomer's influence on concrete damage initiation during impact indentation. Further, the mechanisms of protection were interrogated.

- Two distinct damage initiation mechanisms were observed: Mechanism 1, characterised by severe damage initiation under the corner of the indenter over early timescales and Mechanism 2, characterised by more diffuse, sub-surface damage that develops over longer timescales.
- The addition of the coating served to (i) increase the impact speed required to initiate damage and (ii) shift the damage initiation from Mechanism 1 to Mechanism 2.
- The elastomer achieved its impact mitigating effect via two protective mechanisms: a *temporal effect* (the magnitude of the peak projectile acceleration was reduced and the duration of contact between the projectile and target was increased) and; a *spatial effect* (a more uniform contact pressure and stress triaxiality distribution was produced under the indenter, removing stress concentrations at the corner).
- The *temporal effect* is essentially a 1D phenomenon but the *spatial effect* is only observed when there is indentation. Thus, to achieve both protective effects, the indentation of an elastomer coating is required.

In **Chapter 7**, new analytical models were proposed to predict the onset of failure for an elastomer-coated concrete target subjected to blunt projectile impact. Drawing together the experimental and numerical findings from Chapters 5 and 6, the models were used to interrogate the key parameter sensitivities underlying protective coatings for concrete.

- The analytical models were able to accurately predict trends in critical projectile impact velocities as a function of polymer modulus and thickness, as shown by experiment and finite element analysis.

- Over a realistic range of elastomer moduli, representative of typical spray-on elastomer coatings, a regime change was identified. At lower elastomer moduli, $E_e < 50\,\text{MPa}$, it was predicted that the elastomer will fail first. For stiffer coatings, $E_e > 50\,\text{MPa}$, the concrete was predicted to fail first.
- Key parameter sensitivities were revealed: in the elastomer fails first regime, there was a much higher sensitivity to polymer modulus, E_e compared to polymer thickness, h_e. In the concrete fails first regime, the critical velocity was most sensitive to the polymer thickness, and relatively insensitive to the modulus.

In summary, through a combination of experimentation, numerical modelling and analytical techniques, this thesis has identified the blast and impact response regimes of elastomer-coated concrete. Further, the mechanisms of protection contributed by the elastomer coating have been established and the knowledge gained used to deliver design recommendations for this retrofit solution. It is found that while commercially available coatings are effective in some response regimes (for example, where there is significant local impact or severe blast-induced concrete damage), they offer limited benefit in others (for example, during fluid-structure interaction, and during dynamic flexure of slabs). This work has identified significant scope for future work which will be discussed in the following section.

8.2 Future Work

With some of the immediate next steps for future work already addressed throughout the thesis, this section presents some broader recommendations for further study.

Interrogating homogenised concrete constitutive models

One of the prevailing challenges with this investigation has been accurately modelling the blast and impact response of concrete using Explicit finite element analysis. Although it is commonplace in the literature to use a continuum damage mechanics approach to capture concrete behaviour under extreme loads, a number of limitations of this approach were encountered throughout this study. In Chapter 4, for example, the numerical model struggled to predict global failure of a concrete beam when exposed to a high intensity blast. Severe concrete damage, also encountered in Chapter 5 when modelling concrete's response to local impact, induced mesh sensitivity and thus, these simulations were halted early to avoid relying upon unstable solutions. A further limitation of homogenised concrete constitutive models is that they fail to capture concrete microstructural effects, which may become significant when modelling impact or indentation loading. It is recommended that detailed

interrogation of these continuum approaches is performed, particularly in the context of modelling local indentation of concrete, where the projectile radius is of the order of or indeed, less than the maximum aggregate size. One alternative that has been proposed is using meshless methods; an extension from computational fluid dynamics to a structural context. These techniques have yielded some encouraging results and may present a way forward [80].

Response to combined loading

Combined loading refers to the consideration of a blast pressure pulse, in combination with fragmentation impact on a target structure. These events may occur simultaneously, or at a time offset, with the aim of capturing a more realistic version of the loading endured by a structure when a nearby explosive event takes place. Chapter 2 discussed the relatively limited literature surrounding combined loading effects. It has been reported that there is a "synergistic" effect, in which the damage caused by combined loading is more severe than that caused by adding the results of independent blast and fragment impacts [79]. This may be significant in the design of protective solutions for infrastructure. The work presented in this thesis shows that the protective benefit offered by an elastomer coating applied to a concrete substrate is highly dependent upon the loading and thus response regime of the structure. Thus, a greater understanding should be developed of how to model, or account for these combined loading effects. It is a complex, multi-physics problem, relying on capturing both local and global damage mechanisms to arrive at a prediction for overall structural behaviour (or failure). Experimental and numerical approaches (employing hydrocode software or meshless methods) have been pursued by a few researchers [78–80], but these techniques are computationally expensive and thus the challenge remains as to how to translate these findings into practical design guidance for industry.

Optimising retrofit solutions

Finally, this thesis has provided a fundamental basis for the optimisation of coating retrofits for concrete structural protection against blast and impact load events. It has been shown that commercially available elastomer coatings may be effective in some response regimes (for example, during local impact indentation) but offer limited benefit in others (for example, during fluid-structure interaction in air blast loading). This motivates a range of future studies that aim to answer the question — can we engineer a more effective retrofit solution? Hybrid solutions could be considered (such as a crushable layer, in combination with an elastomeric coating), designed to exploit mitigation effects across a range of structural response regimes.

Alternatively, concepts proven in other fields of research may be adapted for use in structural design. Chapter 2 discussed the idea of "tuning" stress waves from a blast or impact event, to match the characteristic damping frequency of a viscoelastic layer for optimal energy dissipation [13]. This has proven successful in the design of personal protective armour but could perhaps be exploited in the design of novel, polymer-based, multilayer structural armour solutions.

APPENDIX A

Supplementary information: Fluid-structure interactions for air blast loading of elastomer-coated concrete

A.1 Implementing the Concrete Damaged Plasticity model

Empirical relationships were employed to generate the curves required by ABAQUS/Explicit for the complete definition of the Concrete Damaged Plasticity (CDP) material model. The approach taken is similar to that presented in [189].

A.1.1 Defining compressive behaviour

To define the uniaxial compressive stress, σ_c *vs* inelastic strain, $\tilde{\epsilon}_c^{in}$ curve; the empirical relationships proposed by the 1990 CEB-FIP Model Code [84] are used. Figure A.1 illustrates a typical uniaxial compressive stress-strain curve for concrete where the first part of the curve, for $|\epsilon_c| < |\epsilon_{c,lim}|$ can be described using Eq. A.1 and the descending branch can be described using Eq. A.2 [84].

$$\sigma_c = -\frac{\frac{E_0}{E_s}\frac{\epsilon_c}{\epsilon_{c1}} - (\frac{\epsilon_c}{\epsilon_{c1}})^2}{1 + (\frac{E_0}{E_s} - 2)\frac{\epsilon_c}{\epsilon_{c1}}}\,\sigma_{cu} \qquad \text{for} \qquad |\epsilon_c| < |\epsilon_{c,lim}| \tag{A.1}$$

$$\sigma_c = -\left[\left(\frac{1}{\frac{\epsilon_{c,lim}}{\epsilon_{c1}}}\zeta - \frac{2}{(\frac{\epsilon_{c,lim}}{\epsilon_{c1}})^2}\right)\left(\frac{\epsilon_c}{\epsilon_{c1}}\right)^2 + \left(\frac{4}{\frac{\epsilon_{c,lim}}{\epsilon_{c1}}} - \zeta\right)\frac{\epsilon_c}{\epsilon_{c1}}\right]^{-1}\sigma_{cu} \qquad \text{for} \qquad |\epsilon_c| > |\epsilon_{c,lim}| \tag{A.2}$$

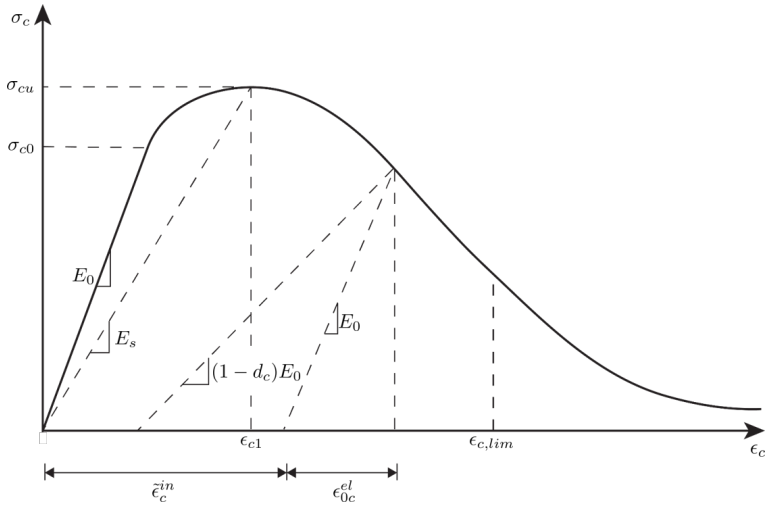

(a) Compressive behaviour

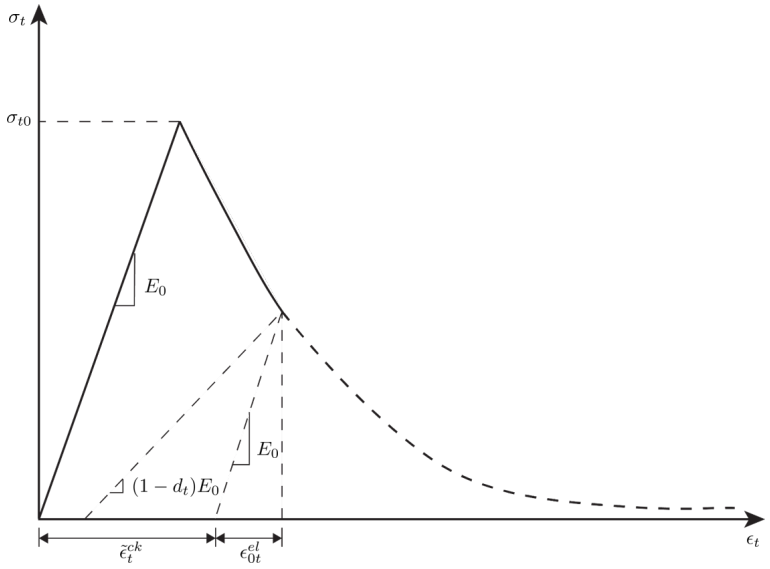

(b) Tensile behaviour

Figure A.1: Compressive and tensile behaviour definitions for the ABAQUS/Explicit Concrete Damaged Plasticity model. Parameters are defined in the text. Adapted from [27].

$$\text{where} \qquad \zeta = \frac{4\left[\left(\frac{\epsilon_{c,lim}}{\epsilon_{c1}}\right)^2\left(\frac{E_0}{E_s}-2\right)+2\frac{\epsilon_{c,lim}}{\epsilon_{c1}}-\frac{E_0}{E_s}\right]}{\left[\frac{\epsilon_{c,lim}}{\epsilon_{c1}}\left(\frac{E_0}{E_s}-2\right)+1\right]^2} \tag{A.3}$$

$$\text{and} \qquad E_0 = E_{c0}\left[\frac{\sigma_{cu}}{\sigma_{cu0}}\right]^{\frac{1}{3}} \tag{A.4}$$

where

σ_c is the compressive stress in MPa;

E_0 is the initial tangent modulus in MPa;

$E_{c0} = 2.15 \times 10^4$ MPa;

σ_{cu} is the peak compressive stress in MPa;

$\sigma_{cu0} = 10$ MPa;

ϵ_c is the compressive strain;

$\epsilon_{c1} = 0.0022$ is the strain corresponding to the peak compressive stress;

$E_s = \sigma_{cu}/0.0022$ is the secant modulus from the origin to the peak compressive stress in MPa;

$\epsilon_{c,lim}$ limits the applicability of Eq. A.1 and is calculated using Eq. A.5.

$$\frac{\epsilon_{c,lim}}{\epsilon_{c1}} = \frac{1}{2}\left(\frac{1}{2}\frac{E_0}{E_s}+1\right)+\left[\frac{1}{4}\left(\frac{1}{2}\frac{E_0}{E_s}+1\right)^2-\frac{1}{2}\right]^{1/2} \tag{A.5}$$

A.1.2 Defining tensile behaviour

There are two methods permitted by ABAQUS for defining the post-failure branch of the uniaxial, tensile stress-strain curve. Typically, tensile stress, σ_t is given as a function of cracking strain, $\tilde{\epsilon}_t^{ck}$ which is defined as the total tensile strain, ϵ_t minus the elastic strain corresponding to the undamaged material, ϵ_{0t}^{el}. This definition is illustrated in Fig. A.1 where $\epsilon_{0t}^{el} = \sigma_t/E_0$.

However, as noted in the ABAQUS User's Manual [27], in cases where the concrete has little or no reinforcement, choosing to define the post-failure behaviour in terms of cracking strain can introduce unreasonable mesh sensitivity. The Manual [27] suggests that it would be more reliable to specify post-failure tensile stress, σ_t as a function of cracking displacement, u_t^{ck}, based on the 1976 work of Hillerborg [190].

To achieve this, the relationship proposed by Hordijk [166] in his work on concrete fatigue is employed, given by Eq. A.6.

$$\frac{\sigma_t}{\sigma_{t0}} = \left[1 + \left(c_1 \frac{u_t^{ck}}{u_t^{crit}}\right)^3\right] \exp\left(-c_2 \frac{u_t^{ck}}{u_t^{crit}}\right) - \frac{u_t^{ck}}{u_t^{crit}} \left(1 + c_1^3\right) \exp(-c_2) \tag{A.6}$$

$$\text{where} \qquad u_t^{crit} = 7 \, \frac{G_F}{\sigma_{t0}} \quad \text{mm} \tag{A.7}$$

$$\text{and} \qquad G_F = G_{F0} \left(\frac{\sigma_{cu}}{\sigma_{cu0}}\right)^{0.7} \quad \text{N/mm} \tag{A.8}$$

where

u_t^{crit} is the critical crack opening displacement, beyond which the tensile stress is zero. This is calculated according to Eq. A.7 which is taken from the CEB-FIP code [84] and is based on a concrete with medium aggregate size of approximately 16 mm;

$c_1 = 3$ and $c_2 = 6.93$ are constants determined by Hordijk [166] based on deformation-controlled uniaxial tests on normal-weight concrete;

σ_{to} is the tensile strength in MPa;

G_F is the tensile fracture energy of concrete in opening mode in N/mm;

G_{F0} is the base value of fracture energy which depends on the maximum aggregate size. Assuming a maximum aggregate size of 16 mm, the CEB-FIP code [84] recommends a value of $G_{F0} = 0.03$ N/mm.

A.1.3 Defining damage parameters

The CDP model in ABAQUS/Explicit allows the user to define compressive and tensile damage parameters, d_c and d_t that quantify how the concrete elastic stiffness becomes degraded when unloaded from the softening branch of the uniaxial curves.

Compressive damage

For the compressive damage case, Birtel and Mark [167] propose the following relationship between the damage parameter, d_c and the compressive inelastic strain, $\tilde{\epsilon}_c^{in}$:

$$d_c = \frac{\tilde{\epsilon}_c^{in}\,(1-b_c)}{\tilde{\epsilon}_c^{in}\,(1-b_c)+\frac{\sigma_c}{E_o}} \qquad 0 \leq d_c \leq 1 \tag{A.9}$$

Through comparison with experimental data, Birtel and Mark determined that the best fit was achieved using $b_c = 0.7$ in Eq. A.9 [167]. Thus, a curve can be obtained for d_c as a function of $\tilde{\epsilon}_c^{in}$.

Tensile damage

An equation of the same form as Eq. A.9 [167] can also be used to define a curve for the tensile damage parameter, d_t in terms of cracking displacement, u_t^{ck} and fitting parameter, b_t. Best fit with experimental data was achieved for $b_t = 0.1$ [167].

A.1.4 Yield surface

The CDP model in ABAQUS/Explicit employs the yield function proposed by Lubliner *et al.* [168] and includes the modifications suggested by Lee and Fenves [169]. The yield surface is most easily visualised when plotted in the deviatoric plane (presented in Fig. A.2). The shape of the yield surface is determined by K_c, a user-defined ratio based on the second stress invariants which must satisfy the condition $0.5 < K_c < 1.0$. The ABAQUS/Explicit default value is 2/3 ($K_c = 1$ reproduces the well-known von Mises yield surface).

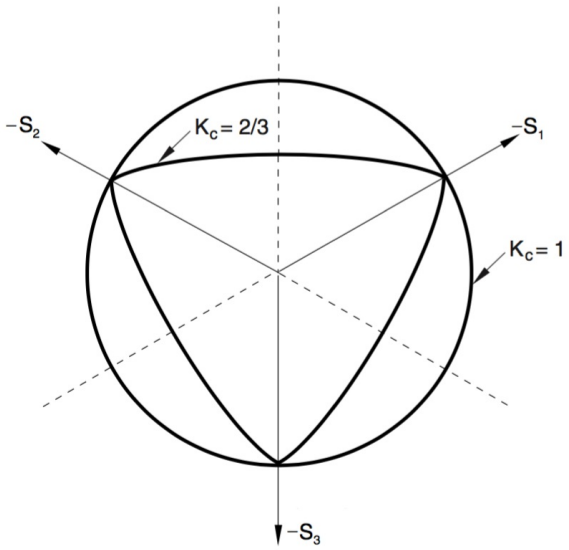

Figure A.2: Yield surfaces plotted in the deviatoric principal stress plane (the π plane), corresponding to different values of K_c. Reproduced from the ABAQUS User's Manual [27].

A.1.5 Plastic flow rule

The flow rule specifies the relationship between the yield surface and the uniaxial stress-strain relationships. Non-associated plastic flow is assumed by the CDP model where the flow potential, G takes the form of the Drucker-Prager hyperbolic function, given by Eq. A.10 and illustrated in Fig. A.3 [27]. The plastic flow, $\dot{\epsilon}^{pl}$ develops along the normal to the plastic flow potential, G and not to the yield surface *i.e.* non-associated flow.

$$G = \sqrt{(\epsilon\, \sigma_{t0}\, \tan(\psi))^2 + \bar{q}^2} - \bar{p} \tan\psi \tag{A.10}$$

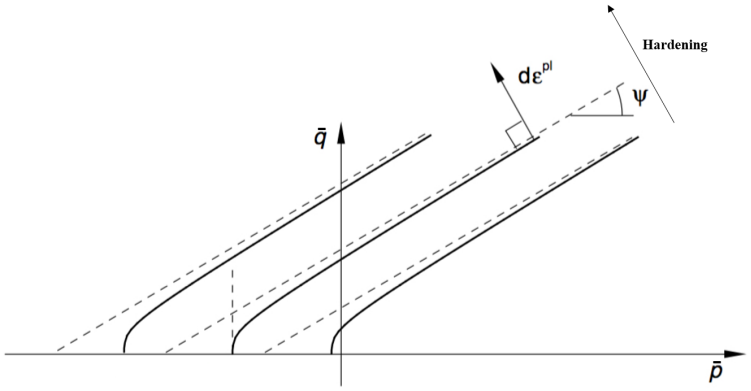

Figure A.3: Family of Drucker-Prager hyperbolic flow potentials, plotted in the $\bar{p}$ (hydrostatic pressure) - $\bar{q}$ (Mises equivalent stress) plane (meridional plane). Figure shows how an increment of plastic strain, $d\epsilon^{pl}$ develops normal to the plastic flow potential, G. Adapted from the ABAQUS User's Manual [27].

Table A.1 presents the parameters required to fully define the yield surface and flow rule. Values used for ϵ, f_{b0}/f_{c0}, K_c and the viscosity parameter are the default parameters suggested by ABAQUS [27]. ϵ is the eccentricity parameter which defines the rate at which the flow potential approaches the asymptote. f_{b0}/f_{co} is the ratio of the initial equibiaxial compressive yield stress to initial compressive yield stress. ψ is the dilation angle measured in the $\bar{p} - \bar{q}$ (hydrostatic pressure-Mises equivalent stress) plane at high confining pressure. The dilation angle, ψ is chosen to be 36° to be consistent with that presented in the ABAQUS Example Problems Manual [191] for the case of a seismic analysis of a concrete gravity dam. This is verified by Malm [192] who studied reinforced concrete beams subject to four-point bending and found numerical results best agreed with experiment for dilation angles between 30° and 40°. Other authors in the literature have reached similar conclusions [193].

Table A.1: User-defined parameters required to define the yield surface and flow rule in the Concrete Damaged Plasticity model in ABAQUS/Explicit.

Dilation angle, ψ	Eccentricity, ϵ	f_{b0}/f_{c0}	K_c	viscosity parameter
36°	0.1	1.16	0.667	0

A.2 Validating the Concrete Damaged Plasticity model

To validate the developed CDP model's predictive capabilities, model predictions are compared with two sets of published experimental results on the blast testing of reinforced concrete slabs [50, 194]. Loading was implemented via the CONWEP option in ABAQUS/Explicit [26], specifying the mass of TNT explosive charge and stand-off distances to match the experiments. While this load application does not capture the full details of the FSI or "close-in" blast effects, it enables broad assessment of the model to first order under realistic conditions.

The concrete and reinforcing steel geometries are modelled according to the literature reference cases [50, 194] and meshed with 5 mm, 3D solid continuum elements. The steel material model is chosen as the Johnson-Cook plasticity model with values based on typical steel 4340 as presented by Wang *et al.* [50]. The reinforcing steel was modelled with a yield strength of 600 MPa, a Young's Modulus of 200 GPa, a Poisson's ratio of 0.3 and the density was specified as $7830\,\mathrm{kg\,m^{-3}}$.

For the concrete; the Concrete Damaged Plasticity model is implemented as described previously. In both cases, the concrete density was chosen as $2550\,\mathrm{kg\,m^{-3}}$, with a Young's Modulus, $E_0 = 28.3\,\mathrm{GPa}$ and a Poisson's ratio of 0.2. For Case A [50]; the concrete has a compressive strength, $\sigma_{cu} = 39.5\,\mathrm{MPa}$ and a tensile strength, $\sigma_{to} = 4.2\,\mathrm{MPa}$. For Case B [194], the concrete under consideration has a compressive strength, $\sigma_{cu} = 39.5\,\mathrm{MPa}$ and a tensile strength, $\sigma_{to} = 8.2\,\mathrm{MPa}$.

The numerical predictions of cracking and spall patterns were qualitatively compared with experimental observations for a concrete slab subjected to 0.31 kg of TNT at a stand-off of 0.4 m [50]. Figures A.4 and A.5 show that the model is capable of predicting well the characteristic crack patterns for both the blast-receiving and non-blast-receiving faces of the slab.

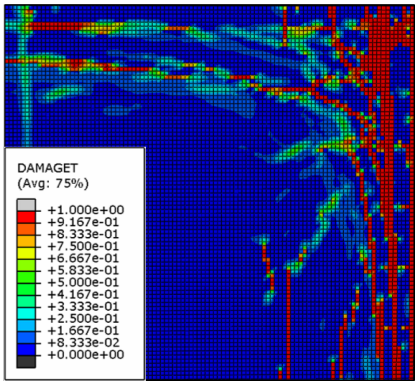

(a) 1/4-model in ABAQUS

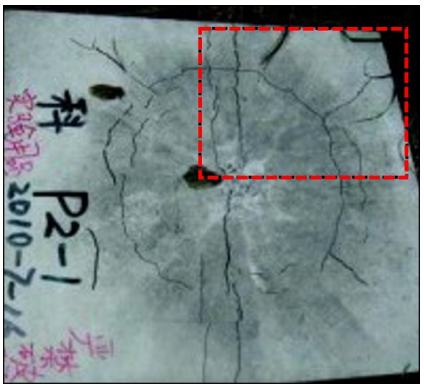

(b) Experiment

Figure A.4: Qualitative comparison between experimental results [50] and a 1/4-model in ABAQUS for the blast-receiving face of a reinforced concrete panel subjected to 0.31 kg of TNT at a stand-off of 0.4 m. Plotting contours of tensile damage parameter, d_t where $0 \leq d_t \leq 1$. Blue contours indicate $d_t = 0$ and red indicate $d_t > 0.9$. Image taken at step time = 0.02 s, well after maximum displacement is reached. Image (b) is reproduced from [50].

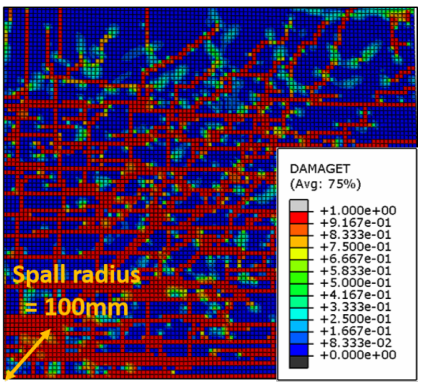

(a) 1/4-model in ABAQUS

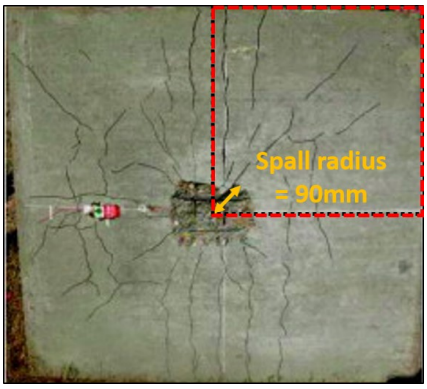

(b) Experiment

Figure A.5: Qualitative comparison between experimental results [50] and a 1/4-model in ABAQUS for the non-blast-receiving face of a reinforced concrete panel subjected to 0.31 kg of TNT at a stand-off of 0.4 m. Plotting contours of tensile damage parameter, d_t where $0 \leq d_t \leq 1$. Blue contours indicate $d_t = 0$ and red indicate $d_t > 0.9$. Image taken at step time = 0.02 s, well after maximum displacement is reached. Image (b) is reproduced from [50].

Quantitatively, comparison of slab deflections in Table A.2 shows that predictions are acceptable within the limitations described above. The largest discrepancy is observed for a close-in blast case (0.31 kg of TNT at 0.4 m) and this discrepancy may be attributable as much to simplifications in the CONWEP load case as to the assumed constitutive model. Hence, it is believed that the CDP model is adequate for the purposes of this investigation.

Table A.2: Comparison between the maximum central slab deflection, δ_{max} predicted using the ABAQUS/Explicit numerical model with that obtained in literature experiments performed by Wang *et al.* (Case A) [50] and Wu *et al.* (Case B) [194].

Case	kg of TNT	Stand-off (m)	Experiment δ_{max} (mm)	ABAQUS δ_{max} (mm)
A	0.31	0.4	15	35
A	0.46	0.4	35	43
B	1	3	1.5	1.3
B	8.1	3	11	15

A.3 1D Coupled Eulerian-Lagrangian model validation

With reference to Fig. 3.5, an air column with dimensions $L = 6\,\text{m}$ and $w_p = 0.01\,\text{m}$ was modelled in ABAQUS/Explicit as an Eulerian part with boundary conditions prescribed to ensure a 1D plane strain analysis throughout. A free-standing, rigid plate of dimensions $h_p = 0.1\,\text{m}$, $w_p = 0.01\,\text{m}$ was modelled as a rigid part and assembled at a distance, $L_t = 3\,\text{m}$ away from the inflow of the air column. The dimensions were chosen to minimise secondary wave reflections disrupting impulse transmission to the plate.

The air material model is based on the assumption that air can be treated as an ideal gas [176]. Table A.3 summarises the material model parameters, where, ρ_0 is the initial air density, p_0 is atmospheric pressure, R is the specific gas constant for dry air and c_v is the specific heat capacity at constant volume.

Table A.3: The user-defined parameters required to define the Eulerian air domain.

ρ_0 (kg m^{-3})	Temperature (K)	R ($\text{J kg}^{-1}\text{K}^{-1}$)	p_0 (Pa)	c_v ($\text{J kg}^{-1}\text{K}^{-1}$)
1.225	290	287	101,957	717.6

As a shock wave propagates in the non-acoustic regime, the wave shape changes. For the CEL model developed in this study, the distance between the inflow of the Eulerian domain and the target is kept as large as possible to avoid secondary wave reflections, as described above. Thus, the wave propagates a large distance before it interacts with the target structure and in turn, the wave shape distorts. An iterative procedure is required to determine the inflow boundary condition required to achieve the desired *free-field* wave profile at the target location.

The blast intensity chosen in this study was selected to be consistent with the intermediate blast intensity case studied by Kambouchev *et al.* [160] corresponding to $p_s/p_0 = 3.29$ and $I_i = 653\,\text{Pa s}$. These are the incident, free-field loading parameters

that the aim is to achieve in the air column at point B in Fig. 3.5. An iterative procedure is performed to determine the velocity-time history necessary at point A, to achieve the desired pressure-time history at point B. A velocity boundary condition is prescribed as it has been shown to provide better modelling stability [195]. Equation A.11 presents this iterative calculation [177], where p_B is the measured free-field overpressure at point B, a_0 is the speed of sound and $u_{A[0]}$ is the particle velocity corresponding to the desired free-field overpressure at point B. The calculation proceeds until reasonable agreement is attained with the desired peak overpressure at point B. The incident impulse is checked against the desired value and the decay time, t_i may need to be adjusted. The iterative process then begins again.

$$u_{A[i+1]} = u_{A[i]} + \left(u_{A[0]} - a_0 \frac{5}{7} \frac{p_B}{p_0} \frac{1}{\sqrt{\frac{6}{7}\left(\frac{p_B}{p_0}\right) + 1}} \right) \tag{A.11}$$

For this case, the chosen inflow velocity boundary condition is given by; $u_A(t) = 701\, e^{-t/0.9\times10^{-3}}\,\mathrm{m\,s^{-1}}$. This generates a free-field peak overpressure at point B of 341 kPa ($p_s/p_0 = 3.34$) and an incident impulse of 698 Pa s.

A number of simulations were performed to investigate how the relative transmitted impulse varies with Kambouchev *et al.*'s non-dimensional FSI parameter, β_s [160]. With reference to Eq. 3.2, different values of β_s were achieved by only varying the density of the rigid part, ρ_p between simulations. The blast intensity was kept constant as well as the plate depth, thereby fixing the values of t_i, ρ_s, U_s and h_p. The comparison between Kambouchev *et al.*'s expression (Eq. 3.1) [160] and that predicted by the numerical model is presented in Fig. A.6 showing good agreement.

It should be noted that the numerical simulations modelled a rigid plate in the middle of an air column *i.e.* there was air on the front and back faces of the plate as illustrated in Fig. 3.5. This is not exactly the case considered by Kambouchev *et al.* [160]. Rather, their analysis was for a plate with no fluid on its back face (though a constant atmospheric pressure was applied to ensure the plate was initially in equilibrium). The close agreement between the simulations and Kambouchev *et al.*'s theory would suggest however, that the presence of air on the back face of the plate does not have a significant effect.

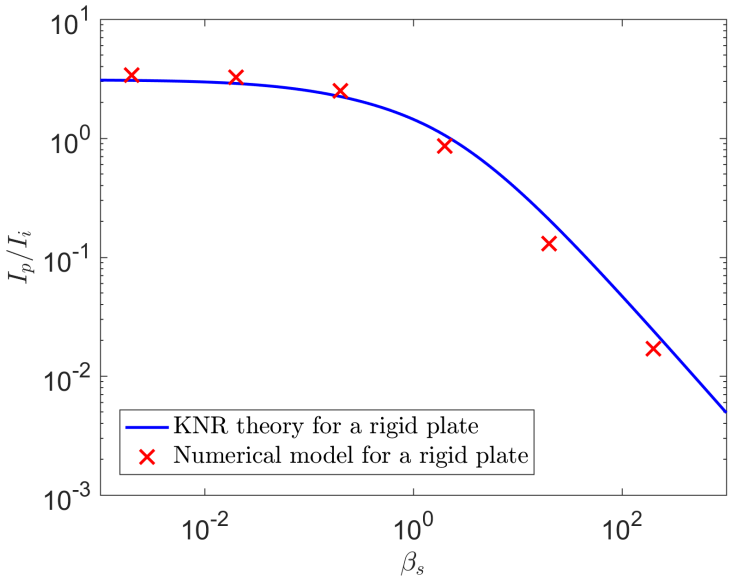

Figure A.6: A log-log plot of Kambouchev *et al.*'s (KNR) expression (Eq. 3.1) [160] for a rigid plate subjected to a blast intensity corresponding to $p_s/p_0 = 3.34$. The plot compares results obtained using the 1D CEL numerical model.

APPENDIX B

Supplementary information: Blast response regimes of elastomer-coated concrete

B.1 Interrogating the transverse shear failure mechanism

To analytically interrogate the transverse shear failure mechanism, Jones' [39] solutions are employed, developed for the transverse shear failure of an impulsively loaded, simply supported beam of length, $2L$.

Jones [39] introduces a non-dimensional parameter, ϕ which represents the ratio between the transverse shear strength per unit width, $\overline{Q_{total}}$ and the bending moment capacity per unit width, $\overline{M_0}$ of the beam cross-section:

$$\phi = \frac{\overline{Q_{total}}\, L}{2\,\overline{M_0}} \tag{B.1}$$

Small values of ϕ ($<< 1$) imply that the beam is relatively weak in shear, whereas larger values, $\phi >> 1$ would suggest that the flexural response is likely to govern beam behaviour. For intermediate values of ϕ, both transverse shear and bending effects contribute to the response and thus Jones [39] has presented solutions for three cases: $0 \leq \phi \leq 1$, $1 \leq \phi \leq 1.5$ and $\phi \geq 1.5$.

B.1.1 Uncoated RC beam

For an uncoated, reinforced concrete beam of the geometry described in Section 4.2; $\overline{Q_c} = 35.6\,\mathrm{kNm^{-1}}$ and from Table 4.1, $\overline{M_0} = 12.4\,\mathrm{kN}$. Thus, $\phi = 0.72$ from Eq. B.1. For a beam with $\phi \leq 1$, Jones [39] postulates a failure mechanism by transverse shear sliding at the supports where for severance, the displacement of the beam at

the support, $W_s \geq kH$ where $0 \leq k \leq 1$ and H is the beam depth. k is a material constant which is unity for complete severance (though it is noted that transverse shear failure may occur for smaller values of k [39]). Jones [39] predicts the initial impulsive velocity which causes severance, V_{of} as;

$$V_{of} = \sqrt{\frac{4\,k\,H\,\phi\,M_0}{m_L\,L^2}} \tag{B.2}$$

B.1.2 Coated RC beam

For coated beams, it is calculated that the polymer coating provides an additional contribution to the shear capacity per unit width of, $\overline{Q_e} = 50\,\mathrm{kNm^{-1}}$. When added to the shear capacity of reinforced concrete, the total shear capacity per unit width is found to be; $\overline{Q_{total}} = 85.6\,\mathrm{kNm^{-1}}$. Using Eq. B.1 and the ultimate moment capacity, $\overline{M_0}$ presented in Table 4.1, it is found that $\phi = 1.71$ for a beam coated on the blast-receiving face and $\phi = 1.67$ for a beam coated on the non-blast-receiving face. Since $\phi > 1.5$, a more complex transverse velocity profile evolution is postulated by Jones [39]. During the first phase of motion, plastic hinges develop at each support and travel inwards towards the midspan where they coalesce. This plastic hinge remains stationary during the final phase of motion when the remaining kinetic energy is dissipated. The threshold severance velocity according to Jones [39] is given by:

$$V_{of} = \sqrt{\frac{16\,k\,H\,\phi^2\,M_0}{3\,m_L\,L^2}} \tag{B.3}$$

APPENDIX C

Supplementary information: Impact response of elastomer-coated concrete

C.1 Dynamic mechanical analysis of the elastomer

Figure C.1 presents measurements of the temperature dependence of the viscoelastic properties of the elastomer coating, obtained using a dynamic mechanical analyser (DMA). The properties were measured in bending mode at a frequency of 1 Hz, using a clamped cantilever beam of length, 12.5 mm, width, 10 mm and thickness, 5.8 mm. The elastomer exhibits only one distinct peak in loss modulus, at approximately $-35°$C, corresponding to the glass transition temperature (T_g). This is accompanied by a significant drop in storage modulus around this temperature.

For the test specimen geometry, the test frequency and displacement amplitude (0.02 mm) correspond to a strain rate of approximately $2 \times 10^{-3}\,\mathrm{s}^{-1}$. According to Yi *et al.* [53], a $4-5°$C shift in T_g per decade increase in strain rate can be expected. Thus, it is unlikely that an impact-induced glass transition would be observed up to the maximum strain rates seen in the impact tests, which is of the order $10^4\,\mathrm{s}^{-1}$. However, the shift may be sufficient for a rise in loss modulus to contribute to energy dissipation at these higher rates.

C.2 Validating the indentation simulations

To validate the choice of indenter geometry and finite element mesh, the stress distribution obtained using the FE model is compared with the theoretical solution for a flat-ended cylinder with a sharp corner, indenting an elastic half space, obtained by Sneddon [196]. As presented in Fig. C.2, the Sneddon solution is given in terms of, $a\,s_{max}/\gamma\,\delta$ where s_{max} is the maximum shear stress, a is the indenter radius, δ is

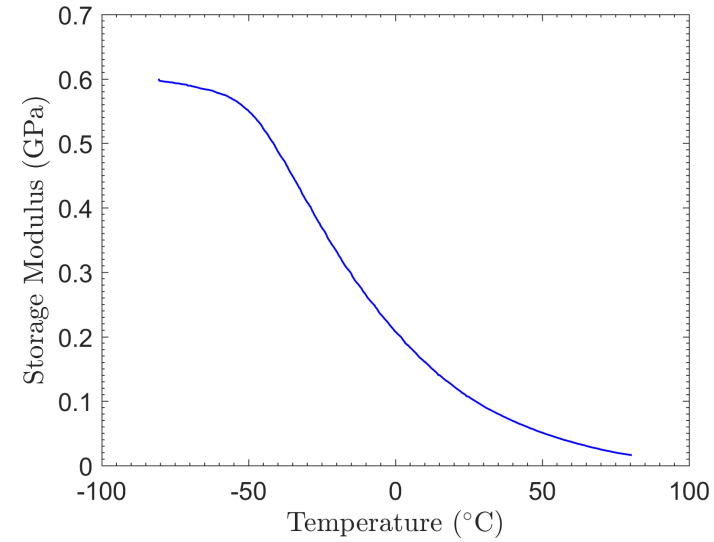

(a) Storage modulus

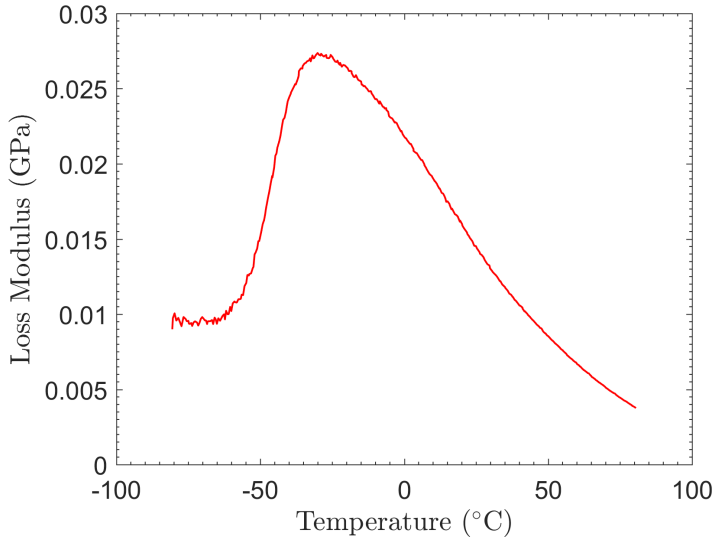

(b) Loss modulus

Figure C.1: Dynamic mechanical analysis results for the elastomer (in cantilever bending mode) at a frequency of 1 Hz and at a heating rate of 5°C per minute.

the depth below the level of the undisturbed boundary that the punch penetrates and γ is the Lamé elastic constant of the deformed medium, $\gamma = \nu E/(1+\nu)(1-2\nu)$ where ν is the Poisson's ratio and E is the Young's modulus.

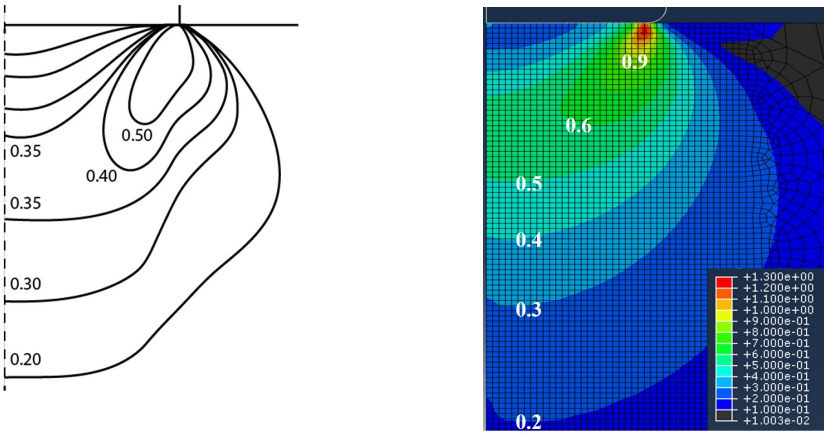

(a) Sneddon's solution [196] (b) FE indentation

Figure C.2: Sneddon's solution (adapted from [196]) for contours of normalised maximum shear stress in an elastic half space indented by a flat-ended cylinder with a sharp corner. Also presented are the contours of normalised maximum shear stress obtained in the axisymmetric FE simulation of the quasi-static indentation of a concrete block with a cylindrical, rigid indenter with a corner radius of 1.5 mm.

ABAQUS/Explicit is used to model the indentation of an axisymmetric concrete block of radius 50 mm and height 100 mm, indented to a depth, $\delta = 0.05$ mm at a speed, $0.1\,\mathrm{mm\,s^{-1}}$. The concrete model remains in its elastic regime under these conditions, and has a Young's Modulus, $E = 28.3$ GPa and Poisson's ratio, $\nu = 0.2$. The indenter is modelled as a rigid circular cylinder of radius 14.25 mm, with a corner radius of 1.5 mm, as described in Section 5.4.1. The contours of normalised maximum shear stress are plotted in Fig. C.2 and are compared with Sneddon's solution. The FE model captures the distribution of stress in the substrate well, but it is noted that this comparison with theory is restricted to the elastic regime.

C.3 Impact model: sensitivity to polymer modelling parameters

Considering again the comparison between the FE model predictions and experimental measurements in Fig. 5.15, this section examines how the FE model (defined in Sections 5.3 and 5.4) may be altered to improve agreement in the unloading phase of the impact.

First, the elastomer/concrete interface condition is reconsidered. In Fig. C.3, the FE prediction for the projectile velocity-time histories is plotted, assuming a frictionless contact condition between the elastomer and concrete. This model tends to provide

a more accurate prediction for the projectile rebound velocities compared to when Coulomb friction (with a friction coefficient of $\mu = 0.8$) is assumed at this interface. However, it is not clear from the current experiments whether there is a sound physical basis for a reduction in interface friction during impact loading.

A further potential source of discrepancy is the Prony series representation of the viscoelastic behaviour, shown in Section 3.2.2 to underpredict the material hysteresis. Therefore, an attempt is made to develop an alternative means of representing the viscoelastic behaviour that does not rely on a Prony series. The built-in, *Hysteresis* material model in ABAQUS/Standard [27] is used. It was developed to model the strain-rate dependent, hysteretic behaviour of elastomers. The hyperelastic definition remains the same as that described in Section 3.2.2. The hysteresis parameters are as defined in the ABAQUS User's Manual [27], with the following values used: stress scaling factor, $S = 3.84$, positive exponent, $m = 7.65$, exponent, $C = -0.467$ and constant, $A = 8.15E - 54$. These parameters are derived using the commercially available *MCalibration* software [197] based on a fit to uniaxial tension data measured at nominal strain rates between, $\dot{\epsilon} = 10^{-2} - 10^{2}\,\mathrm{s}^{-1}$ and a compression load-unload test (described in 3.2.2) at a nominal strain rate, $\dot{\epsilon} = 10^{-3}\,\mathrm{s}^{-1}$.

The use of this material model in ABAQUS requires the implicit time integration version of the code. In contrast to the calculations with explicit time integration, this is not able to solve the later phases of the projectile penetration for higher impact velocities (where there is a combination of large deformations and complex contact conditions). However, for load cases where a solution is obtained (impact speeds of $45\,\mathrm{m\,s}^{-1}$, with a partial solution at $64\,\mathrm{m\,s}^{-1}$ and $101\,\mathrm{m\,s}^{-1}$), there is an improved match with experimental measurements (Fig. C.3).

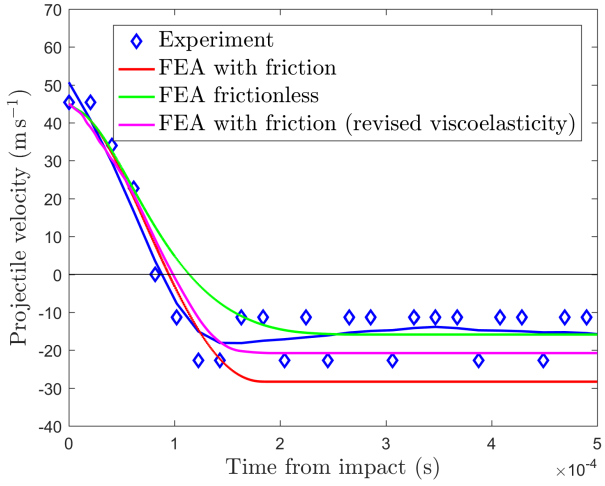

(a) 45 m s^{-1}

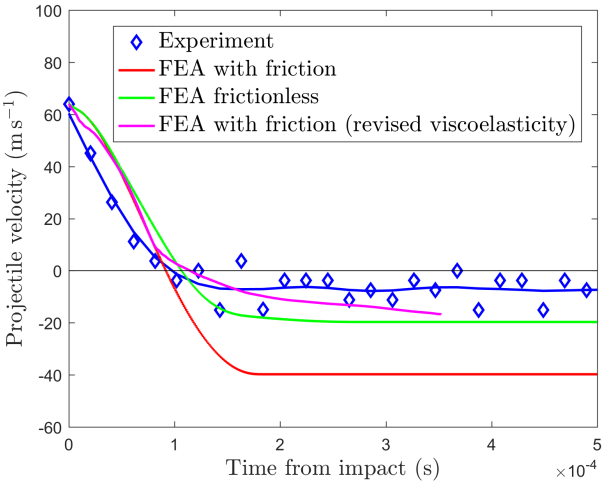

(b) 64 m s^{-1}

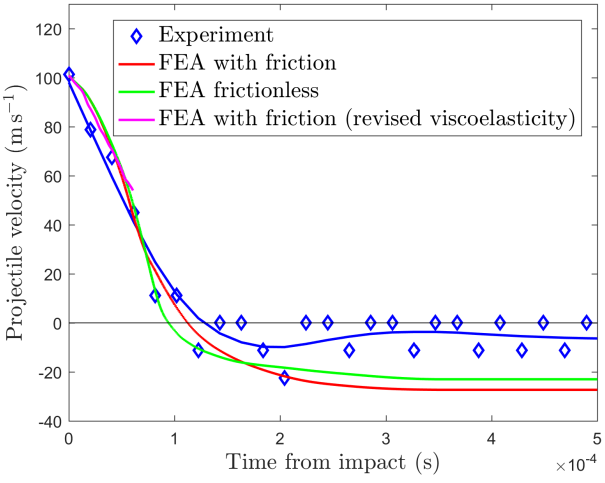

(c) 101 m s^{-1}

Figure C.3: Projectile velocity-time history obtained from the impact experiments and the FE analysis for coated concrete specimens. The first FE model considers a friction coefficient, $\mu = 0.8$ between the elastomer and concrete; the second considers frictionless contact at this interface and the third considers an alternative model to capture polymer hysteresis, as defined in the text.

APPENDIX D

Supplementary information: Impact damage protection mechanisms for elastomer-coated concrete

D.1 Sensitivity to boundary conditions

D.1.1 Edge constraint

Figure D.1 compares the early and developed damage contours for the reference geometry case (Fig. 6.1) with the addition of an edge constraint, constraining the lateral displacement of the outer edges of the elastomer and concrete.

There is no significant effect of the additional edge constraint in terms of concrete damage initiation. Furthermore, the influence of the coating is unchanged — it serves to shift the concrete damage initiation mechanism from Mechanism 1 to Mechanism 2.

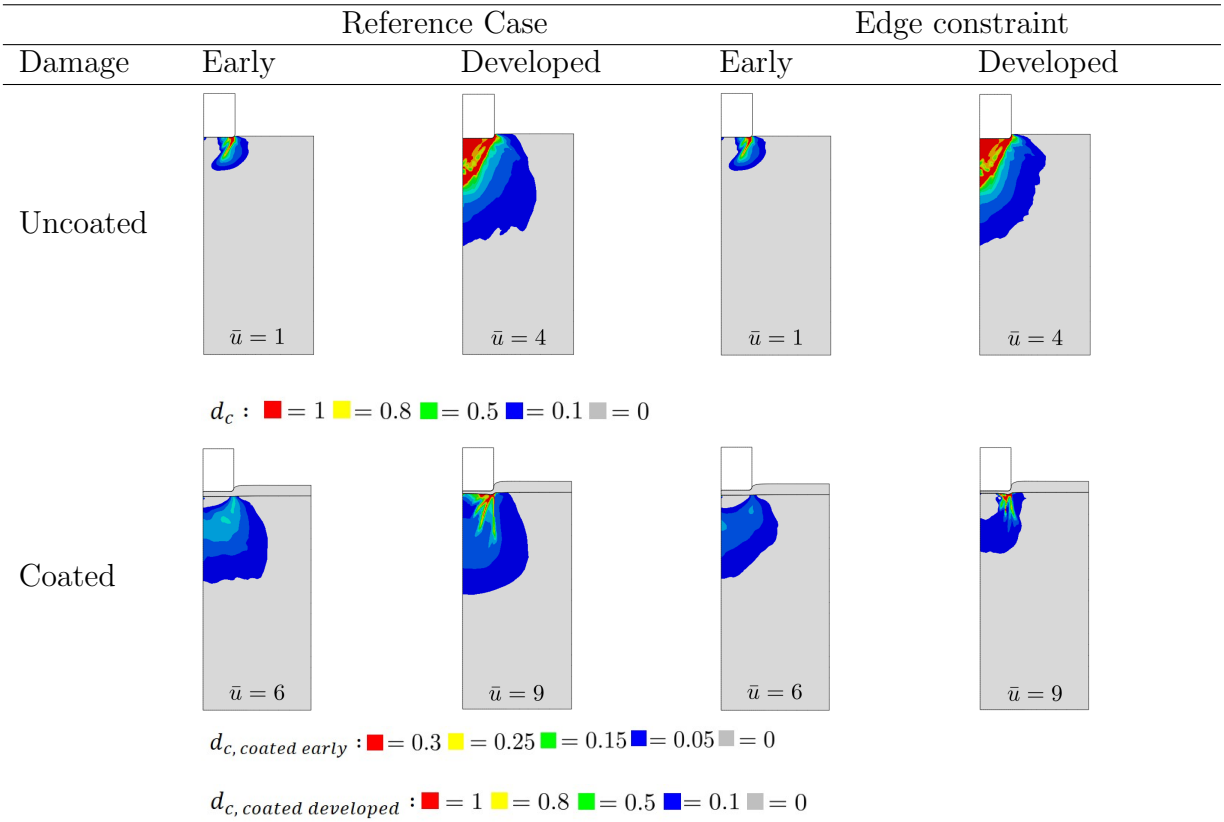

Figure D.1: Comparing contours of the compressive damage parameter, d_c for the reference geometry case (Fig. 6.1) and that with an additional edge constraint. A projectile impact at $V_0 = 100\,\mathrm{m\,s^{-1}}$ is considered.

References

[1] J. S. Davidson, J. W. Fisher, M. I. Mammons, J. R. Porter, and R. J. Dinan, "Failure mechanisms of polymer-reinforced concrete masonry walls subjected to blast," *Journal of Structural Engineering*, vol. 131, pp. 1194–1205, 8 2005.

[2] European Committee for Standardization (CEN), *BS EN 1991-1-7:2006: Eurocode 1: Actions on structures. Part 1–7: general actions-accidental actions*, 2006.

[3] C. M. Roland, D. Fragiadakis, and R. M. Gamache, "Elastomer-steel laminate armor," *Composite Structures*, vol. 92, no. 5, pp. 1059–1064, 2010.

[4] C. M. Roland, D. Fragiadakis, R. M. Gamache, and R. Casalini, "Factors influencing the ballistic impact resistance of elastomer-coated metal substrates," *Philosophical Magazine*, vol. 93, no. 5, pp. 468–477, 2013.

[5] M. R. Amini, J. B. Isaacs, and S. Nemat-Nasser, "Investigation of effect of polyurea on response of steel plates to impulsive loads in direct pressure-pulse experiments," *Mechanics of Materials*, vol. 42, pp. 628–639, 6 2010.

[6] D. Mohotti, T. Ngo, P. Mendis, and S. N. Raman, "Polyurea coated composite aluminium plates subjected to high velocity projectile impact," *Materials and Design*, vol. 52, pp. 1–16, 2013.

[7] I. Mohagheghian, G. J. McShane, and W. J. Stronge, "Impact perforation of polymer-metal laminates: Projectile nose shape sensitivity," *International Journal of Solids and Structures*, vol. 88-89, pp. 337–353, 2016.

[8] Y. A. Bahei-El-Din, G. J. Dvorak, and O. J. Fredricksen, "A blast-tolerant sandwich plate design with a polyurea interlayer," *International Journal of Solids and Structures*, vol. 43, no. 25-26, pp. 7644–7658, 2006.

[9] Y. A. Bahei-El-Din and G. J. Dvorak, "Behavior of sandwich plates reinforced with polyurethane/polyurea interlayers under blast loads," *Journal of Sandwich Structures and Materials*, vol. 9, no. 3, pp. 261–281, 2007.

[10] Y. A. Bahei-El-Din and G. J. Dvorak, "Enhancement of blast resistance of sandwich plates," *Composites Part B: Engineering*, vol. 39, no. 1, pp. 120–127, 2008.

[11] M. Grujicic, W. C. Bell, B. Pandurangan, and T. He, "Blast-wave impact-mitigation capability of polyurea when used as helmet suspension-pad material," *Materials and Design*, vol. 31, no. 9, pp. 4050–4065, 2010.

[12] M. Grujicic, W. C. Bell, B. Pandurangan, and P. S. Glomski, "Fluid/Structure interaction computational investigation of blast-wave mitigation efficacy of the advanced combat helmet," *Journal of Materials Engineering and Performance*, vol. 20, no. 6, pp. 877–893, 2011.

[13] T. Rahimzadeh, E. M. Arruda, and M. D. Thouless, "Design of armor for protection against blast and impact," *Journal of the Mechanics and Physics of Solids*, vol. 85, pp. 98–111, 2015.

[14] J. H. Ha, N. H. Yi, J. K. Choi, and J. H. J. Kim, "Experimental study on hybrid CFRP-PU strengthening effect on RC panels under blast loading," *Composite Structures*, vol. 93, no. 8, pp. 2070–2082, 2011.

[15] S. A. Tekalur, A. Shukla, and K. Shivakumar, "Blast resistance of polyurea based layered composite materials," *Composite Structures*, vol. 84, no. 3, pp. 271–281, 2008.

[16] K. J. Knox, M. I. Hammons, T. T. Lewis, and J. R. Porter, "Polymer Materials for Structural Retrofit," Air Force Research Laboratory, Air Expeditionary Forces Technology Division, Tyndall AFB, Florida, Tech. Rep., 2000.

[17] J. S. Davidson, J. R. Porter, R. J. Dinan, M. I. Hammons, and J. D. Connell, "Explosive testing of polymer retrofit masonry walls," *Journal of Performance of Constructed Facilities*, vol. 18, pp. 100–106, 2 2004.

[18] S. N. Raman, T. Ngo, P. Mendis, and T. Pham, "Elastomeric polymers for retrofitting of reinforced concrete structures against the explosive effects of blast," *Advances in Materials Science and Engineering*, 2012.

[19] G. C. Mays and P. D. Smith, *Blast Effects on Buildings*. London, United Kingdom: Thomas Telford, 1995.

[20] N. Kambouchev, "Analysis of blast mitigation strategies exploiting fluid-structure interaction," PhD thesis, Massachusetts Institute of Technology, 2007.

[21] W. E. Baker, *Explosions in Air*. Austin, Texas, US: University of Texas Press, 1973.

[22] E. L. Guzas and C. J. Earls, "Air blast load generation for simulating structural response," *Steel and Composite Structures*, vol. 10, no. 5, pp. 429–455, 2010.

[23] W. E. Baker, P. Cox, P. S. Westine, J. J. Kulesz, and R. A. Strehlow, *Explosion hazards and evaluation*. New York, US: Elsevier, 1983.

[24] C. N. Kingery and G. Bulmash, *Airblast parameters from TNT spherical air burst and hemispherical surface burst*. Aberdeen Proving Ground, MD: Ballistic Research Laboratories, 1984.

[25] "Structures to resist the effects of accidental explosions. United Facilities Criteria (UFC) 3-340-02," Department of Defense, United States of America, Tech. Rep., 2008.

[26] D. W. Hyde, *CONWEP-Conventional Weapons Effects Programme*. U.S. Army Waterways Experimental Station, 1992.

[27] ABAQUS, *ABAQUS 6.11 Analysis User's Manual*. Providence, RI, US: Dassault Systemes, 2011.

[28] G. F. Kinney and K. J. Graham, *Explosive Shocks in Air*. New York, US: Springer-Verlag, 1985.

[29] J. R. Florek, "Study of simplified models of aircraft structures subjected to generalized explosive loading," PhD thesis, Rutgers, The State University of New Jersey, 2007.

[30] D. O. Dusenberry, Ed., *Handbook for blast resistant design of buildings*. New Jersey, US: John Wiley and Sons, 2010.

[31] R. W. Gurney, "The initial velocities of fragments from bombs, shells, and grenades," Aberdeen Proving Ground, MD: Ballistic Research Laboratory, Tech. Rep., 1947.

[32] M. E. Backman and W. Goldsmith, "The mechanics of penetration of projectiles into targets," *International Journal of Engineering Science*, vol. 16, no. 1, pp. 1–99, 1978.

[33] V. Karlos and G. Solomos, *Calculation of Blast Loads for Application to Structural Components. European Commission, Joint Research Centre, Institute for the Protection and Security of the Citizen*. Luxembourg: Publications Office of the European Union, 2013.

[34] J. M. Biggs, *Introduction to structural dynamics*. New York, US: McGraw-Hill, 1964.

[35] T. Ngo, P. Mendis, A. Gupta, and J. Ramsay, "Blast loading and blast effects on structures — an overview," *EJSE Special Issue: Loading on Structures*, 2007.

[36] F. Parisi, C. Balestrieri, and D. Asprone, "Out-of-plane blast capacity of load-bearing masonry walls," presented at the Proceedings of the 16^{th} International Brick & Block Masonry Conference (Padova, Italy), 2016.

[37] Y. Shi, H. Hao, and Z. X. Li, "Numerical derivation of pressure-impulse diagrams for prediction of RC column damage to blast loads," *International Journal of Impact Engineering*, vol. 35, pp. 1213–1227, 2008.

[38] W. W. El-Dakhakhni, S. H. Changiz Rezaei, W. F. Mekky, and A. G. Razaqpur, "Response sensitivity of blast-loaded reinforced concrete structures to the number of degrees of freedom," *Canadian Journal of Civil Engineering*, vol. 36, no. 8, pp. 1305–1320, 2009.

[39] N. Jones, *Structural Impact*. Cambridge, UK: Cambridge University Press, 1989.

[40] G. S. Langdon and G. K. Schleyer, "Inelastic deformation and failure of clamped aluminium plates under pulse pressure loading," *International Journal of Impact Engineering*, vol. 28, pp. 1107–1127, 2003.

[41] N. Jacob, G. N. Nurick, and G. S. Langdon, "The effect of stand-off distance on the failure of fully clamped circular mild steel plates subjected to blast loads," *Engineering Structures*, vol. 29, pp. 2723–2736, 2007.

[42] B. M. Luccionia and M. Luege, "Concrete pavement slab under blast loads," *International Journal of Impact Engineering*, vol. 32, pp. 1248–1266, 2006.

[43] J. Lubliner, *Plasticity theory*. New York, US: Macmillan, 1990.

[44] LS-DYNA, *LS-DYNA Version 970 Manual*. CA, USA: Livermore Software Technology Corporation (LSTC), 2003.

[45] AUTODYN, *AUTODYN Manual*. Concord, CA, USA: CenturyDynamics, Inc., 2003.

[46] C. F. Zhao and J. Y. Chen, "Damage mechanism and mode of square reinforced concrete slab subjected to blast loading," *Theoretical and Applied Fracture Mechanics*, vol. 63-64, pp. 54–62, 3 2013.

[47] X. Lin, Y. X. Zhang, and P. J. Hazell, "Modelling the response of reinforced concrete panels under blast loading," *Materials & Design*, vol. 56, pp. 620–628, 2014.

[48] B. Yan, F. Liu, D. Song, and Z. Jiang, "Numerical study on damage mechanism of RC beams under close-in blast loading," *Engineering Failure Analysis*, vol. 51, pp. 9–19, 2015.

[49] C. P. Pantelides, T. T. Garfield, W. D. Richins, T. K. Larson, and J. E. Blakeley, "Reinforced concrete and fiber reinforced concrete panels subjected to blast detonations and post-blast static tests," *Engineering Structures*, vol. 76, pp. 24–33, 2014.

[50] W. Wang, D. Zhang, F. Lu, S. Wang, and F. Tang, "Experimental study and numerical simulation of the damage mode of a square reinforced concrete slab under close-in explosion," *Engineering Failure Analysis*, vol. 27, pp. 41–51, 2013.

[51] W. Riedel, "Beton unter dynamischen lasten, meso. und makromechanische modelle und ihre parameter," PhD thesis, Universitat der Bundeswehr Munchen, Freiburg, 2000.

[52] S. Astarlioglu, K. Krauthammer, D. Morency, and T. P. Tran, "Behavior of reinforced concrete columns under combined effects of axial and blast-induced transverse loads," *Engineering Structures*, vol. 55, pp. 26–34, 2013.

[53] Y. Huan, Q. Fang, L. Chen, and Y. Zhang, "Evaluation of blast-resistant performance predicted by damaged plasticity model for concrete," *Trans. Tianjin Univ.*, vol. 14, pp. 414–442, 2008.

[54] P. F. Silva and B. Lu, "Blast resistance capacity of reinforced concrete slabs," *Journal of Structural Engineering*, vol. 135, pp. 708–716, 2009.

[55] P. F. Silva and B. Lu, "Improving the blast resistance capacity of RC slabs with innovative composite materials," *Composites Part B: Engineering*, vol. 38, no. 5-6, pp. 523–534, 2007.

[56] W. Wang, D. Zhang, F. Lu, S. Wang, and F. Tang, "Experimental study on scaling the explosion resistance of a one-way square reinforced concrete slab under a close-in blast loading," *International Journal of Impact Engineering*, vol. 49, pp. 158–164, 2012.

[57] D. Zhang, S. Yao, F. Lu, X. Chen, G. Lin, W. Wang, and Y. Lin, "Experimental study on scaling of RC beams under close-in blast loading," *Engineering Failure Analysis*, vol. 33, pp. 497–504, 2013.

[58] Q. M. Li, S. R. Reid, H. M. Wen, and A. R. Telford, "Local impact effects of hard missiles on concrete targets," *International Journal of Impact Engineering*, vol. 32, no. 1-4, pp. 224–284, 2006.

[59] R. P. Kennedy, "A review of procedures for the analysis and design of concrete structures to resist missile impact effects," *Nuclear Engineering and Design*, vol. 37, no. 2, pp. 183–203, 1976.

[60] G. G. Corbett, S. R. Reid, and W. Johnson, "Impact loading of plates and shells by free-flying projectiles: a review," *International Journal of Impact Engineering*, vol. 18, no. 2, pp. 141–230, 1995.

[61] G. E. Sliter, "Assessment of empirical concrete impact formulas," *ASCE Journal of the Structural Division*, vol. 106, pp. 1023–1045, 5 1980.

[62] *TM-5-855-1 Fundamentals of protective design for conventional weapons*, Department of the Army, Washington Headquarters, 1986.

[63] G. C. Mays and M. S. Williams, *Assessment, strengthing, harding, repair and demolition of structures, military engineering*. London: Ministry of Defence, 1992.

[64] S. R. Reid and H. M. Wen, "Predicting penetration, cone cracking, scabbing and perforation of reinforced concrete targets struck by flat-faced projectiles," UMIST, Tech. Rep., 2001.

[65] BNFL (British Nuclear Fuels Ltd.), *Reinforced concrete slab local damage assessment. R3 impact assessment procedure, Appendix H, vol. 3*, Magnox Electric plc & Nuclear Electric Limited, 2003.

[66] T. Krauthammer, S. Shahriar, and H. M. Shanaa, "Response of reinforced concrete elements to severe impulsive loads," *Journal of Structural Engineering*, vol. 116, no. 4, pp. 1061–1079, 1990.

[67] K. Fujikake, B. Li, and S. Soeun, "Impact response of reinforced concrete beam and its analytical evaluation," *Journal of Structural Engineering*, vol. 135, no. 8, pp. 938–950, 2009.

[68] A. D. Adhikary, B. Li, and K. Fujikake, "Low velocity impact response of reinforced concrete beams: experimental and numerical investigation," *International Journal of Protective Structures*, vol. 6, no. 1, 2015.

[69] Y. S. Tai and C. C. Tang, "Numerical simulation: The dynamic behavior of reinforced concrete plates under normal impact," *Theoretical and Applied Fracture Mechanics*, vol. 45, no. 2, pp. 117–127, 2006.

[70] S. J. Hanchak, M. J. Forrestal, E. R. Young, and J. Q. Ehrgott, "Perforation of concrete slabs with 48 MPa (7 ksi) and 140 MPa (20 ksi) unconfined compressive strengths," *International Journal of Impact Engineering*, vol. 12, no. 1, pp. 1–7, 1992.

[71] N. Trivedi and R. K. Singh, "Prediction of impact induced failure modes in reinforced concrete slabs through nonlinear transient dynamic finite element simulation," *Annals of Nuclear Energy*, vol. 56, pp. 109–121, 2013.

[72] M. Zineddin and T. Krauthammer, "Dynamic response and behavior of reinforced concrete slabs under impact loading," *International Journal of Impact Engineering*, vol. 34, no. 9, pp. 1517–1534, 2007.

[73] S. N. Mokhatar and R. Abdullah, "Computational analysis of reinforced concrete slabs subjected to impact loads," *International Journal of Integrated Engineering*, vol. 4, no. 2, pp. 70–76, 2012.

[74] M. J. Forrestal, B. S. Altman, J. D. Cargile, and S. J. Hanchak, "An empirical equation for penetration depth of ogive-nose projectiles into concrete targets," *International Journal of Impact Engineering*, vol. 15, no. 4, pp. 395–405, 1994.

[75] M. J. Forrestal, D. J. Frew, J. P. Hickerson, and T. A. Rohwer, "Penetration of concrete targets with deceleration-time measurements," *International Journal of Impact Engineering*, vol. 28, no. 5, pp. 479–497, 2003.

[76] A. N. Dancygier, D. Z. Yankelevsky, and C. Jaegermann, "Response of high performance concrete plates to impact of non-deforming projectiles," *International Journal of Impact Engineering*, vol. 34, no. 11, pp. 1768–1779, 2007.

[77] S. Kataoka, M. Beppu, H. Ichino, T. Mase, T. Nakada, and R. Matsuzawa, "Failure behavior of reinforced concrete slabs subjected to moderate-velocity impact by a steel projectile," *International Journal of Protective Structures*, vol. 8, no. 3, pp. 384–406, 2017.

[78] J. Leppanen, "Experiments and numerical analyses of blast and fragment impacts on concrete," *International Journal of Impact Engineering*, vol. 31, pp. 843–860, 7 2005.

[79] U. Nystrom and K. Gylltoft, "Numerical studies of the combined effects of blast and fragment loading," *International Journal of Impact Engineering*, vol. 36, pp. 995–1005, 8 2009.

[80] W. Hu and Z. Chen, "Model-based simulation of the synergistic effects of blast and fragmentation on a concrete wall using the MPM," *International Journal of Impact Engineering*, vol. 32, no. 12, pp. 2066–2096, 2006.

[81] P. H. Bischoff and S. H. Perry, "Compressive behaviour of concrete at high strain rates," *Materials and Structures*, vol. 24, no. 6, pp. 425–450, 1991.

[82] J. W. Tedesco and C. A. Ross, "Strain-rate-dependent constitutive equations for concrete," *Journal of Pressure Vessel Technology*, vol. 120, pp. 398–405, 4 1998.

[83] D. Grote, S. Park, and M. Zhou, "Dynamic behavior of concrete at high strain rates and pressures: I. experimental characterization," *International Journal of Impact Engineering*, vol. 25, no. 9, pp. 869–886, 2001.

[84] Comité Euro-International du Béton, *CEB-FIP model code 1990: design code*. London: Thomas Telford, 1993.

[85] C. Ross, D. Jerome, J. Tedesco, and M. Hughes, "Moisture and strain rate effects on concrete strength," *ACI Materials Journal*, vol. 93, pp. 293–300, May 1996.

[86] Q. M. Li and H. Meng, "About the dynamic strength enhancement of concrete-like materials in a split Hopkinson pressure bar test," *International Journal of Solids and Structures*, vol. 40, no. 2, pp. 343–360, 2003.

[87] P. A. Buchan and J. F. Chen, "Blast resistance of FRP composites and polymer strengthened concrete and masonry structures - A state-of-the-art review," *Composites Part B: Engineering*, vol. 38, pp. 509–522, 2007.

[88] L. J. Gibson and M. F. Ashby, *Cellular Solids: Structure and Properties*, 2nd ed., ser. Cambridge Solid State Science Series. Cambridge, UK: Cambridge University Press, 1997.

[89] Z. Xue and J. W. Hutchinson, "Preliminary assessment of sandwich plates subject to blast loads," *International Journal of Mechanical Sciences*, vol. 45, pp. 687–705, 4 2003.

[90] N. A. Fleck and V. S. Deshpande, "The resistance of clamped sandwich beams to shock loading," *Journal of Applied Mechanics*, vol. 71, no. 3, p. 386, 2004.

[91] K. P. Dharmasena, H. N. Wadley, Z. Xue, and J. W. Hutchinson, "Mechanical response of metallic honeycomb sandwich panel structures to high-intensity dynamic loading," *International Journal of Impact Engineering*, vol. 35, pp. 1063–1074, 2008.

[92] Z. Xue and J. W. Hutchinson, "A comparative study of impulse-resistant metal sandwich plates," *International Journal of Impact Engineering*, vol. 30, pp. 1283–1305, 2004.

[93] G. I. Taylor, "The pressure and impulse of submarine explosion waves on plates," in *The scientific papers of Sir Geoffrey Ingram Taylor, volume III: Aerodynamics and the Mechanics of Projectiles and Explosions*, G. K. Batchelor, Ed., Cambridge University Press, 1963.

[94] V. Deshpande and N. Fleck, "High strain rate compressive behaviour of aluminium alloy foams," *International Journal of Impact Engineering*, vol. 24, no. 3, pp. 277–298, 2000.

[95] D. D. Radford, G. J. McShane, V. S. Deshpande, and N. A. Fleck, "The response of clamped sandwich plates with metallic foam cores to simulated blast loading," *International Journal of Solids and Structures*, vol. 43, no. 7-8, pp. 2243–2259, 2006.

[96] W. Goldsmith and J. L. Sackman, "An experimental study of energy absorption in impact on sandwich plates," *International Journal of Impact Engineering*, vol. 12, no. 2, pp. 241–262, 1992.

[97] H. J. Rathbun, D. D. Radford, Z. Xue, M. Y. He, J. Yang, V. Deshpande, N. A. Fleck, J. W. Hutchinson, F. W. Zok, and A. G. Evans, "Performance of metallic honeycomb-core sandwich beams under shock loading," *International Journal of Solids and Structures*, vol. 43, no. 6, pp. 1746–1763, 2006.

[98] D. D. Radford, G. J. McShane, V. S. Deshpande, and N. A. Fleck, "Dynamic Compressive Response of Stainless-Steel Square Honeycombs," *Journal of Applied Mechanics*, vol. 74, no. 4, p. 658, 2007.

[99] K. P. Dharmasena, D. T. Queheillalt, H. N. Wadley, P. Dudt, Y. Chen, D. Knight, A. G. Evans, and V. S. Deshpande, "Dynamic compression of metallic sandwich structures during planar impulsive loading in water," *European Journal of Mechanics, A/Solids*, vol. 29, no. 1, pp. 56–67, 2010.

[100] B. Russell, A. Malcom, H. Wadley, and V. Deshpande, "Dynamic compressive response of composite corrugated cores," *Journal of Mechanics of Materials and Structures*, vol. 5, no. 3, pp. 477–493, 2010.

[101] H. N. Wadley, K. P. Dharmasena, M. R. O'Masta, and J. J. Wetzel, "Impact response of aluminum corrugated core sandwich panels," *International Journal of Impact Engineering*, vol. 62, pp. 114–128, 2013.

[102] D. J. Sypeck and H. N. Wadley, "Multifunctional microtruss laminates: Textile synthesis and properties," *Journal of Materials Research*, vol. 16, no. 3, pp. 890–897, 2001.

[103] S. McKown, Y. Shen, W. K. Brookes, C. J. Sutcliffe, W. J. Cantwell, G. S. Langdon, G. N. Nurick, and M. D. Theobald, "The quasi-static and blast loading response of lattice structures," *International Journal of Impact Engineering*, vol. 35, no. 8, pp. 795–810, 2008.

[104] M. Smith, W. J. Cantwell, Z. Guan, S. Tsopanos, M. D. Theobald, G. N. Nurick, and G. S. Langdon, "The quasi-static and blast response of steel lattice structures," *Journal of Sandwich Structures and Materials*, vol. 13, no. 4, pp. 479–501, 2011.

[105] C. Qi, A. Remennikov, L. Z. Pei, S. Yang, Z. H. Yu, and T. D. Ngo, "Impact and close-in blast response of auxetic honeycomb-cored sandwich panels: Experimental tests and numerical simulations," *Composite Structures*, vol. 180, pp. 161–178, 2017.

[106] M. Schenk, S. D. Guest, and G. J. McShane, "Novel stacked folded cores for blast-resistant sandwich beams," *International Journal of Solids and Structures*, vol. 51, no. 25-26, pp. 4196–4214, 2014.

[107] E. Medvedovski, "Ballistic performance of armour ceramics: Influence of design and structure. Part 2," *Ceramics International*, vol. 36, no. 7, pp. 2117–2127, 2010.

[108] R. L. Woodward and B. J. Baxter, "Ballistic evaluation of ceramics: Influence of test conditions," *International Journal of Impact Engineering*, vol. 15, no. 2, pp. 119–124, 1994.

[109] I. Horsfall, S. Austin, and W. Bishop, "Structural ballistic armour for transport aircraft," *Materials & Design*, vol. 21, no. 1, pp. 19–25, 1999.

[110] M. Lee and Y. H. Yoo, "Analysis of ceramic/metal armour systems," *International Journal of Impact Engineering*, vol. 25, no. 9, pp. 819–829, 2001.

[111] W. W. Chen, A. M. Rajendran, B. Song, and X. Nie, "Dynamic fracture of ceramics in armor applications," *Journal of the American Ceramic Society*, vol. 90, no. 4, pp. 1005–1018, 2007.

[112] E. Medvedovski, "Ballistic performance of armour ceramics: Influence of design and structure. Part 1," *Ceramics International*, vol. 36, no. 7, pp. 2103–2115, 2010.

[113] D. A. Shockey, A. H. Marchand, S. R. Skaggs, G. E. Cort, M. W. Burkett, and R. Parker, "Failure phenomenology of confined ceramic targets and impacting

rods," *International Journal of Impact Engineering*, vol. 9, no. 3, pp. 263–275, 1990.

[114] B. G. Compton and F. W. Zok, "Impact resistance of TiC-based cermets," *International Journal of Impact Engineering*, vol. 62, pp. 75–87, 2013.

[115] W. R. Blumenthal, G. T. Gray, and T. N. Claytor, "Response of aluminium-infiltrated boron carbide cermets to shock wave loading," *Journal of Materials Science*, vol. 29, no. 17, pp. 4567–4576, 1994.

[116] B. Klein, N. Frage, M. P. Dariel, and E. Zaretsky, "Dynamic response of ceramic-metal composites: The TiC-steel system," *Journal of Applied Physics*, vol. 93, no. 2, pp. 968–976, 2003.

[117] A. Pettersson, P. Magnusson, P. Lundberg, and M. Nygren, "Titanium–titanium diboride composites as part of a gradient armour material," *International Journal of Impact Engineering*, vol. 32, pp. 387–399, 2005.

[118] Y. Sun, Z. Yu, Z. Wang, and X. Liu, "Novel protective covering to enhance concrete resistance against projectile impact," *Construction and Building Materials*, vol. 96, pp. 484–490, 2015.

[119] L. J. Malvar, K. B. Morrill, and J. E. Crawford, "Numerical modeling of concrete confined by fiber-reinforced composites," *Journal of Composites for Construction*, vol. 8, no. 4, pp. 315–322, 2004.

[120] K. M. Mosalam and A. S. Mosallam, "Nonlinear transient analysis of reinforced concrete slabs subjected to blast loading and retrofitted with CFRP composites," *Composites Part B: Engineering*, vol. 32, pp. 623–636, 8 2001.

[121] G. Tanapornraweekit, N. Haritos, and P. Mendis, "Behavior of FRP-RC slabs under multiple independent air blasts," *Journal of Performance of Constructed Facilities*, vol. 25, no. 5, pp. 433–440, 2011.

[122] C. A. Ross, M. R. Purcell, and E. L. Jerome, "Blast response of concrete beams and slabs externally reinforced with fibre reinforced plastics (FRP)," presented at the Proceedings of the Struct. Cong. XV - building to last (Portland, USA), 1997.

[123] L. C. Muszynski and M. R. Purcell, "Composite reinforcement to strengthen existing concrete structures against air blast," *Journal of Composites for Construction*, vol. 7, pp. 93–97, 2 2003.

[124] J. E. Crawford, J. Malvar, J. W. Wesevich, J. Valancius, and A. D. Raynolds, "Retrofit of reinforced concrete structures to resist blast effects," *ACI Structural Journal*, vol. 94, pp. 371–377, 4 1997.

[125] L. C. Muszynski and M. R. Purcell, "Use of composite reinforcement to strengthen concrete and air-entrained concrete masonry walls against air blast," *Journal of Composites for Construction*, vol. 7, pp. 98–108, 2 2003.

[126] A. A. Mutalib and H. Hao, "Development of P-I diagrams for FRP strengthened RC columns," *International Journal of Impact Engineering*, vol. 38, no. 5, pp. 290–304, 2011.

[127] A. A. Mutalib and H. Hao, "Numerical analysis of FRP-composite-strengthened RC panels with anchorages against blast loads," *Journal of Performance of Constructed Facilities*, vol. 25, no. 5, pp. 360–372, 2011.

[128] A. Ghani Razaqpur, A. Tolba, and E. Contestabile, "Blast loading response of reinforced concrete panels reinforced with externally bonded GFRP laminates," *Composites Part B: Engineering*, vol. 38, no. 5-6, pp. 535–546, 2007.

[129] C. Wu, D. J. Oehlers, M. Rebentrost, J. Leach, and A. S. Whittaker, "Blast testing of ultra-high performance fibre and FRP-retrofitted concrete slabs," *Engineering Structures*, vol. 31, no. 9, pp. 2060–2069, 2009.

[130] T. M. Pham and H. Hao, "Review of concrete structures strengthened with FRP against impact loading," *Structures*, vol. 7, pp. 59–70, 2016.

[131] D. Jerome and C. Ross, "Simulation of the dynamic response of concrete beams externally reinforced with carbon-fiber reinforced plastic," *Computers & Structures*, vol. 64, no. 5-6, pp. 1129–1153, 1997.

[132] W. J. Cantwell and K. Smith, "The static and dynamic response of CFRP-strengthened concrete structures," *Journal of Materials Science Letters*, vol. 18, no. 4, pp. 309–310, 1999.

[133] M. A. Erki and U. Meier, "Impact loading of concrete beams externally strengthened with CFRP laminates," *Journal of Composites for Construction*, vol. 3, pp. 117–124, 3 1999.

[134] T. Tang and H. Saadatmanesh, "Behavior of concrete beams strengthened with fiber-reinforced polymer laminates under impact loading," *Journal of Composites for Construction*, vol. 7, no. 3, pp. 209–218, 2003.

[135] J. Shan, R. Chen, W. Zhang, Y. Xiao, W. Yi, and F. Lu, "Behavior of concrete filled tubes and confined concrete filled tubes under high speed impact," *Advances in Structural Engineering*, vol. 10, no. 2, pp. 209–218, 2007.

[136] N. Uddin, J. D. Purdue, and U. Vaidya, "Feasibility of thermoplastic composite jackets for bridge impact protection," *Journal of Aerospace Engineering*, vol. 21, no. 4, pp. 259–265, 2008.

[137] X. Yan and S. Yali, "Impact behaviors of CFT and CFRP confined CFT stub columns," *Journal of Composites for Construction*, vol. 16, no. 6, pp. 662–670, 2012.

[138] A. Q. Bhatti, N. Kishi, and K. H. Tan, "Impact resistant behaviour of RC slab strengthened with FRP sheet," *Materials and Structures*, vol. 44, no. 10, pp. 1855–1864, 2011.

[139] J. Radin and W. Goldsmith, "Normal projectile penetration and perforation of layered targets," *International Journal of Impact Engineering*, vol. 7, pp. 229–259, 1988.

[140] G. Ben-Dor, A. Dubinsky, and T. Elperin, "On the order of plates providing the maximum ballistic limit velocity of a layered armor," *International Journal of Impact Engineering*, vol. 22, no. 8, pp. 741–755, 1999.

[141] G. Ben-Dor, A. Dubinsky, and T. Elperin, "Effect of the order of plates on the ballistic resistance of ductile layered shields perforated by nonconical impactors," *Journal of mechanics of materials and structures*, vol. 1, pp. 1161–1177, 2006.

[142] E. A. Flores-Johnson, M. Saleh, and L. Edwards, "Ballistic performance of multi-layered metallic plates impacted by a 7.62-mm APM2 projectile," *International Journal of Impact Engineering*, vol. 38, no. 12, pp. 1022–1032, 2011.

[143] R. B. Bogoslovov, C. M. Roland, and R. M. Gamache, "Impact-induced glass-transition in elastomer coatings," *Applied Physics Letters*, vol. 90, 2007.

[144] S. S. Sarva, S. Deschanel, M. C. Boyce, and W. Chen, "Stress-strain behavior of a polyurea and a polyurethane from low to high strain rates," *Polymer*, vol. 48, pp. 2208–2213, 2007.

[145] M. R. Amini, J. B. Isaacs, and S. Nemat-Nasser, "Experimental investigation of response of monolithic and bilayer plates to impulsive loads," *International Journal of Impact Engineering*, vol. 37, pp. 82–89, 1 2010.

[146] M. R. Amini, A. V. Amirkhizi, and S. Nemat-Nasser, "Numerical modeling of response of monolithic and bilayer plates to impulsive loads," *International Journal of Impact Engineering*, vol. 37, pp. 90–102, 1 2010.

[147] K. Ackland, C. Anderson, and T. D. Ngo, "Deformation of polyurea-coated steel plates under localised blast loading," *International Journal of Impact Engineering*, vol. 51, pp. 13–22, 2013.

[148] L. Xue, W. Mock, and T. Belytschko, "Penetration of DH-36 steel plates with and without polyurea coating," *Mechanics of Materials*, vol. 42, no. 11, pp. 981–1003, 2010.

[149] Z. Xue and J. W. Hutchinson, "Neck retardation and enhanced energy absorption in metal–elastomer bilayers," *Mechanics of Materials*, vol. 39, no. 5, pp. 473–487, 2007.

[150] Z. Xue and J. W. Hutchinson, "Neck development in metal/elastomer bilayers under dynamic stretchings," *International Journal of Solids and Structures*, vol. 45, no. 13, pp. 3769–3778, 2008.

[151] S. A. Morales, A. B. Albrecht, H. Zhang, K. M. Liechti, and K. Ravi-Chandar, "On the dynamics of localization and fragmentation: V. Response of polymer

coated Al 6061-O tubes," *International Journal of Fracture*, vol. 172, no. 2, pp. 161–185, 2011.

[152] H. Zhang, K. M. Liechti, and K. Ravi-Chandar, "On the dynamics of localization and fragmentation - III. Effect of cladding with a polymer," *International Journal of Fracture*, vol. 155, no. 2, pp. 101–118, 2009.

[153] M. S. Hoo Fatt, X. Ouyang, and R. J. Dinan, "Blast Response of Walls Retrofitted with Elastomer Coatings," presented at the Structures under Shock and Impact VIII: Proceedings of the Eighth International Conference on Structures under Shock and Impact (Crete, Greece), 2004.

[154] J. Baylot, B. Bullock, T. Slawson, and S. Woodson, "Blast Response of Lightly Attached Concrete Masonry Unit Walls," *Journal of Structural Engineering*, vol. 131, no. 8, pp. 1186–1193, 2005.

[155] S. Raman, M. Jamil, T. Ngo, P. Mendis, and T. Pham, "Preliminary investigation on the behaviour of RC panels with polymer coatings under blast loads," presented at the Proceedings of the 20th Australasian Conference on the Mechanics of Structures & Materials (Toowoomba, Australia), 2008, pp. 637–643.

[156] S. Raman, M. Jamil, T. Ngo, P. Mendis, and T. Pham, "Retrofitting of RC panels subjected to blast effects using elastomeric polymer coatings," presented at the Concrete Solutions - Proceedings of Concrete Solutions, 5th International Conference on Concrete Repair (Belfast, UK), 2014, pp. 353–360.

[157] N. Iqbal, P. K. Sharma, D. Kumar, and P. K. Roy, "Protective polyurea coatings for enhanced blast survivability of concrete," *Construction and Building Materials*, vol. 175, pp. 682–690, 2018.

[158] M. Grujicic, B. P. D'Entremont, B. Pandurangan, J. Runt, J. Tarter, and G. Dillon, "Concept-level analysis and design of polyurea for enhanced blast-mitigation performance," *Journal of Materials Engineering and Performance*, vol. 21, no. 10, pp. 2024–2037, 2012.

[159] N. L. Carey, J. J. Myers, D. Asprone, C. Menna, and A. Prota, "Polyurea Coated and Plane Reinforced Concrete Panel Behavior under Blast Loading: Numerical Simulation to Experimental Results," *Trends in Civil Engineering and its Architecture*, vol. 1, no. 4, pp. 1–12, 2018.

[160] N. Kambouchev, L. Noels, and R. Radovitzky, "Nonlinear compressibility effects in fluid-structure interaction and their applications on the air-blast loading of structures," *Journal of Applied Physics*, vol. 100, 2006.

[161] J. C. Simo and J. W. Ju, "Strain- and stress-based continuum damage models – I. Formulation," *International Journal of Solids and Structures*, vol. 23, no. 7, pp. 821–840, 1987.

[162] J. C. Simo and J. W. Ju, "Strain- and stress-based continuum damage models – II. Computational aspects," *International Journal of Solids and Structures*, vol. 23, no. 7, pp. 841–869, 1987.

[163] J. Mazars and G. Pijaudier-Cabot, "Continuum damage theory-application to concrete," *ASCE Journal of Engineering Mechanics*, vol. 115, no. 2, pp. 345–365, 1989.

[164] F. Gatuingt and G. Pijaudier-Cabot, "Coupled damage and plasticity modelling in transient dynamic analysis of concrete," *International Journal of Numerical and Analytical Methods in Geomechanics*, vol. 26, pp. 1–24, 2002.

[165] W. B. Kratzig and R. Polling, "An elasto-plastic damage model for reinforced concrete with minimum number of material parameters," *Computers and structures*, vol. 82, pp. 1201–1215, 2004.

[166] D. A. Hordijk, "Local approach to fatigue of concrete," PhD thesis, Delft University of Technology, 1991.

[167] V. Birtel and P. Mark, "Parameterised finite element modelling of RC beam shear failure," presented at the ABAQUS User's Conference (Taiwan), 2006.

[168] J. Lubliner, J. Oliver, S. Oller, and E. Onate, "A plastic-damage model for concrete," *International Journal of Solids and Structures*, vol. 25, pp. 229–329, 1989.

[169] J. Lee and G. L. Fenves, "A plastic-damage model for cyclic loading of concrete structures," *Journal of Engineering Mechanics*, vol. 124, no. 8, pp. 892–900, 1998.

[170] I. Mohagheghian, "Impact response of polymers and polymer nanocomposites," PhD thesis, University of Cambridge, 2013.

[171] ASTM, *D1822-13 Standard Test Method for Tensile-Impact Energy to Break Plastics and Electrical Insulating Materials*, 2013.

[172] T. K. Mauchien, "A fracture mechanics approach to accelerated life testing for cathodic delamination at polymer/metal interfaces," Master's thesis, University of Texas at Austin, 2013.

[173] M. Di Paola, A. Pirrotta, and A. Valenza, "Visco-elastic behavior through fractional calculus: An easier method for best fitting experimental results," *Mechanics of Materials*, vol. 43, no. 12, pp. 799–806, 2011.

[174] K. D. Papoulia, V. P. Panoskaltsis, N. V. Kurup, and I. Korovajchuk, "Rheological representation of fractional order viscoelastic material models," *Rheologica Acta*, vol. 49, no. 4, pp. 381–400, 2010.

[175] F. Dinzart and P. Lipinski, "Improved five-parameter fractional derivative model for elastomers," *Archives of Mechanics*, vol. 61, no. 6, pp. 459–474, 2009.

[176] C. E. Needham, *Blast Waves*. Berlin Heidelberg: Springer-Verlag, 2010.

[177] A. Chen, L. A. Louca, and A. Y. Elghazouli, "Behaviour of cylindrical steel drums under blast loading conditions," *International Journal of Impact Engineering*, vol. 88, pp. 39–53, 2016.

[178] US National Counterterrorism Centre (NCTC). (2006). Bomb threat stand-off distance chart, [Online]. Available: `https://www.dni.gov/files/NCTC/documents/features_documents/2006_calendar_bomb_stand_chart.pdf` (visited on 12/12/2018).

[179] British Standards Institution, *BS 8110-1:1997: Structural use of concrete. Code of practice for design and construction*, 1997.

[180] European Committee for Standardization (CEN), *BS EN 1992-1-1: 2004: Eurocode 2: Design of concrete structures*, 2004.

[181] S. Timoshenko, D. H. Young, and J. W. Weaver, *Vibration Problems in Engineering*, 4th ed. New York, USA: John Wiley and Sons, 1974.

[182] D. Mohotti, T. Ngo, S. N. Raman, M. Ali, and P. Mendis, "Plastic deformation of polyurea coated composite aluminium plates subjected to low velocity impact.," *Materials and Design*, vol. 56, pp. 696–713, 2014.

[183] D. Mohotti, T. Ngo, S. N. Raman, and P. Mendis, "Analytical and numerical investigation of polyurea layered aluminium plates subjected to high velocity projectile impact.," *Materials and Design*, vol. 82, pp. 1–17, 2015.

[184] I. Mohagheghian, G. J. McShane, and W. J. Stronge, "Quasi-static and impact perforation of polymer-metal bi-layer plates by a blunt indenter.," *Thin-Walled Structures*, vol. 117, pp. 35–48, 2017.

[185] Teychenne, D. C. and Franklin, R. E. and Erntroy, H. C., *Design of normal concrete mixes*, 1975.

[186] R. A. Serway and J. W. Jewett, *Physics for scientists and engineers*, 4th ed. Belmont, CA, USA: Thomson-Brooks/Cole, 2004.

[187] G. A. Holzapfel, *Nonlinear Solid Mechanics: A Continuum Approach for Engineering*. Chichester, England: John Wiley and Sons, Ltd., 2000.

[188] N. M. Hawkins, "The bearing strength of concrete loaded through rigid plates," *Magazine of concrete research*, vol. 20, pp. 31–40, 62 1968.

[189] F. An, "Modelling of FRP-concrete interfacial bond behavior," PhD thesis, University of Edinburgh, 2015.

[190] A. Hillerborg, M. Modeer, and P. E. Petersson, "Analysis of crack formation and crack growth in concrete by means of fracture mechanics and finite elements," *Cement and Concrete Research*, vol. 6, pp. 773–782, 1976.

[191] ABAQUS, *ABAQUS 6.12 Example Problems Manual, Volume 1: Static and Dynamic Analyses*. Providence, RI, USA: Dassault Systemes, 2011.

[192] R. Malm, "Shear Cracks in Concrete Structures Subjected to in-plane stresses," PhD thesis, Royal Institute of Technology (KTH), 2006.

[193] Y. Jankowiak and T. Lodygowski, "Identification of parameters of concrete damaged plasticity constitutive model," *Foundations of Civil and Environmental Engineering*, vol. 6, pp. 53–69, 1 2005.

[194] C. Wu, D. J. Oehlers, M. Rebentrost, J. Leach, and A. S. Whittaker, "Blast testing of ultra-high performance fibre and FRP-retrofitted concrete slabs," *Engineering Structures*, vol. 31, pp. 2060–2069, 2009.

[195] C. Mougeotte, P. Carlucci, S. Recchia, and H. Ji, "Novel approach to conducting blast load analyses using ABAQUS/Explicit-CEL," presented at the Proceedings of 2010 Simulia Customer Conference (Providence, Rhode Island, USA), 2007.

[196] I. N. Sneddon, "Boussinesq problem for a flat-ended cylinder," *Proceedings of the Cambridge Philosophical Society*, vol. 42, pp. 29–39, 1946.

[197] Veryst Engineering, *MCalibration, Version* 4.6.0, 2017.